STRUCTURE-PROPERTY RELATIONSHIPS: MODEL STUDIES ON MELT EXTRUDED UNIAXIALLY ORIENTED HIGH DENSITY POLYETHYLENE FILMS HAVING WELL DEFINED MORPHOLOGIES

by

Hongyi Zhou

Dissertation submitted to the faculty of the
Virginia Polytechnic Institute and State University
in partial fulfillment of the requirements for the degree of

DOCTOR OF PHILOSOPHY
in
MATERIALS ENGINEERING SCIENCE

APPROVED:

Garth L. Wilkes, Chairman

David A. Dillard

Ronald G. Kander

Hervé Marand

Thomas C. Ward

February 1997
Blacksburg, Virginia

Keywords: Polyethylene, Tensile property, Mechanical relaxation, Creep, Lamellar thickness

STRUCTURE-PROPERTY RELATIONSHIPS: MODEL STUDIES ON MELT EXTRUDED UNIAXIALLY ORIENTED HIGH DENSITY POLYETHYLENE FILMS HAVING WELL DEFINED MORPHOLOGIES

by

Hongyi Zhou

Garth L. Wilkes, Chairman

Materials Engineering Science Program

ABSTRACT

High density polyethylene (HDPE) films having simple and well-defined stacked lamellar morphology, either with or without a distinct presence of row-nucleated fibril structures, have been utilized as *model* materials to carry out investigations on solid state structure-property relationships. Four different subjects that were addressed are: 1) mechanical properties and deformation morphologies, 2) orientation anisotropy of the dynamic mechanical α relaxation, 3) orientation dependence of creep behavior, and 4) crystalline lamellar thickness and its distribution.

For the first three topics, appropriate mechanical tests, including tensile (INSTRON), creep (TMA), and dynamic mechanical (DMTA) tests, were performed at *different angles with respect to the original machine direction (MD)* of the melt extruded films; morphological changes as a result of these mechanical tests were detected by WAXS, SAXS, and TEM. For the forth topic, crystalline lamellar thickness and its distribution were determined by DSC, SAXS, TEM and AFM experiments.

In the *large strain deformation* study (chapter 4.0), samples were stretched at 00°, 45° and 90° angles with respect to the original MD. A distinct orientation dependence of the tensile behavior was observed and *correlated* to the corresponding deformation modes and morphological changes, namely 1) lamellar separation and fragmentation by chain slip for the 00° stretch, 2) lamellar break-up via chain pull-out for the 90° stretch, and 3) lamellar shear, rotation

and break-up through chain slip and/or tilt for the 45° stretch. A strong strengthening effect was observed for samples with row-nucleated fibril structures at the 00° stretch; whereas for the 90° stretch, the presence of such structures significantly limited deformability of the samples.

In the *dynamic strain mechanical* α *relaxation* study (chapter 5.0), samples were tested at nine different angles with respect to the original MD, and the morphologies of samples *before* and *after* the dynamic tests were also investigated. The mechanical dispersions for the 00° and 90° tests were believed to arise essentially from the crystalline phase, and they contain contributions from two earlier recognized sub-relaxations of α_I and α_{II}. While for the 45° test, in addition to a high temperature α_{II} relaxation, a interlamellar shear induced low temperature mechanical relaxation was also observed. It is concluded that the low temperature relaxation is related to the characteristics of the interface between the crystalline lamellae and amorphous layers.

In the *small strain creep* study (chapter 6.0), samples were tested at the 00°, 45° and 90° angles at the original MD. Both creep strain and creep rate for samples at the three angles were very different. An Eyring-rate model was utilized to analysis the observed creep behavior, and structural parameters associated with this model, including population of creep sites, activation energy and volume, were obtained by fitting the experimental data to the Eyring-rate equation. It was concluded that the plateau creep rate in these model materials is primarily controlled by the density and physical state of tie-chains in the amorphous phase.

For the lamellar thickness and distribution study, DSC, SAXS, TEM and AFM experiments were conducted for samples having a well-defined stacked lamellar morphology. It was found that the most probable lamellar thickness from SAXS and TEM agreed very well; however, these values did not match with those obtained by DSC and AFM. It was pointed out that the use of DSC to determine lamellar thickness and distribution is so sensitive to heating rate and numerical values for the parameters in the Gibbs-Thomson equation that it is not believed to be suitable for quantitative analysis.

ACKNOWLEDGMENTS

First and foremost, I would like to thank my advisor, Dr. Garth. L. Wilkes, for his guidance in my graduate study and research at VPI. He has been an excellent *educator* who always cares about students. Working with him has been a wonderful and rewarding experience. Likewise, I would like to thank Drs. Dillard, Kander, Marand and Ward for serving as my committee members, and their advises have been greatly appreciated.

All the members in Dr. Wilkers' research group, Bryan, Christ, David, Jianye, Kurt, Rob, Ta-hua, Varun, and Watson, are acknowledged for their helping hand in all kinds of experiments and discussions on many subjects.

Thanks are due to the sponsors for my dissertation research: Hoechst Celanese Corporation and Virginia Center of Innovative Technology, for their kindly providing materials used in the experiment and financial support.

I would like to thank my family, my wife Yumei and my son Boyang, for their patience to go through this endeavor hand-in-hand with me. Without their dearly accompaniment, both physically and spiritually, there would be no such an achievement. Also, I would like to thank my parents for their understanding. Without their support and encouragement, all I could have today is just a dream but not the reality of an advanced education.

Finally, I would like to thank those, who know who they are, for making the past four and half year a valuable time in my life..

TABLE OF CONTENTS

LIST OF FIGURES

LIST OF TABLES

Chapter 1.0 INTRODUCTION

Understanding the relationships between morphology and properties is of great importance with respect to the application of polymeric materials, particularly for semicrystalline polymers due to their diverse morphologies. From an engineering point of view, the successfulness of a product's performance depends upon the properties it displays which often depends, to a major degree, on the morphology it possesses. From a research point of view, knowing the exact molecular mechanisms by which the structure and the properties are interrelated is a great challenge and has been the basis of many studies.

There are a variety of morphologies for semicrystalline polymers due to different thermal treatments and processing conditions. Although the pervasive morphology for unoriented semicrystalline polymers is often that of the spherulite, it is not an "ideal" candidate for the study of structure-property relationships, because of its complex aggregation of crystalline lamellae and of amorphous regions, as well as the boundary regions between spherulites. Therefore, in order to more directly address the effect of crystalline morphology on the mechanical behavior of a given polymer, it is desirable to use relatively simple and well-defined morphological systems.

Furthermore, it is a common practice to orient semicrystalline polymers to a certain extent to ensure the desired properties. The major approaches include either inducing the orientation prior to the crystallization, such as applying an elongational and/or shear flow in the melt, or promoting the orientation afterwards, i.e. plastically deforming the materials in the solid state. Although these two approaches involve very different physical processes, they both result in a similar distinct anisotropy of the morphology as well as the mechanical property for the polymer in question. Therefore, it is also important to understand this orientation dependence of structure-property relationships.

Many model polymeric systems have been used in the past. Single crystals, highly drawn fibers, thin films with single- or double-texture, and specially prepared ultra-thin ultra-drawn films are some examples. In the studies presented in this dissertation, however, a different model morphological system of high density polyethylene (HDPE) was used. The HDPE films are

extruded from the melt under suitable processing conditions to promote crystalline orientation along the machine direction (MD), but essentially there is no significant orientation generated in the amorphous phase. Detailed investigations on the orientation state of the crystalline phase and the amorphous phase for different molecular weight and distribution as well as under different processing conditions have been the focus of a previous dissertation study[1]. Specifically, two kinds of simple and well-defined morphologies are of interest to this dissertation. One is a stacked lamellar morphology, in which the crystalline lamellae are well stacked with their normals more or less parallel to the MD. The other morphology has a distinct presence of row-nucleated fibril structures in the matrix of the well-stacked crystalline lamellae.

The principle objective of this doctoral research is to investigate the orientation dependence of mechanical properties, including large strain tensile properties (INSTRON), the small dynamic strain mechanical α relaxation (DMTA), and small strain creep behavior (TMA), of the model HDPE films. All the above-mentioned mechanical tests were carried out *at different angles with respect to the original MD* of the extruded films, and the morphological changes induced by these mechanical tests were investigated by wide angle X-ray scattering (WAXS), small angle X-ray scattering (SAXS) and transmission electron microscopy (TEM). In addition, the HDPE films having a stacked lamellar morphology were also utilized as a model material to study crystalline lamellar thickness and its distribution by four different techniques, including differential scanning calorimetry (DSC), SAXS, TEM and atomic force microscopy (AFM).

This dissertation is documented in the following format: It begins with chapter 2.0 that presents a *general* overview of the literature in the area of crystalline morphology and mechanical properties for semicrystalline polymers. Its objectives are to help the reader build some fundamentals related to the studies undertaken by the author. The model HDPE films having relative simple and well-defined morphologies are then introduced in chapter 3.0, which are founded on the previous characterization study of these materials[1]. Chapters 4.0, 5.0 and 6.0 present the studies on tensile properties, the dynamic mechanical α relaxation and creep behavior, respectively. The study on crystalline lamellar thickness and its distributions is provided in chapter 7.0. A summery of the complete dissertation is given in chapter 8.0. Since chapters 4.0 ~ 7.0 have

been written as manuscripts for publications in different scientific journals (*Journal of Materials Science, Macromolecules, Journal of Polymer Science - Physics Edition* and *Polymer*), these somewhat "expanded" manuscripts form the respective chapters 4.0 to 7.0. Hence, the corresponding chapters are essentially "manuscript-based", and therefore, certain material may be repeated in the different chapters. References are given at the end of each chapter.

Reference

1. Ta-Hua Yu, *Ph.D. Dissertation,* Virginia Tech, May 1996

Chapter 2.0 LITERATURE REVIEW

The study of structure-property relationships in semicrystalline polymers has been one of the main themes in polymer science, as evidenced by the extensive body of literature which has dealt with their morphologies and/or properties. Although a complete review on topics like this broad and active is not attempted, some basics on these two subjects need indeed to be discussed and therefore can serve as background for the investigations presented in chapters 4.0 ~ 7.0 of this dissertation. Complementary reviews with more detailed information about each specific study will be given in corresponding chapter dealing with that particular subjects.

The first part of this review addresses the morphology in semicrystalline polymers from the following four perspectives: 1) chain-folding crystalline lamellae, which are unique crystalline structures for polymer crystals; 2) spherulites, which are the pervasive crystalline aggregates for semicrystalline polymers crystallized under quiescent conditions; 3) row structure, which represents the morphology for semicrystalline polymers crystallized under elongational flow conditions; 4) microfibril morphology, which is typical for ultra-drawn semicrystalline polymers in the solid state.

In the second part of this chapter, some important properties concerned with the engineering applications of semicrystalline polymers are discussed, and they include 1) tensile stress-strain properties (large strain), 2) dynamic mechanical relaxation (small dynamic strain), and 2) creep behavior (small strain). Wherever possible, the main focus of this dissertation, i.e. structure-property relationships, will be emphasized. A detailed review on crystalline lamellar thickness and its distribution is not included in this chapter, and it will be provided separately in the introduction section of chapter 7.0 of this document.

2.1 Morphologies in Semicrystalline Polymers

The morphology of semicrystalline polymers has been extensively studied over the past four decades, and excellent books[1-4] and review papers[5-8] on this topic are available. The following

cursory discussion provided here is aimed at familiarizing readers with the variety of morphologies of crystalline polymers generated under different conditions, by quoting HDPE as an example. The morphologies addressed in this review will include those crystallized from either solution or the melt state, either with or without external flow, and those undergone a large extent of plastic deformation in the solid state. Most of the fundamentals discussed in this section will be utilized in one or more of the studies which are presented in chapters 4.0 ~ 7.0 of this dissertation.

2.1.1 Crystalline Lamellae

In the 1950's, based on the remarkable work by Jaccodine[9], Till[10], Fischer[11], and Keller[12] on polyethylene (PE) samples crystallized from dilute solutions, the concept of chain-folding lamellae, initially formulated by Storks[13], was proved and established for polymer crystals. Since then, a massive amount of research has been carried out with an emphasis on samples crystallized from the melt state, and the results accumulated from these studies have further confirmed the existence of the chain-folding lamellae, as reviewed by Phillips[6], Basset[7], Baham[8] as well as intensively discussed in a meeting of the Faraday Discussion in 1979[14]. Currently, single crystals of chain-folding lamellae are used not only as ideal materials to investigate local chain packing, crystal structure and defect structures in the crystalline phase, but also as suitable materials to study crystallization kinetics, crystal growth and plastic deformation.

The main features of crystalline lamellae can be illustrated by a PE single crystal lamella grown from dilute solutions, as shown in Fig. 2.1[8]. The polymer crystal is slightly pyramidal with an overall tent-like structure in a lozenge shape (Figs. 2.1a-d). From the electron diffraction pattern (central figure in Fig. 2.1a-d), the polymer chains are found to be more or less parallel to the thickness direction of the lamella; therefore, the polymer chains are believed to be folded back and forth on the upper and lower lamellar surfaces, (Fig. 2.1e). In the central part of the lamella (lamellar core), polymer chains are in an all-trans conformation, and they form a orthorhombic crystal unit cell with polymer chains parallel to the c-axis[4] (Fig. 2.1f). On the

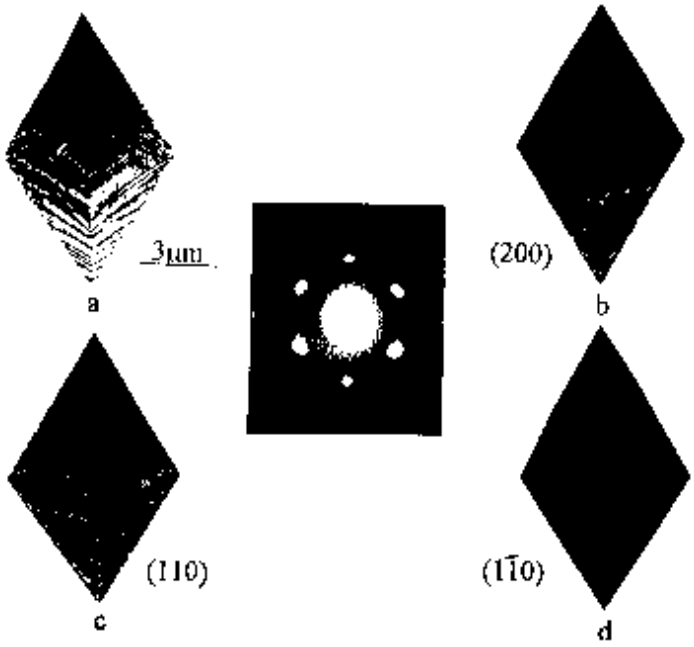

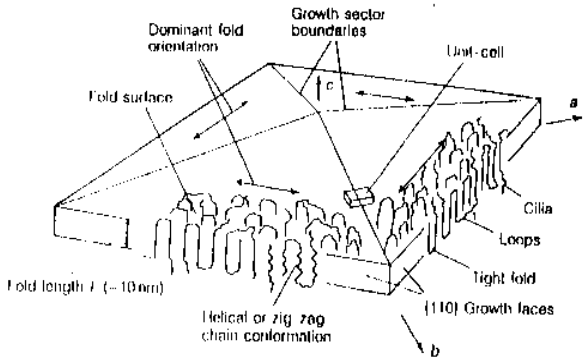

e

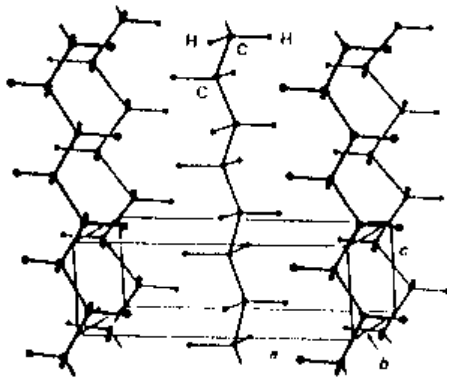

f

Figure 2.1 Morphological features of lamellar crystals. (a-d): selected area electron diffraction pattern (center) of a PE single crystal seen in bright field (a) and dark field (b-d) by different diffraction spots indicated; [8] (e): schematic representation of a PE single crystal with main features of molecular conformation; [8] (f): the orthorhombic unit cell of PE.[4]

surfaces of the lamella (chain-folding surfaces) reside dangling chain ends (cilia) and different types of chain folds (tight folds and loose loops), as illustrated in Fig. 2.1e. It should be pointed out that the drawing in Fig. 2.1e is a bit of speculative, since the exact nature of chain folding is not yet completely understood.

Lamellar Core

This part of a lamella provides an ideal specimen to carry out crystallographic studies for polymer crystals[4]. Important information obtained from such investigations includes chain conformation, unit cell structure, defect structures, etc. The conformation of a polymer chain in a crystal is primarily governed by its chemical sequence and configuration[4], i.e. *intramolecular* interactions. However, intermolecular interactions within the crystal lattice, such as hydrogen bonding, can also influence chain conformation[4].

Most polymer chains adopt a helical conformation in the crystalline phase, due to the balance between covalent bonds, intramolecular rotational potentials and, sometimes, non-bonded intermolecular interactions[3]. The helices usually have simple symmetrical conformations, such as a 2_1 helix (commonly known as all-trans conformation) for PE, a 3_1 helix for isotactic polypropylene (*i*-PP) and a 4_1 helix for poly(4,4-dimethyl-1-pentene). Furthermore, conformation polymorphism for a given polymer chain also exist[3,4]. Typical examples for chain conformation polymorphism include poly(tetrafluoroethylene) (PTFE) - a 13_6 helix at temperatures below 19°C and another slightly less twisted 15_7 helix above this temperature, and poly(vinylidenefluoride) (PVDF) - an all-trans conformation and two other conformations with different sequences of trans- and gauche-bonds[3].

Parallel packing of polymer chain helices in a crystal lattice results in a highly anisotropic structure, i.e., the chain axis (usually chosen to be the crystal c-axis), which is characterized by covalent bonding along the helical backbone, is distinctly different from all other orientations, which are characterized by weak secondary bonding. This feature excludes the presence of simple cubic structure for all polymer crystals[3,4]. Chain packing is usually driven by optimizing

intermolecular interactions. For example, the formation of hydrogen bonds in polycaprolactam (Nylon 6) results in a sheet-like structure with essentially three different forces within the crystal lattice - covalent bonding along the chain axis, interchain hydrogen bonding within the sheets, and weak Van der Walls force between the sheets [4].

Crystal polymorphism is also a frequent event for polymers crystals, partially as a consequence of chain conformation polymorphism[3,4]. A good example for crystal polymorphism is poly-1-butene (PB) - hexagonal, tetragonal, and orthorhombic unit cells corresponding to 3_1, 13_4 and 4_1 helices in the respective crystal lattices[8]. For PE, given the simplest backbone chemistry, three different types of crystal structures have also been reported[8]: a orthorhombic unit cell with a = 0.747nm, b = 0.494nm and c = 0.253nm; a monoclinic unit cell with a = 0.804nm, b = 0.479nm, c = 0.253nm and $\gamma = 107°9'$; a hexagonal unit cell with a = 0.488nm and c being equivalent to the chain length. For the three crystalline phases, the orthorhombic structure is the most encountered crystalline form; the monoclinic structure often exists in a plastically deformed crystalline material; the hexagonal structure has been observed to occur in highly oriented materials at temperatures close to the melting temperature as well as materials crystallized under high pressure.[1]

Defect Structures

A common type of disorder for polymer crystals is the "up and down" directional disorder of the helical chains[15]. Using *i*-PP as an example, the unit cells are statistically occupied by either left- and right-handed 3_1 helices, and packing defects can be created or annihilated by the replacement of a left-handed helix with a right-handed helix, or *vice versa*, through a translational motion along the c-axis of the crystal by half the pitch (*helical jump*)[16,17]. In the case of crystals with a 2_1 helical chain conformation (e.g. PE), departure from the perfect all-trans conformation can generate a *kink*, caused by the introduction of g^+ and g^- along the all-trans conformation, or even a *jog*, caused by a severe shift of the chain axis such that two segments of the chain occupy two different crystal sites along either the crystal a- or b-axes[18,19].

Dislocations (both edge and screw) are another common type of defects[15]. Edge dislocations correspond to the creation or annihilation of one or several crystallographic planes in

a crystal lattice, and a convenient means to asses the existence of edge dislocations is by the change of Moiré patterns produced by two overlapping and slightly rotated (off-set) single crystals[20]. It has been found that for polymer crystals the concentration of edge dislocations is relative low, ca. $10^{11}m^{-2}$ for as-grown PE single crystal from solution, and it may increase by almost 1000 times upon annealing[21,22]. Screw dislocations, on the other hand, is caused by a mismatch between two parts of the crystal lattice, and its existence can be accounted for by the spiral growth steps around the center of a single crystal[23]. It has been recognized that the magnitude of the Burgers vector of a screw dislocation is equivalent to the crystalline lamellar thickness - in sharp contrast with atomic crystals in which the Burgers vector is often as small as the crystallographic dimensions[24].

The strongest indication of the existence of crystal defects is the broadening of the {hk0} reflections from the WAXS peaks for semicrystalline polymers. A straightforward calculation based on the Scherrer equation shows that the lateral dimensions for a PE crystal lamella is about 30nm[25]; this number is much less than the observed size of the single crystals, which is usually in the order of microns[26]. Therefore, *mosaic block* sub-structures within crystalline lamellae were proposed to account for this discrepancy. However, such structures have not yet been observed directly by electron microscopy[27,28]. On the other hand, the same line broadening phenomena in WAXS experiments has been reappraised from the viewpoint of the defect structure distributions in polymer crystals, i.e. the *paracrystalline* state of polymer crystals[30]. A schematic representation of the paracrystalline state of a crystal structure with a variety of defects, such as chain ends, kinks, voids, etc., is shown in Fig. 2.2.

Chain Folding and Chain-Folding Surface

The exact nature of the chain folding has been controversial and is still open to debate, due to the fact that very few definitive experimental probes are available to detect the structural features on this surface, although recent work based on atomic force microscopy (AFM) have made some promising advances in this aspect[31-33]. On the one hand, the regularity and perfection

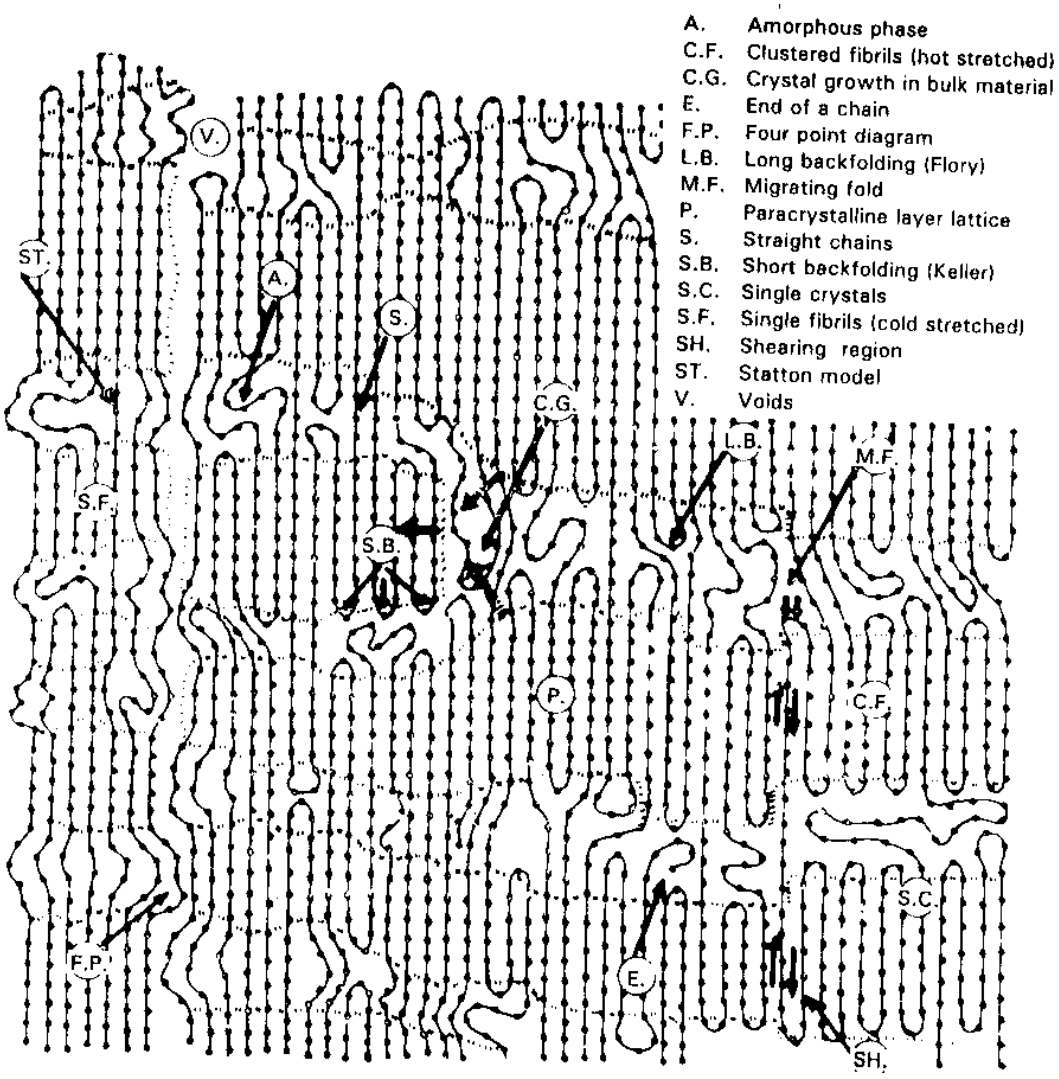

Figure 2.2 Schematic illustration of different type of defects in a linear PE paracrystal [30].

of polymer crystals strongly suggest a high degree of regularity on the chain-folding surface, and the adjacent re-entry model (Fig. 2.3a), with sharp or tightly folded chains re-entering the lamella within specific planes, was so proposed originally[34]. On the other hand, the random coil conformation of the polymer chains prior to crystallization seems to imply that the chain-folding surface is essentially amorphous in nature, as postulated by the switchboard model (Fig. 2.3b), with random re-entry and irregular loose folds allowing the chains complete free in direction before re-entering the lamella[35]. It is generally agreed, at present, that the chain-folding surface is somewhat between the above two extremes and varies significantly according to the crystallization conditions[36].

Small angle neutron scattering (SANS) has been a major technique the allows the determination of chain trajectory in the solid state[37]. For solution-grown single crystals, SANS data are quite consistent with the adjacent re-entry model[38]. Furthermore, it was found that the radius of gyration is proportional to the one tenth power of the weight average molecular weight[39], instead of the one half power of the weight average molecular weight as expected for Gaussain chains. Based on this finding, a superfolding adjacent re-entry model was proposed (Fig. 2.3c), where two chains on the same folding strip meet and then continue to crystallize by folding a new strip parallel to and adjacent to the original strip[38]. In another SANS study[40], the adjacent re-entry model found failed to fit the experimental data (scattering intensity), thus the superfold model was further modified into a stem-dilute superfolding model (Fig. 2.3d)[40] to explain the data.

For melt-crystallized crystals, SANS experiments showed that the radius of gyration in solid crystalline polymers is very close to that in the melt state[13,41]; therefore, it was suggested that the random chain entanglements in the melt state must be largely preserved - implying that the original adjacent re-entry folding is an oversimplification[42]. Some analyses have predicated a non adjacent re-entry (Fig. 2.3b)[15], i.e., the stems in a given chain are separated by at least two stems from another chain. In the case of non-adjacent re-entry, the problem of overcrowding

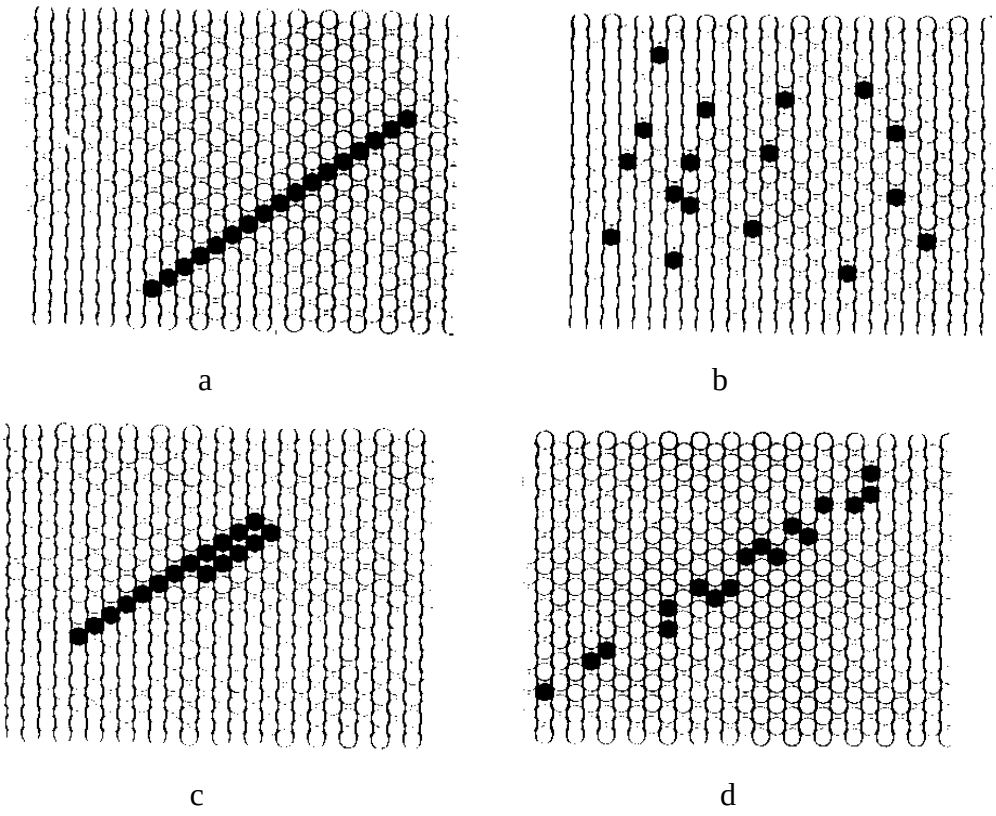

Figure 2.3 Models of stem reentry for single crystal from solution. (a): adjacent reentry with regular fold;[38] (b): random reentry with irregular folds;[35] (c): regular folds with superfolding;[39] (d): stem-dilute superfolding.[40]

near the fold surface is thought to be alleviated by the inclination of chains at an angle with respect to the fold surface (chain tilt)[43] within lamellae. However, more detailed studies have shown that the maximum known amount of chain tilt, ca. 55°[13], is still not sufficient to permit a totally non-adjacent re-entry. It has been argued that the maximum amount of non- adjacent re-entry is about one third, provided that the polymer chains can be described by Gaussian statistics in the melt state[36].

Closely related to the nature of chain folding is the physical state of the chain-folding surface, and the concept of constrained amorphous phase adjacent to the chain-folding surface[44] has been proposed. In this case, a semicrystalline polymer is considered as composed of three phases, i.e. the lamellar core, a interfacial constrained amorphous region and random amorphous regions. For PE, the existence of the interfacial zone was proposed from a study of percent crystallinity by using a combination of DSC, density column and Raman spectroscopy[45]. It was suggested that the crystallinity determined by DSC corresponds to the actual crystalline fraction, whereas that measured by density column is a *sum* of the crystalline and interfacial fractions[46]. Raman spectroscopy, on the other hand, is sensitive to all the three phases[45]. According to this and other similar studies, depending on the molecular weight and thermal treatment, 5 to 15% of the material (based on mass) may belong to the interfacial constraint amorphous phase. Along the same line is the proposal of a ridge amorphous phase, which is more pertinent for semicrystalline polymers having rigid or semi-rigid (high T_g) chains[47].

2.1.2 Spherulites

Spherulites are the most prevalent morphology for melt-crystallized polymers under quiescent conditions. It has been well-established that the crystalline lamellae in a spherulite are embedded in a matrix of amorphous material; they grow out from a common nucleus and are often twisted about the radial growth directions, as shown in Fig. 2.4[15]. Under polarized optical microscope, a spherulite often displays the characteristic Maltese cross extinction pattern and, sometimes, regular concentric banding as well. Both features can be explained by the

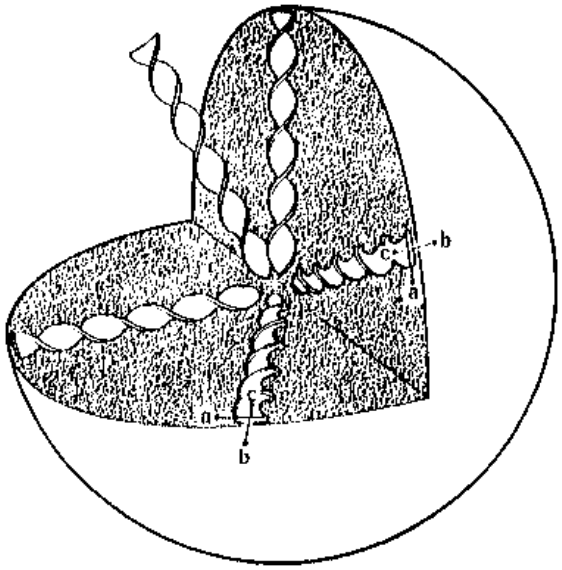

Figure 2.4 Schematic illustration of a spherulite showing the crystal orientation.[15]

birefringent nature of polymer chains. The Maltese cross extinction pattern arises from the coincidence of the principle optical axis of the crystal with the extinction direction of the polarizer and analyzer used in optical microscope. The regular concentric bands, on the other hand, is due to a regular twist of radiating lamellae along the growth directions[48].

The development of a spherulite is believed to be through several steps (Fig. 2.5a)[1]. First, a chain-folding monolayer single lamella fans out by branching at its ends and grows into sheaf-like multilayered lamellae. Further radial growth of the intermediate lamellar aggregate leads to a spherical and symmetric arrangement of ribbon-like lamellae. During the growth of the spherulite, the lamellae may branch by developing adjacent "shoots" at small angles with each other to satisfy the necessary requirement of spacing filling. The remaining material between the branches may solidify at a later stage by subsequent secondary crystallization, or simply remain amorphous. Depending on the characteristics of branching, two types of spherulites have been reported as shown in Figs 2.5b and c[1]. Figure 2.5b represents a heterogeneiously nucleated complex crystal aggregate with many substructures radiating in all directions, whereas Fig. 2.5c represents the development of a spherulite from a small initial crystal lamella.

For PE, it has been recognized that the crystal b-axis is parallel to the radial growth direction, and the crystal a- and c-axes are perpendicular to this direction[49]. The chain-folding plane for lamellae in spherulites has been found to be the {100} type, instead of the {110} type as in the case of solution-grown single crystal lamellae[50,51]. Interestingly, the transformation between these two types of chain-folding planes has been reported[52]. Furthermore, large degree of chain tilt with respect to chain-folding surface have been noted, and this is consistent with the more constrained environment of the crystalline lamellae within melt crystallized spherulites, as compared with the solution-grown lamellae[53].

More importantly, the lamellae in spherulites are believed to be interconnected by tie-chains that run from one lamella to another or even from one spherulite to another[54]. The existence of tie-chains was initially proposed to account for the reasonable toughness of semicrystalline polymers with spherulitic morphology - i.e., they can often undergo a large amount of plastic deformation under tensile stress. Direct evidence for the significant

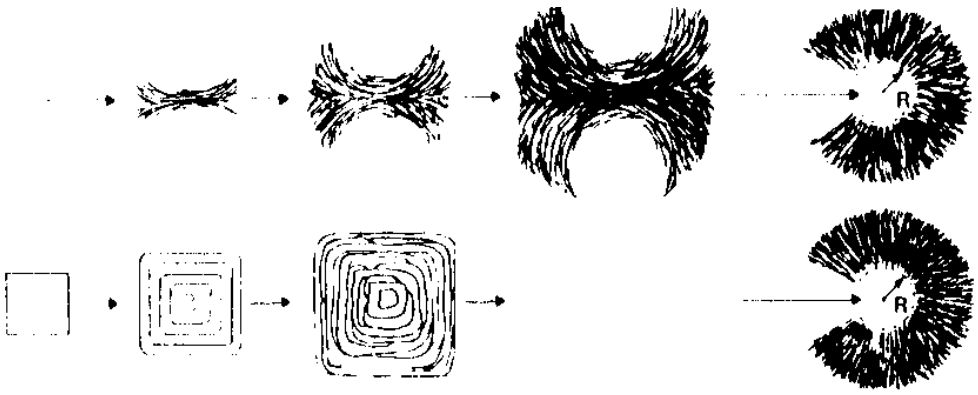

a

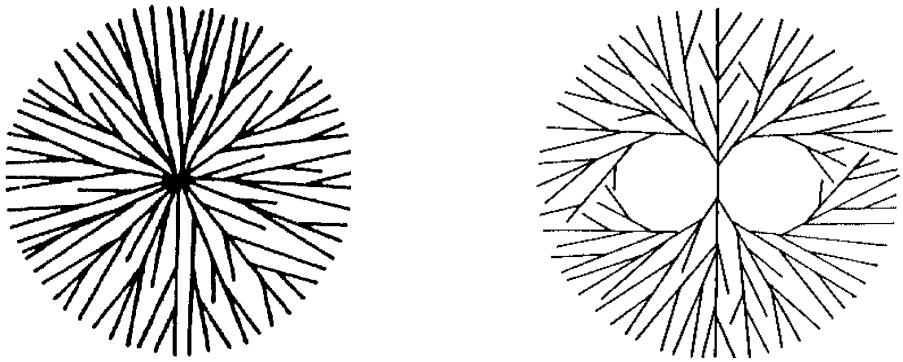

b c

Figure 2.5 Formation and structural features of spherulites. (a): schematic representation of successive stages in the development of a spherulite;[1] (b): spherulitic radiation of the substructure is achieved initially by perhaps a heterogeneous nucleus and by space filling branch;[1] (c): spherulitic radiation of the substructure is achieved by branching starting from a single substructure.[1]

concentration of tie-chains has been provided by electron microscopy[55]. It is generally believed that faster cooling from the melt state, a higher molecular weight or a broader molecular weight distribution (with the same average molecular weight) can give rise to a higher concentration of tie-chains. However, a quantitative description of the physical state of tie-chains, such as number density, chain length and its distribution, tautness, etc., is not yet available[56-58].

2.1.3 Shear-induced Crystallization and Its Morphology

The unique long chain nature of polymers imparts the advantageous properties along the chain direction; therefore, orientation of polymers continues to be an important issue in practical applications[59]. For semicrystalline polymers, orientation can exist in both the crystalline phase and amorphous phase. In principle, there are two different routes towards this goal: 1) stretching polymer chains in the melt or solution state first and then a fixation due to the subsequent crystallization and 2) drawing an initially unoriented crystalline polymer in the solid state to a large degree. The first method is addressed in this section, and the second method will be discussed in the next section of this chapter.

There are two stages to be considered for the first method - first being the development of chain orientation in the melt or solution itself and second being the crystallization from such an oriented state. Most of the chain orientation studies have been concentrated on the solution state[60], and comparable investigations focusing on the melt state has been a bit more problematic due to the lack of reliable techniques to monitor chain orientation[60]. To simplify the discussion below, orientation of polymer chains can be assumed either essentially fully stretched out or basically in a random coil conformation with no intermediate orientation state. This simplification can only be justified by assuming that the melt or solution has reached a steady state. Additionally, an intermediate *morphological* orientation state can be regarded as a specific combination of the above two extremes *chain* orientation states.

Chain Extension Under Elongation Flow

To achieve fully-extended chain conformation, the flow has to be, or at least partially contains, an elongational shear force, i.e., the dominant component of velocity gradient has to be parallel to the flow direction[1,60]. At steady state, the effect of elongational flow on a random-coiled chain has been worked out theoretically by De Gennes[61], and the theory predicts that for a given chain there is a sharp transition from random coil conformation to an extended-chain conformation at a critical strain rate ($\dot{\varepsilon}_c$) without an intermediate chain orientation state. This predication has been well supported by direct birefringence observation for dilute polymer solutions[62-66], and it is strongly believed that a similar situation exists in concentrated solutions and/or polymer melts[60].

At a given temperature, the critical shear rate ($\dot{\varepsilon}_c$) is a function of molecular weight, i.e., a higher molecular weight corresponds to a lower critical shear rate - meaning that longer polymer chains can be extended by a lower strain rate and hence less strong flow field[62]. Therefore, for a given polymer with a specific molecular weight distribution, there is a kind of bimodal distribution of chain conformation constituted by practically fully-extended chains and essentially unstretched chains[63]. For a system possessing a molecular weight distribution, increasing the shear rate does not substantially increases the *degree* of chain extension; rather, it increase the *amount* of the chains that are in the extended-chain state. Certainly, flow induced chain scission can also take place due to the further stretching of the fully extended chains[63].

In concentrated solutions as well as polymer melts, chain overlaps and entanglements exist. In these cases, with the increase of shear rate, two critical shear rates, $\dot{\varepsilon}_c$ and $\dot{\varepsilon}_n$ are present[60]. The first critical shear rate, $\dot{\varepsilon}_c$, corresponds again to the transition from a random coil to a extended chain conformations; the second critical shear rate, $\dot{\varepsilon}_n$, however, represents the formation of mechanically effective networks of stretched polymer chains, as shown by Figs. 2.6a and b[64]. When strain rate reaches $\dot{\varepsilon}_c$, the chains disentangled and are stretched out

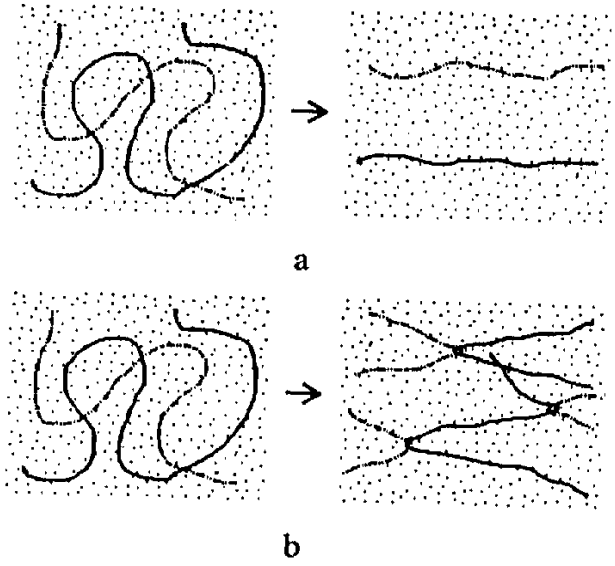

Figure 2.6 Schematic drawing of the responses of dissolved molecules to an elongational flow field at c > c+ (chain overlap concentration).[64] (a): $\dot{\varepsilon}_c < \dot{\varepsilon} < \dot{\varepsilon}_n$ and b): $\dot{\varepsilon}_c < \dot{\varepsilon}_n < \dot{\varepsilon}$

individually. As strain increases further and reaches $\dot{\varepsilon}_n$, the chains act, at shorter time scale, like a mechanically connected network. At this point, the viscosity of the polymer solution increases drastically, and chain scission is potentially expected to happen, if the elongational stress is sufficient[62].

The relation between the critical shear rates and polymer concentration (c) are represented by Figs. 2.7a and b. As can be seen from these plots, both critical shear rates decrease with the increase of concentration; but the rate of the decrease for $\dot{\varepsilon}_c$ is smaller than that for the $\dot{\varepsilon}_n$. However, it is not clear at present weather there is a cross-over like what is shown in Fig. 2.7b. The existence of such a cross-over is highly important, since it implies that a given polymer chain cannot be extended entirely due to chain overlaps or entanglements, and this would certainly influence the morphology thus resulted.

Crystallization form Sheared-oriented Chains

Because of the existence of two types of chain conformations under elongational flow, i.e. extended-chains and random-coiled chains, the morphology resulted from the subsequent crystallization includes fibril type crystals from the extended chains and conventional chain-folding lamellae from the random chains, and a combination of the above two structures is commonly refereed as shish-kebab (crystallize from solution) or row morphology (crystallize from the melt)[60]. Since different degrees of shear strain promote different amount of extended-chains, the concentration of fibril type structures is expected to be affected by external flow. Additionally, the degree of shear can also influence the lateral growth of the lamellae[60].

In an unstressed state, crystallization usually starts at some kind of isolated and discontinuous nuclei and lamellae grow radially, often with twisting, along the growth direction and form the spherulitic morphology. Under elongational shear, certain polymer chains are extended; therefore, thermodynamically as well as kinetically, these portions of the chains can crystallize faster and form row-nucleated fibril crystals[66]. The first-formed row-nucleated fibril

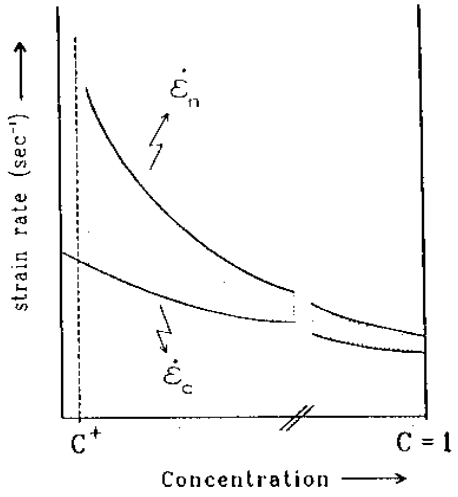

a

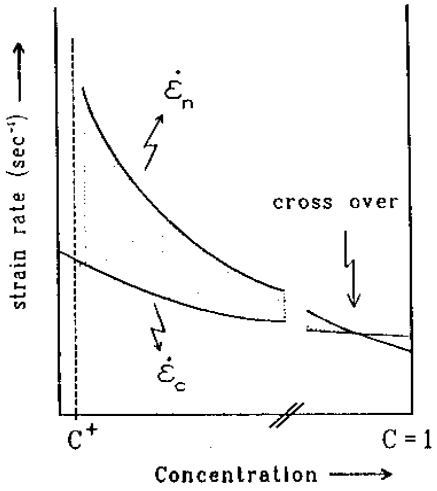

b

Figure 2.7 Strain rate versus concentration plots showing the critical strain rate for the coil → stretch-out conformation transition ($\dot{\varepsilon}_c$) and the critical strain rate for network formation ($\dot{\varepsilon}_n$).[60] (a): a finite strain rate window ($\dot{\varepsilon}_n - \dot{\varepsilon}_c$) pertains up to c = 1 (single component melt); (b): a cross over of $\dot{\varepsilon}_c$ and $\dot{\varepsilon}_n$ vs. concentration lines in which the strain rate window ceases to pertain with increasing concentration.

crystals can then serve as nuclei for the later development of chain-folding lamellar crystals[60,65,66]. Depending on how many polymer chains are stretched out and crystallized into the row-nucleated fibril structures, three types of morphologies can be generated[67], as shown in Figs. 2.8a-e.

If the applied stress (extension) is low, the amount of row-nucleated fibril structures is limited, and the transverse growth and twisting of the lateral lamellae is not very much affected (Fig. 2.8a). The corresponding WAXS pattern for this type of structure is shown in Fig. 2.8b, which resembles neither a random pattern nor fiber-like pattern. The other extreme morphology corresponds to a high stress (extension) induced highly oriented structure, with the formation of a large amount of fibril structures and less twisted overgrown lamellae with c-axis highly oriented along the shear direction (Figs. 2.8c and d). Intermediate orientation states between the above situations can exist, as shown by the WAXS pattern in Fig. 2.8e. In this case, the fiber-lamella duality remains true, and it is their combination with certain amount of each structure that results in different *morphological* orientation states, like the one shown in Fig 2.8e. This argument has been strongly supported by theoretical calculations[60].

The nature of the fibril structure is currently not complete clear[68-70]. In many cases, distinct row-nucleated fibril structures can be directly detected by WAXS and TEM; while in other cases, the morphology is composed of stacked lamellae with no sign of central fibril structures. For the shish-kebab morphology that are formed from polymer solutions, the central fibril structures can often be observed clearly. However, for the row structure that results from melt-crystallized systems, such observation may be limited. Therefore, the existence and the characteristics of the fibril structure is still not totally understood.

2.1.4 Ultra-drawn Mircofibril Morphology

Under sufficient uniaxial drawing of a spherulitic semicrystalline polymer in the solid state, the original morphology can be transformed into highly oriented microfibril morphology[71]. Transformation from chain-folding lamellae into microfibrils begins with a uniform deformation

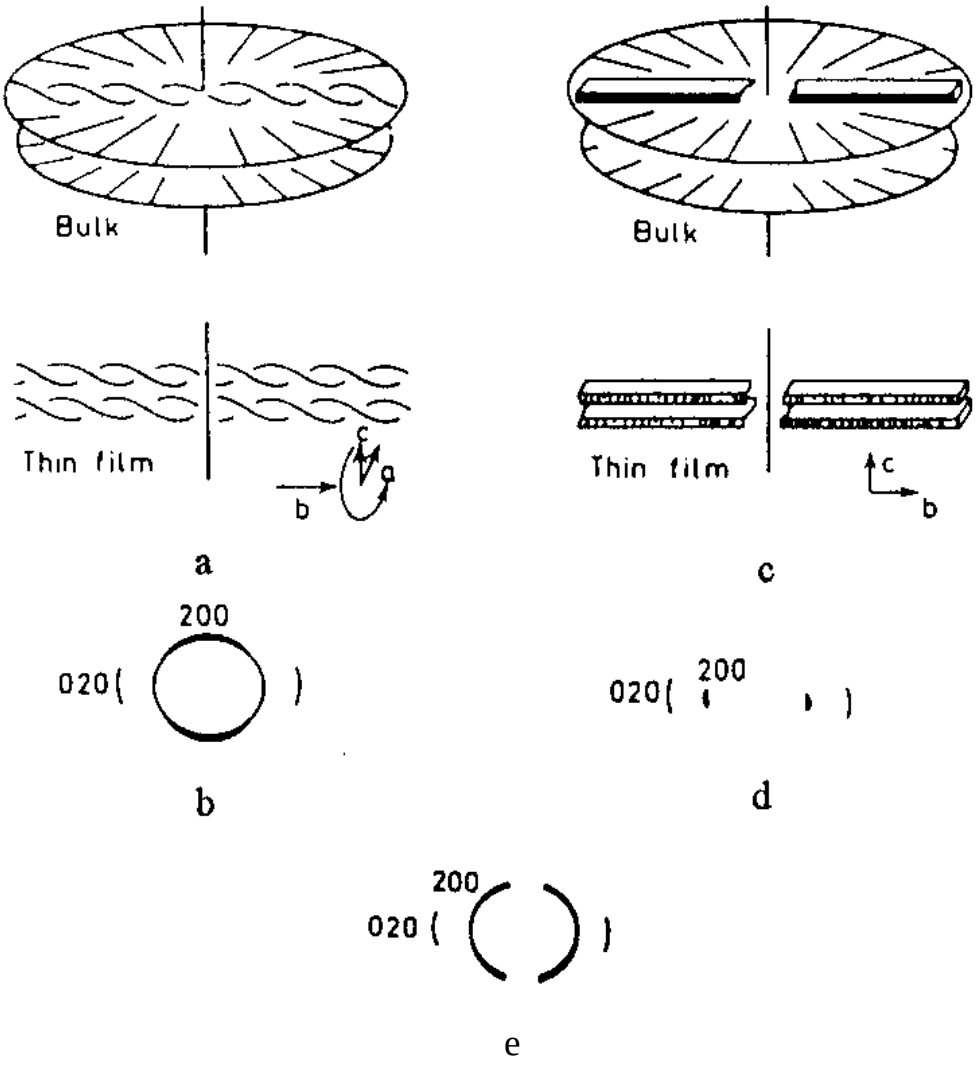

Figure 2.8 Schematic representation of the crystal texture originated from a crystallization from oriented polymeric melts under different stress conditions.[67] (a) low stress; (b) the main features of the WAXS pattern corresponding to (a); (c): high stress; (d): the main features of the WAXS pattern corresponding to (c); (e): the main features of the WAXS pattern for stresses that intermediate between those in (b) and (d).

of the constituent spherulites. In this case, all regions of a spherulite extend simultaneously (in an "affine" fashion), and the extension in different parts of the spherulite is in approximately constant proportion in macroscopically scale. What follows is a non-uniform deformation of the spherulite. Microscopically, microcrazes can be detected at different regions of the spherulite, and one region of a spherulite can be drawn to very different degree as compared to the other regions within the same spherulite.

The basic deformation processes, in sequential order, are the following[72]: the stressed spherulitic lamellae shear into crystal blocks via chain tilt/slip within lamellae and longitudinal slip at mosaic block interfaces; the blocks rotate such that the molecular chains align along the local principal stress direction; the crystal blocks decrease in width by chain slip and unfolding until microfibrils of alternating crystal and amorphous regions are formed. Each lamellar stack forms numerous micronecks once the yield stress is reached. Each microneck in turn is associated with the formation of a microfibril morphology.

The models proposed to address the structural features in microfibril morphology for drawn semicrystalline polymers are summarized in Fig. 2.9. In Peterlin's model[73], microfibrils consist of alternating crystal blocks and noncrystalline regions connected by taut tie-chains. According to this model, the modulus of a drawn semicrystalline polymer is proportional to the number of load-bearing taut tie-chains that cross the noncrystalline regions connecting adjacent crystalline blocks along the microfibrils. Prevorsek[74] modified this model by suggesting that 1) the number of tie-chains increases with draw ratio and 2) the properties of the final product are controlled by the densely packed matrix of highly oriented molecular chains that originated primarily from the amorphous phase. Similarly, Fischer's model consists of a homogeneous crystalline matrix with a high concentration of defects that are not completely statistically distributed in the crystalline phase[75].

A common feature for the above morphological models is the existence of crystalline lamellae. A different kind of extended-chain morphological models has also been proposed. Porter[76] suggested that the extended-chain crystals are the basic feature of drawn semicrystalline polymers, and chain ends are incorporated into the extended chain crystalline phase as defects.

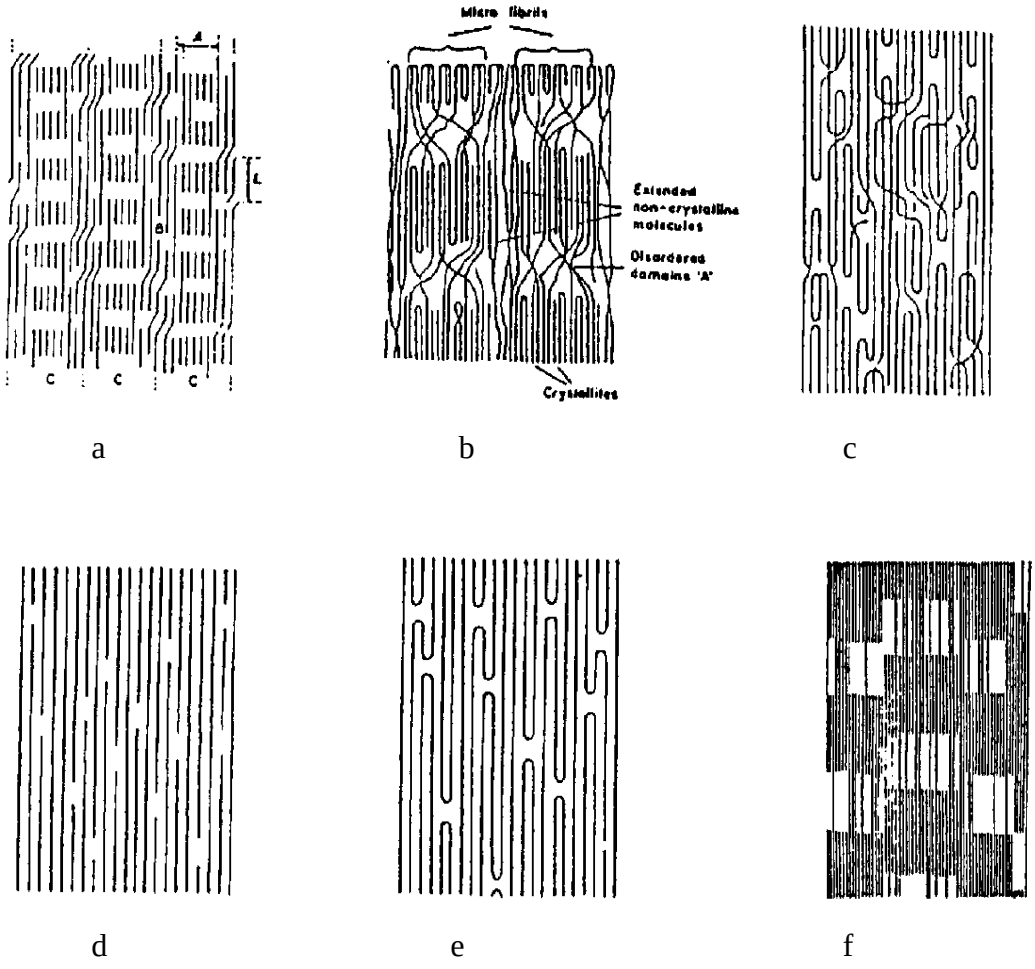

Figure 2.9 Various structural models of microfibril morphology for drawn semicrystalline polymers proposed by (a): Peterlin;[73] (b): Prevorsek;[74] (c): Fischer;[75] (d): Porter;[76] (e): Clark[77] and (f): Ward.[78]

The ultrahigh modulus of the ultra-drawn PE fibers is a strong support for this model, where the tie-chains can not give rise to such a high modulus, neither can the oriented amorphous matrix. Consistent with this is a model proposed by Clark[77] that consists of continuous crystal fibers with a certain amount of chain folds being incorporated as defects.

Ward proposed another morphological model[78], which somewhat combines both features of lamellar morphological models and extended-chain morphological models. In this model, the drawn morphology consists of stacks of short lamellar-type crystallites linked by intercrystalline bridges - a continuous and essentially extended-chain crystalline phase containing disordered regions along the fibril direction. Since the crystalline phase is essentially continuous in the draw direction, the modulus of the drawn materials should be quite high. Additionally, the degree of crystallinity also increases with draw ratio.

2.2 Mechanical Properties for Semicrystalline Polymers

Mechanical properties are one of the primary criteria to meet for engineering applications. The desired properties can be achieved by a variety of approaches, such as designing new chemistry, making polymer blends, and applying unique processing techniques. A better understanding of structure-property relationships can service as a guide to manipulate mechanical properties by these approaches. In what follows, a brief literature survey is provided to highlight some fundamentals of structure-property relationships, with a focus on semicrystalline polymers again using PE as an example. More detailed information dealing with specific topics that are covered in this dissertation will be given in the introduction sections of chapters 4.0 ~ 7.0.

The properties of a polymer fall roughly into two classes, material properties (e.g. density), which are mainly determined by the structure of the polymer, and specimen properties (e.g. strength), which are properties measured under certain conditions and are affected by sample preparation procedures[79]. Material properties can be further divided into two categories, fundamental properties (e.g. molecular weight and distribution), which depend upon the chemistry and physics of the materials, and derivative properties (e.g. glass transition temperature), which

are simply a reflection of fundamental properties in one particular aspect. Although fundamental material properties should be the target of structure-property investigations, in most cases, derivative properties are the ones that are used to correlate with the structure of materials[80-82].

Different methods have been utilized to predict fundamental or derivative properties of polymers, such as the group contribution technique developed by Van Krevelen[83,84], the group theory used by Yang, et al.[85-87] and a "new" method (modified group theory) discussed by Bicerano[79,88]. However, the predication of properties for polymers is still in a primitive stage, and the few cases in which such predications are indeed successful are essentially limited to amorphous polymers and rubbery polymers[79-83]. For semicrystalline polymers, the complex structural features as outlined in the first section of this chapter makes it impossible to form even general correlations for property predications. Nevertheless, extensive knowledge about the molecular origins of a specific mechanical property is available, and this will be discussed in this section

2.2.1 Tensile Stress-strain Properties

When a tensile load is applied to a specimen, the properties of the material can be quantified by stress-strain behavior (curve). For polymers, the stress-strain behavior is a sensitive function of temperature and strain rate, due to the viscoelastic nature of the polymers. Young's modulus, stress and strain at yield point, and stress and strain at break point (which are indications for cold-drawn ability) are some important properties associated with a tensile test. The Young's modulus and yield stress will be the focus of the following discussion, since they are the most studied properties for such investigations. The structural parameters used to which the properties are correlated depend on the particular model chosen, and they may include orientation, percent crystallinity and/or crystalline lamellar thickness, etc.

Young's Modulus

Three types of models have been utilized to interpret the relationships between microscopic structures and Young's modulus[89], namely the aggregate model, the Tagayanagi model, and the composite mechanics models. The aggregate model considers the effects of orientation in detail, but it ignores morphological features such as crystallinity. The Takayanagi model assumes certain boundary conditions between the crystalline phase and amorphous phase, assuming their orientation being either perfectly extended-chain for the crystalline phase or totally random for the amorphous phase. The composite mechanics model regards semicrystalline polymers as a mixture of a crystalline phase and a amorphous phase with complex mathematical treatment with one or more fitting parameters.

The one-phase aggregate model has been used in a wide range of polymers to model the Young's modulus of oriented semicrystalline polymer samples (Fig. 10a)[90,91]. In this model, a partially oriented sample is treated as an aggregate of anisotropic units with transverse isotropy. The orientation distribution of the aggregate is considered to be that of the sample, and the Young's moduli of the anisotropic units are those of the material in an fully oriented state. In the calculation of Young's modulus, both iso-strain (parallel or Voigt) model and iso-stress (series or Reuss) model have been used. It is believed that the properties of the aggregate, i.e. the sample, must lie somewhere between the above two limits (lower and upper bonds)[92]. The successful applications of this model include low density PE (LDPE) and poly(ethylene terephthalate) (PET) as well as materials with rigid chains[93,94]. However, for HDPE and Nylon 6, the application of this model has not been successful[91,95].

The Tagayanagi model considers semicrystalline polymers to be made up of blocks of the crystalline phase and the amorphous phase (Fig. 10b)[96]. Each block has either a uniform stress or strain distribution and is connected to the other blocks in either series or parallel. There is no consideration of any transverse contraction/expansion or any shear motion between blocks. The Takayanagi model normally includes different types of boundary conditions between the blocks, such as the parallel model, the series model and more complex representations of one phase

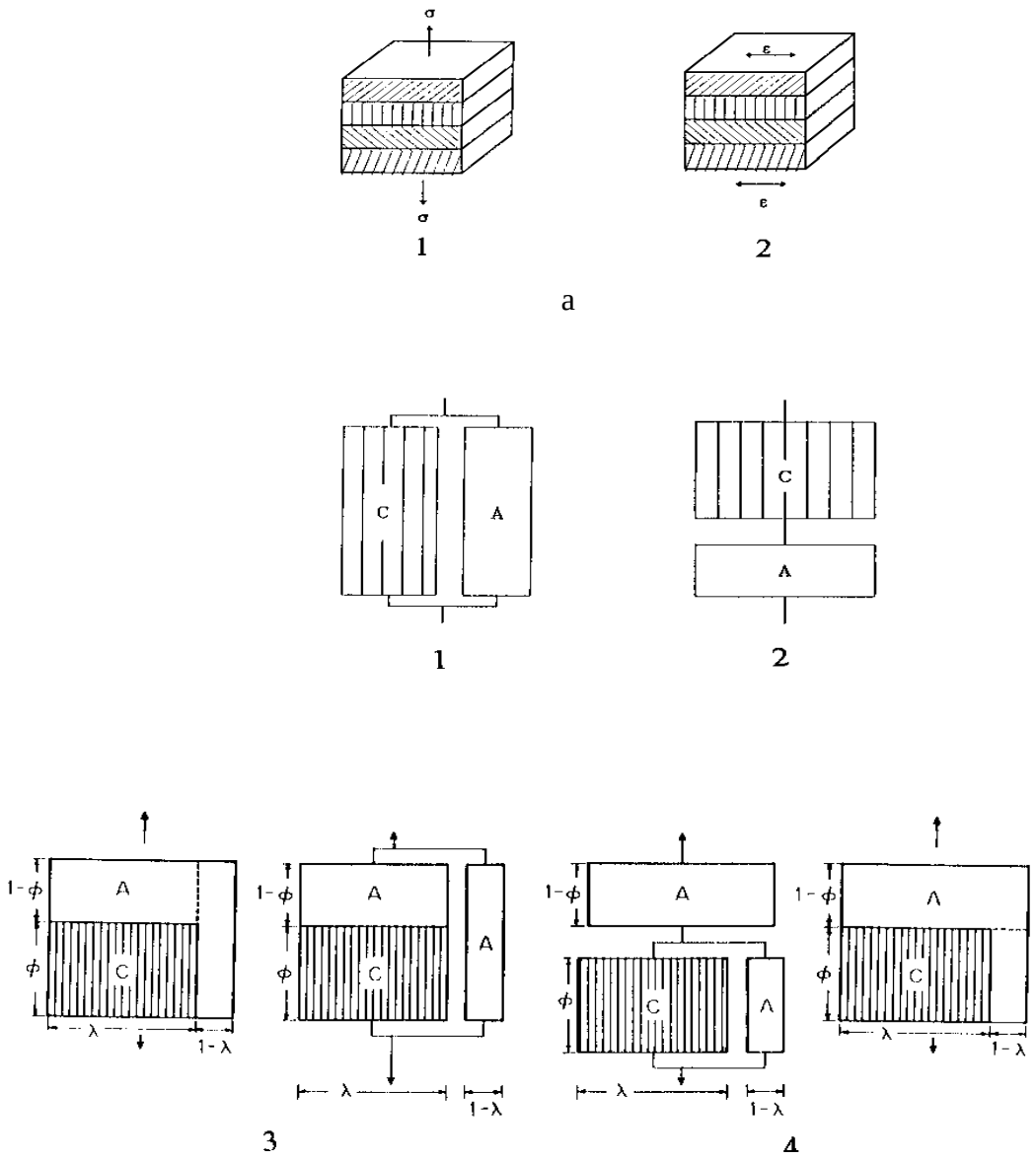

Figure 2.10 Models to predict Young's modulus for semicrystalline polymers. (a): the aggregate model for the case of 1) uniform stress and 2) uniform strain;[90] (b): the Tagayanagi model with crystalline and amorphous being 1) parallel, 2) series, 3) series-parallel and 4) parallel-series.[96]

dispersed in another phase (Fig. 10c)[97,98]. These models have been utilized to explain the complex change of storage and loss moduli for the mechanical relaxation for PE[99] and Nylon 6[100], as well as the calculation of Young's modulus for ultra-drawn PE fibers[101,102].

The relationship between Young's modulus and crystallinity for semicrystalline polymers in an unoriented state has been treated from a composite mechanics standpoint. The first constitutive relation was proposed by Flory, et al[103], in which the shear moduli were calculated based on the theory of rubbery elasticity - with the assumption that the crystalline phase acts as physical crosslinks. However, the predicated modulus was an order of magnitude smaller than the measured values[103]. Since then the application of micromechanics composite theories for predicting Young's modulus by assuming a two phase mixture has been extensively investigated[104-107] and critically reviewed by McCullough[108] and by Janzen[109]. It has been pointed out that the satisfactory demonstration of this approach needs to cover enough experimental data for samples with a large range of crystallinity or density[109]. Another type of composite model that takes into account of the lamellar feature for the crystalline phase in semicrystalline polymers has been proposed by Boyd[92].

Yield Stress

Yielding in unoriented semicrystalline polymers can show different characteristics, such as a local maximum as well as a gradual deviation from a initial elastic linearity[124]. The fundamentals of yielding in semicrystalline polymers are not yet completely understood[89]. It has long been recognized that yield stress increases with crystallinity, if the material is deformed at temperatures between the glass transition temperature and the melting temperature of the respective amorphous and crystalline phases[110-113]. According to these investigations, the fundamental quantity with which to correlate yield stress (σ_y) is the crystallinity (X_c). However, interpretation of such a dependence falls into two camps that have led to quite different explanations of yielding in semicrystalline polymers. In addition, since crystalline lamellar thickness (l_c) usually changes with

percent crystallinity, it has been argued the fundamental parameter is the *thickness* not the *amount* of crystalline lamellae[111,113].

The first type of explanation of yielding is proposed by Harrison, et al.[29] and Mandelkern, et al[111], and it states that the dominant processes in yielding and post-yielding deformation is sequential events of partial or local melting, stretching of the molten chains, and recrystallization under stress. Viscous heating in localized necking regions is thought to cause the melting of crystalline lamellae, and the chains are then stretched in response to the applied stress and crystallized forming an oriented fibril morphology. This process continues until the original spherulitic morphology is converted into the microfibril structure. Such a phase transition model can account for the positive dependence of σ_y on l_c as well as the negative dependence of σ_y on temperature. However, this model predicts a *negative* dependence of σ_y on strain rate, i.e., a greater strain rate should increase the adiabatic heating and presumably make it easy for the melting of the crystalline lamellae, and this is in contradiction with experimental observations.

The strongest evidence supporting this mechanism is the observation that the long period from SAXS is a function of deformation *temperature* and is essentially *independent* of the initial lamellar thickness before drawing[73]. Furthermore, a *decrease* in long period induced by deformation has been noted in these experiments[73]. Such a "quasi-melting" can also be coupled with the classic drawn model by Peterlin[73]. Phillips, et al.[115] have reported electron microscopy evidence for a yielding zone on the order of 5-10μm, which is speculated to be caused by localized melting, for PE samples drawn at room temperature. Additional support for this proposal comes also from real-time SANS studies focusing on the plastic deformation processes of PE samples[116-119]. Interestingly, the "quasi-melting" did not occur in PE which was initially crystallized in an extended-chain morphology[114].

The second type of explanation is based on the conventional crystal plasticity theory, in which deformation mechanisms include dislocation slip, mechanical twinning and (martensitic) phase transformation[120-122]. Slip of covalently bonded chains on (kk0) planes in either the chain axis direction [001] or transverse direction [uv0] have received most attention[120]. It is assumed that a crystal structure is defined conventionally with the chain axis in the crystallographic [001]

direction. Therefore, (hk0) [001] slip is the most likely mechanism for achieving large macroscopic strains and through which the initial structure is converted into a microfibril morphology as suggested by Peterlin[73]. Furthermore, this mechanism have been used to *quantitatively* estimate the dependence of σ_y [123] on l_c based on the nucleation of screw dislocations in a crystalline lamella[110,124]. Another promising feature of this model is that it indeed predicts a *positive* strain rate dependence of yield stress on crystalline lamellar thickness[110].

Yielding by (hk0)[001] slip involves perturbation of chain folds which must exist in lamellar crystals of polymer molecules, and this has been ignored in the crystal plasticity model. Flory, et al.[42] contend that the irregular chain-folding surface in melt crystallized polymers excludes substantial amount of shear displacements as required in the dislocation model, since it basically assumes adjacent reentry with a regular fold surface. Nevertheless, X-ray diffraction showed clearly that [001] slip is the mechanism by which yielding and plastic deformation occurs in PE[126]. More detailed X-ray pole figure studies reached the same conclusion for uniaxial extension, uniaxial compression and plane strain compression tests[127]. These findings have been further confirmed by plane strain compression experiments at different temperatures[128,129]. Furthermore, electron microscopy experiments on specially prepared ultra-thin ultra-drawn HDPE films deformed under tension[130] have also provided direct supports for this mechanism. In these experiments, the [001] slip is directly seen to occur on both (100) and (010) planes[130]. Therefore, regardless of the constraints imposed by chain reentry at chain-folding surface, it has been well demonstrated that chain slip can occur by (hk0) slip.

To summarize, for the best studied case of HDPE, it appears that yielding (the onset of plastic deformation) at or near room temperature is controlled by crystal plasticity via nucleation and propagation (slip) of screw dislocations. Whereas post-yielding deformation with the formation and stabilization of a neck involves “quasi-melting” or decrystallization - defined as the destruction of the crystalline phase under mechanical stress. For polymers other than HDPE, it is not possible to make any conclusive arguments due to the lack of experimental data on this particular subject.

2.2.2 Mechanical Relaxation Behavior

Physical properties of semicrystalline polymers can be influenced by the presence of mechanical relaxations at different temperatures; therefore, the study of mechanical relaxation processes is of continuous scientific and technological interests[131]. Compared with amorphous polymers, mechanical relaxations in semicrystalline polymers are much more complex due to the presence of the crystalline phase, as well illustrated by McCrum, et al.[131] and Boyd[132,133]. This complex nature of dynamic small strain mechanical relaxation will be briefly reviewed to serve as a introduction to the subject, and a more detailed review focusing on the mechanical α relaxation in HDPE will be provided in chapter 5.0 of this document.

In general, there are two or three types of relaxations for semicrystalline polymers in isochronal (frequency scan) experiments in the temperature interval between liquid nitrogen temperature (-196°C) and melting temperature[131-133]. These relaxations are indexed by using Greek letters, α, β and γ, in the order of decreasing temperature[131]. There have been some confusion about this kind of labeling. For example, generally for polymers that possess all three relaxations, the high temperature relaxation is donated as α, and it is commonly related to the crystalline phase. The medium temperature relaxation is denoted as β, and it is more connected to the amorphous phase and associated with the glass transition temperature. A low temperature γ relaxation is due to very localized motions in amorphous phase as well as in crystalline. On the other hand, for materials that show only two relaxations, the high temperature α relaxation may actually originate from the amorphous phase, like the β relaxation in the first case, and the β relaxation has similar meanings as the γ relaxation in the first case.

Therefore, to generalize mechanical relaxations in semicrystalline polymers, it is convenient to "classify" them into three categories[132]. First, "low" crystallinity polymers that can be quenched completely to the amorphous state but are difficult to crystallize with more than 50% crystallinity, such as PET and isotactic polystyrene (*i*-PS). Secondly, "high" crystallinity polymers, such as linear polyethylene (LPE) and *i*-PP, that can have crystallinity higher than 60% and can not be quenched into a completely amorphous phase. Thirdly, polymers with "medium

crystallinity" that can neither ordinarily be quenched a to completely amorphous state nor crystallized to the degree of 60% crystallinity. Such systems include aliphatic polyamides (e.g. Nylon 6) and aliphatic polyesters.

Low crystallinity polymers generally only show two relaxation processes (α and β), and high crystallinity polymers often have all three relaxations (α, β and γ)[132,133]. To clarify the confusion about the α relaxation, they have been denoted as α_a for the former case and α_c for the latter case to emphasize their amorphous and crystalline origins, respectively. Similar identifications have not been designated for the β and γ relaxations. Polymers with medium crystallinity can show either two or three relaxations[134-138]. In the following two sections, PET, HDPE and an aliphatic polyester with repeat unit of $-O-(CH_2)_X-O-CO-(CH_2)_Y-CO-$ are used as examples for the three type of materials to illustrate the basic relaxation processes, and a brief discussion about their molecular mechanisms will be given afterwards.

Relaxation Phenomena

Mechanical relaxation spectra of PET samples covering the crystallinity range of 0 ~ 46% are shown in Figs. 2.11a and b, which show both α_a (Fig. 11a) and β (Fig. 11b) relaxations[139]. It is obvious that at temperatures between the glass transition temperature and the melting temperature the samples with crystalline phase have higher stiffness than sample at totally amorphous phase, a character expected for a composite in which one (amorphous) phase softens but the other (crystalline) phase does not relax. In addition, one sees the peak temperature of G″ is displaced to higher temperatures with the increase of crystallinity. Furthermore, the width of the G″ relaxation peak is much broader as compared with the pure amorphous sample. For the sub-glass β relaxation, it is apparent that both the shape and location of the G″ relaxation peaks are not sensitive to either the presence or the degree of crystallinity - in sharp contrast to the α_a relaxation.

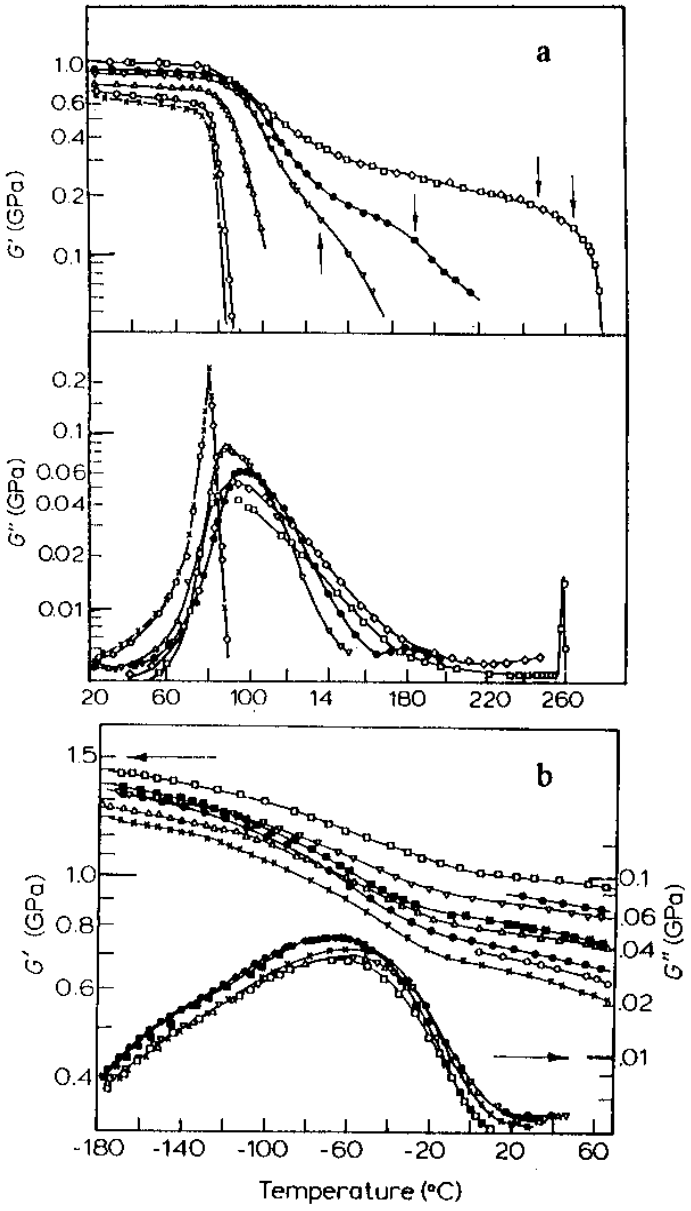

Figure 2.11 Mechanical relaxation data for PET (low crystallinity polymer) a) α_a relaxation and b) β relaxation[139].

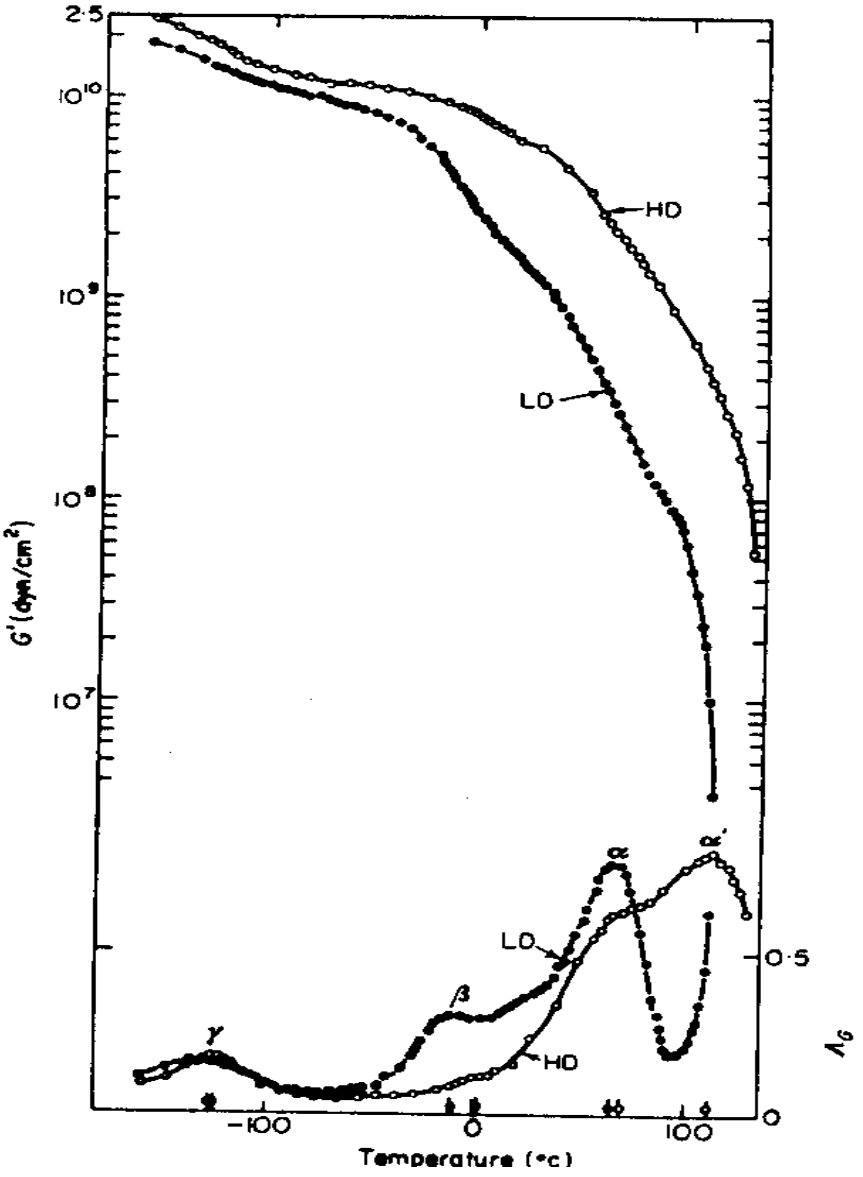

Figure 2.12 Mechanical relaxation for high density PE (HDPE) and low density PE (LDPE) (high crystallinity polymer) showing the α_c, β and γ relaxations[131].

Mechanical relaxation spectra for high density (HD) and low density (LD) PE samples are presented in Fig. 2.12[131]. The most distinguishable feature of this set of data is the presence of an α_c relaxation in addition to the β and γ processes. The fact that the high temperature relaxation is indeed due to the crystalline phase was confirmed by comparing relaxation data obtained in the solid state with that obtained for the same material in the melt state[141,142]. The peak temperature of the α_c relaxation (G″) is found to be dependent on the crystalline lamellar thickness[143-145]. In addition, this relaxation also tends to show a sign of multiple relaxation behavior[146,147], and this will be discussed further in chapter 5.0. The β relaxation is not a prominent feature for HDPE, but it shows as a strong relaxation for LDPE[148]. The γ processes was believed to originate solely from the amorphous phase[149,150], although the contribution of the crystalline phase has also been proposed[151].

The interesting mechanical relaxation features of medium crystallinity polymers has just been investigated recently[134-138]. For example, Ito, et al.[134] have studied the mechanical relaxation behavior of a linear aliphatic polyester based on the chemical structure of $–O–(CH_2)_X–O–CO–(CH_2)_Y–CO–$. The relaxation spectra for a series of samples with the X:Y ratio of 2:4, 2:6, 2:8, 6:4, 6:8 and 10:16 are presented in Fig. 13. One sees clearly that all the samples showed a low temperature γ relaxation, and its broad and asymmetric features led the authors to suspect that it is comprised of multiple processes originated from amorphous as well as crystalline phase, as also initially proposed for PE[151]. The β and α relaxations were pointed out to be associated with the molecular motions within the amorphous phase and crystalline phase, respectively, and their relaxation strengths are influenced by the values of X and Y. Another notable feature is that the intensity of the α and β relaxations are closely coupled - the appearance of the α relaxation strongly restrains the β relaxation, and this phenomenon has been investigated by Boyd[135,137].

Molecular Mechanisms

As mentioned earlier, the α_c relaxation is proposed to originate from the crystalline phase, and it is believed to be due to the translational motion of polymer chains along the c-axis[148]. Also, according to McCrum[131], this crystal process is closely coupled with the amorphous phase, i.e.,

the achievement of crystal stem mobility through repeated translational motions along the crystal c-axis can lead to a redistribution of the tight folds and loose loops, cila and tie-chains that make up the interlamellar amorphous region (shown in Fig. 2.14a). Therefore, although there is no strain induced by the "flip-over" of polymer chains within the crystal, the associated molecular motions in chain-folding surface and the amorphous region (Fig 2.14c) can promote mechanical relaxation(s).

It is interesting examining why some crystalline polymers display an α_c relaxation while others do not. From the above discussion, the essential feature of this relaxation is the ability to form a mobile localized structure that can move translationally along the chain axis and brings the chain back to its crystallographic register. Therefore, the mobile unit must have a low "creation" energy and easy to move to ensure a relaxation time short enough giving rise to an observable relaxation at temperatures below the melting temperature[132]. For PE, *i*-PP, poly(ethylene oxide) (PEO) and poly(oxymethylene) (POM), which all have the α_c relaxation[131], such localized mobile units can be formed with a small amount of energy that permits their advancement along the chain helix. Specifically, for PE, a rotation about the c-axis by 180° advances the chain by half of a unit (c/2 = 0.127nm) along the zig-zag chain[152]. For POM, a twist of 200° about the helix results in a compression or extension by half of a helical patch (h/2 = 0.190nm)[133]. For polymers with a bulky chain structure (e.g. PET, *i*-PS), which tend to have a low crystallinity, an obvious reason for the lack of such a relaxation is that the creation of mobile units requires too high an activation energy. For medium crystallinity polymers, such as aliphatic polyesters and aliphatic polyamides, although they may have a zig-zag chain conformation in the crystalline phase and therefore the formation of mobile units might be possible, the propagation of these units might involve too many repeat steps in the crystal lattice, which leads to a much longer relaxation time for the relaxation being observed by dynamic mechanical tests at temperature below the melting temperature. Similarly, if the size of the mobile unit is too large, the expected mechanical relaxation can not be observed.

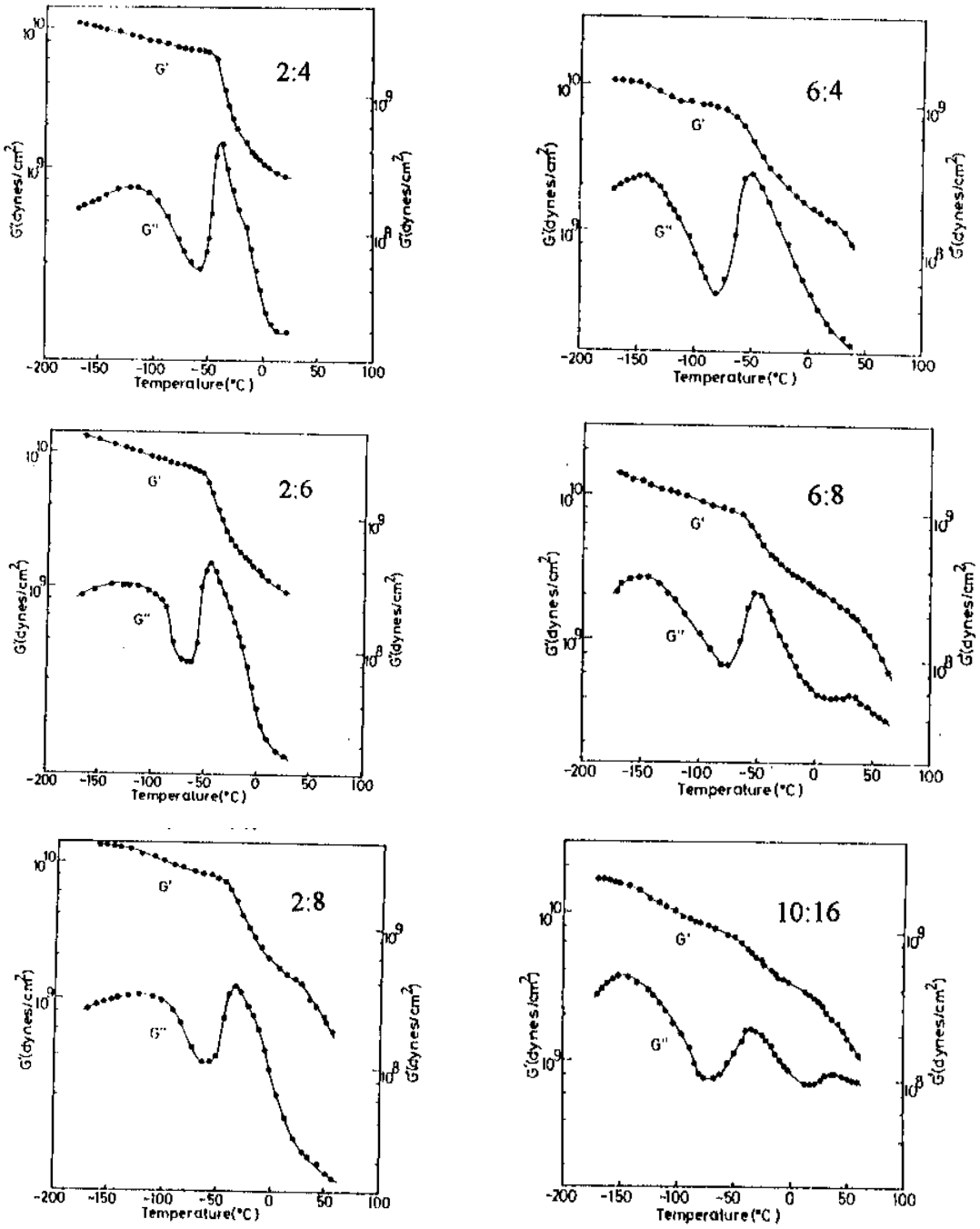

Figure 2.13 Mechanical relaxation for an aliphatic polyester of $-O-(CH_2)_X-O-CO-(CH_2)_Y-CO-$ (medium crystallinity polymer) at different X and Y values.[134]

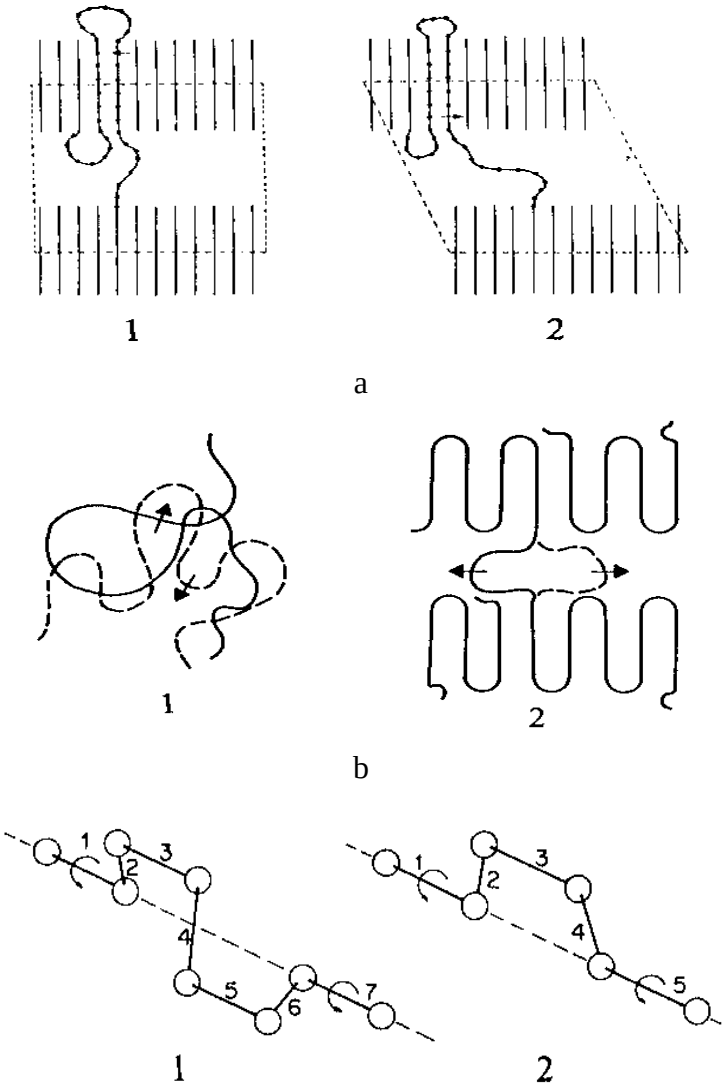

Figure 2.14 Molecular mechanisms for (a) crystalline α_c relaxation through 1) shortening of two loose loops and 2) lengthening of a tight tie chain which in turn originates a deformation in amorphous phase; [148] (b) β relaxation for 1) free amorphous chains and 2) amorphous chains confined by crystals; [138] (c) localized γ relaxation with 1) three bond (Boyer) motion [162] and 2) five bonds (Shatzki) motion [164].

The β relaxation is associated with the glass transition of the amorphous phase, but it differs from that in wholly amorphous polymers - being much broader and shifted to higher temperatures. These features are believed to be due to the effect of the crystalline phase in restricting the generalized long-range segmental motion that is required for the glass transition (Fig. 14b)[153]. Several attempts have been made to model the constraint effects of the crystalline phase on the adjacent amorphous regions[147-150]. In addition, the three phase model for semicrystalline polymers has also been utilized[44] in which semicrystalline polymers are considered as consisting of three phases - a crystal phase, an amorphous phase, and a third interfacial region. The prominent β relaxation in LDPE (Fig. 2.12) has been explained by the characteristics of the interfacial region. During crystallization, the rejection of branches leads to a more loosely organized amorphous fraction with large loops with less tight folds, leaving the amorphous phase less constrained by the crystalline phase[133]. The less restricted amorphous fraction is thus capable of relaxing to a larger degree and, therefore, leads to a prominent relaxation[133].

The complex molecular nature of the β relaxation is also reflected in the interpretation of the glass transition temperature for "high" crystallinity polymers[131]. Since the β relaxation in this type of polymer is not well-defined and difficult to resolve, it has been suggested that the glass transition temperature corresponds to the corresponding γ relaxation[158]. For the case of HDPE, both -120°C[159] and -20°C[160] have been suggested to be the glass transition temperature, corresponding to the γ relaxation and β relaxations, respectively. In addition, a third temperature in the neighborhood of -80°C[161] has also been proposed to represent the glass transition temperature, and this temperature is supported by the calculation base on the group contribution theory[83].

The γ relaxation is well-agreed to be due to molecular motions at very localized scales[131-133]; therefore, it is insensitive to both the presence of crystalline phase and morphological features such as crystallinity. But there are still arguments about the contribution from the crystalline phase[134,151]. According to Illers, three sub-relaxations in this temperature are possible, due to the interlamellar region, highly constrained chain motions and defect motions in crystal lattices[151]. Proposed molecular motions that are responsible for the γ relaxation involve simple

conformational transitions of polymer chains in an otherwise glassy matrix, as outlined in Fig. 2.14c.

One type of conformation transition is a "three bond" motion, in which a tgt conformation changes to a tg′t without disturbing the chain stems (Fig. 14c-1)[162,163]. The other type is a "five bond" crank-shaft motion which involves a transformation from a sequence of tgtgt to a tg′tg′t one, with no conformational changes for the collinear stems and simple rotations of the internal stems around the collinear stems (Fig. 2.14c-2)[164,165]. Both motional modes can be viewed as the simplest allowed moves of a tetrahedrally bonded chain without disruption for the local chain stems in question. The differences between these two modes are: the internal energy of the "five bond" motion is modest, but it apparently requires a large swept volume; whereas for the "three bond" motion, the associated volume is relatively small, while the energy barrier is large.

2.3.3 Creep Behavior

Creep is a slow and continuous deformation of a material under constant stress. For polymers, creep is not only an important phenomenon in its own right within the framework of viscoelasticity, but also is of great significance in the design of engineering products, as it reflects the long-time load-bearing capacity of structural products. A better understanding on the creep behavior is necessary for an reliable assessment of durability to prevent an intolerable amount of deformation or time-dependent failure of polymer structures in engineering applications.

Three different approaches have been attempted to describe the time-dependent creep behavior of polymers[166]: engineering approaches, rheological approaches and molecular approaches. In an engineering approach, the goal is set to predict the creep behavior (usually creep strain) for a particular loading situation based on a low number of experiments, and empirical relationships are then proposed. Different relations such as a power law equation have been found to be valuable to describe creep strain for certain polymers under specific loading conditions, although these equations may not have a solid physical base. Some of these relations will be reviewed in chapter 6.0.

For the rheological approach, attempts are directed to extend the linear viscoelastic relations, e.g. Boltzmann superposition principle, to a non-linear regime. One way of doing this is to preserve the separability of stress, strain and time in their functional representations, and this leads to the sophisticated form of single integral representations developed by Leaderman[167], Bernstein, Kearsley and Zapas[168], Valanis and Landel[169], and Schapery[170]. Another method is to use multiple integral representations[171], which has led to considerable mathematical complexity. An excellent introduction on this subject can be obtained in reference 172.

The molecular approach is aimed at incorporating a molecular model that describes the molecular event of creep deformation to a physical property that can be measured experimentally. This approach has the attraction of possible identification of the molecular mechanisms and structural origins responsible for creep. The disadvantages of this approach is the lack of precise mathematical treatment/description as compared with the rheological method. However, this drawback is somewhat balanced by the built-in merit of non-linearity and temperature dependence[166]. The molecular approach is the focus of the following discussion.

The only molecular model that has been widely used in creep studies was developed by Eyring and co-workers[173]. In this model, the creep deformation of a polymer involves the motion of chain molecules or parts (segments) of a chain molecule over potential barriers, as illustrated in Fig. 15. The basic molecular processes could be either intermolecular (such as chain sliding) and/or intramolecular (like a change of chain conformation). With no stress acting upon the material, it is at a dynamic equilibrium state, the frequency (ν) at which chain segments move across the potential energy barrier (ΔH) can be expressed as

$$\nu = \nu_o \exp\left(-\frac{\Delta H}{RT}\right) \qquad (2.1)$$

where ν_o is a pre-exponential factor that is dependent upon the fundamental vibration frequency and entropy contribution to the free energy.

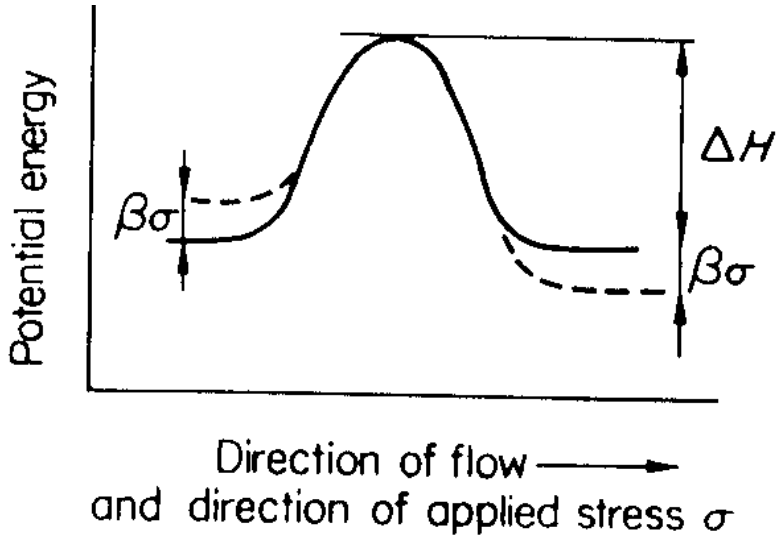

Figure 2.15 Molecular mechanism for the Eyring creep model.[173]

Applying a stress (σ) to the material produces a linear shift ($\sigma\beta$) of the energy barrier in a "symmetrical" fashion (Fig. 2.15). Therefore, a flow in the forward direction (i.e. the direction of the applied stress) is

$$\nu_1 = \nu_o \exp\left(-\frac{\Delta H - \beta\sigma}{RT}\right) \tag{2.2}$$

and the flow in a backward direction is

$$\nu_2 = \nu_o \exp\left(-\frac{\Delta H + \beta\sigma}{RT}\right) \tag{2.3}$$

Therefore, the net flow in the forward direction is

$$\Delta\nu = \nu_o \exp\left(-\frac{\Delta H}{RT}\right)\left[\exp\left(\frac{\beta\sigma}{RT}\right) - \exp\left(-\frac{\beta\sigma}{RT}\right)\right] \tag{2.4}$$

It is assumed that the net flow in the applied stress direction is directly related to the rate of deformation, i.e. creep rate, therefore

$$\frac{de}{dt} = \dot{e} = \dot{e}_o \exp\left(-\frac{\Delta H}{RT}\right)\sinh\left(\frac{v\sigma}{RT}\right) \tag{2.5}$$

where $\dot{e}_o$ is a pre-exponential constant and the symbol β is replaced by v, which is termed the activation volume for the molecular event. A unique feature of this model is that the parameters in the equation, particular the activation energy and activation volume, can give some indications to the underlying creep mechanisms. The pre-exponential factor, on the other hand, is an representation for the population of potential sites that can contribute to creep (availability of creep sites).

The Eyring-rate model has been used initially by Leaderman[174] for the creep studies on silk and other fibers. It was shown that this model gave a good fit over four decades of time at a given stress level, by appropriate choice of the parameters for the elements in Fig. 16a. Sherby and Dorn[175] examined the creep behavior of PMMA under constant stress in a temperature range of 263-320K. The creep rates at different temperatures and stresses were determined by the so-call Sherby-Dorn plot, in which creep strain rate (in logarithmic scale) is plotted against creep strain. Their results showed a linear relationship between applied stress and creep rate in

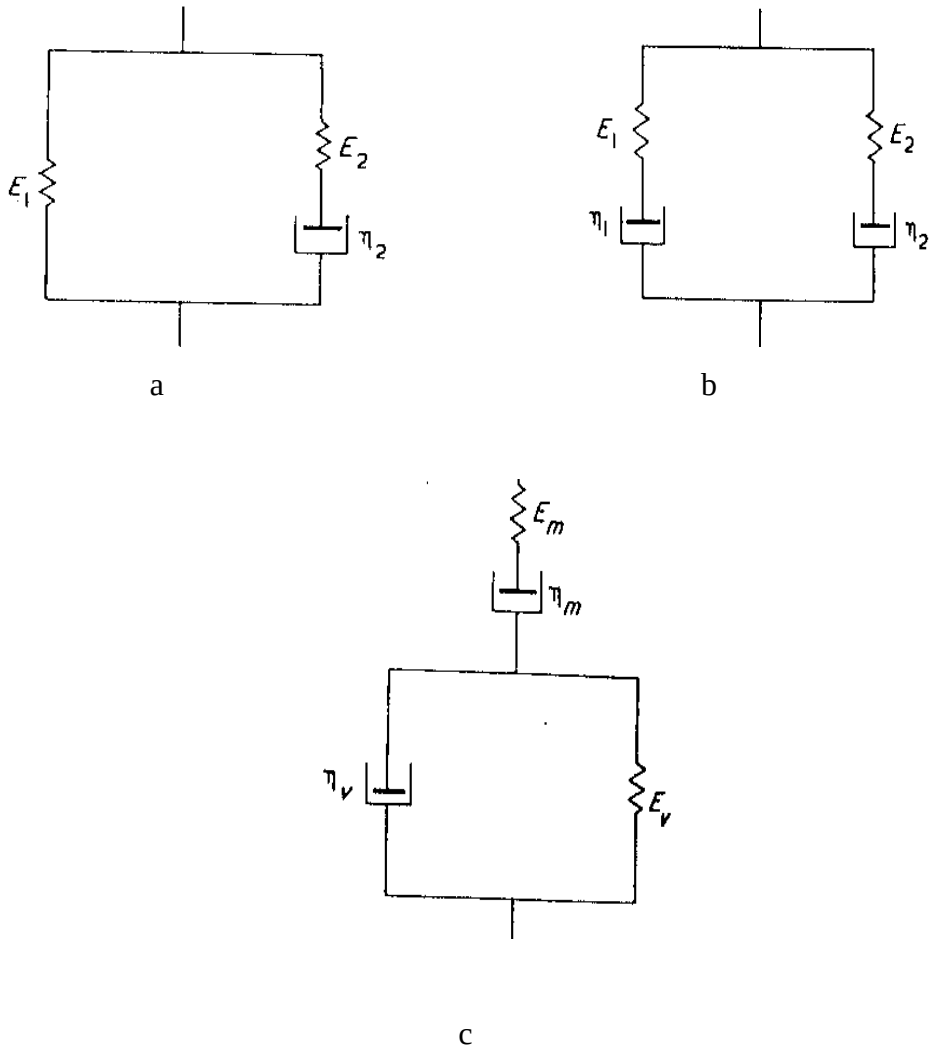

Figure 2.16 Mechanical analogs for (a) standard three elements solid with a thermally activated dashpot; (b) two Eyring-rate processes model and (c) modified two processes Eyring-rate model.

logarithmic scale. This has been regarded as a specific case of the Eyring-rate equation (equation 2.5) at a higher stress level, where the sinh function is simplified into an exponential function, i.e. $\sinh(x) \approx 1/2 \exp(x)$ when x is larger than 3.

This model has also been used extensively in the creep studies of highly oriented PE fibers[176-180]. It has been shown that for low molecular weight samples, the stress and temperature dependence of the creep rate could be modeled well by a single Eyring-rate process with an activation volume of $0.08nm^3$. This is a reasonable value as it probably means that the activation volume is just the swept-out volume of a single molecular chain moving through the crystal lattice via defect motion. However, for high molecular weight samples and copolymer samples, two activated Eyring-rate processes coupled in parallel, as shown in Fig. 16b, had to be used to satisfactorily describe the creep rates. The two Eyring-rate processes differ with regard to the activation volumes and pre-exponential factors. One process has a small activation volume ($\sim 0.05nm^3$) and a large pre-exponential factor, and it only activates at higher stress level. This process is more related to the crystalline phase of the material. The other process is associated with a large activation volume ($\sim 1.0nm^3$) and a small pre-exponential factor, and it is speculated to represent the deformation of the entangled amorphous network in the material.

The applicability of the two Eyring-rate process model certainly depends on its capability of providing a comprehensive description of time-dependent behavior in general. Ward, et al.[178] carried out an investigation aimed at using the two Eyring-rate processes model to describe viscoelastic the behavior of high modulus LPE, including creep as well as stress-relaxation properties. In this study, the initial model (Fig. 16b) was modified into Fig. 16c without loosing its significance to a major extent. The modified model is essentially a standard linear solid in series with a dashpot, and the latter element is introduced to account for the small amount of plastic deformation, which occurred even at small stress. The creep data was fit to the modified model (Fig. 16c), and the parameters thus obtained were used to predict the stress relaxation behavior from the original model (Fig. 16b). It was found that the predicted stress relaxation behavior was in good agreement with that observed experimentally.

Finally, it is worth pointing out that stress relaxation is also a common loading situation in engineering applications, and it is closely related with creep in that both behaviors reflect the same fundamental viscoelastic nature of a given polymer[181]. If a material behaves in a perfectly linear viscoelastic manner, creep compliance and stress relaxation modulus can indeed be coupled with integral transformations[182]. However, since polymers, particularly semicrystalline polymers, tend to be non-linear viscoelastic[172], the relationship between creep and stress relaxation is complex[182] and has not been studied very often, expect for few cases[178,183,184].

References

1. B. Winderlich, *Macromolecular physics*, Vol.I, II, and III, New York, Academic Press 1973, 1976 and 1986

2. D. C. Bassett, *Principle of Polymer Morphology*, Cambridge, Cambridge University Press 1980

3. P. H. Geil, *Polymer Single Crystals*, New York, Wiley-Intersince 1963

4. H. Todokoro, *Structure of Crystalline Polymers*, New York, John Wiley 1979

5. A. Keller, *Rep. Progr. Phys.*, 622, **31**, 1968

6. P. J. Phillips, *Rep. Progr. Phys.*, 549, **53**, 1990

7. D. C. Bassett (Ed.), *Developments in Crystalline Polymers*, Vol. I and II, London, Applied Science Publisher 1980 and 1982

8. P. J. Barham, in "*Materials Science and Technology: A Comprehensive Treatment*", Vol.12. Ed. by E. J. Thomas. Weinheim, VCH 1993

9. R. Jaccodine, *Nature*, 305, **176**, 1955

10. P. H. Till, *J. Polym. Sci.*, 301, **24**, 1957

11. E. W. Fischer, *Z. Naturforsch*, 753, **12a**, 1957

12. A. Keller, *Phil. Mag.*, 21, **2**, 1957

13. K. H. Stroks, *J. Am. Chem. Soc.*, 1753, 60, 1938

14. *Faraday Discussions of the Chemical Society*, Vol. 68, 1979

15. B. Lotz and J. C. Wittmann, in "*Materials Science and Technology: A Comprehensive Treatment*", Vol. 12. Ed. by E. J. Thomas. Weinheim, VCH 1993

16. M. Hikosaka and T. Seto, *Polymer*, 111, **5**, 1973

17. P. Corradini, G. Giunchi, J. Petracone, B. Pirozzi and H. M. Vidal, *Gazz. Chim. Ital.*, 413, **110**, 1980

18. D. H. Reneker and J. Mazur, *Polymer*, 3, **29**, 1988

19. D. H. Reneker, in "*Computer Simulation of Polymers*": Ed. by R. J. Roe, Englewood Cliffs, Princeton Hall 1991

20. K. Abe, M. Niiomi and M. Tagayanagi, *J. Macromol. Sci.-Phys.*, 87, **B4**, 1970

21. V. F. Holland, *J. Appl. Phys.*, 3235, **35**, 1964

22. D. C. Bassett, *Phil. Mag.*, 595, **10**, 1964

23. B. Lotz, A. J. Kovacs and J. C. Wittmann, *J. Polym. Sci., Polym. Phys. Ed.*, 909, **13**, 1975

24. A. Keller, *Kolloid-Z. u. Z. Polymere*, 118, **219**, 1967

25. M. Tagayanagi and T. Matsuo, *J. Macromol. Sci., Phys.*, 407, **B1**, 1967

26. M. Tagayanagi, *J. Macromol. Sci.*, 391, **B9**, 1974

27. E. L. Thomas, S. L. Sass and E. J. Kramer, *J. Polym. Sci., Polym. Phys. Ed.*, 1115, **12**, 1974

28. I. R. Harrsion, A. Keller, D. M. Sadler and E. J. Thomas, *Polymer*, 736, **17**, 1976

29. T. Juska and R. I. Harrsion, *Polym. Eng. Rev.*, 13, **2**, 1982

30. R. Hosemann, in "*The Paracrystalline State of Synthetic Polymers": C.R.C. Critical Review in Macromolecules*, Boca Raton, CRC Press 1972

31. R. Patil and D. H. Reneker, *Polymer*, **34**, 1993

32. W. Stocker, M. Schumacher, S. Graff, J. Lang, J. C. Wittmann, A. J. Lovinger and B. Lotz, *Macromolecules*, 6948, **27**, 1994

33. D. Snetivy and G. J. Vancso, *Polymer*, 461, **35**, 1994

34. D. C. Bassett, F. C. Frank and A. Keller, *Phil. Mag.*, 1739, **8**, 1963

35. L. Mandelkern, *J. Polym. Sci., C*, 457, **68**, 1975

36. P. J. Flory, *J. Am. Chem. Soc.*, 2857, **84**, 1962

37. D. M. Sadler, in "*Structure of Crystalline Polymers*", Ed. by I. H. Hall, London, Elsevier Applied Science Publish 1984

38. D. M. Sadler and A. Keller, *Polymer*, 37, **17**, 1976

39. D. M. Sadler and A. Keller, *Science*, 263, **203**, 1979

40. D. Y. Yoon and P. J. Flory, *Polymer*, 509, **18**, 1977

41. J. Schelten, G. D. Wignall and D. G. H. Ballard, *Polymer*, 682, **15**, 1974

42. P. J. Flory and D. Y. Yoon, *Nature*, 226, **272**, 1978

43. I. G. Voigt and E. W. Fischer, *J. Polym. Sci. Polym. Phys. Ed.*, 2347, **18**, 1980

44. L. Mandekern, *Acc. Chem. Res.*, 81, **9**, 1976

45. G. R. Strobl and W. Hagedorn, *J. Polym. Sci., Polym. Phys. Ed.,* 1181, **16**, 1978

46. M. Goltin and L. Mandelkern, *Colloid Polym. Sci.,* 182, **260**, 1982

47. B. Wunderlinch and S. Z. D. Cheng, *Gazz. Chim. Ital.,* 345, **116**, 1986

48. P. J. Bassett, in "*Materials Science and Technology: A Comprehensive Treatment*", Vol. 12. Ed. by E. J. Thomas. Weinheim, VCH 1993

49. D. C. Bassett and A. M. Hodge, *Proc. Roy. Soc.,* 25, **A377**, 1981

50. M. I. Mark and S. Krimm, *J. Polym. Sci.,* 1785, **A-2 (7),** 1969

51. R. J. Young and P. B. Bowden, *J. Mater. Sci.,* 1177, **8**, 1973

52. Y. Kikuchi and S. Krimm, in "*Plastic Deformation of Polymers*", Ed. by A. Peterlin, New York 1971

53. D. C. Bassett, A. M. Hodge and R. H. Olley, *Proc. Roy. Soc.,* 39, **A377**, 1981

54. H. D. Keith and F. J. Padden, *J. Polym. Sci.,* 525, **4**, 1959

55. H. D. Keith, F. J. Padden and R. G. Vadimsky, *J. Polym. Sci.,* 267, **A-2(4)**, 1966

56. A. Peterlin, *J. Polym. Sci.,* 1151, **A-2(7)**, 1969

57. E. W. Fischer, K. Hahn, J. Kufler and R. Born, *J. Polym. Sci., Polym. Phys. Ed.*, 1491, **32**, 1971

58. S. Nagou and K. L. Azuma, *J. Macromol. Sci.-Phys.,* 435, **B-16**, 1979

59. I. M. Ward (Ed), *Developments in Oriented Polymers,* Vol. I, London, Applied Science 1982

60. A. Keller and J. W. H. Kolnaar, *Prog. Coll. Polym. Sci.,* 81, **92**, 1993

61. P. G. De Gennes, *J. Phys. Chem,* 15, **60**, 1974

62. A. Keller, A. J. Muller and J. A. Odell, *Prog. Coll. Polym. Sci.,* 175, **75**, 1985

63. J. A. Odell, A. Keller and A. J. Muller, *Prog. Coll. Polym. Sci.,* 301, **270**, 1992

64. J. A. Odell, A. Keller and A. J. Muller, *Polymer,* 1219, **26**, 1985

65. A. Keller and M. J. Machin, *J. Macromol. Sci.-Phys.,* 41, **B1(1)**, 1967

66. K. Kobayashi and T. Nagasawa, *J. Macromol. Sci.-Phys.,* 331, **B4(2)**, 1970

67. A. Keller and M. R. Mackley, *Pure Appl. Chem.,* 195, **39**, 1974

68. J. M. Salazar, J. V. G. Ramos and J. Petermann, *Inter. J. Polymeric Mater.,* 111, **21**, 1993

69. A. J. Pennings, J. M. A. A. Von der Mark and H. C. Booij, *Kooloid Z. u. Z. Polymere*, 99, **236**, 1970

70. D. T. Grubb and M. J. Mill, *J. Crystal Growth*, 321, **48**, 1980

71. I. L. Hay and A. Keller, *Kolloid Z. Z. Polym.*, 43, **204**, 1965

72. J. M. Brady and E. L. Thomas, *J. Mater. Sci.*, 3311, **24**, 1989

73. A. Peterlin, *Polym. Eng. Sci.*, 488, **18**, 1978

74. D. C. Prevorsek, H. B. Chin and S. Murthy, *ACS Prepr., PMSE*, 43, **70**, 1993

75. E. W. Fischer and H. J. Goddar, *J. Polym. Sci., Part C*, 4405, **16**, 1969

76. R. S. Porter, *ACS Polym. Prepr.*, 39, **12(2)**, 1971

77. E. S. Clark and L. S. Scott, *Polym. Eng. Sci.*, 682, **14**, 1974

78. J. Clements, R. Jakeways and I. M. Ward, *Polymer*, 639, **19**, 1978

79. J. Bicerano, *J. Macromol. Sci.- Rev. Macromol. Chem. Phys.*, 161, C36(1), 1996

80. S. Matsuoka, *Polym. J.*, 321, **17**, 1985

81. A. I. Melker and T. V. Vorobyeva, *Polym. Eng. Sci.*, 163, **36**, 1996

82. B. Crist and P. G. Herena, *J. Polym. Sci., Polym. Phys. Ed.*, 449, **34**, 1996

83. D. W. Van Krevelen, *Properties of Polymers*, 2nd Ed., Elsevier Science (1976)

84. D. W. Van Krevelen, in "*Computational Modeling of Polymers*", Ed. by J. Bicerano., New York 1992

85. O. Mekenyan, S. Dimitrov and D. Bonchev, *Eur. Polym. J.*, 1185, **19**, 1983

86. A. J. Polak and R. C. Sundahl, *Polymer*, 1314, **30**, 1989

87. M. R. Surgi, A. J. Polak and R. C. Sundahl, *J. Polym. Sci., Polym. Chem. Ed.*, 2761, **27**, 1989

88. J. Bigerano, *Predication of Polymer Properties*, Marcel Dekker, Inc./New York (1993)

89. D. T. Grubb, in "*Materials Science and Technology: A Comprehensive Treatment*", Vol. 12. Ed. by E. J. Thomas. Weinheim, VCH 1993

90. I. M. Ward, *Proc. Phys. Soc.*, 1176, **80**, 1962

91. D. W. Hadley, P. R. Pinnock and I. M. Ward, *J. mater. Sci.*, 152, **4**, 1969

92. R. H. Boyd, *J. Polym. Sci., Polym. Phys. Ed.*, 493, **21**, 1983

93. M. G. Northolt and J. J. Van Aartsen, *J. Polym. Sci., Part C,* 283, **58**, 1978

94. D. L. Green, A. P. Unwin, G. R. Davies and I. M. Ward, *Polymer,* 579, **31**, 1990

95. I. M. Ward and D. W. Hadley, *Mater. Forum,* 5, **11**, 1988

96. M. Tagayanagi and T. Kajiyama, *J. Macromol. Sci.-Phys.,* 1, **B8**, 1973

97. M. Tagayanagi, H. harima and Y. Iwata, *Men. Fac. Eng., Kyushu Univ.* 41, **23**, 1963

98. D. T. Grubb, *J. Polym. Sci., Polym. Phys. Ed.,* 165, **21**, 1983

99. M. Tagayanagi, K. Imada and T. Kajiyama, *J. Polym. Sci., C,* 263, **C15**, 1963

100. E. L. V. Lewis and I. M. Ward, *J. Macromol. Sci.,* 75, **B19**, 1981

101. M. Matsuo and C. Sawatari, *Macromolecules,* 1653, **21**, 1988

102. K. Nakamae and T. Nishino, in "*Integration of Fundamental Polymer Science and Technology*", London, Elsevier 1991

103. B. Jackson, P. J. Flory, R. Chiang and M. J. Richardson, *Polymer,* 237, **4**, 1963

104. J. C. Halpin and J. L. Kardos, *J. Appl. Phys.,* 2235, **43**, 1972

105. L. E. Nielsen, *J. Appl. Polym. Sci.,* 1485, **19**, 1975

106. P. J. Phillips and J. Patel, *Polym. Eng. Sci.,* 943, **18**, 1978

107. R. Popli and L. Mandelkern, *J. Polym. Sci., Polym. Phys. Ed.,* 458, **25**, 1987

108. R. L. McCullough, in "*Treatise on Materials Science and Technology*", Vol. 10, Part B, Ed. by J. M. Shultz, New York, Academic Press 1977

109. J. Janzen, *Polym. Eng. Sci.,* 1242, **17**, 1992

110. B. Crist, C. J. Fischer and P. R. Howard, *Macromolecules,* 1709, **22**, 1989

111. R. Popli and L. Mandelkern, *J. Polym. Sci., Polym. Phys. Ed.,* 441, **25**, 1987

112. F. J. Balta Calleja, *Adv. Polym. Sci.,* 117, **66**, 1985

113. L. Mandelkern, *Polym. J.,* 337, **17**, 1985

114. H. H. Chuan, J. S. Lin and R. S. Porter, *Macromolecules,* 2732, **19**, 1986

115. P. J. Phillips and R. J. Philpot, *Polym. Commun.,* 307, 1986

116. W. Wu, G. D. Wignall and L. Mandelkern, *Polymer,* 4137, **33**, 1992

117. S. J. Spells and E. U. Okoroafor, *Polymer,* 4590, **35**, 1994

118. B. K. Anns, J. Strizak, G. D. Wignall, R. G. Alamo and L. Mankelkern, *Polymer*, 137, **37**, 1996

119. C. Schipp, M. J. Hill, P. J. Barham, V. M. Cloke, J. S. Huggins and L. Oiarzabal, *Polymer*, 2291, **37**, 1996

120. P. B. Bowden and R. J. Young, *J. Mater. Sci.*, 2034, **9**, 1974

121. R. J. Young, in *"Development in Polymer Fracture"*, Ed. by E. D. Andrews, London, Applied Science 1979

122. R. F. Saraf and R. S. Porter, *J. Polym. Sci., Polym. Phys.*, 1049, **26**, 1988

123. L. Lin and A. S. Argon, *Macromolecules*, 4011, **25**, 1992

124. O. Darras and R. Seguela, *J. Polym. Sci.,., Polym. Phys. Ed.*, 759, **31**, 1996

125. C. G'Sell and J. J. Jonas, *J. Mater. Sci.*, 583, **14**, 1979

126. R. J. Young, P. W. Bowden, J. M. Ritchie and J. G. Rider, *J. Mater. Sci.*, 23, **8**, 1973

127. S. J. Krause, W. G. Hosford, *J. Polym. Sci., Polym. Phys. Ed.*, 1867, **27**, 1989

128. Z. Bartczak, A. S. Argon and R. E. Cohen, *Macromolecules*, 4692, **25**, 1992

129. Z. Bartczak, A. S. Argon and R. E. Cohen, *Macromolecules*, 5036, **25**, 1992

130. W. W. Adams, D. Yang and E. J. Thomas, *J. Mater. Sci.*, 2239, **21**, 1986

131. N. G. McCrum, B. E. Read and G. Williams, *Anelastic and Dielectric Effects in Polymeric Solids*, Wiley, New York 1967

132. R. H. Boyd, *Polymer*, 323, **26**, 1985

133. R. H. Boyd, *Polymer*, 1123, **26**, 1985

134. M. Ito, M. Kubo, A. Tsuruta and K. Tanaka, *J. Polym. Sci., Polym. Phys. Ed.*, 1435, **16**, 1978

135. P. A. Aylwin and R. H. Boyd, *Polymer*, 323, **25**, 1984

136. R. H. Boyd and P. A. Aylwin, *Polymer*, 330, **25**, 1984

137. R. H. Boyd and P. A. Aylwin, *Polymer*, 340, **25**, 1984

138. R. H. Boyd and P. A. Aylwin, *Polymer*, 347, **25**, 1984

139. K. H. Illers and H. J. Breuer, *J. Colloid Sci.*, 1, **18**, 1963

140. K. H. Illers, *Koll. Z. Z. Polym.*, 394, **251**, 1973

141. R. K. Eby, *J. Acoust. Soc. Sm.*, 1485, **36**, 1964

142. R. H. Boyd and K. Biliyar, *Am. Chem. Soc. Div. Polym. Chem. Polym. Prepr.*, 329, **14**, 1973

143. C. R. Ashcraft and R. H. Boyd, *J. Polym. Sci., Polym. Phys. Ed.*, 2153, **14**, 1976

144. M. Tagayanagi, *Pure Appl. Chem.*, 555, **15**, 1967

145. K. M. Sinnott, *J. Appl. Phys.*, 3385, **37**, 1966

146. N. G. McCrum and E. L. Norris, *Proc. Roy. Soc.*, London, 506, **A292**, 1966

147. H. Nakayasu, H. Markovitz and D. J. Plazek, *Trans. Soc. Rheol.*, 261, **5**, 1961

148. R. Popli, L. Mandelkern and R. S. Benson, *J. Polym. Sci., Polym. Phys. Ed.*, 407, **22**, 1984

149. R. H. Boyd, *Polym. Eng. Sci.*, 1010, **14**, 1979

150. F. C. Stehling and L. Mandekern, *Macromolecules*, 242, **3**, 1970

151. K. H. Illers, *Kolloid Z. Z. Polym.*, 622, **231**, 1969

152. M. L. Mansfield and R. H. Boyd, *J. Polym. Sci., Polym. Phys. Ed.*, 1227, **16**, 1978

153. R. W. Gary and N. G. McCrum, *J. Polym. Sci., Part A-2*, 1329, **8**, 1969

154. P. Schemdding and H. G. Zachmann, *Koll. Z. Z. Polym.*, 1105, **250**, 1972

155. K. Rosenke, H. Sillescu and H. W. Spiess, *Polymer*, 757, **21**, 1980

156. D. C. Douglass, V. J. McBriety and T. A. Weber, *J. Chem. Phys*, 1533, **64**, 1976

157. D. C. Douglass, V. J. McBriety and T. A. Weber, *Macromolecules*, 178, **10**, 1977

158. R. F. Boyer, *J. Macromol. Sci., Symp.*, 189, **50**, 1975

159. M. Baccaredda, E. Butta and V. Frosini, *Makromol. Chem.*, 14, **61**, 1936

160. E. A. Cole and D. R. Holmes, *J. Polym. Sci.*, 245, **46**, 1960

161. R. F. Boyer, *Rubber Rev.*, 1303, **34**, 1963

162. R. F. Boyer, *Rubber Chem. Tech.*, 1303, **34**, 1963

163. R. F. Boyer and S. M. Breitling, *Macromolecules*, 855, **7**, 1974

164. T. F. Schatzki, *J. Polym. Sci.*, 496, **57**, 1962

165. T. F. Schatzki, *J. Polym. Sci. Part C*, 139, **14**, 1966

166. I. M. Ward, *Mechanical Properties of Solid Polymers*, John Wiley & Sons, 1983

167. H. Leadmann, *Trans. Soc. Rheol.*, 361, **6**, 1962

168. B. Berstein, E. A. Kearsley and L. P. Zapas, *Trans. Soc. Rheol.*, 391, **7**, 1963

169. K. C. Valanis and R. F. Landel, *Trans. Soc. Rheol.*, 243, **11**, 1967

170. R. A. Schapery, *Polym. Eng. Sci.*, 295, **9**, 1969

171. I. M. Ward and E. T. Onat, *J. Mech. Phys. Solids*, 217, **11**, 1963

172. W. N. Findley, J. S. Lai and K. Onaran, *Creep and Relaxation of Nonlinear Viscoelastic Materials*, North-Holland Publisher, 1976

173. G. Hasley, H. J. White and H. Eyring, *Text. Res. J.*, 295, **15**, 1945

174. H. Leadmann, *Elastic and Creep Properties of Filaments Materials and Other High Polymers*, Textile Fundamental, Washington, D.C., 1943

175. O. D. Sherby and J. E. Dorn, *J. Mech. Phys. Solids*, 145, **6**, 1958

176. M. A. Wilding and I. M. Ward, *Polymer*, 969, **19**, 1978

177. M. A. Wilding and I. M. Ward, *Polymer*, 870, **22**, 1981

178. M. A. Widling and I. M. Ward, *J. Mater. Sci.*, 629, **19**, 1984

179. J. P. Penning, H. E. Preas and A. J. Penning, *Colloid Polym. Sci.*, 664, **271**, 1994

180. M. A. Wilding and I. M. Ward, *Polymer*, 4579, **25**, 1995

181. J. J. Aklonis and W. J. MacKnight, *Introduction to Polymer Viscoelasticity*, 2nd. Ed. John Wiley & Sons Publication 1992

182. J. D. Ferry, *Viscoelastic Properties of Polymers*, 3rd Ed., Wiley, New York 1980

183. S. K. Reif, K. J. Amberge and D. A. Woodford, *Materials & Design*, 15, **16**, 1995

184. G. G. Grzywinski and D. A. Woodford, *Materials & Design*, 279, **14**, 1993

Chapter 3.0 MATERIALS AND CHARACTERIZATION DATA

The HDPE films utilized in the studies described in chapters 4.0~7.0 of this document were kindly provided by Hoechst Celanese Cooperation. All the films are based on two resins, designated as Resin 1 and Resin 2, respectively. Both resins have the same number average molecular weight of 14,600g/mol, but different weight average molecular weight of 150,000 and 290,000g/mol, respectively. Many characterizations have been performed by the supplier as well as in a previous doctoral study that focus on processing-structure relationships for these films[1]. The following introduction is presented as a brief summary on these studies. More detailed information can be obtained from ref. 1.

The HDPE films were produced by melt extruding the two resins through an industrial scale blown-film system with a blow-up ratio of 1.0 (uniaxial), as schematically shown in Fig. 3.1. Four processing parameters (shown in Fig. 3.1) have been manipulated to promote different crystalline orientation states and morphologies for the melt-extruded HDPE films. They include: 1) the melt temperature at the exit of the die; 2) the quench height which is the distance from the die exit to the cooling ring; 3) the air flow rate in the cooling ring; 4) the line speed at which the melt-extruded film is collected. The effects of these parameters on the final structure of the melt-extruded films have been well studied previously[1]. It needs to be pointed out that the term uniaxial is used here to emphases the nature of the morphologies generated by the melt-extrusion, although there is a degree of thinning-down in the transverse direction (TD) (thickness direction) of the extruded films.

Under comparable processing conditions, the melt-extruded films based on Resin 1 and Resin 2 possess similar high crystalline orientation state and near zero amorphous orientation state but different morphological features. Resin 1 films tend to have a stacked lamellar morphology with crystalline lamellae stacked with their normals more or less along the machine direction (MD). The morphology for Resin 2 films contains, in addition to the stacked lamellae, a distinguishable amount of row-nucleated fibril structures along the MD. As stated above, in both cases, the amorphous phase is essentially at an unoriented state.

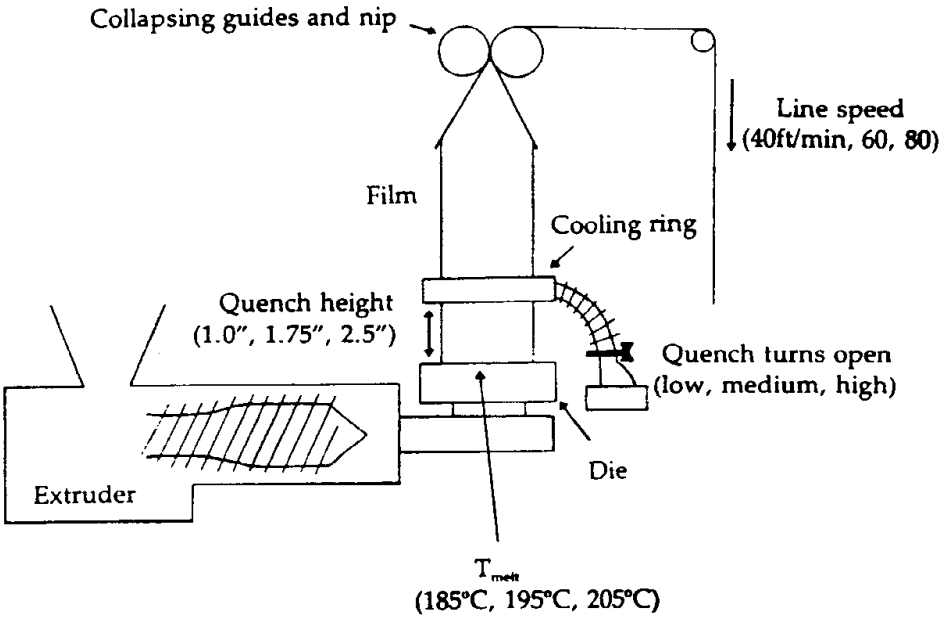

Figure 3.1 Schematic drawing of the melt extrusion processing used for the preparation of the the HDPE films used in this dissertation study[1].

The effect of molecular weight distribution on the morphological features of the melt-extruded HDPE films have been investigated[1]. By fitting the complex viscosity data to the Carreau-Yasuda equation, it was found that the characteristic relaxation time, which is an index of molecular relaxation time in the melt state at 190°C, are 81sec and 526sec for Resin 1 and Resin 2, respectively. It was concluded that the somewhat higher orientation and the distinct presence of the row-nucleated fibril structure in Resin 2 film is due to the much longer melt relaxation time possessed by this material. For the Resin 1 film, on the other hand, the relative small melt relaxation time allows a lower orientation state and, more importantly, the absence of (at least visually) the row nucleated fibril structure.

These two "model" morphologies employed in this dissertation research are uniaxially oriented well-stacked lamellar morphology, either with or without the distinct presence of row-nucleated fibril structures. Figures 3.2a and b and 3.3a and b present the TEM and AFM micrographs for the two kinds of morphologies. The detailed procedures for these experiments will be introduced in chapters 4.0~7.0. One can see the stacked lamellae morphology for the Resin 1 film (Figs. 3.2a and 3.3a) and the distinct presence of fibril or row-nucleated fibril structure in the matrix of stacked lamellae for Resin 2 film (Figs. 3.2b and 3.3b). WAXS experiments with the X-ray beam parallel to the machine direction (MD), transverse direction (TN) and normal direction (ND) are presented in Figs. 3.4a-d and Figs. 3.5a-d for films based on Resin1 and Resin 2. From these WAXS patterns, it can be concluded that both films were essentially uniaxially oriented with respect to the MD. Additionally, sharp reflection spots at the equator were observed for the Resin 2 films (Figs. 3.5c and d), and they arise from the highly oriented row-nucleated fibril structures in the materials.

In addition to the melt-extruded films, two kinds of annealed films, tension-annealed films and free-annealed films, were also used in this study. The former are films that were annealed by passing the corresponding melt-extruded films through an oven, under a small amount of tension (ca. 3% strain) at 120°C with a line speed that allowed the materials to stay at this temperature for ca. 20min. The latter are films that were annealed by simply putting the melt-extruded films in an oven at 120°C for 20min without applying any force. As noted in an earlier study, these two

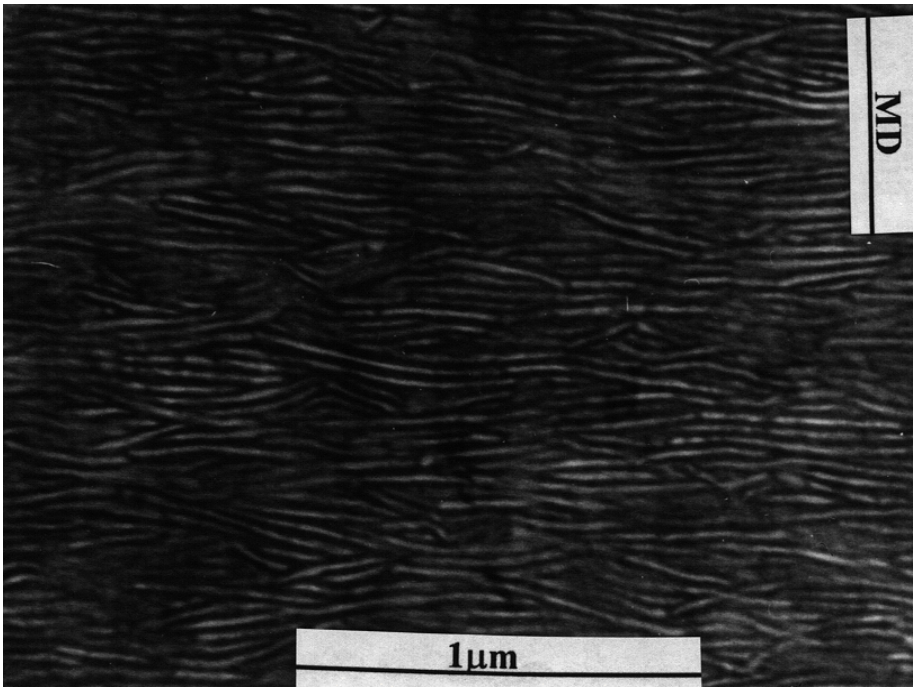

a

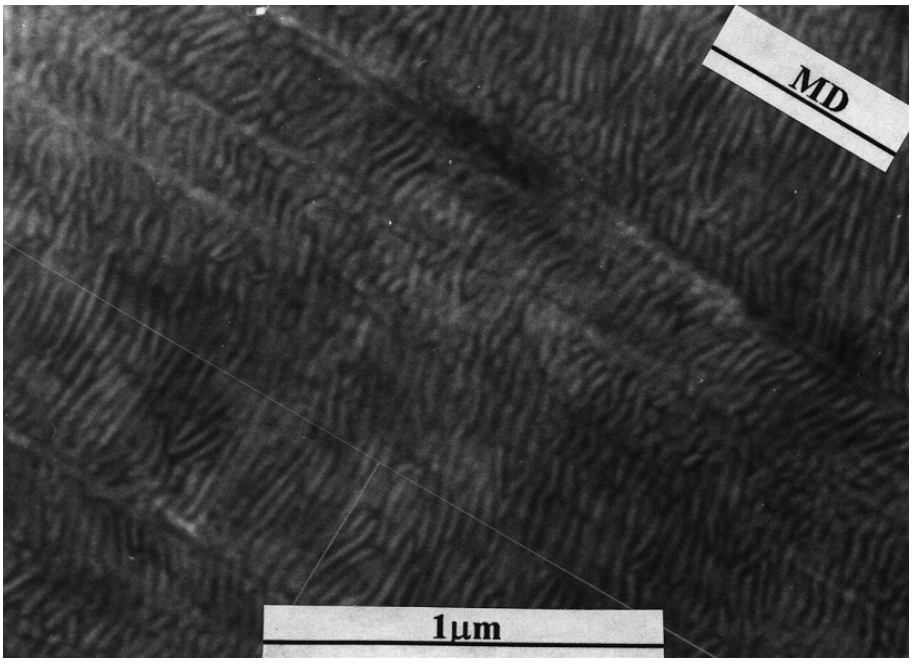

b

Figure 3.2 TEM micrographs for (a) the tension-annealed film of Resin 1 and (b) the tension-annealed film of Resin 2.

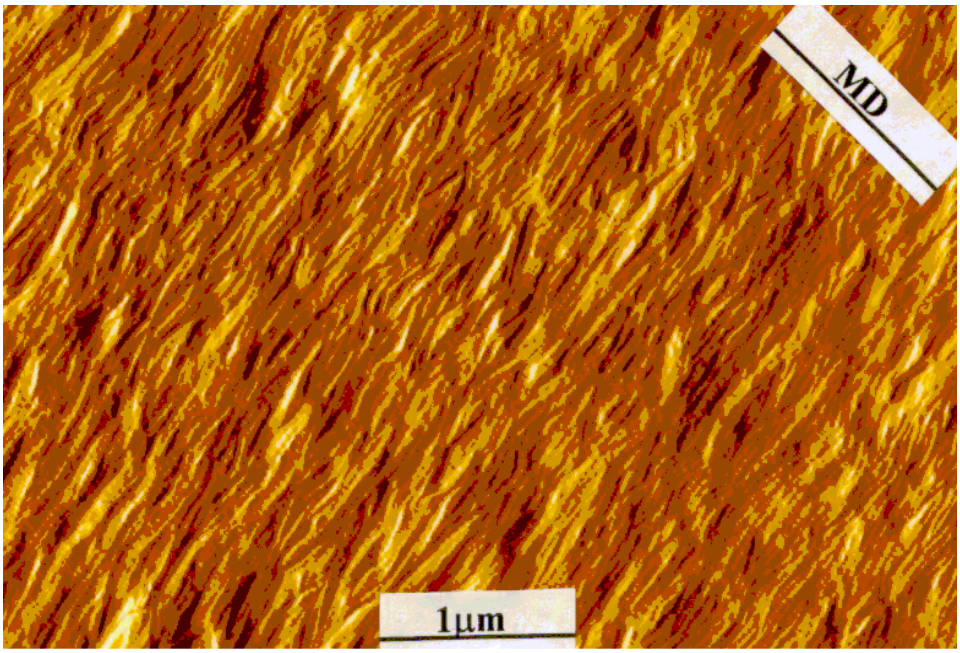

a

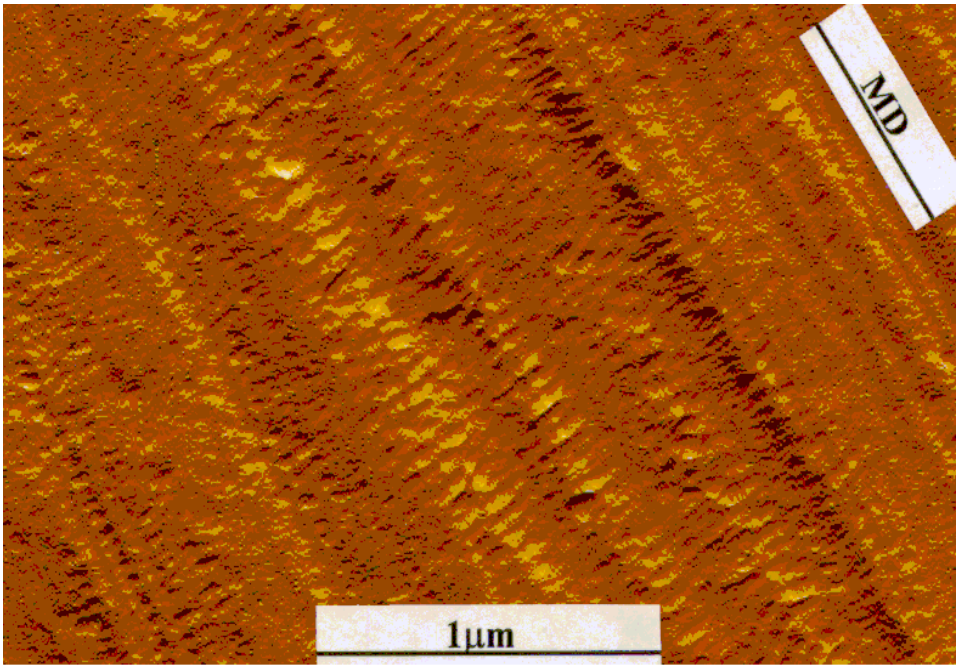

b

Figure 3.3 AFM images for (a) the tension-annealed film of Resin 1 and (b) the tension-annealed film of Resin 2.

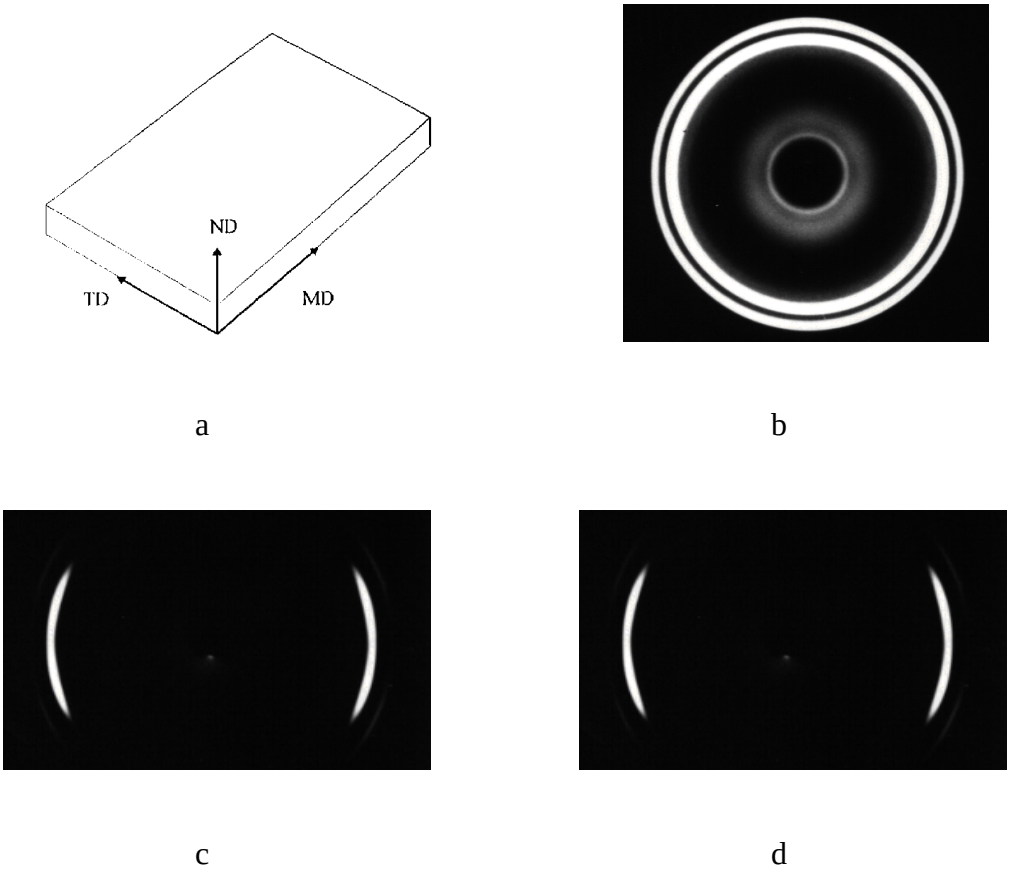

Figure 3.4 WAXS patterns for the tension-annealed film of Resin 1 with X-ray beams directed at (b) MD, (c) TD and (d) ND

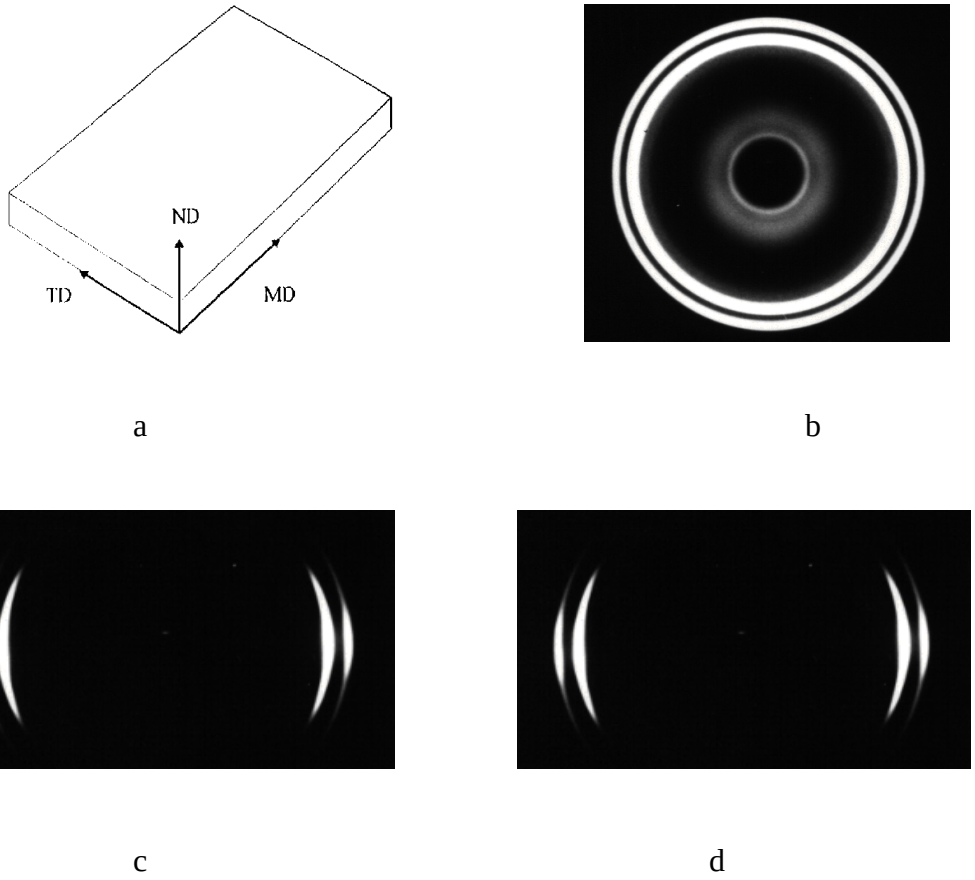

Figure 3.5 WAXS patterns for the tension-annealed film of Resin 2 with X-ray beams directed at (b) MD, (c) TD and (d) ND.

kinds of annealed films are different, not only in their final orientation state but also in morphological features such as degree of perfection and thickness of the crystalline lamellae[2].

The orientation of the HDPE films has been thoroughly investigated by a variety of techniques, including birefringence, WAXS, and infrared dichroism[1]. Generally, orientation of a polymer chain is defined by Hermans orientation function which has the following formula[3,4]

$$f = \frac{1}{2}\left(3 < \cos^2\theta > -1\right) \qquad (3.1)$$

in which θ is the angle between the chain axis and a reference axis (usually the machine direction), and $<\cos^2\theta>$ means the average value of $\cos^2\theta$ over space. Therefore, if all the chains are perfectly orientated along the reference direction, then θ = 0° and f = 1. On the other hand, if all the chains are oriented perpendicular to the reference direction, then θ = 90° and f = –0.5.

Optical birefringence is a simple way to study the overall orientation of a polymer[5]. For semicrystalline polymers, however, since the material have multiple phases, i.e. a crystalline phase and a amorphous phase, this technique needs to be used in conjunction with others to provide a description of the orientation state for each phase[4]. Total birefringence (Δ) of a semicrystalline polymer can be expressed as

$$\Delta = X_c \cdot f_c \cdot \Delta_c^o + (1 - X_c) \cdot f_{am} \cdot \Delta_{am}^o + \Delta_{form} \qquad (3.2)$$

where f_c and f_{am} are the crystalline and amorphous orientation functions, Δ^o_c and Δ^o_{am} are the intrinsic birefringences for perfectly uniaxially oriented crystalline and amorphous phase, Δ_{form} is the form birefringence due to the distortion of the incident light wave at asymmetric phase boundaries, and X_c is crystallinity. Assuming Δ^o_c =0.058 and Δ^o_{am} =0.200 and the contribution of Δ_{form} is negligible[4,7], the orientation of the HDPE films has been characterized[1]. Combining the birefringence data with those from WAXS, it has been shown that the amorphous phase is basically in a near unoriented state for the films based on Resin 1 and Resin 2.

WAXS is a another common way to investigate the orientation of the crystalline phase. According to Stein, et al[8], orientation functions for the crystal a- and b-axes of an orthorhombic structure, like that for HDPE, in uniaxial orientation condition can be determined by utilizing the

azimuthal intensity distribution of the (200) and (020) reflections by applying the following equation

$$f_a = \frac{1}{2}\left(3 \cdot \cos^2\theta_{200} \cdot < \sin^2\psi_{200} > -1\right) \qquad (3.3a)$$

$$f_b = \frac{1}{2}\left(3 \cdot \cos^2\theta_{020} \cdot < \sin^2\psi_{020} > -1\right) \qquad (3.3b)$$

where θ_{200} and θ_{020} are the Bragg angles for the (200) and (020) reflections, $<\sin^2\psi_{200}>$ and $<\sin^2\psi_{020}>$ represent the intensity distribution of the (200) and (020) reflection arcs. Often, the sine square average values are estimated by the half-width of the appropriate reflection arcs[9,10]. Since HDPE has an orthorhombic unit cell, the crystal c-axis is perpendicular to both a- and b-axes; therefore, the orientation of the crystal c-axis, i.e. chain axis, can be obtained by

$$f_a + f_b + f_c = 0 \qquad (3.4)$$

The crystalline orientation function calculated by this way for the HDPE films are shown in Table 3.1. It should be pointed out the calculation of the orientation function for the films based on Resin 2 did not take into account the highly concentrated reflection spots at the equator, which are due to the row-nucleated fibril structures in the materials.

IR dichroism has also been used for the purpose of orientation determination. This technique has the capability of detecting the orientation state for each individual component[12]. In this technique, an orientation function for a specific chromophoric group can be calculated by the following[3,4]

$$f = \frac{D_o + 2}{D_o - 1} \cdot \frac{D - 1}{D + 2} \qquad (3.5)$$

where D is the dichroic ratio defined as $A_{||}/A_{\perp}$, with $A_{||}$ and $A_{\perp}$ being the IR absorbances with polarized IR beam parallel and perpendicular to sample's reference direction, D_o is the intrinsic dichroic ratio and it can be calculated by $D_o = 2\cot^2\beta$, with β being the angle between the transition moment of the chromophoric group and the chain axis ($D_o = \infty$ for PE). For the case of HDPE, by utilizing absorptions at wavenumbers of $720cm^{-1}$ and $730cm^{-1}$, which correspond to a rocking vibration of $-CH_2-$ in the crystalline phase[11,12], and $1368cm^{-1}$, which is a characteristic

band for the amorphous phase[11,12], the orientation functions for the amorphous phase have been calculated[1] and also included in Table 3.1

Table 3.1 also lists the crystallinity and some brief remarks on the structural features for the precursor and tension-annealed HDPE films. The crystallinity data (mass-based) were generated by DSC, choosing ΔH_f (heat of fusion for PE crystal) = 293J/g[13]. The well-defined and very comparable structures for the HDPE films based on the two resins, in terms of orientation state and crystallinity, allows for a clear demonstration and a fair comparison for the structure-property relationship, as will be presented in chapters 4.0~ 7.0.

Table 3.1 Orientation state, percent crystallinity and structural features for HDPE films (1 mil thick) used in this dissertation study.

Sample	f_c WAXS	f_a IR	X_c DSC	Structural Features
R1-pre	0.67	0.03	0.60	Stacked lamellae without a distinct presence of row-nucleated fibril structures
R1-anl	0.80	0.04	0.67	
R2-pre	0.71	0.04	0.61	Stacked lamellae with a distinct presence of row-nucleated fibril structures
R2-anl	0.81	0.03	0.71	

References

1. Ta-hua Yu, *Ph. D. Dissertation*, Virginia Tech, 1995

2. Hongyi Zhou and G. L. Wilkes, *Macromolecules*, submitted

3. G. L. Wilkes, *Encyl. Polym. Sci. and Eng.*, John Wiley & Sons, Inc., **14**, 1988

4. R. J. Samules, *"Structured Polymer Properties"* John Wiley & Sons, Inc., New York, 1974

5. R. S. Stein, *"Newer Methods in Polymer Characterization"* Wiley - Interscience, New York, 1964

6. W. T. Mead, C. R. Desper and R. S. Porter, *J. Polym. Sci. Polym. Phys. Ed.*, 859, **17**, 1979

7. M. Pietralla, H. P. Grossman and J. K. Kruger,*J. Polym. Sci. Polym. Phys. Ed.*, 1193, **20**, 1982

8. R. S. Stein and F. H. Norris, *J. Polym. Sci.*, 381, 21, 1956

9. R. S. Stein, *J. Polym. Sci.*, 327, **31**, 1958

10. R. S. Stein, *J. Polym. Sci.*, 335, **31**, 1958

11. B. E. Read, in *"Structure and Properties of Oriented Polymers"*, Ed. by I. M. Ward, John Wiley & Sons, Inc., 1975

12. B. E. Read and R. S. Stein, *Macromolecules*, 116, **1**, 1968

13. L. Mandelkern, *"Crystallization of Polymers"*, New York, 1964

Chapter 4.0 ORIENTATION DEPENDENT MECHANICAL PROPERTIES AND DEFORMATION MORPHOLOGIES FOR UNIAXIALLY MELT EXTRUDED HIGH DENSITY POLYETHYLENE FILMS HAVING AN INITIAL STACKED LAMELLAR TEXTURE *

Abstract

Mechanical properties and the associated plastically deformed morphologies of high density polyethylene films were investigated by tensile testing, WAXS and TEM. Uniaxially oriented films having a well-defined stacked lamellar morphology, both with and without row-nucleated structure were deformed at three angles, 0°, 45° and 90°, with respect to the original machine (extrusion) direction. A distinct orientation dependence of the mechanical properties was observed and this dependence has been related to the different morphologies developed during the plastic deformation processes. It was shown that lamellar separation, lamellar shear and lamellar break-up were the dominant initial deformation mechanisms for the respective 0°, 45° and 90° deformations. As a result, the 45° and 90° deformations generated a final microfibril morphology oriented along the stretch direction; while the 0° deformation resulted in broken (mosaic) blocks of crystalline lamellae. The presence of distinct row-nucleated crystalline fibrils in the initial structure stiffens the material in the 0° deformation; however, it significantly limits the ability of the materials to cold draw at the 90° deformation. Morphological models were proposed to explain the plastic deformation process for the different deformation angles, as well as for the deformation behavior of semicrystalline polymers with an isotropic spherulitic morphology.

* This chapter, formatted as required, has been submitted to *Journal of Materials Science* for publication.

4.1 Introduction

Polymers represent a very important and still rapidly growing class of engineering materials. Among them, semicrystalline polymers are of particular interest. Often, their remarkable drawability makes it possible to highly orient them in the solid state. Solid state processing techniques, such as drawing fibers or stretching films, depend upon the plastic deformation characteristics of the given polymer. During solid state processing, macromolecular chains are often preferentially oriented along a specific direction, e.g. the machine direction, so that the final products possess the desired properties at this particular orientation, this generally being the loading direction in most applications. From an engineering point of view, in order to manipulate the final properties of the materials, it is important to understand the physical orientation process and therefore to be able to control the orientation state of both the crystalline and amorphous phases. On the other hand, the detailed molecular rearrangement in the process of plastic deformation is also an interesting topic for fundamental research. Thus, it is not surprising that there has been a tremendous amount of research that has been focused on this area [1-10].

Semicrystalline polymers that crystallize under quiescent conditions often have a spherulitic morphology. For these unoriented semicrystalline polymers, there are three basic levels of microstructures that are important in the deformation process [11]: 1) the 2 to 20Å level, which represents the interactions between neighboring chain segments in both the crystalline phase and the amorphous phase; 2) the 100 to 300Å level, which represents the thickness of the crystalline lamellae and of the amorphous layers between the crystalline lamellae; 3) the 0.5 to 100 μm level, which represents the dimension of larger scale superstructures such as spherulites, which are complex arrangements of crystalline lamellae and amorphous regions. Therefore, semicrystalline polymers possessing a spherulitic morphology must be regarded as microstructural and mechanical complex systems, as depicted in Fig. 4.1 (according to ref.12), in which all the three levels of structure influence the deformation process. Certainly, there are cases where all the above three levels are not always present such as, for example, semicrystalline polymers that have already undergone extensive drawing.

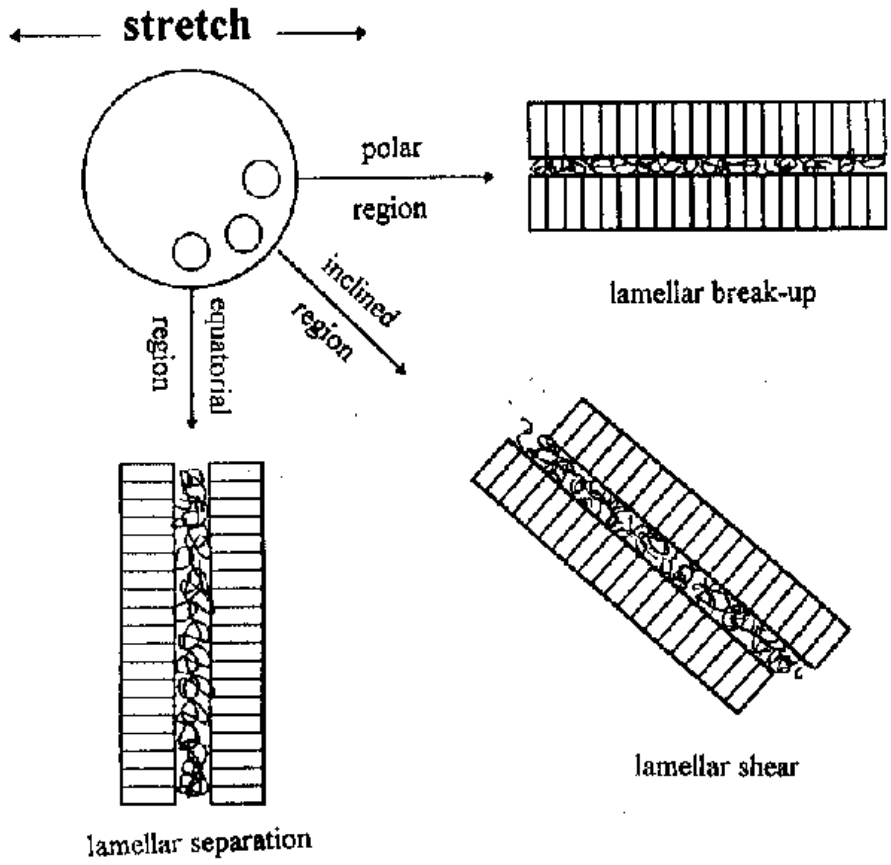

Figure 4.1 A schematic drawing that shows the complexity of the deformation of spherulitic morphology.

A variety of experimental techniques have been utilized to investigate the morphological changes during the plastic deformation process at the three structural levels: optical microscopy (OM) [13], scanning electron microscopy (SEM) [14-17], transmission electron microscopy (TEM) [18-27], atomic force microscopy (AFM) [28-30], electron diffraction (ED) [31-32], small angle light scattering (SALS) [34], wide angle X-ray scattering (WAXS) and small angle X-ray scattering (SAXS) [34-50], small angle neutron scattering (SANS) [51-54], infrared spectroscopy (IR) [41,55], Raman spectroscopy (RAM) [41,45,56], electron paramagnetic resonance (EPR) [57], differential scanning calorimetry (DSC) [58], dynamic mechanical thermal analysis (DMTA) [59], stress-strain deformation [60], and microhardness [61]. Most of the studies quoted above have utilized high density polyethylene (HDPE) as a model material due to its high commercial importance but also due to its *relatively* simple backbone chemical structure and relatively better understood crystallization behavior and morphology as well.

In the following paragraphs, and utilizing HDPE as the principal example, a brief overview is provided to summarize the current understanding about the deformation mechanisms and the final morphologies for semicrystalline polymers, obtained primarily by X-ray scattering and electron microscopy studies. More thorough and detailed reviews can be obtained from refs. 1-10, especially refs. 2,3,8. By combining the use of SAXS and WAXS, *either real time or via post deformation investigations*, it has been possible to detect the deformation processes at the crystalline lamellae and amorphous interlayer level as well as at the crystallographic level. With the help of electron microscopy, particularly TEM, more details of the locally deformed morphologies of crystalline lamellae have been observed and have generally confirmed the deformation mechanisms proposed based on X-ray scattering experiments.

According to the theory of crystal plasticity, which was originally developed for metals, plastic deformation at the crystallographic level can be achieved by three different mechanisms - these being slip, mechanical twinning and martensitic phase transformation [34-36]. Furthermore, the plastic deformation of semicrystalline polymers has also been considered as a decrystallization process, defined as mechanically induced destruction of crystalline lamellae (unfolding) followed by a recrystallization process [17,51]. These two interpretations have been supported by some

experimental results, but neither have successfully explained all the experimental observations. It appears that, at least for HDPE, yielding at or near room temperature is basically controlled by crystal plasticity processes; while for large post-yielding deformations, decrystallization and recrystallzation are involved. However, by examining the final morphology of the deformed material, it seems impossible to distinguish the mechanisms by which the deformation may have occurred. Therefore, other techniques such as mechanical testing have to be used in conjunction with scattering and microscopy to better understand this topic.

slip: When the resolved shear stress on a particular slip plane in specific slip directions for a given crystal is larger than that of the critical shear stress for the slip system, dislocation motion occurs. The speculations about the existence of dislocations in polymer crystals has been confirmed by the formation of moiré fringes between crystalline lamellae as well as by direct observation by electron microscopy [32]. The long-chain nature of polymer crystals requires that the *most preferred* slip plane contains the polymer chains-meaning that the slip planes must be of the {hk0} types - assuming that the c-axis is parallel to the chain axis and chain folding is of tight-folds - such that the polymer chains remain unbroken during slip. Slip can be either in the chain direction (*chain slip*), which is the dominate event, or perpendicular to the chain direction (*transverse slip*), which is further restricted to the chain-folding planes to prevent the disruption of the chain folds of the crystalline lamellae. It is expected that chain slip must be influenced by the nature of chain folding, such as fold tightness, chain re-entry, etc. It is also expected that crystallization kinetics can affect the feasibility of chain slip, i.e., it is certainly easier for chain slip to take place if the crystallization is confined within regime I, as compared to the cases of regimes II and III - assuming the crystallization can be described by the regime theory [62].

From the WAXS and SAXS studies on stretched HDPE [35,39], chain slip has been proposed to occur by two different routes for a slip system to achieve the same amount of strain. Deformation can be introduced by *fine slip*, where a small amount of slip occurs equally on a large number of parallel planes. On the contrary, the deformation can also be generated by *course slip (block slip)*, where slip takes place on fewer number of planes with a large amount of slip.

Microscopically, fine slip results in a change of the angle between the molecular chain axis and the normal of the crystalline lamella, whereas for course slip this angle remains unchanged.

Mechanical twinning and martensitic phase transformation: According to the theory of crystal plasticity, other deformation modes, namely mechanical twinning and martensitic phase transformation, can also produce plastic strain. Mechanical twinning is characterized by shearing part of a crystal with respect to a shear plane which is common for both the product and the parent crystals. The result of this is the formation of a mirror symmetry with respect to the shear plane. Martensitic phase transformation is a strain-induced phase transition, where the product phase and the parent phase share a common invariant plane and/or a common invariant direction. Mechanical twinning has been detected on rolled HDPE by WAXS [34,36], and the development of a monoclinic crystalline phase as a result of a martensitic phase transformation has also been found in the same study [36] as well as others for the cold-drawn PE [41,44-47,49].

Again, the long-chain nature of polymers limits the shear and invariant planes for the mechanical twinning and martensitic phase transformation to the {hk0} types. For HDPE, the proposed shear planes include {310} and {110}, which result in lattice rotations about the chain axis by 55° and -67°, respectively. For martensitic phase transformation, the orthorhombic crystalline structure (a = 0.742nm, b = 0.495nm, and c = 0.254nm) is transformed into the monoclinic crystalline structure (a = 0.809nm, b = 0.479nm, and c = 0.254nm, $\gamma = 107.9°$) at a shear strain of either 0.201 or 0.318, corresponding to two types of shear that can most favorably result in the transformation from the orthorhombic unit cell to that of the monoclinic unit cell [63]. It is necessary to point out, however, that the amount of strain produced by the latter two deformation modes is less than that from chain slip.

Decrystallization and recrystallization processes*:* According to this proposal, the dominant mechanism for yielding and further plastic deformation for semicrystalline polymers are sequential events of partial or local melting, stretching of the melted polymer chains, and recrystallization under the applied stress. When a polymer yields, the local temperature may rise through viscous heating in that region that undergoes necking, and this may cause the melting of crystalline lamellae in the necked region. The chains in the melt are then stretched towards the

direction of the applied stress, and finally recrystallize into an oriented microfibrillar crystalline phase. This process continues as necking proceeds along the specimen. By this route the original (spherulitic) structure is converted into a highly oriented microfibril structure which contains alternating crystalline lamellae and amorphous regions.

At the crystalline lamellae and amorphous layers level, semicrystalline polymers can be regarded as consisting of crystalline lamellae separated by an amorphous phase and held together by tie chains, although the nature of the chain-folding surface and the adjacent amorphous phase as well as the exact physical state of the tie-chains are still not completely understood due to their complex dependence on chain structure, crystallization kinetics, processing, etc. In light of the above consideration, three deformation modes, namely lamellar shear, lamellar separation and lamellar rotation, have been postulated as being associated with the deformation at this structural level.

Lamellar shear: This deformation mode involves a simple shear of the amorphous regions between the crystalline lamellae, with the shear direction being parallel to the lateral direction of the crystalline lamellae. This deformation mode has been observed by SAXS for rolled HDPE [38]. It is believed that this deformation mode is relatively easy to induce since the amorphous phase is in a rubbery state at ambient temperature for HDPE. Also, it is interesting that WAXS and SAXS results suggest that, during the deformation process, lamellar shear and chain slip, which are relatively easy to promote, are in competition, i.e., lamellar shear induced rotation of crystalline lamellae towards the applied stress direction and chain slip induced rotation of chains towards the same stress direction provide constraints on each other [37].

Lamellar separation: In the same experiments in which lamellar shear has been proposed [37,38], the total change in the long-spacing calculated from the SAXS data did not match with that due to chain slip (corrected by chain tilting); therefore, lamellar separation was proposed and has successfully explained the experimental results. This deformation mode has been shown to be especially valid in the deformation of hard-elastic fibers due to the special stacked lamellar morphology possessed by these fibers [25]. For HDPE, this deformation mode was found to be highly reversible, and this was believed to be due to the rubbery state of the

amorphous phase [37]. In the case of hard-elastic fibers, the processes of elastic bending of the crystalline lamellae as well as an opening or splaying of the amorphous phase between the crystalline lamellae (resulting in a localized decrease in density) have been proposed [25].

Lamellar rotation: The existence of this kind of deformation mode has initially been speculated to explain the fact that semicrystalline polymers can be deformed relatively easily, regardless that they rarely possess five independent slip systems which are necessary for a crystal to be deformed based on crystal plasticity theory [64]. Later, such deformation was indeed observed by SAXS [37] and SEM [14] on stretched HDPE. In order to accommodate any structural distortion, it is often necessary for the crystalline lamellae to rotate in the process of deformation [6]. For HDPE, the rubbery amorphous phase makes this much easier to occur at room temperature. Therefore, although lamellar rotation does not produce any major strain by itself; rather, it serves as an important process in which the crystalline lamellae can adjust themselves during the deformation process to generate a larger amount of strain in the amorphous phase.

Based on both X-ray scattering and electron microscopy studies, several morphological models have been proposed to describe the plastic deformation process for semicrystalline polymers, more specifically the drawing process that transforms an isotropic spherulitic structure into a microfibril structure [65-70]. All the models share some of the basic deformation stages, while the differences lie in the elements of the final morphology as well as their origins. The basic deformation processes have been proposed as follows: the stressed spherulitic lamellae shear into crystal blocks by chain slip; then the crystal blocks rotate such that the polymer chains align towards the local principal stress directions. During this transition, the crystal blocks decrease in width, by chain slip and/or lamellar break-up (unfolding of crystalline lamellae), until a microfibrillar structure is formed, which is the basic structural element of these models.

In Peterlin's model [65], the microfibrils are considered as being composed of alternating crystal blocks and amorphous regions connected by taut tie-chains. Therefore, the modulus of a drawn semicrystalline polymers along the drawing direction is proportional to the number of the taut tie-chains which serve as load transfer agents. Similar models have also been proposed by

Prevorsek [66] and Fischer [67], in which the amount of the taut tie-chains was related to the draw ratio of the respective drawn material. However, Porter [68] and Clark [69] suggested a different kind of extended-chain model, in which the microfibrils are considered as a extended-chain crystalline phase with chain ends being incorporated into the crystalline phase as defects. This type of model has been used to explain the ultra-high modulus of the ultra-drawn fibers. Furthermore, Ward [70] proposed a third kind of model, which somewhat combines both features of microfibril models and the extended-chain model, i.e., the morphology of highly drawn semicrystalline polymers consists of stacks of crystalline lamellae linked by short crystalline bridges, in which polymer chains are in an extended-chain conformation. This model has also been used to explain the enhanced modulus of highly drawn fibers.

Given the above mentioned massive, fruitful and sometimes imaginative investigations, there is still a need to 1) clearly display or observe the development of the morphological changes during the deformation process for general semicrystalline polymers, and more importantly, 2) closely relate the observed morphology to the relevant mechanical properties of the materials. In most of the deformation studies for semicrystalline polymers, the WAXS and SAXS results have not been directly related to mechanical properties, i.e., the samples used for the mechanical tests and those for WAXS and SAXS experiments were either different or the same but without knowing the precise amount of strain. Although there were studies in which such an effort has been made [43,47], they lacked direct support from either electron microscopy studies or mechanical testing. For the TEM studies, the majority of the investigations have utilized specially prepared ultra-thin ultra-drawn films that are suitable for direct TEM observation [32]. Although such films are excellent for direct visualization, they have often possessed a shish-kebab morphology, and the presence of the shishes certainly influences the deformation morphology and mechanical property of the films (see later discussion in this paper as well). Therefore, the conclusions drawn from the studies that have made use of the ultra-thin ultra-drawn films need to be further confirmed by comparable investigations by utilizing other more conventional morphological systems. Additionally, it is also hard to conduct mechanical tests on ultra-thin films, although such a measurement has been reported [20].

In the study now presented, HDPE films having simple and well-defined stacked lamellar morphology, *either with or without* a distinct presence of row-nucleated fibril structure, have been utilized as model materials to *elucidate* and *demonstrate* the morphological changes during the process of plastic deformation. In addition, the *microscopic morphologies* developed during the deformation, as revealed by WAXS and TEM, have been related to the *macroscopic properties*, as measured by direct tensile tests. The samples for the WAXS and TEM experiments studies were deformed to specific amount of stain according to the corresponding stress-strain curves. The mechanical properties have been explained by the development of the deformation induced morphologies. The specific morphological features of these films also allowed us to carry out plastic deformation at different orientations with respect to the original machine direction, it is possible, therefore, to not only present a model structure-property study about the effect of orientation on the deformation morphology and the mechanical properties, but also to partially mimic the heterogeneous (position-dependent) deformation process that one encounters in the spherulitic morphology. Furthermore, with the availability of comparable materials either with and without the presence of a distinct row-nucleated fibril structure, it is also possible to understand how the mechanical property and the deformation morphology are influenced by this structure.

4.2 Experimental

Materials: The HDPE materials used in this study were based on two resins having the same number average molecular weight of 14900g/mol but a different weight average molecular weight of 150,000g/mol (Resin 1) and 290,000g/mol (Resin 2). The 1 mil thick melt-extruded films were kindly provided by Hoechst Celanese Co. Both precursor films (melt-extruded films) and annealed films (passing the same precursor films through a heating oven at 120°C with certain on-line speed, under ca. 3% strain, that allows the material to stay at this temperature for ca. 20min) were investigated. Films based on Resin 1 are designated as Pre-1 and Anl-1 for the precursor and annealed films, and films based on Resin 2 are designated as Pre-2 and Anl-2 for the precursor and the annealed films. Under similar extrusion conditions, both precursor films

were quite highly uniaxially oriented. This was quantified by determination of the Hermans' orientation function, f_c, for the crystalline phase using X-ray scattering, where f_c is defined as

$$f_c = \frac{1}{2}(3 < \cos^2 \theta > -1) \qquad (4.1)$$

In equation 4.1, the quantity $<\cos^2\theta>$ represents the average value of $\cos^2\theta$, with θ being the angle between the c-axis in the crystal (chain axis direction) and the MD. The crystalline orientation function (f_c) calculated from the WAXS patterns are 0.67 and 0.71 for the respective Pre-1 and Pre-2 films. The corresponding annealed films (Anl-1 and Anl-2) had a slightly higher crystalline phase orientation state, with f_c increased to 0.80 and 0.81, respectively. The films based on the Resin 1 (both Pre-1 and Anl-1) had a stacked lamellar morphology with no sign of row structures as detected by both WAXS and TEM; whereas the films based on Resin 2 (both Pre-2 and Anl-2) possessed a morphology which contained a very distinguishable amount of row-nucleated fibril structures in the matrix of stacked lamellae - the existence of the row-nucleated fibril structure having been verified by both WAXS and TEM. A detailed investigation on the morphology and orientation state of the undeformed "as processed" HDPE films used in this study has been recently published elsewhere [71,72].

***Mechanical properties and plastic deformations*:** Stress-strain curves for all the HDPE films were obtained by utilizing an Instron (Model 1122) at ambient conditions with a crosshead speed of 15mm/min. Dogbone shape samples of 23mm x 8mm were used for the stress-strain tests, and they were cut directly from the HDPE films at one of three angles, 0°, 45° and 90°, with respective to the original machine direction (MD). Tensile tests were carried out for samples at each angle and are designated as 0°, 45° and 90° deformations accordingly. For each stretch angle, samples with different amounts of plastic deformation (just beyond the yield point, the break point, and one or two points between the two extremes) were obtained by stretching the dogbone samples up to specific (engineering) strains as determined from the corresponding stress-strain curves. These deformed samples were then used for the WAXS and TEM studies.

***Wide angle X-ray scattering (WAXS)*:** All the WAXS experiments were performed by utilizing a Philips tabletop X-ray Generator (Model PW1720) with CuK_α irradiation (λ=0.154nm)

and equipped with a standard vacuum sealed Warhus photographic pinhole camera. The instrument was operated at 40KV and 50mA. For undeformed films, stacks of multiple layers of films were used as samples for the experiments. For deformed (stretched) films, however, in order to minimize the effect of misalignment in stacking the samples, only a single layer of films with known strains were used as samples for the experiments. In this case, the sample was stretched to a designated strain and held for certain period of time to allow ca. 30% of the instantaneous stress to relax - this large amount of relaxation is due to the "springy characteristic" of these somewhat hard-elastic type materials and it has also been noted by others [25]. The same samples were saved for later use in the TEM study.

***Transmission Electron Microscopy (TEM)*:** The samples for TEM studies were prepared from the stretched samples possessing a specific amount of strain. These samples were stained with chlorosulphonic acid at 60°C for 6 hours, and then they were washed with sulfuric acid and water. In order to prevent the samples from curling in the staining process, the samples were clipped between two glass plates while staining. However, the sample still shrunk somewhat after staining due to the large amount of plastic deformation the sample had underdone within the prior mechanical test. The stained samples were embedded in an epoxy resin and cured at 65°C overnight. The embedded samples were microtomed at room temperature with a diamond knife; thin sections of ca. 80nm were collected and used for the TEM study. The microtoming direction was parallel to the stretch direction (SD). The TEM studies were performed using a Philips EM420 microscope operated at 100KV.

4.3 Results

Figure 4.2 shows the WAXS patterns for the Pre-1 and Pre-2 films, with the incident X-ray beam perpendicular (a and c) and parallel (b and d) to the MD. It can clearly be seen that the crystalline phase of the two films are well-oriented along the MD - with the $(110)_o$ and $(200)_o$ reflections more or less concentrated towards the equatorial region (a and c), where the subscript o stands for the orthorhombic crystalline structure of HDPE (to differentiate the reflections from

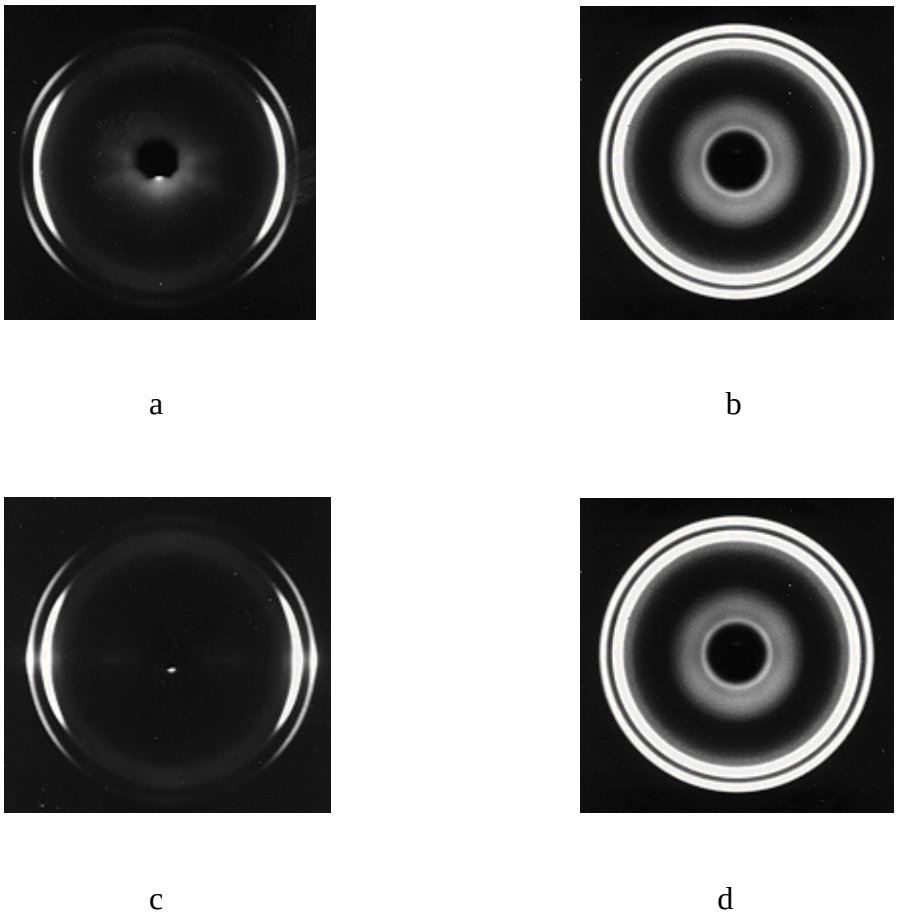

Figure 4.2 WAXS patterns for the Pre-1 (a and b) and Pre-2 (c and d) films. a and c for X-ray beam perpendicular to the MD, and b and d for X-ray beam parallel to the MD.

the monoclinic structure, as will be seen later). From Figs. 4.2b and d, one sees that the $(110)_o$ and $(200)_o$ reflections are quite uniformly distributed azimuthally-implying a random orientation state of the crystalline lamellae in the plane perpendicular to the MD. Therefore, the c-axis (chain axis) in the crystal can be considered as quite uniaxially oriented with respect to the MD (i.e. cylindrical symmetry). In addition, the WAXS patterns for the Pre-2 films (Fig. 4.2c) shows highly concentrated reflections at the equator superimposed on broader or more azimuthally spreaded reflections of the same Bragg planes - implying the existence of a second population of highly oriented crystalline structures along the MD. No such high intensity spots were observed for the Pre-1 film (Fig. 4.2a). It should be pointed out that the calculation of the crystalline orientation function (f_c), which is based on the azimuthal position of the reflection arcs in the WAXS patterns, did not take into account these latter azimuthally concentrated reflection spots for the R2 films.

Figures 4.3a and b present the TEM micrographs for the Anl-1 and Anl-2 films, respectively. Sample Anl-1 displays a stacked lamellar morphology; while for sample Anl-2, row-nucleated fibril structures are unambiguously revealed in addition to the well stacked lamellae. The same kinds of morphologies were observed for the respective precursor films of Pre-1 and Pre-2, except that 1) the contrast for the precursor films is not as sharp as that for the annealed films, and 2) the average thickness of the crystalline lamellae for the precursor films is less than that for the annealed films. The increase in lamellar thickness for the annealed films is due to lamellar thickening in the annealing process at 120°C for ca. 20min, and it has also been detected by SAXS, AFM and DSC in an earlier study [73]. The existence of the row-nucleated fibril structure observed within the R2 film morphology is responsible for the high intensity scattering spots at the equator of the WAXS patterns for these materials, such as Fig. 4.2c for the Pre-2 film.

Stress-strain Curves of the HDPE Films: Shown in Figs. 4.4a and b are the stress-strain curves at the 0°, 45° and 90° deformations for the Pre-1 and Anl-1 films, respectively. The same form of data for the Pre-2 and Anl-2 films are shown in Figs. 4.4c and d. These data, which

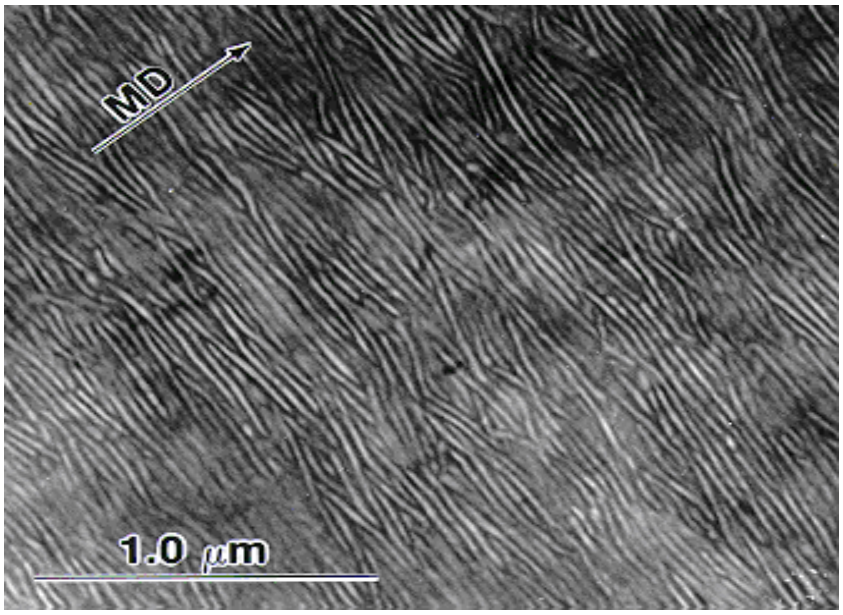

a

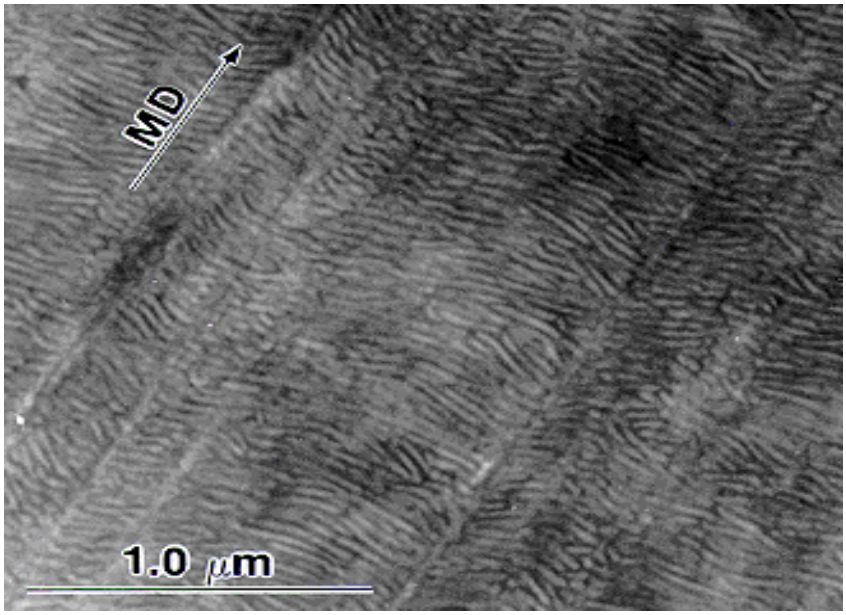

b

Figure 4.3 TEM micrographs for the Anl-1 (a) and Anl-2 (b) films.

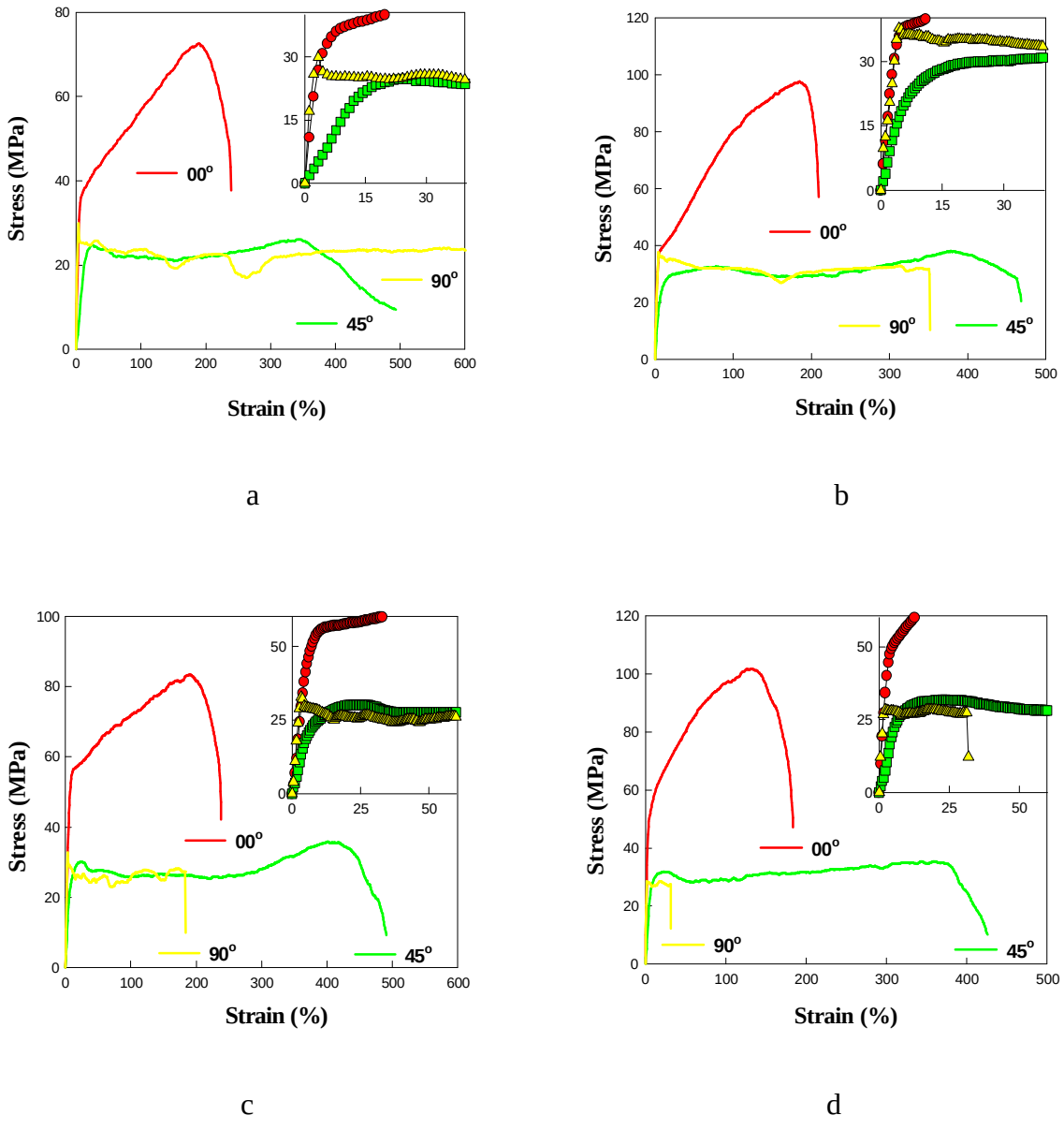

Figure 4.4 Stress-strain curves for the Pre-1 (a), Anl-1 (b), Pre-2 (c) and Anl-2 (d) films.

are very reproducible, clearly demonstrate the dramatic differences in the mechanical properties of these films - particularly those with and without row structures and those with and without thermal annealing. The properties of Young's modulus (E), yield stress (σ_y) and strain (ε_y), cold-drawn stress (σ_d) and strain (ε_d), break stress (σ_b) and strain (ε_b), determined from these curves are listed in Table 4.1 and will be discussed later. It needs to be pointed that, although the data presented in Table 4.1 is only for one group of samples at the three orientations, the observed mechanical behavior at each orientation is very representative and can be reproduced in the range of ±6%.

For the 0° deformation, after yielding, which *in this case is denoted by where a deviation from initial linearity* occurs, all the samples displayed a significant degree of strain hardening, indicated by the large positive slopes following yielding. That is, no neck formation was found over the entire deformation. However, strain-whitening was found in the neighborhood of yielding for all the samples. For the 90° deformation, all samples displayed a very different yielding style - *a sharp "conventional" yield peak*, as compared with the case of 0° deformation, and necked at very early stages of the deformation (less than 5% strain), and then underwent cold drawing to different amount of strains for different samples. Eventually, the samples broke in a "brittle" fashion with no or a slight amount of strain hardening. Also noticed is the uneven feature of these stress-strain curves in the drawing region, particularly for the Pre-1 and Pre-2 films. The 45° deformation showed a behavior which is similar to those of unoriented semicrystalline polymers with a spherulitic morphology, i.e., a well-defined local yielding maximum, strain softening, cold drawing, and finally strain hardening before failure. Necking took place by shear at ca. 45° inclined with respect to the SD. At the last stage of deformation, the samples failed by tearing slowly at the end of the clamps, shown as downward tails at the end of the respective stress-strain curve.

WAXS Results: Figures 4.5a, b and c are the WAXS patterns for the Pre-1 films deformed at the 0° stretch to strains of 15%, 100% and 180%, respectively. Comparing these WAXS patterns with that pattern from the respective undeformed sample (Fig. 4.2a), it can be

Table 4.1. Young's modulus (E), yield stress (σ_y) and strain (ε_y), cold-draw stress (σ_d), breaking stress (σ_b) and strain (ε_b) for the four HDPE films investigated. (The values listed here were only for one sample whose stress-strain curves are shown in Fig. 4.4)

Properties at different orientation		Pre-1	Anl-1	Pre-2	Anl-2
E (MPa)	00	530	920	892	1500
	45	290	430	395	460
	90	750	940	1040	1600
σ_y (MPa)	00	35	36	55	56
	45	23	27	28	31
	90	30	35	33	28
ε_y (%)	00	8	6	10	8
	45	14	9	3	11
	90	3	3	15	3
σ_d (MPa)	00	x	x	x	x
	45	22	32	26	28
	90	22	32	26	27
σ_b (MPa)	00	72	98	82	102
	45	>26	>38	>38	>35
	90	>24	32	30	27
ε_b (%)	00	220	185	170	125
	45	>350	>380	>410	>360
	90	>960	350	185	32

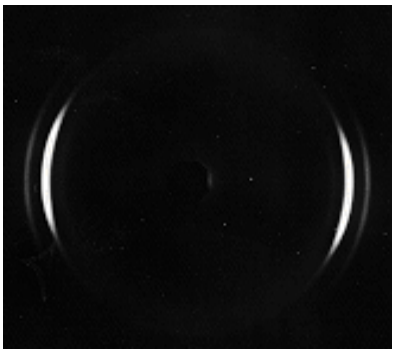

a

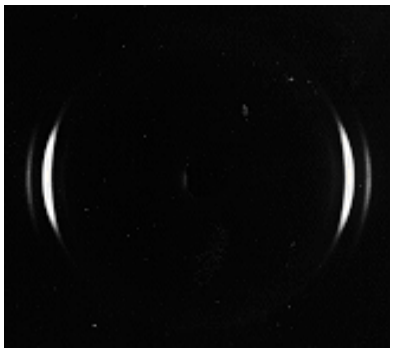

b

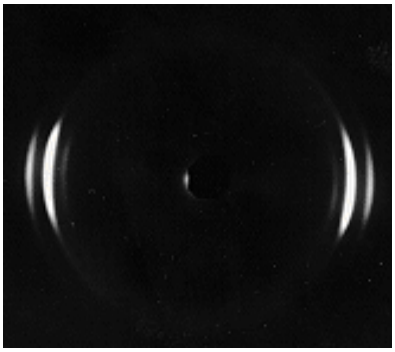

c

Figure 4.5 WAXS patterns for the Pre-1 film for the 0° deformation at (a) ε=15%, (b) ε=100% and (c) ε=180%.

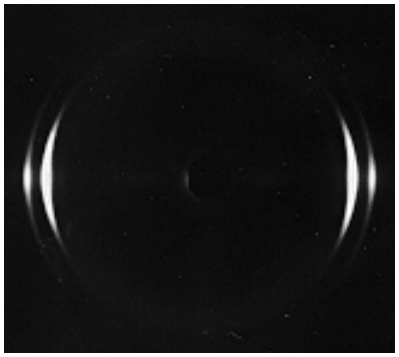

a

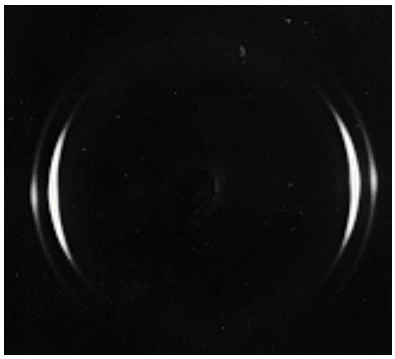

b

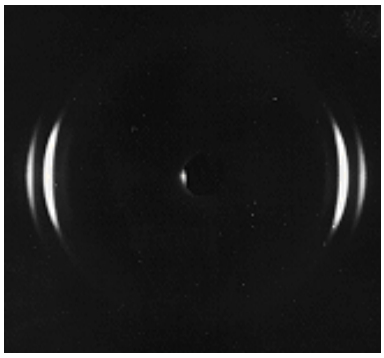

c

Figure 4.6 WAXS patterns for the Pre-2 film for the 0° deformation at (a) ε=15%, (b) ε=50% and (c) ε=120%.

seen that there is a trend to increase the orientation state of the crystalline phase, manifested by the more concentrated $(110)_o$ and $(200)_o$ scattering intensities in the equatorial region. Additionally, it can also be seen, from Fig. 4.5c, that there is an extra weak reflection developed inside the $(110)_o$ scattering, which is the $(100)_m$ of the monoclinic crystalline phase of HDPE due to the martensitic phase transformation. Figures 4.6a, b and c are the WAXS patterns for the Pre-2 films deformed at the 0° stretch to strains of 15%, 50%, and 120%, respectively. In addition to the same trend showing an increase in the orientation state of the crystalline phase in the process of plastic deformation, the decrease (Fig. 4.6b) and disappearance (Fig. 4.6c) of the intense scattering spots at the equator were also clearly noticed. Interestingly, the existence of the $(100)_m$ reflection is not observed at the highest strain of 120%.

For the 90° stretch, the samples necked immediately at ca. 3-5% strain, and what followed was the expansion of the neck along the entire length direction of the sample. It was expected that samples in the necked region should essentially possess the same kind of morphology regardless of strains. The WAXS patterns for the 90° stretch for the Pre-1 and Pre-2 films are shown in Figs. 4.7a and b, respectively; they show basically the same general highly oriented state of the crystalline phase with respect to the SD, *which is now perpendicular to the original MD*. It is also noted that the monoclinic crystalline phase exists in the necked region.

Figures. 4.8a-c and Figs. 4.9a-c present the morphological changes for the 45° stretch for the Pre-1 and Pre-2 films, respectively. For the Pre-1 film, at 30% strain (Fig. 4.8a), there was no significant change in crystalline orientation that has been found by WAXS. However, at a strain of 60% (Fig. 4.8b), the WAXS patterns became asymmetric, seeing the $(110)_o$ reflections in Fig. 4.8b. The crystalline orientation state in this case is not much different with that at 30% strain - judged by the "spreading" of the $(110)_o$ reflection; but the rotation of crystalline lamellae towards the SD is suspected - such a rotation can be speculated by a change in the angular position of the $(110)_o$ reflections with respect to the SD (as shown in Fig. 4.8b). At a further strain of 180% (Fig. 4.8c), a new symmetric scattering pattern with respect to the SD is now established. Again, the monoclinic crystalline structure was observed for the sample with 180% strain. A similar trend of the formation of a new orientation state along the SD was also observed for the Pre-2 film, as

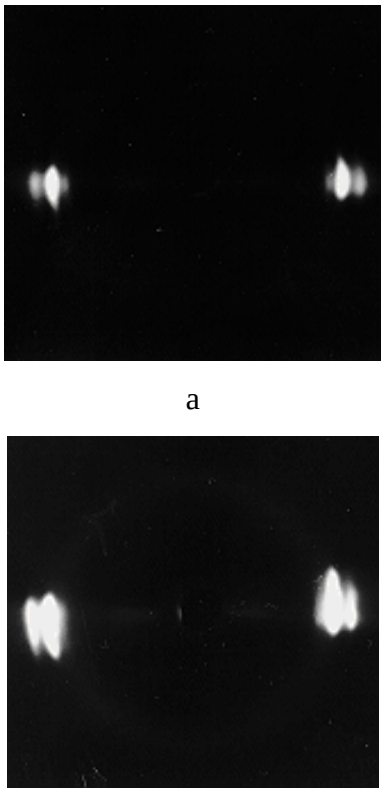

a

b

Figure 4.7 WAXS patterns for the Pre-1 (a) and Pre-2 (b) films at 90° deformation. Both SD and MD are vertical.

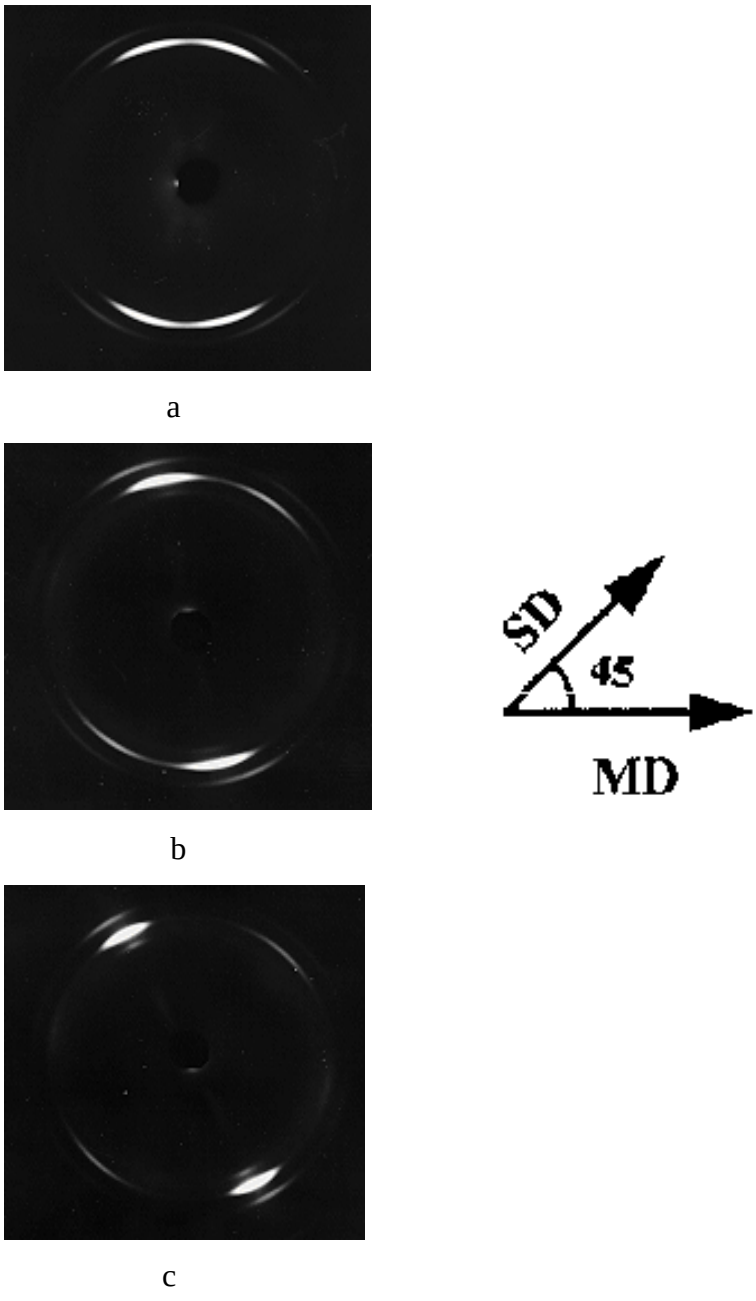

Figure 4.8 WAXS patterns for the Pre-1 film for the 45° deformation at (a) ε=30%, (b) ε=160% and (c) ε=180%. Both SD and MD are shown in the figure.

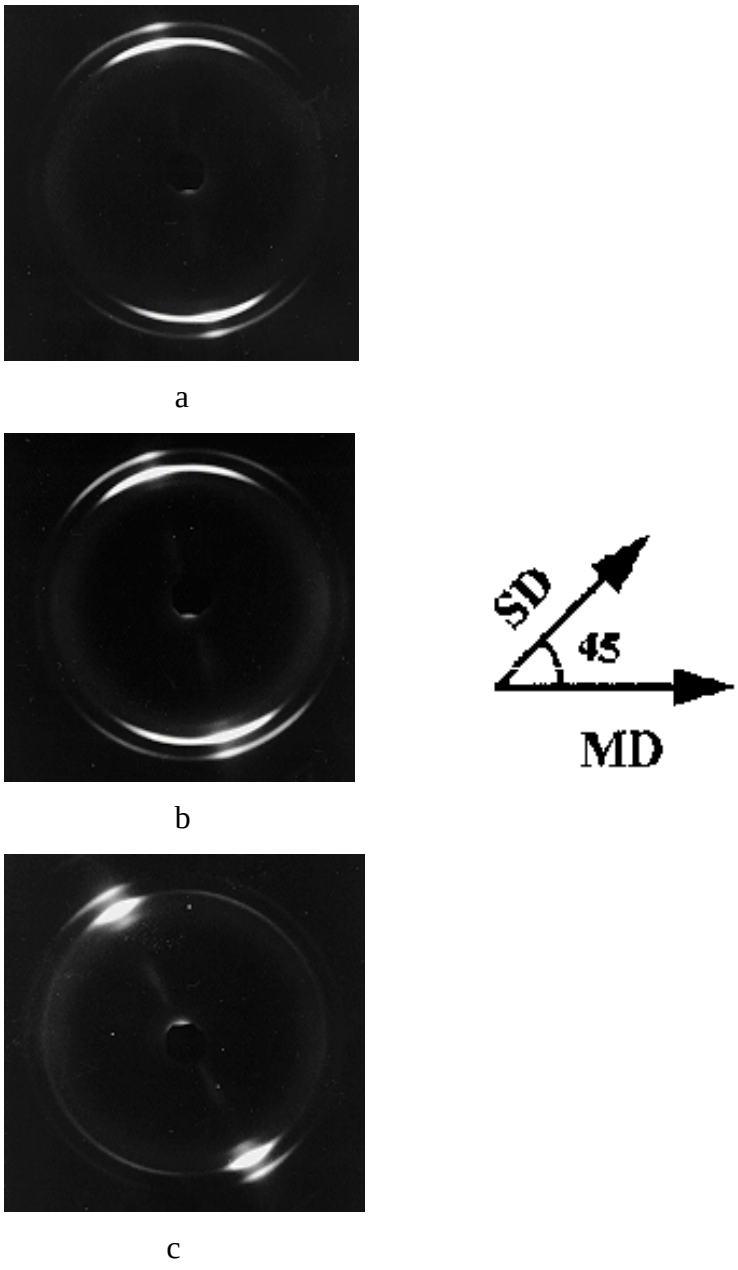

Figure 4.9 WAXS patterns for the Pre-2 film for the 45° deformation at (a) ε=25%, (b) ε=50% and (c) ε=150%. Both SD and MD are shown in the figure.

shown in Figs. 4.9a, and in this case the rotation of crystalline lamellae with respect to the SD, based on the above conjecture, took place at the early stages of the deformation (Fig. 4.9a).

TEM Results: Figures 4.10a and b present the TEM micrographs for the Anl-1 and Anl-2 films at the 0° deformation with individual strains of 100% and 50%, respectively. For the stacked lamellar morphology (the Anl-1 film), broken blocks of the crystalline lamellae are observed (Fig. 4.10a); while for the row containing morphology (the Anl-2 film), the localized break-up of row-nucleated fibril structure is observed (shown by arrows in Fig. 4.10b). It is noticed that the crystalline lamellae in the deformed samples (Fig. 4.10) are not as well-defined as those in the undeformed samples (Fig. 4.3), likely because of the large amount of defects in the crystalline lamellae due to plastic deformation. Samples with smaller amount of strains (just beyond the yield point) were also investigated, but no significant changes could be seen by TEM, possibly partially due to some sample shrinkage during the staining treatment.

Figures 4.11a and b present the dramatic morphological changes at the sharp boundary of the necks for the Anl-1 and Anl-2 films at the 90° deformation. The top and bottom portions of each of these micrographs represent the necked and un-necked regions, respectively. There are also transition regions between the necked and un-necked regions, but the detailed features can not be well-resolved. For the Anl-1 film (Fig. 4.11a), the un-necked region shows the original stacked lamellar morphology oriented along the MD; while the necked region displays considerable void fraction and broken white lines (shown by arrows A in Fig. 4.11a) oriented along the SD - these lines may be an indication of a microfibril crystalline phase. For the Anl-2 film (Fig. 4.11b), the un-necked region shows the crystalline lamellae and the row structures along the SD; while in the necked region, more and larger voids along the SD are seen without the presence of the broken white lines. The crystalline lamellae in the un-necked regions in Figs. 4.11a and b do not look the same as the those in Fig. 4.3 since the microtoming direction in this case is *perpendicular* to the MD. Additionally, the plastic deformation can also influence the lamellar morphology, as mentioned in the case of the 00° deformation.

Figures 4.12a and b present the TEM micrographs for the Anl-1 and Anl-2 films stretched at a 45° deformation. For the Anl-1 film (a), at low strain (ca. 25%), “shear banding” type

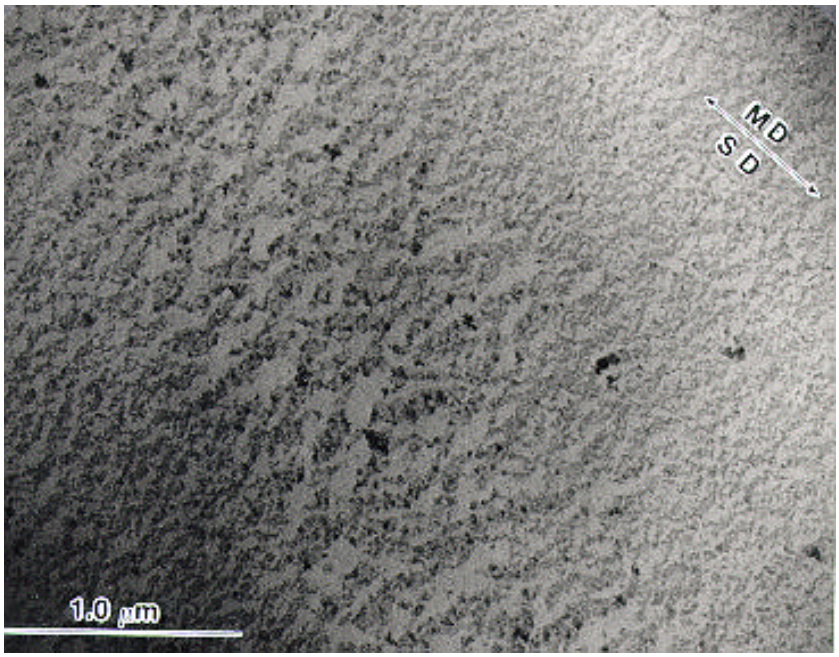

a

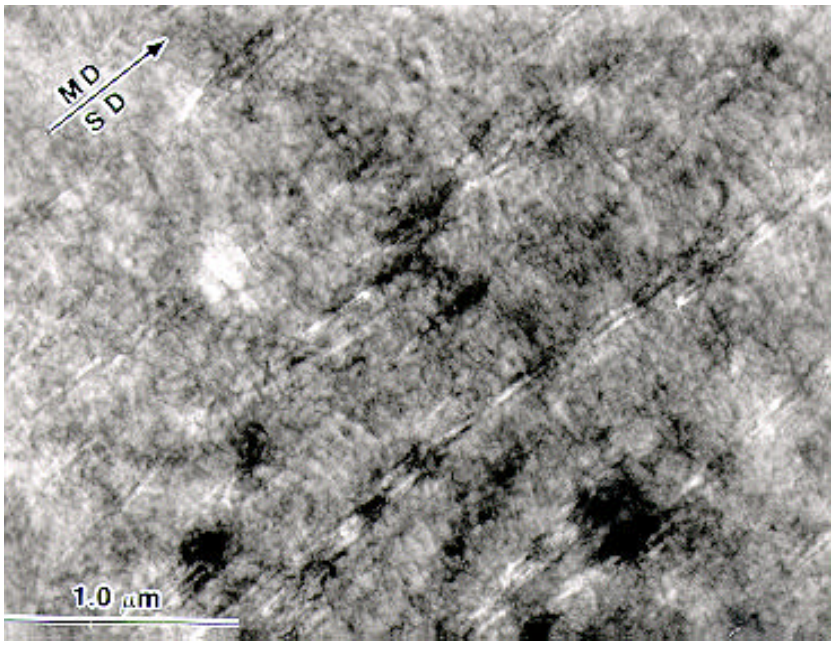

b

Figure 4.10 TEM micrographs for the Anl-1 film (a) at 100% deformation and Anl-2 film (b) at 50% deformation. Arrows indicate broken row-nucleated structures.

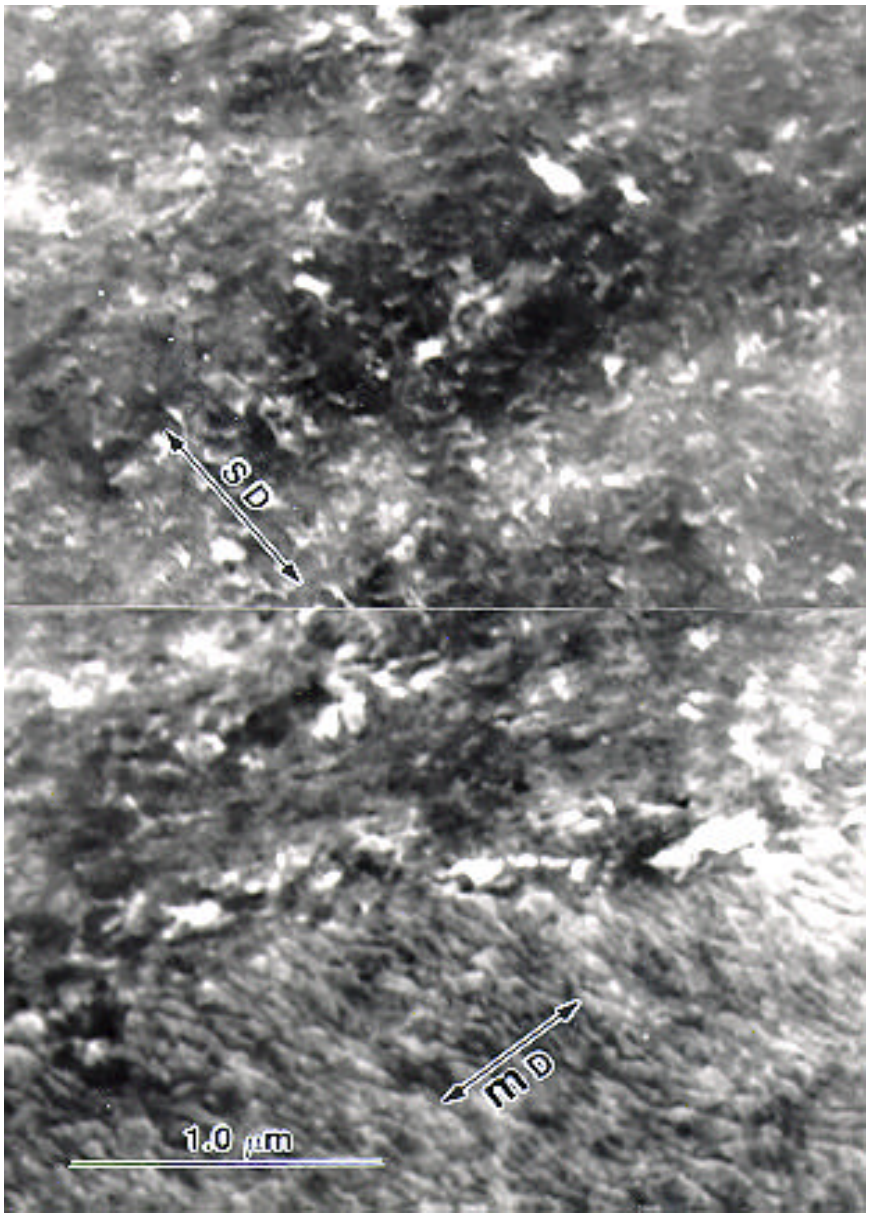

a

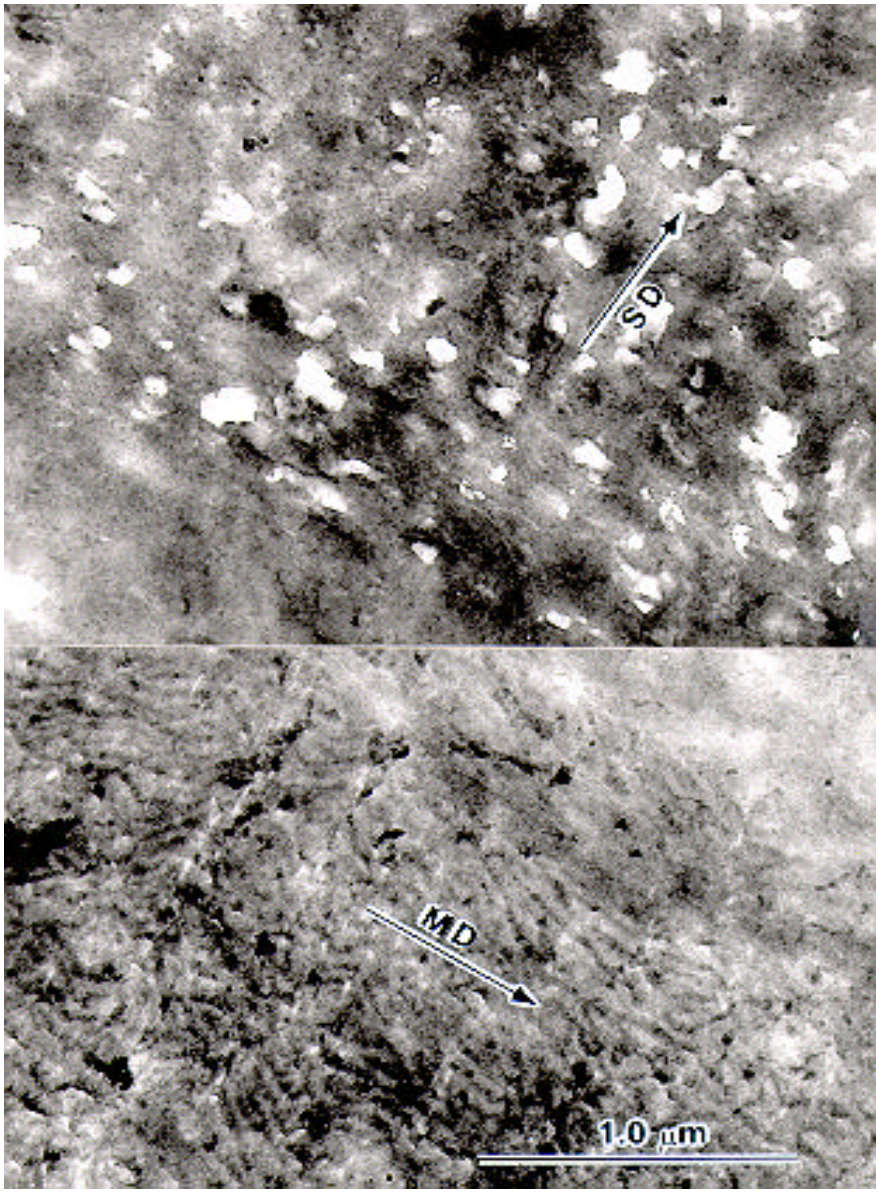

b

Figure 4.11 TEM micrographs for the 90° deformation for the Anl-1 (a) and Anl-2 (b) films showing the boundary of necked and un-necked regions. Arrows A point at broken white lines which indicate the presence of microfibril crystalline material, and arrow B points at broken line which is drawn to represent the sharp boundary between the necked and un-necked regions.

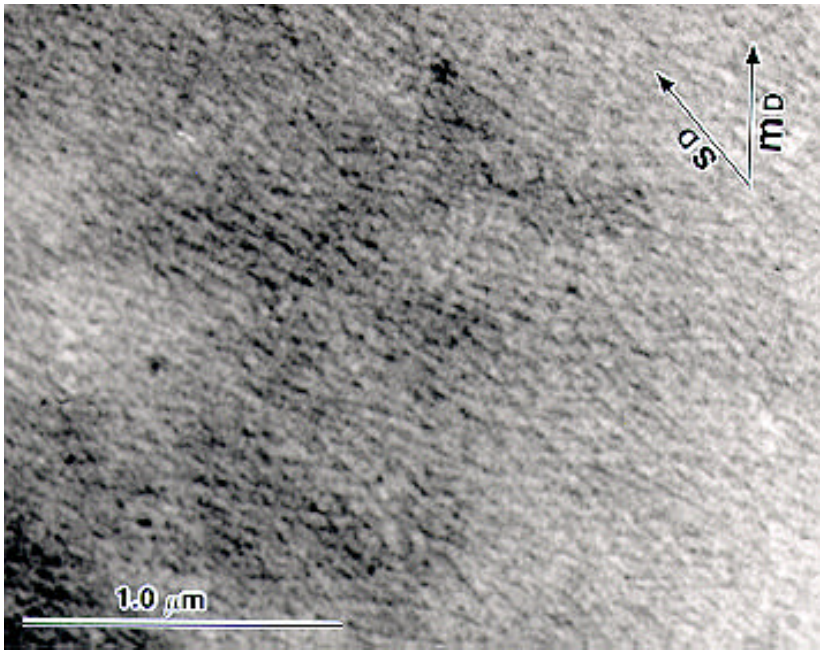

a

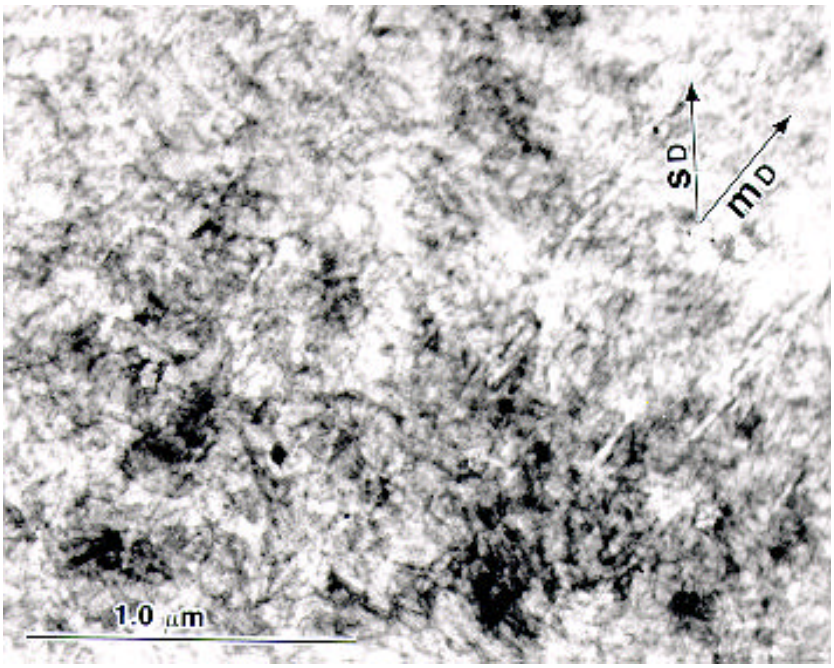

b

Figure 4.12 TEM micrographs at the 45° deformation for the Anl-1 at ε=25% (a) and Anl-2 at ε=30% (b). Arrows in (b) represent localized broken row-nucleated fibril structures.

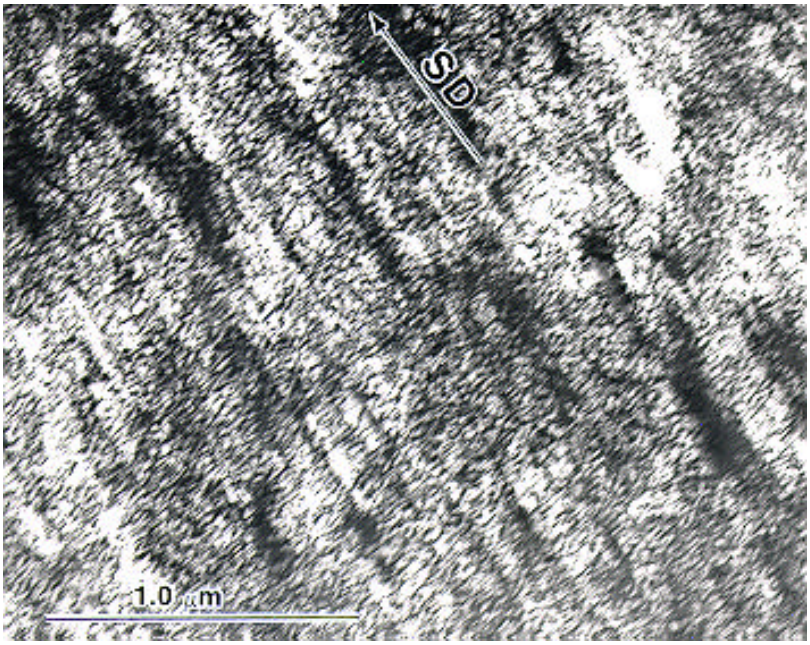

a

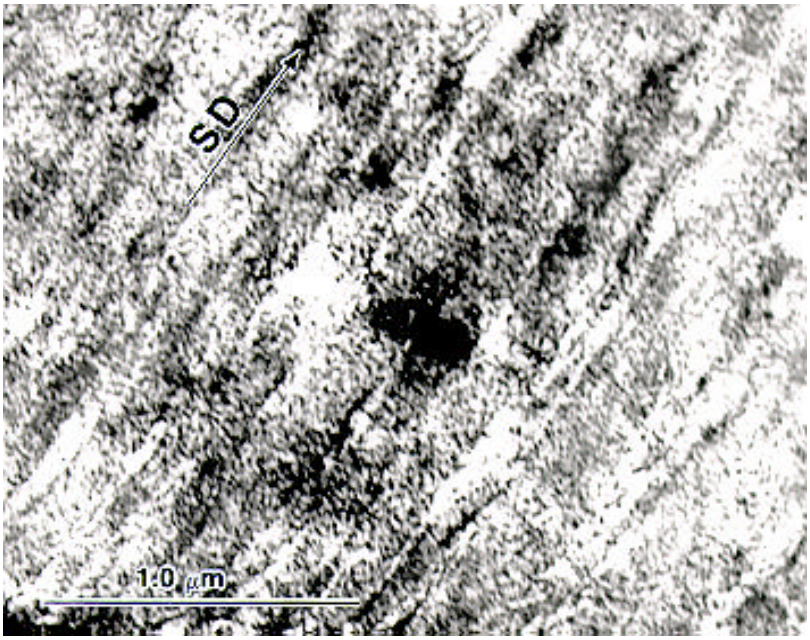

b

Figure 4.13 TEM micrographs at the 45° deformation for the Anl-1 film at ε=180% (a) and Anl-2 film at ε=150% (b).

features are observed, which is an implication of lamellar shear deformation. However, for the Anl-2 film (b), localized break-up of the row structures is noted. Again, the crystalline lamellae become deteriorated, and the morphology observed by TEM becomes also less and less well-defined as the deformation proceeded. Finally, at a strain of 200%, a highly oriented morphology was observed for both the Anl-1 and Anl-2 films (Figs. 4.13a and b). However, the expected microfibril crystalline structure was not observed, and other fine textures in these micrographs can not be addressed ambiguously, due to the absence of the original MD. However, by using the knife marks on the samples and/or samples edges as a indication of the SD, the rotation of the crystalline lamellae can indeed be distinctly inferred.

4.4 Discussion

Young's Modulus at Different Orientations: The variation in mechanical properties listed in Table 4.1 can be explained by the specific *initial* morphologies and also those *developed* during the deformation processes of these HDPE films. We will first address the Young's modulus, since it depends on the low deformation elastic behavior of the materials. Structural models for the HDPE films will be established according to the morphological features of the films and will also be utilized in the discussion of the other properties associated with the plastic deformation of the materials.

For the films based on Resin1 (Pre-1 and Anl-1), the crystalline lamellae are uniaxially oriented with the lamellar normal preferentially aligned parallel to the MD. Therefore, as a first approximation, these specific materials based on Resin 1 can be considered as a "laminated composite" of a hard crystalline phase and a soft amorphous phase stacked along the MD. At the 0° deformation, the material can be considered as the composite being deformed in an iso-stress case, i.e., the crystalline phase and the amorphous phase are deformed in series; therefore the modulus is dominated by that of the soft amorphous phase. On the other hand, at the 90° deformation, the material can be considered as the composite being deformed in an iso-strain case, i.e., the crystalline phase and the amorphous phase are deformed in parallel; therefore the modulus

is dominated by that of the hard crystalline phase. Thus, although the modulus of the *crystalline phase (lamellae)* at the 90° orientation (perpendicular to the chain direction) is much less than that at the 0° orientation (more parallel to the chain direction), the modulus for the *sample* at the 90° orientation is *higher* than that for sample at the 0° orientation. As for the 45° deformation, since there is a maximum resolved shear stress in the plane of the crystalline lamellae, interlamellar shear is the most probable deformation event, and this results in a even smaller modulus at this particular orientation than those for the 0° and 90° deformations.

For the films based on Resin 2 (Pre-2 and Anl-2), in addition to the uniaxially oriented stacked crystalline lamellae, many row-nucleated fibril structures also exist, as observed directly by TEM. From previous studies concerning HDPE films having a shish-kabob morphology, three different structural models have been proposed, i.e., interlocking lamellae [74], fiber reinforced composite [75] and crystalline network [76]. we select to use the fiber reinforced composite model in this study, since it best represents the structural features of these materials shown by the TEM micrograph in Fig. 4.3b; additionally, this model is closely coupled with the laminated composite model proposed for the stacked lamellar morphology.

The row structures in the films based on Resin 2 serve as reinforcement fibers having a large aspect ratio (Fig. 3b) in the MD, and this give rise to the higher modulus at the 00° deformation, as compared with that for the films based on Resin 1 (the Pre-2 film *versus* the Pre-1 film as well as the Anl-2 film *versus* the Anl-1 film). However, at the 90° deformation, the strengthening effect of the row structures (fiber reinforcements) is not as effective as for the 00° deformation; therefore, the increase in Young's modulus at this orientation is not as significant as that for the 00° deformation-again comparing Young's modulus for the Pre-2 film versus that for the Pre-1 film and those for the Anl-2 film versus the Anl-1 film. For the 45° deformation, although limited by the existence of the row structures, lamellar shear still dominated in the initial stage of the deformation, and this gives rise to the lowest modulus of the three deformation orientations. We realize that the above analysis is somewhat *qualitative* and may not be fully correct due to the small difference in the crystalline orientation state (f_c values) possessed by these two films.

Plastic Deformation Morphologies at Different Orientations: Other properties, namely yield stress (σ_y) and strain (ε_y), cold-drawn stress (σ_d) and strain (ε_d), and break stress (σ_b) and strain (ε_b), are related to the plastic deformation behavior of the materials. As can be seen from the stress-strain curves in Fig. 4.4, the mechanical behavior of the films strongly depended on the orientation of the deformation, and they will be discussed separately below. Other factors, such as molecular weight distribution, thermal annealing and orientation state of the crystalline phase, will also certainly affect these properties; however, they will not be discussed in this report.

1) 00° deformation: Considering the "laminated composite" model proposed earlier for films based on Resin 1, its deformation along the MD direction would occur by lamellar separation. Such a deformation mechanism can be justified by the appearance of strain whitening for samples stretched along the MD direction and the disappearance of such a phenomenon for relaxed samples upon removal of the stress. Similar statements have been made from the deformation studies on other hard-elastic polyethylene [25] and polypropylene [77], which have a similar morphology to the Resin 1 samples deformed along the MD direction. Lamellar separation cause crystalline lamellae to "open-up" or splay, and this results in the strain-whitening shown by all the samples. As the deformation proceeded, the crystalline lamellae have to be deformed to generate higher strains, and this promotes the yielding of the sample. Since the c-axis in the crystal is more or less oriented along the stress direction (MD), chain slip is the dominant deformation mode for the crystalline phase, especially [100] chain slip. The slip of the crystalline phase also causes the large degree of strain hardening, as shown in the stress-strain curves.

As mentioned earlier, chain slip can be achieved by either fine slip or course slip; however, the physical process for both types of slip is the same, i.e. the sliding between chains in polymer crystals. For fine slip, the sliding is between chains in the same crystal unit cell; whereas for the course slip, the sliding is believed to be between chains at the boundary of the mosaic blocks within the crystalline lamellae [78]. The result from TEM observations (Fig. 4.10a) suggested that course slip has taken place, and by doing this the crystalline lamellae were fragmented into much smaller crystal blocks, which likely originate from the mosaic blocks within the crystalline

lamellae. The same observation of course slip induced fragmentation of large crystalline lamellae has also been made by others [14]

As for the films based on Resin 2, the existence of row-nucleated fibril structure obviously affected the initial stage of the deformation, as shown by the higher values of Young's modulus. However, the basic plastic deformation processes described above were not expected to change. Once the yield point was passed, the row structures began to break up gradually at certain localized points (see Fig. 4.10b), indicating that the fibril structure is not likely to be of a complete extended-chain type crystalline phase [79]. The strengthening effect on the further plastic deformation became less and less. From the stress-strain curves, the films with and without row structures had similar behaviors from yield point to break point, i.e., *the degree of strain hardening (slope of the curve) for the Pre-1 and Pre-2 films and for the Anl-1 and Anl-2 films were similar*.

2) 90° deformation: At this orientation, since the c-axis (chain axis) in the crystalline lamellae was more or less perpendicular to the direction of the applied stress (SD), the deformation on the level of the crystalline lamellae and amorphous layers, via lamellar separation, lamellar shear and lamellar rotation, was significantly limited. Therefore, the samples yielded sharply after a small amount (3-5%) of iso-strain elastic deformation of the crystalline phase and amorphous phase, and what followed was the localized break-up (decrystallization) of the crystalline lamellae, by transverse slip in the crystal. During the decrystallization process, polymer chains are pulled-out of the crystalline lamellae and realigned and recrystallized parallel to the SD, which is perpendicular to the original MD. The pull-out of the chains is basically a cold-drawing process and, therefore, it occurred as a horizontal plateau in the stress-strain curves at the 90° deformation.

However, the films based on the two resins behave very differently. As shown in the stress-curves, those having the stacked lamellar morphology showed a large degree of cold-drawing; while those having the row morphology showed only a very limited amount of cold-drawing. This difference can be explained by the different kinds of morphologies developed for the respective films, as revealed by the TEM micrographs shown earlier in Fig. 4.12. For the

stacked lamellar morphology, there is no rotation of the crystalline lamellae in the un-necked region, and the chain pull-out allows a deformation strain as high as 1000% for the Pre-1 film (shown by the stress-strain curve). The same lamellar break-up via chain pull-out has also been noted by other authors [18,19]. However, it was seen that the row-nucleated fibril structure in the un-necked region were oriented along the SD, and such a rotation of shish structure has also been reported by other authors based on TEM studies on specially prepared ultra-thin and ultra-drawn HDPE films [24]. It was speculated that the rotation of the row-nucleated fibril structure is very limited thus the cold-drawn strain induced was also very small. Hence within this context, it seems that the crystalline network model for the row morphology serves better to explain the constrained rotation of the row-nucleated fibril structures and associated stacked lamellae.

3) 45° deformation: As mentioned earlier, interlamellar shear was the dominate deformation mode at the early stage of the deformation at this orientation. Also this corresponded to a larger observed yield strain and lower yield stress, as compared to the deformations at the 00° and 90° orientations. To accommodate the lamellae shear, however, chain slip, either fine or course, takes place through the sliding of tie-chains, and this corresponds to the yielding of the crystalline phase. A closer examination of the stress-strain curves at the 45° orientation indeed showed a hint of double yielding. Double yielding has been reported previously for HDPE [80,81], and in that case the two yield points were speculated to originate from lamellar shear and the subsequent deformation of the crystalline phase, respectively.

In the process of yielding, lamellar rotation occurred as a result of lamellar shear and/or chain slip, and the re-orientation of polymer chains towards the SD, which is at 45° away from the original MD, was shown by the WAXS patterns (Figs. 4.8 and 4.9). At this stage of the deformation, crystalline lamellae began to break up due to the competitive constraint between lamellar shear and chain slip, as also proposed by other authors [63]. The break-up of the crystalline lamellae is essentially a cold-drawing process by chain slip within the crystalline lamellae, as in contrast to the pull-out of chains as in the case of the 90° deformation. Indeed, the stress-strain curves showed a horizontal plateau in this region of strain. It is interesting to notice that the cold-drawing stress for the same sample at these two stretch orientations (45° and 90°)

were almost identical. However, the cold-draw strains at the 45° deformation seemed to be higher than that at the 90° deformation, due to a greater degree of chain-slip rather than chain pull-out.

Plastic Deformation of Spherulitic Morphology: Due to the complex arrangement of the crystalline phase and amorphous phase in this particular crystal texture, the deformation of a spherulite is highly heterogeneous, as already depicted earlier in Fig. 4.1. At the polar region, the crystalline lamellae are deformed as in the situation of the 90° deformation; while at the equatorial region, the crystalline lamellae are deformed as in the case of the 00° deformation, the inclined region in the spherulite resembles the 45° deformation. Using the stress-strain curves in Fig. 4.4 as a general guide, it can be conjectured that the break-up of a spherulite occurs first in the polar region since the 90° deformation results in lamellar break-up at the smallest strain level, followed by the splaying of the equatorial region where the 00° deformation lamellar separation causes the materials to yield by course slip with the formation of craze, and by the distortion of the inclined region in which the 45° deformation induces lamellar shear and lamellar rotation. The above argument is supported by direct observations from polarized optical microscopy [16] and SEM [13,58,82].

However, large amounts of intercrystalline links and geometrical constraints are expected between crystalline lamellae within a spherulite [83]; therefore, the orientation dependence of the plastic deformation in different regions of the spherulite is not as sharply different as those noted here for the HDPE films having the stacked lamellar textures. Also, due to the often prevalent twisting of the crystalline lamellae during the growth of the spherulite [84], lamellar rotation is believed to take place initially in all the regions of the spherulite [16], and this results in a small amount of initial homogeneous (pseudo-affine) deformation of the spherulite initially.

The above discussion can be summarized by the following schematic drawings in Fig. 4.14, showing the deformation at the three angles for the stacked lamellar morphology. For the 00° deformation (a [14]), lamellar separation induces the fragmentation of the stacked lamellae by chain slip, and this process shown as a strong strain hardening event in the corresponding stress-

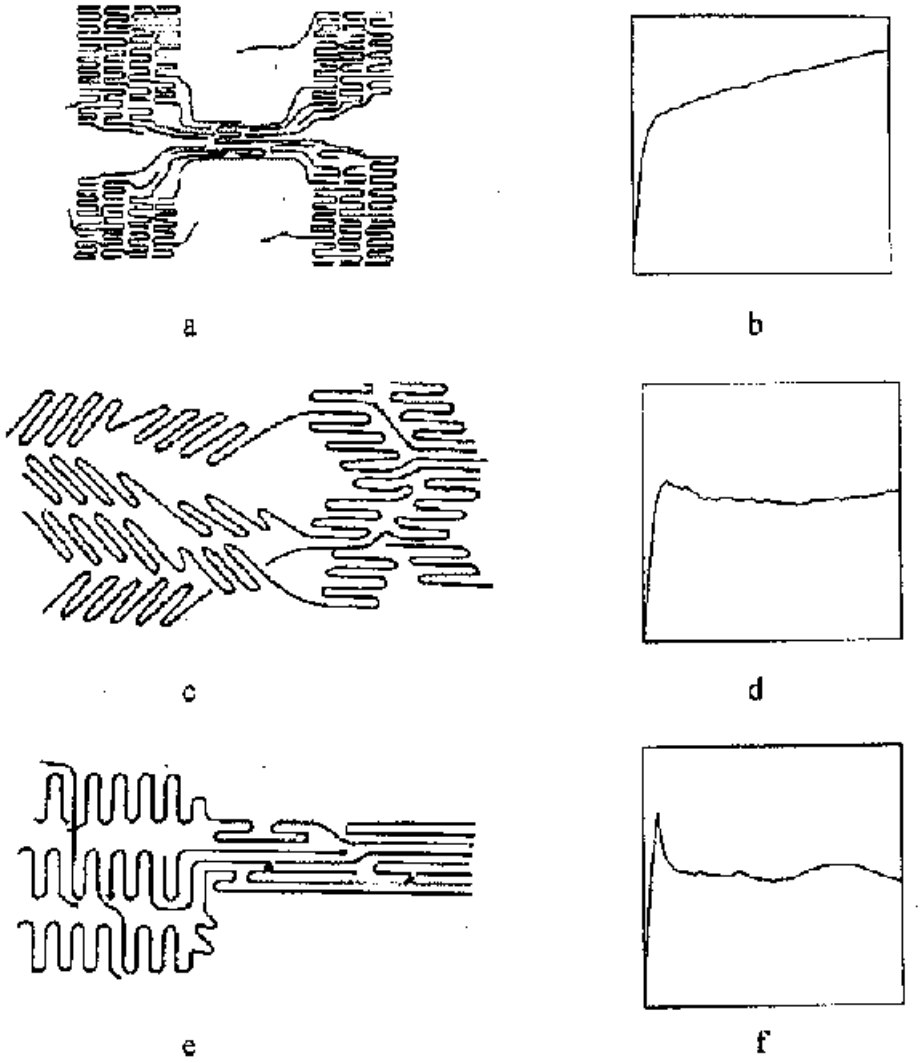

Figure 4.14 Schematic drawings that show the molecular mechanisms and corresponding stress-strain curves for the stacked lamellar morphology under 00°, 45° and 90° deformations.

strain curve (b). For the 90° deformation, plastic strain is generated by lamellar break-up via chain pull-out (e [19]), and this event corresponds to a large amount of cold drawing as shown by curve

f. For the 45° deformation, the mechanisms may include many molecular processes such as chain slip, chain tilt, lamellar break-up, etc (c [2]), and the corresponding stress-strain curve (d) is also somewhat between those for the 00° and 90° deformation. Hence, while this deformation is more complex, *it is likely more "generic" to that observed for semicrystalline polymers having a spherulitic morphology when deformed above their glass transition temperatures.*

4.5 Conclusions

By carrying out plastic deformation studies on HDPE films having well-defined stacked lamellar morphology, with and without row-nucleated fibril structures, we have shown that the mechanical properties and morphological changes are strongly dependent on the angle of the deformations with respective the original orientation direction. Comparing the mechanical properties obtained from tensile tests and the deformation morphology from WAXS and TEM at specific strain, a model structure-property investigation has been presented.

Stretching parallel to the MD results in lamellar separation, followed by break-up of the crystalline lamellae via chain slip in coarse fashion. The existence of the row-nucleated fibril structure increases the Young's modulus in this particular orientation, but the strengthening effect reduces as deformation proceeds due to the localized break-up of the row structures. Stretching perpendicular to the MD causes the crystalline lamellae to break-up or rupture by chain pull-out. The effect of row-nucleated fibril structure is to alter the chain pull-out into the rotation of the row-nucleated fibril structure, and this results in a large cold-drawing for the stacked lamellar morphology and a small amount of cold-drawing for those with distinct row-nucleated fibril structures. When the stretching is between the above two extremes, lamellar shear is the dominate initial deformation mode, followed by chain slip that can eventually cause lamellar break-up. The row-nucleated fibril structure does not display a major influence at this particular orientation.

References

1. W. G. Perkins and R. S. Porter, *J. Mater. Sci.* **12** (1977) 2355

2. A. Peterlin, *Colloid & Polym. Sci.* **265** (1987) 357

3. R. S Porter and L. H. Wang, *J. M. S.- Macromol Chem. Phys.*, **C35(1)** (1995) 63

4. I. L. Hay and A. Keller, *J. Mater. Sci.*, **1** (1966) 41

5. I. L. Hay and A. Keller, *J. Mater. Sci.*, **2** (1967) 538

6. A. Cowking, J. G. Rider, I. L. Hay and A. Keller, *J. Mater. Sci.*, **3** (1968) 646

7. J. J. Point, G. A. Homes, D. Gezovich and A. Keller, *J. Mater. Sci.*, **4** (1969) 908

8. L. Lin and H. S. Argon, *J. Mater. Sci.*, **29** (1994) 294

9. I M. Ward (Ed.), *Structure and Properties of Oriented Polymers, Applied Science,* 1975

10. H. Van Der Werll and A. J. Pennings, *Colloid & Polym. Sci.*, **269** (1991) 747

11. J. M. Shultz, *Polym. Eng. Sci.*, **24** (1984) 770

12. R. J. Samules, *Structured Polymer Properties*, John & Wiley, 1974

13. I. L Hay and . A. Keller, *Kolloid Z. Z., Polym.*, **204** (1965) 43

14. T. Tagawa, and K. Ognra, *J. Polym. Sci., Polym. Phys. Ed.*, **18** (1980) 971

15. J. Lin and Y. Lee, *J. Mater. Sci.*, **28** (1993) 6496

16. M. Aboulfaraj, C. G'Sell, B. Ulrich and A. Dahoum, *Polymer*, **36** (1995) 731

17. T. Juska and I. R. Harrsion, *Polym. Eng. Rev.*, **2** 1 (1982) 13

18. R. M. Gohil and J. Petermann, *J. Polym. Sci., Polym. Phys. Ed.*, **17** (1979) 52

19. J. Petermann, W. Kluge and G. Leiter, *J. Polym. Sci., Polym. Phys. Ed.*, **17** (1979) 1043

20. J. Petermann, R. M. Gohil, M. Massud and D. Goritz, *J. Mater. Sci.*, **17** (1982) 100

21. R. M. Gohil and J. Petermann, *J. Polym. Sci., Polym. Phys. Ed.*, **17** (1979) 525

22. W. W. Adams, D. Yang and E. L. Thomas, *J. Mater. Sci.*, **21** (1986) 2238

23. J. M. Brady and E. L. Thomas, *J. Polym. Sci., Polym. Phys. Ed.*, **26** (1988) 2398 (1988)

24. J. M. Brady and E. L. Thomas, *J. Mater. Sci.*, **24** (1989) 3311

25. B. Cayrol and J. Petermann, *J. Polym. Sci., Phys. Ed.*, **12** (1974) 2169

26. G. H. Michler, *Colloidal. & Polym. Sci.,* **270** (1992) 627

27. H. J. Kestenbach and J. Petermann, *Polymer,* **24** (1994) 5217

28. K. D. Jandt, M. Buhk, M. J. Miles and J. Petermann, *Polymer,* **35** (1994) 2459

29. S. Hild, W. Gutmannsbauer, R. Luthi, J. Fuhrmann and H. J. Guntherodt, *J. Polym. Sci.,* **34** (1996) 1953

30. H. Schonberr, G, J, Vansco and A. S. Argon, *Polymer,* **36** (1995) 2115

31. P. Allan and M. Bevis, *Phil. Magaz. A* **35** (1977) 405

32. J. Petermann and R. M. Gohil, *Polymer,* **20** (1979) 596

33. P. B. Bowden and R. J. Young, *J. Mater. Sci.,* **9** (1974) 2034

34. G. L. Wilkes, *J. Mater. Sci.,* **6** (1971) 1465

35. D. M. Shinozaki and G. W. Groves, *J. Mater. Sci.,* **8** (1973) 1021

36. I. L. Hay and A. Keller, *J. Polym. Sci., Part C,* **30** (1970) 289

37. D. P. Pope and A. Keller, *J. Polym. Sci.,* **13** (1975) 533

38. A. Keller and D. P. Pope, *J. Mater. Sci.,* **6** (1971) 453

39. S. G. Burnay, M. D. D. Aere and G. W. Groves, *J. Mater. Sci.,* **13** (1978) 639

40. V. I. Gerasimov, Ya. V. Genin and D. Ya. Tsvankin, *J. Polym. Sci., Polym. Phys. Ed.,* **12** (1974) 2035

41. P. J. Hendra, M. A. Taylor and H. A. Willis, *Polymer,* **26** (1985) 1501

42. N. S. J. A. Gerrits and Y. Tervoort, *J. Mater. Sci.,* **27** (1992) 1385

43. Z. Bartczak, A. S. Argon and R. E. Cohen, *Polymer,* **35** (1994) 3427

44. C. P. Lafrance, J. Debigare and R. E. Prudhome, *J. Polym. Sci., Polym. Phys., Ed.,* **31** (1993) 255

45. J. A. H. M. Moonen, W. A. C. Roovers, R. J. Meier and B. J. Kip, *J. Polym. Sci., Ed.,* **30** (1992) 361

46. M. F. Butler, A. M. Donald, W. Bras, G. R. Mant, G. E. Derbyshire and A. J. Ryan, *Macromolecules,* **28** (1995) 6383

47. M. E. Vickers and H. Fischer, *Polymer,* **36** (1995) 2667

48. J. W. H. Kolnaar, A. Keller, S. Seifert, C. Zschunke and H. G. Zachmann, Polymer,

36 (1995) 3969

49. V. Gaucher-Miri, P. Francois and R. Seguela, *J. Polym. Sci., Phys. Ed.,* **34** (1996) 1113
50. D. Hofmann, D. Geiss, A. Janke, G. H. Michler, P. Fiedler, *J. Appl. Polym. Sci.,* **39** (1990) 1595
51. W. Wu, G. D. Wignall and L. Mandelkern, *Polymer,* **33** (1992) 4137
52. S. J. Spells and E. U. Okoroafor, *Polymer,* **35** (1994) 4590
53. B. K. Anns, J. Strizak, G. D. Wignall, R. G. Alamo and L. Mandelkern, *Polymer,* **37** (1996) 137
54. C. Schipp, M. J. Hill, P. J. Barham, V. M. Cloke, J. S. Huggins, and L. Oiarzabal, *Polymer,* **37** (1996) 2291
55. E. U. Okoroafor and S. J. Spells, *Polymer,* **35** (1994) 4578
56. D. I. Bower, E. L. V. Lewis and I. M. Ward, *Polymer,* **36** (1995) 3473
57. V. Strauch and M. Schara, *Polymer,* **36** (1995) 3435
58. J. C. Rodriguez-Cabello, M. Alonso, J. C. Merino and J. M. Pastor, *J. Polym. Sci., Polym. Phys. Ed.,* **60** (1996) 1709
59. N. Alberloa and J. Perez, *J. Mater. Sci.,* **27** (1991) 2921
60. A. N. Gent and S. Madan, *J. Polym. Sci., Phys. Ed.,* **27** (1989) 1529
61. C. S. Cruz, F. J. B, Calleja, T. Asano and I. M. Ward, *Phil. Mag.,* **68** (1993) 209
62. J. D. Hoffman, *Polymer,* **23** (1982) 656
63. M. Bevis and E. B. Crellin, Polymer, **12** (1971) 666
64. A. Kelley and G. W. Groves, *Crystallography of Crystal Defects,* Longman, London, 1970
65. A. Peterlin, *Polym. Eng. Sci.,* **18** (1978) 488
66. D. C. Prevorsek, H. B. Chin and S. Murthy, *ACS Prepr., PSME,* **70** (1993) 43
67. E. W Fischer and H. J. Goddar, *J. Polym. Sci., Part C,* **16** (1969) 4405
68. R. S. Porter, *ACS Polym. Prepr.,* **12** (2) (1971) 39
69. E. S. Clark and L. S. Scott, *Polym. Eng. Sci.,* **14** (1974) 682

70. J. Clements, R. Jakeways and I. M. Ward, *Polymer,* **19** (1978) 639

71. Ta-Hua Yu and G. L. Wilkes, *Polymer,* **37** (1996) 4675

72. Ta-Hua Yu and G. L. Wilkes, *J. Rheo.,* **40** (1996) 1079

73. Hongyi Zhou and G. L. Wilkes, *Polymer,* to appear

74. J. A. Odell, D. T. Grubb and A. Keller, *Polymer,* **19** (1978) 617

75. R. G. C. Arridge and P. J. Barham, *J. Polym. Sci., Polym. Phys. Ed.,* **16** (1978) 1297

76. D. Goritz, *unpublished work*

77. C. J. Chou, A. Hiltner and E. Bear, *Polymer,* **27** (1986) 369

78. T. Kajiyama and M. Takayanagi, *J. Macromol. Sci., Phys.,* **B10**(1) (1974) 131

79. J. Martinez-Salazar, J. V. Garcia Ramos and J. Petermann, *Intern. J. Polymeric Mater.,* **21** (1993) 111

80. N. W. Brooks, R. A. Duckett and I. M. Ward, *Polymer,* **22** (1992) 1975

81. N. W. Brooks, A. P. Unwin, R. A. Duckett and I. M. Ward, *J. Macromol. Sci.,* **34** (1&2) (1995) 29

82. B. K. Carter, Ph.D. Dissertation, Vol. I, Virginia Tech

83. H. O. Keith, F. J. Padden and R. G. Vadimsky, *J. Polym. Sci., Part 2,* **4** (1966) 267

84. J. R. Burns, *J. Polym. Sci.,* **A-2** (1969) 593

Chapter 5.0 ORIENTATION ANISOTROPY OF THE MECHANICAL α RELAXATION OF HIGH DENSITY POLYETHYLENE FILMS HAVING A WELL DEFINED STACKED LAMELLAR MORPHOLOGY *

Abstract

Dynamic mechanical experiments were conducted on melt-extruded uniaxially oriented high density polyethylene films having a well-defined stacked lamellar morphology. Samples were cut at different angles with respect to the original machine direction (MD) and tested by increasing the temperature from 20 to 130 °C at a heating rate of 0.5°C/min in the frequency range from 0.01 to 10Hz. Samples before and after the dynamic mechanical tests was also investigated by using WAXS, SAXS and DSC. Oscillating parallel (0°) and perpendicular (90°) to the MD gave rise to a single Tanδ dispersion peak, while oscillating at angles between the above two extremes generated a secondary dispersion peak at lower temperatures, with a maximum relaxation strength occurring at 45° orientation. It was concluded that, for the 0 ° and 90° orientations, the mechanical dispersion arise essentially from the crystalline phase, and it contains the contributions of earlier recognized intralamellar (α_I) and intracrystalline (α_{II}) relaxations. For the 45° orientation, the mechanical dispersion is believed to originate from an activated interlamellar shear motion that is related to the characteristics of the interface between crystalline lamellar and amorphous phase.

* The chapter, formatted as required, has been submitted to *Macromolecules* for publication.

5.1 Introduction

Under dynamic small strain studies, polyethylene (PE) displays at least three mechanical relaxations, designated as α, β and γ in the order of decreasing temperature, in addition to the melting point. [1] The γ relaxation, displayed by bulk crystallized linear and branched PE and solution grown PE single crystal mats, is found in the temperature range of -150 °C to -120°C. The β relaxation, distinctly displayed only by bulk crystallized branched PE, is in the temperature range of -30°C to 10°C. The α relaxation, shown by bulk crystallized linear and branched PE and solution grown PE single crystal mats, is in the temperature range of 30 °C to 120°C.[1-3] As expected, all peak positions increase with frequency, and each may be influenced by thermal history.

The origins of the three mechanical relaxations have been *extensively studied* in the past. [2-22] Although some detailed molecular assignments are still open to debate, the reality of the basic relaxation processes are clear; these have been well summarized by Boyd. [2,3] The α and β relaxations are commonly attributed to the relaxation mechanisms in the crystalline phase and amorphous phase, respectively; the γ relaxation is, according to different authors, due to the localized motions of either chain ends or branches associated with the amorphous phase [1,5] although originally, it was proposed to arise also from the crystalline phase. [6] Complementary dielectric relaxation studies on the respective α, β and γ relaxations in PE have also been carried out and well-summarized. [23]

The mechanical α relaxation for HDPE covers a wide temperature range from 30 °C to 120°C, and the calculated activation energy is a somewhat "diffuse" value, ranging from 90kJ/mol to more than 300kJ/mol. [1-3] In addition, the mechanical dispersion, as measured by Tanδ, is not symmetric, as exemplified by the data in Fig. 5.1 that were obtained for a compression molded slow cooled unoriented HDPE film utilizing the same resin that was used to produce the uniaxially oriented HDPE films that will be the focus of this report. All these facts have led to the assumption that the major mechanical α relaxation consists of several sub-relaxations, and this is

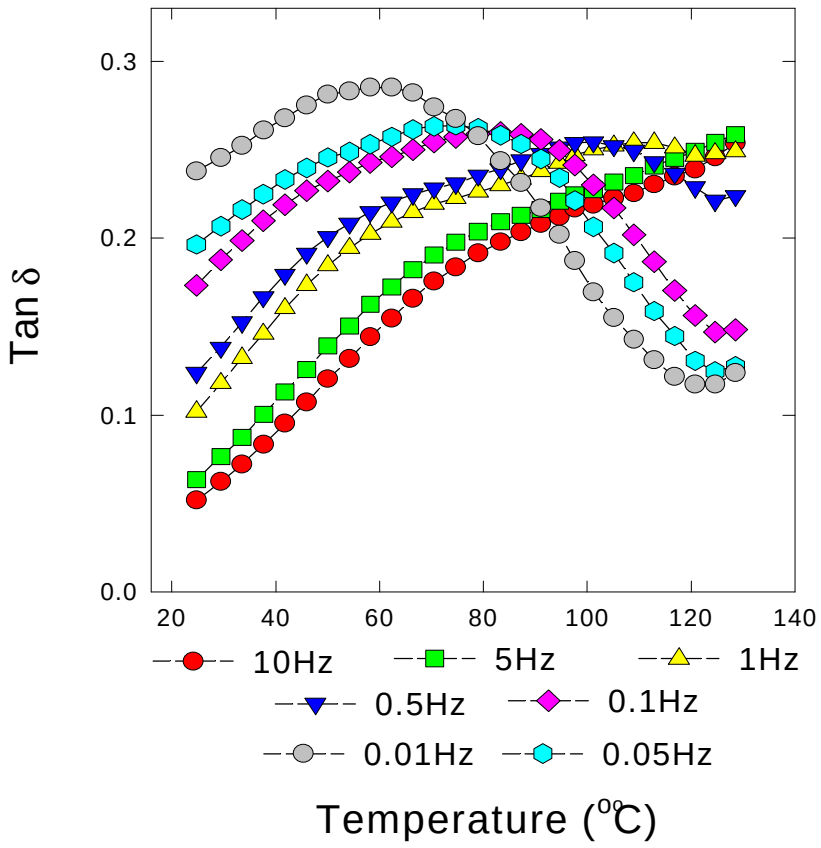

Figure 5.1 A typical Tanδ plot for unoriented HDPE materials

known as the multiplicity of the mechanical α relaxation for HDPE. At least three sub-relaxations, namely α_I, α_{II} and α_{III} in the order of increasing temperature, have been proposed. [7-22]

The resolution of the mechanical α relaxation into two components was first reported by Nakayasu, et al. [7] The sub-relaxations were designated as mechanism I (later α_I) at lower temperatures and mechanism II (later α_{II}) at higher temperatures, and they were stated to display activation energies of 117kJ/mol and 210kJ/mol, respectively. The authors suggested that the α_I process was associated with intercrystalline (grain boundary) relaxation phenomena, and the α_{II} process was related to intracrystalline (single chain) relaxation phenomena. The existence of a third sub-relaxation at even higher temperature was also speculated, but no molecular assignment and activation energy were provided by the authors.

By comparing the dynamic mechanical test data for melt crystallized HDPE films, which showed two relaxation peaks (α_I and α_{II}), with that of PE single crystal mats, which showed only one relaxation peak (α_{II}), Takayanagi, et al. concluded that the α_I mechanism was complicated thermorheologically; however, the α_{II} mechanism was viewed as a thermorheological simple process. [8-10] Their justifications were based on the construction of the master curves (based on the loss modulus E") for both relaxations. The construction of master curves for the α_{II} relaxation needed only horizontal shifts; whereas, for the α_I relaxation, both horizontal shifts and vertical shifts were needed. By plotting horizontal shift factors versus reciprocal temperature, the activation energies for the α_I and α_{II} relaxations were found to be 125kJ/mol and 192kJ/mol, respectively - these values being close to those expressed above. The authors suggested that the deformation of intermosaic regions within the crystalline lamellae was the origin of the α_I relaxation, and the α_{II} relaxation arose from the rotational oscillation of polymer chains in the crystal lattice.

Dynamic mechanical tests (parallel to the orientation axis), dynamic X-ray scattering experiments, and NMR experiments for oriented PE films have been carried out by McCrum, et al, [11,12] Stein, et al. [13,14] and Ward, et al. [15,16] These authors concluded that interlamellar shear, or interlamellar slip, was the origin of the α_I relaxation, and it was sensitive to the morphology of the specimens used. The α_{II} relaxation was believed to originate from the viscous nature of polymer

chain motions in the crystal lattice at high temperatures, including twisting motion about the c-axis as well as transitional motion along the c-axis.

Since most of the studies dealing with the mechanical α relaxation were performed on HDPE having spherulitic morphology or initially spherulitic texture prior to deformation, it has therefore been difficult to give unambiguous interpretations of the relaxation mechanisms because of the structural complexities of the spherulites or remnants of that texture. Depending on the local orientation of the lamellae and associated interlamellar amorphous layers, all types of inter- and intra- lamellar motions might be expected to take place in the specimen during the dynamic mechanical test at the appropriate frequency and temperature. Therefore, it is desirable to utilize materials having a more simplified and well defined morphology to carry out dynamic mechanical experiments, with the hope that such morphologies may assist a better definition the nature and origin of a given mechanical relaxation.

Matsuo, et al, [17] Ogita, et al [18] and Ohta, et al. [19] also carried out dynamic mechanical experiments and creep experiments for ultra-high molecular weight polyethylene (UHMwPE) that had been ultra-drawn into fibers. These authors showed the existence of the third relaxation (α_{III}), in addition to the α_I and α_{II} relaxations. It was suggested that the α_{III} relaxation was related to the transition from the orthorhombic phase to the hexagonal-packed phase at high temperatures. Furthermore, by using fibers at different draw ratios (orientation states), it was shown that the strength of the α_{II} relaxation (along the fiber axis) became smaller with increasing draw ratio and finally reached zero at a draw ratio of 400. In addition, the calculated activation energy of the α_{II} relaxation changed with the orientation state of the fibers. Therefore, the strength of the α_{II} relaxation was suggested to be related to the anisotropy of the crystal lattice potential. The α_I mechanism, however, was suggested to be related to an intralamellar grain boundary phenomenon that was associated with a rotational motion of crystal grains in the direction of external excitation.

Since most of the dynamic mechanical tests were done by isochronal scans at specific heating rates, it has been suspected that the morphology of the specimen might have been changed during the experiments; therefore, it is desirable to carry out the tests isothermally. By doing

isothermal dynamic mechanical tests for HDPE and lightly crosslinked low density polyethylene over a wide region of frequency (10^{-4} to 1Hz), Amparo, et al. concluded that the multiplicity of the mechanical α relaxation was due to the size (thickness) distribution of the crystalline lamellae. [20-22] In other words, these researchers proposed that the α_I and α_{II} relaxations originate from the same molecular mechanism (defect motions in crystalline lamellae) within thinner and thicker crystalline lamellae, respectively. The confusion about the multiplicity of the mechanical α relaxation, according to the authors, were mainly due to the fact that the lamellar thickness distribution was probably changed at high temperatures during the isochronal dynamic mechanical measurements.

The review of literature on the mechanical α relaxation for HDPE has shown that the long-standing controversy has not been resolved. Two principle reasons are: 1) the complex morphologies of the specimens, and 2) the speculated morphological changes during the dynamic mechanical tests. More specifically addressing the former, in the case of a spherulitic morphology, the inter- and intra- lamellar motions can always happen simultaneously during the dynamic tests, and this could result in the concurrence of both the α_I and α_{II} relaxations. For the fibril morphology possessed by the UHMwPE ultra-drawn fibers, the existence of the chain-extended crystalline phase and the orientation state of the ordered amorphous phase must certainly have some influence on the mechanical α relaxation. In addition, the morphology of the samples before- and after- dynamic mechanical tests are not to be expected to be exactly the same due to lamellar thickening, etc; thus, it should be further investigated to assure the effects of such morphological changes on the mechanical α relaxation.

In the study presented here, melted extruded uniaxially oriented HDPE films were used, and mechanical oscillations were applied at different orientations with respect to the original machine direction (MD). In contrast, for the case of UHMwPE ultra-drawn fibers, the original MD is the only possible oscillation direction. Oscillation in different directions may excite specific relaxation processes due to the different molecular motions generated, and this in principle may make it easier to understand the separate relaxation processes. Isochronal tests were carried out in this study, since it has the advantage of covering a large range of temperatures. In this case,

morphological features for the specimens before- and after- dynamic mechanical tests were also investigated.

On the other hand, the orientation anisotropy of a ny mechanical dispersion itself is an important issue for many polymers that are used at an oriented state (such as packing films, etc.) in engineering applications. For example, the damping character of a material, which is closely coupled to the dynamic mechanical dispersion, may be more or less activated at different orientations with respect to the loading direction and therefore influence the character of the energy dissipation ability of the material. Therefore, it is also the purpose of this study to provide dynamic mechanical test data that reflect information on this issue as well.

5.2 Experimental

***Materials*:** The linear HDPE homopolymer resin studied had a number average molecular weight and a weight average molecular weight of 14,600g/mol and 150,000g/mol, respectively. The 1 mil thick melt-extruded films were kindly provided by Hoechst Celanese Co.. Under the film extrusion processing conditions, the crystalline phase became quite highly uniaxially oriented with the c-axis along the MD. This was quantified by determination of the Hermans' orientation function, f_c, for the crystalline phase using X-ray scattering, where f_c is defined as

$$f_c = \frac{1}{2}(3 < \cos^2\theta > -1) \qquad (5.1)$$

In equation 5.1, the quantity $<\cos^2\theta>$ represents the average value of $\cos^2\theta$, with θ being the angle between the c-axis in the crystal (chain axis direction) and the MD axis. The amorphous phase, however, had no significant orientation as determined from a previous study. [24] In the present study, both melt-extruded film (precursor film) and annealed precursor films were used. Two different kinds of annealed films were used. One was provided by Hoechst Celanese Co., where annealing was done by passing the precursor films through an oven at 120 °C with certain on-line speed that allowed the materials to remain at this temperature for ca. 20min. Since there

was a small amount of tension (ca. 3% strain) associated with this process, this kind of annealed film will be referred as tension-annealed films. In addition, free-annealed films, produced simply by annealing the precursor films without tension at 120°C for 20min were also used.

***Dynamic Mechanical Analysis*:** Samples (5cm wide and 10cm long) for dynamic mechanical tests were carefully cut directly from the HDPE films at different angles with respect to the original MD, with 00° being parallel and 90° perpendicular to the MD. The dynamic mechanical parameters of storage modulus (E'), loss modulus (E"), and loss factor (Tan δ) were determined using a Seiko DMS instrument (Model 210). Temperature was increased from 20 to 130°C at a heating rate of 0.5°C/min. Frequencies covered a wide range from 0.01 to 10Hz. During the experiments, the applied tensile force was kept small to assure a linear viscoelastic response from the specimen.

***WAXS and SAXS*:** All the WAXS experiments were performed by utilizing a Philips tabletop X-ray Generator (Model PW1720) equipped with a standard vacuum-sealed Warhus photographic pinhole camera. The instrument with a CuKα radiation (λ=1.54Å) was operated at 40KV and 20mA. Single layer film and stacks of films were used as the specimens for the experiments. A Kratky slit-collimated camera was used for the SAXS experiments. In this case, the scattered intensity was monitored by a one-dimensional position sensitive detector and corrected for sample thickness, counting time, transmission and standardized to a Lupolen based standard. In all the SAXS experiments, the specimen's MD was aligned parallel to the width's direction of the sample holder so that X-ray scans were along the MD (MD scans).

***Differential Scanning Calorimetry*:** DSC experiments were carried out by using a Seiko DSC instrument (Model 220C). A heating rate of 10°C/min was used. In all the experiments, the samples' weight was kept constant (ca. 5mg). An estimate of lamellar thickness and its distribution were obtained by applying the Gibbs-Thomson equation to the DSC data, [25] and the heat flow versus temperature curves were transformed into plots of relative probability versus lamellar thickness by using the same equation as proposed by the authors of reference 19. In the calculations, the heat of fusion of the crystal phase and free energy of basal surface of the crystalline lamellae used were $290.10^{6}J/m^{3}$ and $90.10^{-3}J/m^{2}$, and the equilibrium melting

temperature was chosen as 145.5 °C. [26] [A detailed study on the applicability of DSC to determine the crystalline lamellar thickness and its distribution has recently been carried out by the same authors of this report and submitted for publication. [27]]

***Transmission Electron Microscopy*:** Samples for TEM study were treated by chlorosulfonic acid at 60°C for 6 hours; then, they were washed with sulfuric acid and water and dried overnight. The stained samples were embedded in an epoxy resin and cured at 65 °C overnight. The embedded samples were microtomed at room temperature by cutting along the MD. The microtomed thin sections of ca. 80nm thick were used for the TEM observations after being treated by uranyl acetate. All the TEM work was performed by using a Philips EM420 instrument operated at 100kV.

5.3 Results

Figure 5.2 shows the WAXS patterns for the tension-annealed film used in this study. It is obvious from these patterns that the crystalline phase is quite well oriented with the c-axis along the MD (c and d). In addition, the patterns also illustrate that the a- and b-axes are principally uniformly distributed in the plane perpendicular to the MD (b), which contains the transverse direction (TD) and the normal direction (ND) of the film. The Hermans' orientation function for the crystalline phase (f_c), calculated from the WAXS patterns, are 0.67, 0.80, and 0.68 for the precursor film, tension-annealed film, and free-annealed film, respectively. The TEM micrograph shown in Fig. 5.3 presents a direct visualization of the well defined stacked lamellar morphology possessed by the same films whose WAXS patterns were shown in Fig. 5.2. TEM experiments for the precursor film and the free-annealed film revealed the same kind of well defined stacked lamellar morphology, except that for the precursor film, the crystalline lamellae were somewhat thinner and displayed less contrast than those of the annealed films. No distinct difference was observed between tension- and free- annealed films by TEM.

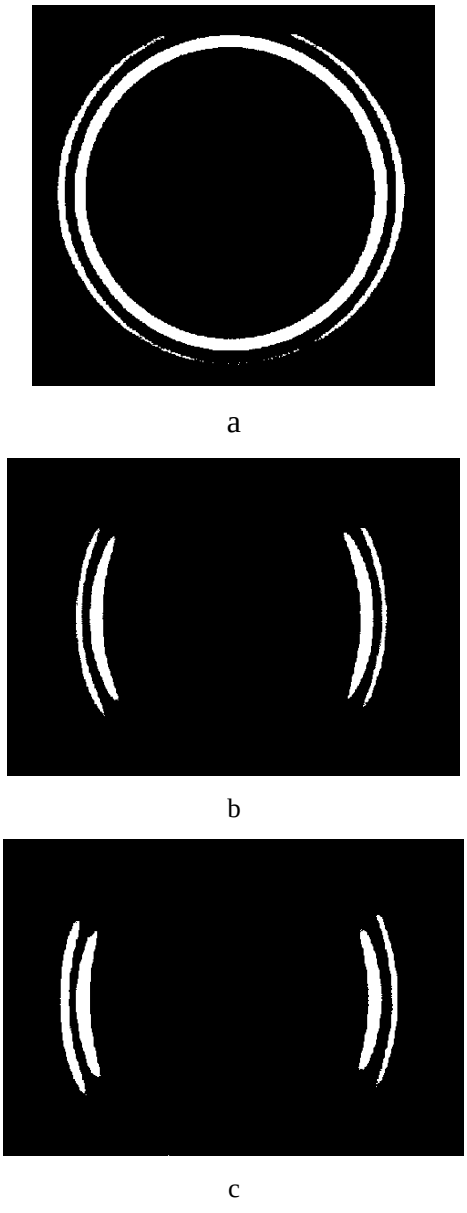

a

b

c

Figure 5.2 WAXS patterns for the tension-annealed film with X-ray beam parallel to the a) MD, b) ND and c) TD.

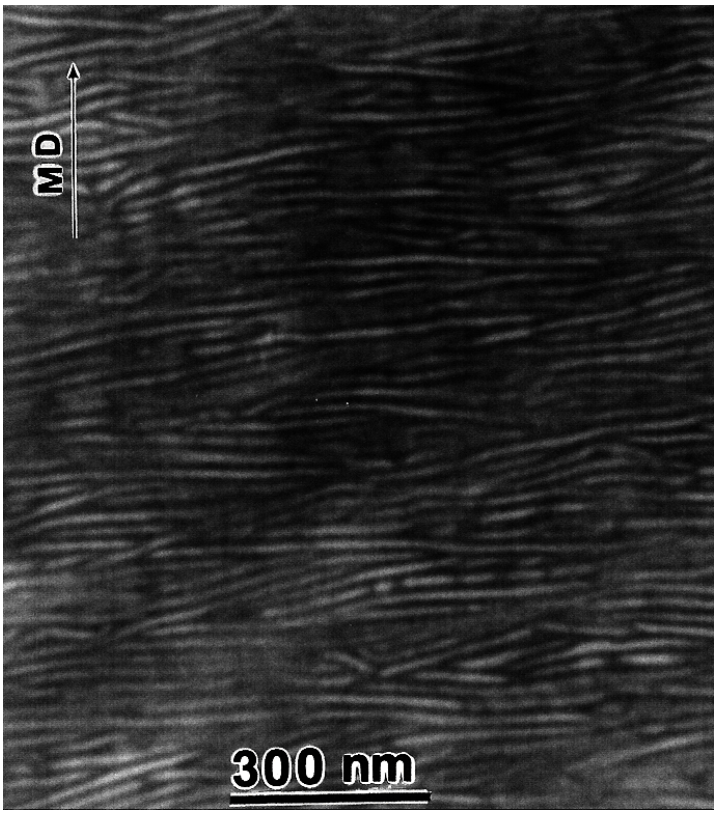

Figure 5.3 A TEM micrograph showing the stacked lamellar morphology for the tensile-annealed film. MD represent the machine direction.

***Anisotropy of the mechanical α relaxation*:** The relaxation behavior for the precursor film determined at different orientations with respect to the MD are presented in Fig. 5.4. These data clearly show the anisotropy (orientation dependence) of the mechanical α relaxation. For the 0° oscillation (dynamic mechanical test parallel to the MD), only one single dispersion peak was observed, at approximately 84°C at 0.1Hz. The 90° oscillation (dynamic mechanical test perpendicular to the MD) also showed only one dispersion peak, but this time the peak occurred at ca. 96°C at the same frequency - a distinctly higher temperature than that of the 0 ° oscillation. For all the other orientations investigated, a secondary dispersion peak at low temperatures was found. The existence of the secondary peak was confirmed by duplicating the experiment for the same type of sample to make sure that it was not coming from experimental errors. The strength of the secondary dispersion peak was dependent on the sample orientation in the DMTA experiment, with a maximum in dispersion strength occurring at ca. 45° orientation. However, the temperature of the secondary dispersion peak remained essentially unchanged with sample orientation. It is worth noticing that, although the intensity of the major peak and that of the secondary peak varied with sample orientation, total dispersion (the area under the whole Tan δ curve) remained basically constant for all sample orientations when compared in the temperature range investigated.

The results of Tanδ at the frequency of 0.1Hz for all the orientations are shown in Fig. 5.5, where Tanδ is plotted against temperature and orientation. Again, the orientation dependence of the mechanical α relaxation is clearly shown. We now address some features of the relaxation peaks in Fig. 5.5, the first being the calculation of the respective activation energies. In order to do so, master curves were constructed. From the Arrhenius-type plot of horizontal shift factors versus reciprocal temperatures utilized in constructing these plots, the activation energies were obtained. Mechanical loss modulus (E") were used in the construction of master curves since it is

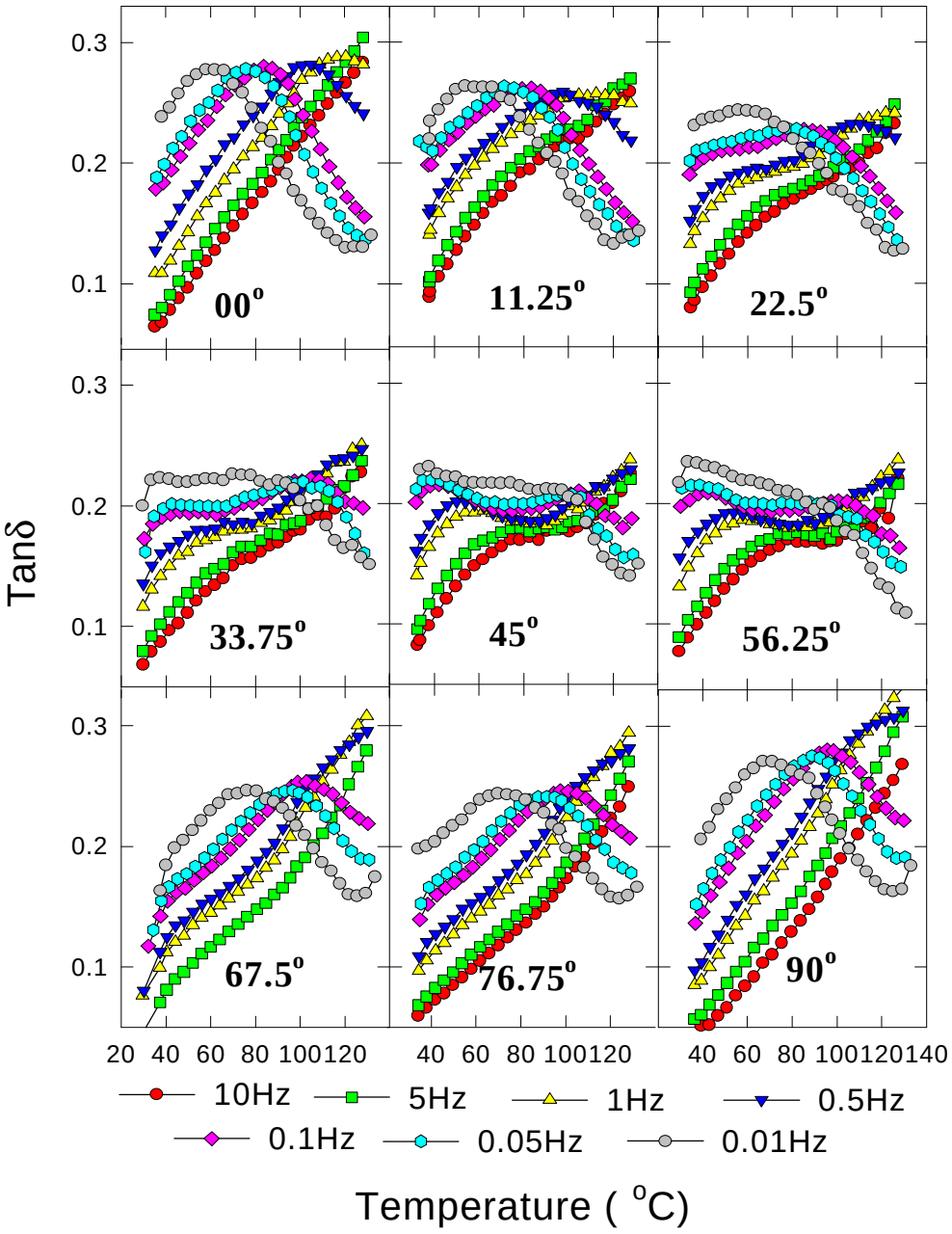

Figure 5.4 Mechanical relaxation for the precursor film at different orientations (angles shown on each plot) with respect to the original MD.

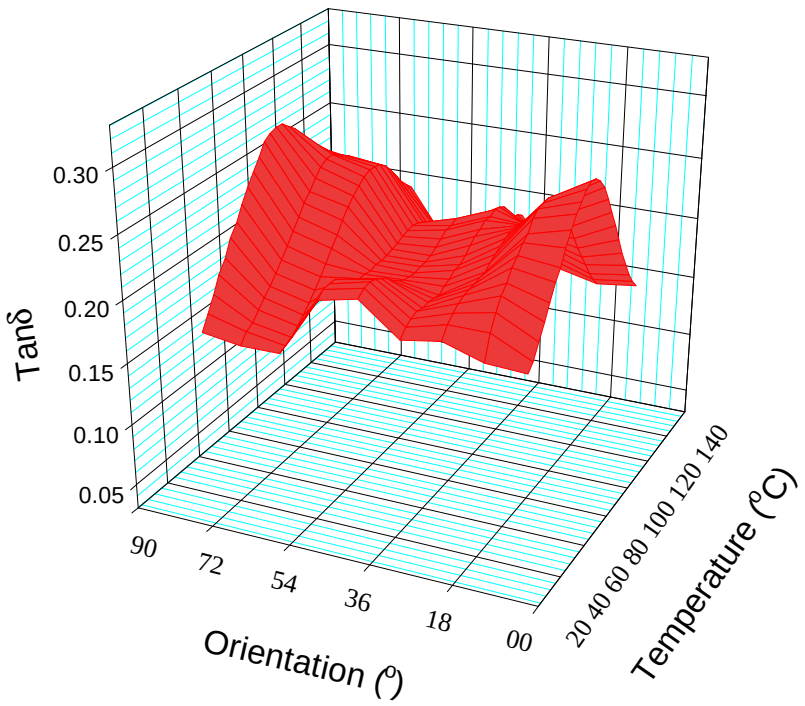

Figure 5.5 Tanδ surface plot for the precursor film showing the orientation dependence of the mechanical α relaxation at 0.1Hz frequency.

a single variable as compared to the mechanical dispersion Tanδ, which is dependent upon both the storage modulus (E') and loss modulus (E").

The loss modulus for the 0°, 45° and 90° oscillations are shown in Fig. 5.6. For each orientation, a master curve based on the loss modulus was constructed by shifting each individual curve to the reference temperatures horizontally and then vertically to obtain the best superposition. The master curves thus obtained are shown in Fig. 5.7. It can be seen that the superposition was quite good, except at lower frequencies; this is especially true for the case of the 45° oscillation. It is noticed that these master curves are somewhat diffuse, which is very representative of its expected behavior based on past studies of high density polyethylene. [16-18] However, the orientation dependence behavior is still obvious, i.e., those for the 0 ° and 90° oscillations had a broader and *flatter* peak while that for the 45° oscillation showed a broad dispersion with the existence of *two sub-peaks*.

Figure 5.8 represents the corresponding horizontal shift factors (at) and vertical shift factors (bt) for the construction of the master curves at the three orientations. The horizontal shift factors were plotted against reciprocal temperature to calculate activation energy, and the vertical shift factors were plotted against temperature to take into account of the change of modulus with respect to temperature. It is evident that the vertical shifts became larger at temperatures *higher than* 110°C, and this suggests that the time-temperature superposition is not valid and therefore consistent with the poor superposition of the master curves shown in Fig. 5.7. Therefore, all the data used in the calculation of the activation energy were at temperatures below 110 °C. The slopes of the linear regions on these plots were obtained by using linear regression when the R values were larger than 0.99. The calculated activation energies are shown on the Arrhenius plot at each orientation.

Effect of conditions of thermal annealing on Tanδ: The Tanδ plot similar to that of Fig. 5.5 for the tension-annealed film is presented in Fig. 5.9. Once again, at the 0 ° and 90° orientations, Tanδ showed only one overall relaxation peak, with the 0 ° orientation displaying the peak at a lower temperature than that of the 90 ° oriented sample at the same frequency. A

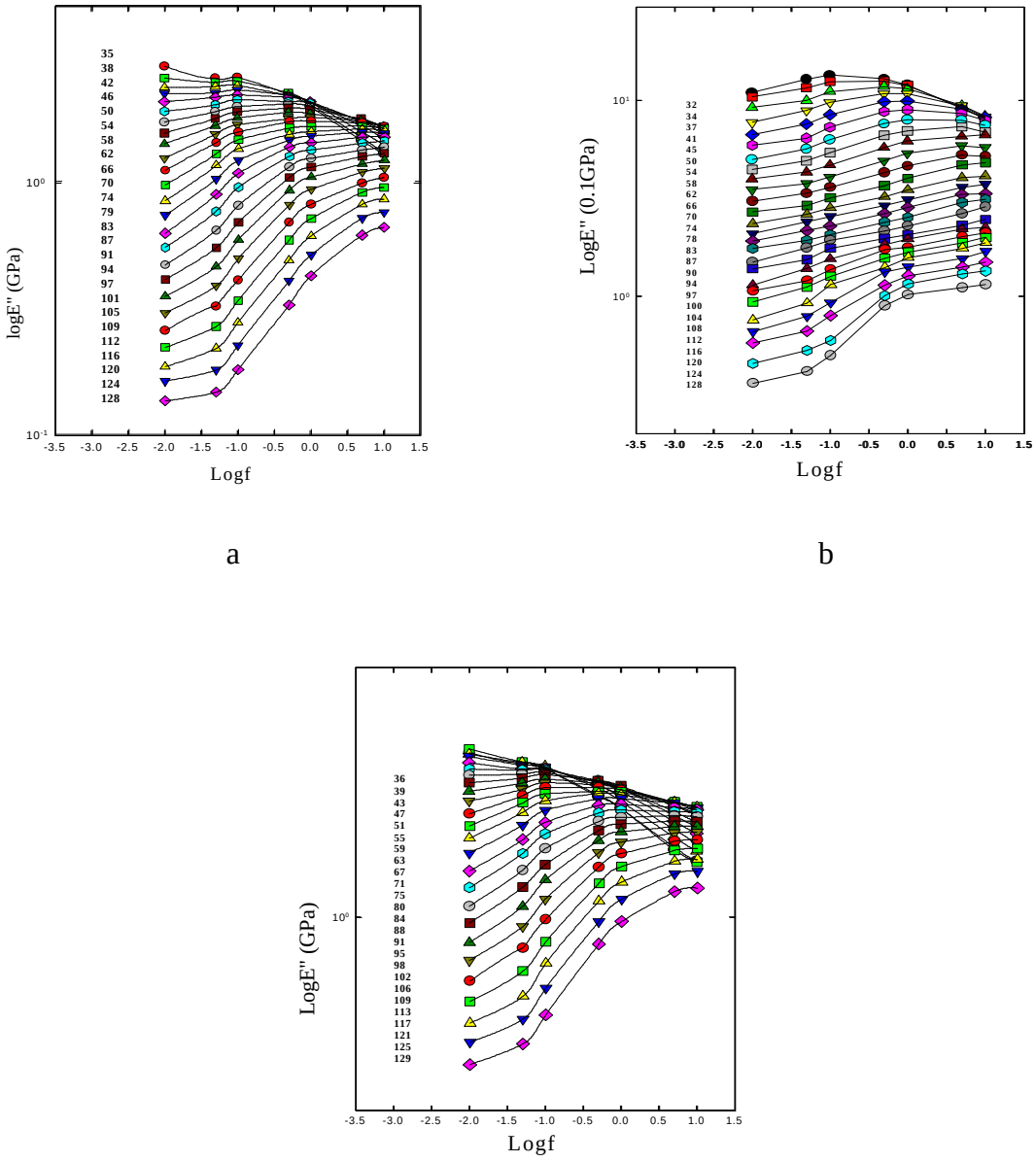

Figure 5.6 Dynamic loss modulus at varies temperatures of the precursor film at 00° (a), 45° (b) and 90° (C) orientations

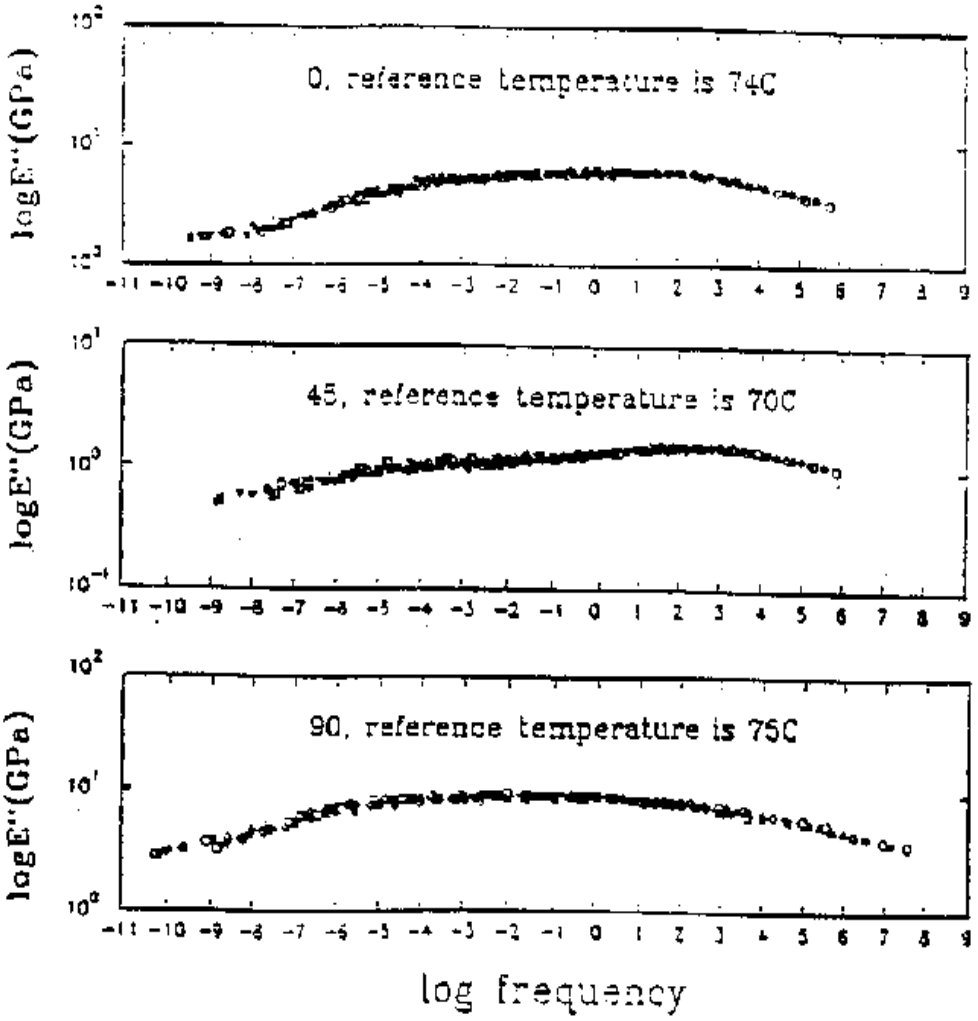

Figure 5.7 Master curves based on the dynamic loss modulus for the precursor film at the 00 ° 45° (b) and 90° orientations.

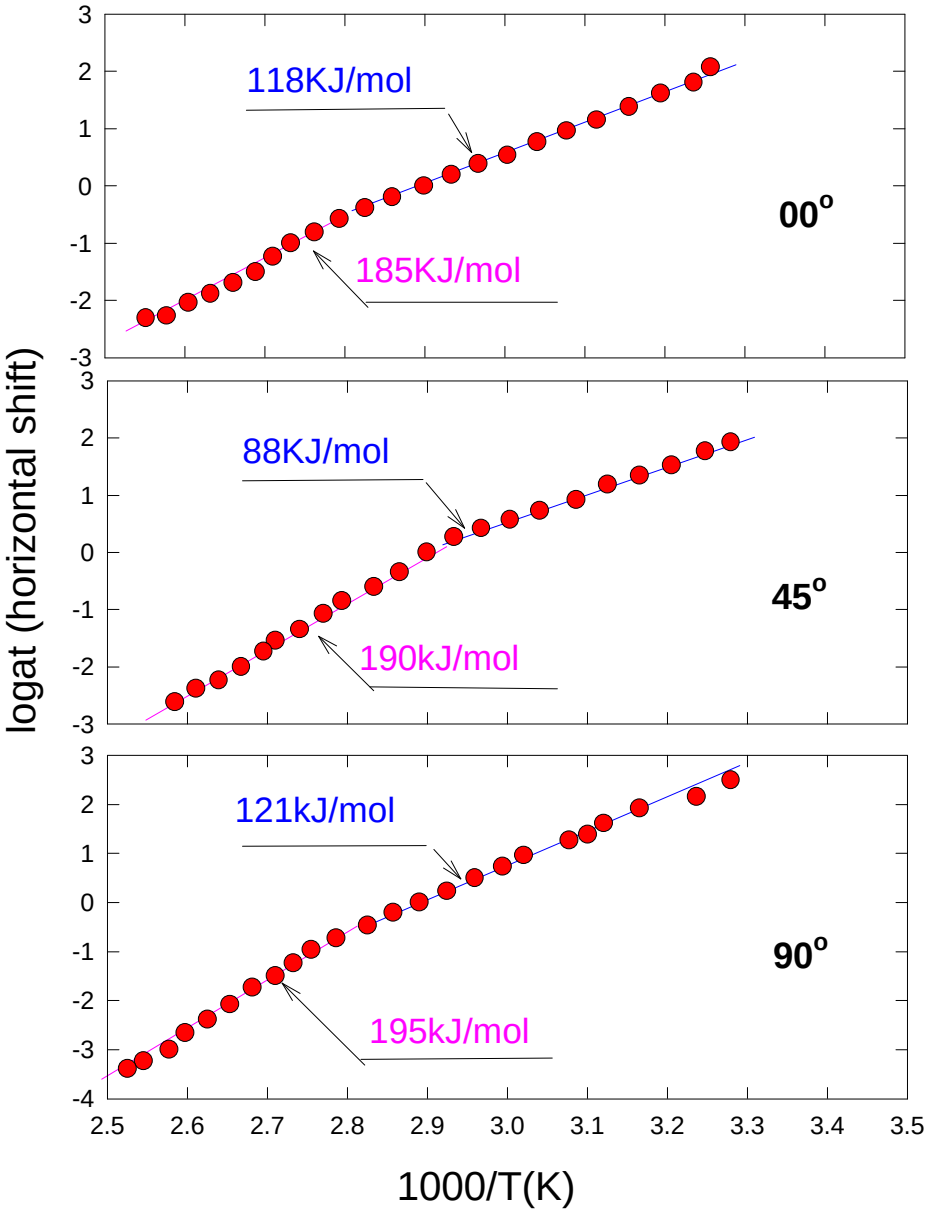
118KJ/mol
185KJ/mol
00°
88KJ/mol
190kJ/mol
45°
121kJ/mol
195kJ/mol
90°
logat (horizontal shift)
1000/T(K)
3
2
1
0
-1
-2
-3
-4
2.5
2.6
2.7
2.8
2.9
3.0
3.1
3.2
3.3
3.4
3.5

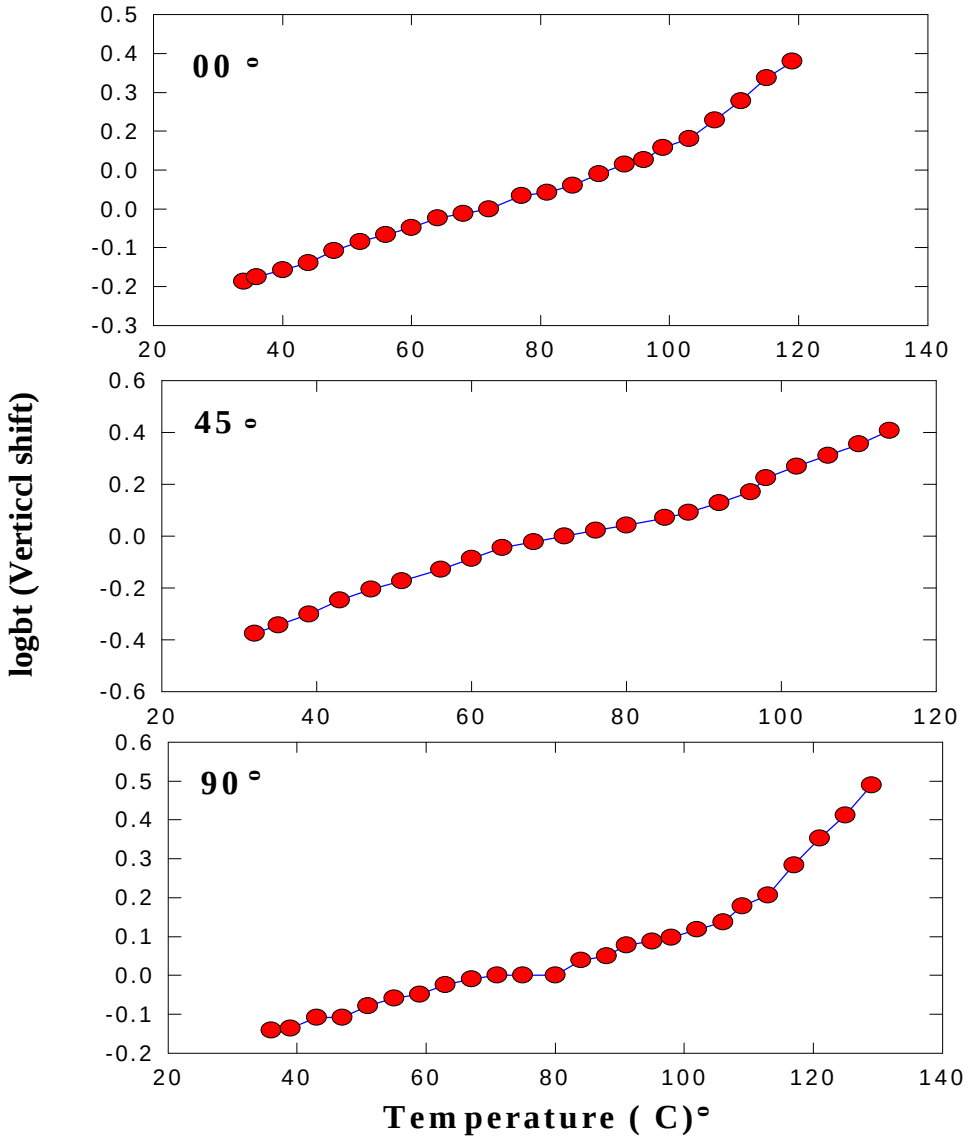

Figure 5.8 Horizontal shift factors for the construction of master curves for the precursor film at the 00°, 45° and 90° orientation.

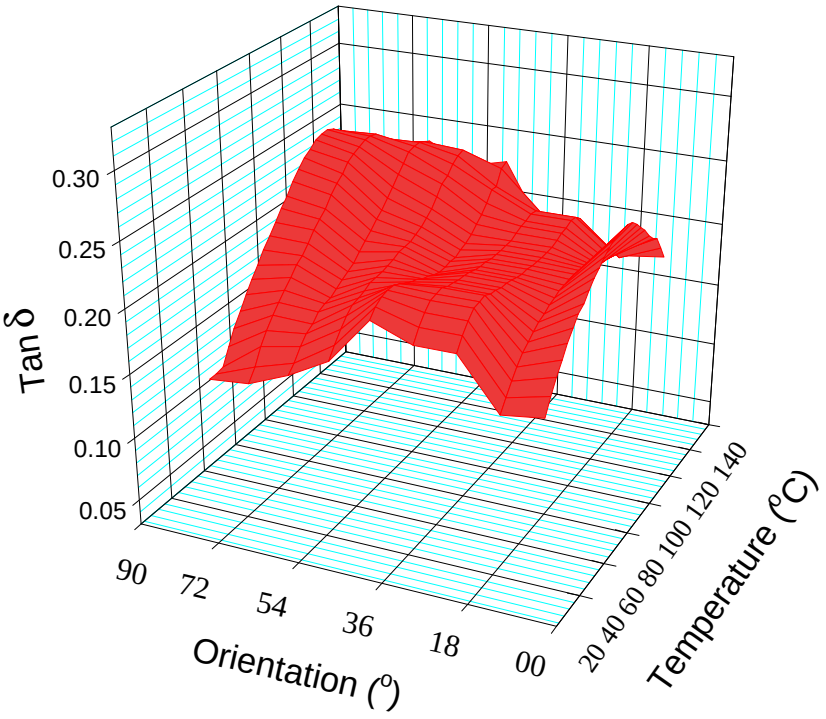

Figure 5.9 Tanδ surface plot for the tension-annealed film showing the orientation dependence of the mechanical α relaxation at 0.1Hz frequency.

secondary relaxation peak existed at all other orientations, with a maximum occurring at the 45 ° orientation. For a given orientation, other noticeable features as compared to Fig. 5.4 are: 1) the strength of the primary dispersion was decreased, and 2) the primary relaxation peaks became broader.

In Fig. 5.10, Tanδ (at 0.1Hz) has been plotted against temperature for the melt-extruded film (pre), tension-annealed film (T120), and free-annealed film (F120) at the three orientations of 0°, 45° and 90°. In addition to the above-mentioned differences in Tan δ, the effects of tension in the annealing process deserve particular attention. For the free-annealed samples, the major change observed relative to the behavior of the precursor sample was a decrease in dispersion strength; for the tension-annealed samples, a distinct shifting of the dispersion peak to higher temperatures occurred, in addition to a decreased dispersion intensity, especially noted for the 0 ° orientation. For the case of the 45 ° orientation, the low temperature relaxation remained basically intact, with all data overlapping for the three films. However, there were subtle changes for the high temperature relaxation- this being a shift to higher temperatures for the free-annealed samples, and a disappearance of the relaxation maximum for the tension-annealed samples.

5.4 Discussion

***Assignments of mechanical α relaxations in this work*:** For the cases of 0° and 90° oscillations, the oscillations during the dynamic mechanical tests involved the deformation of the crystalline phase and the amorphous phase as well. Due to the specific stacked lamellar texture, the HDPE film used in this study can be considered a laminated composite composed of with stacks of crystalline layers and amorphous layers. It needs to be noted that such a treatment is based on the same considerations as the two variants (parallel and series) of the Tagayanagi model; [28] however, the well-defined stacked lamellar morphology of the samples provides a good justification of the above simplification. Therefore, at the 0° orientation, the two phases principally deform in series, while at the 90° orientation, they deform more in parallel. During the

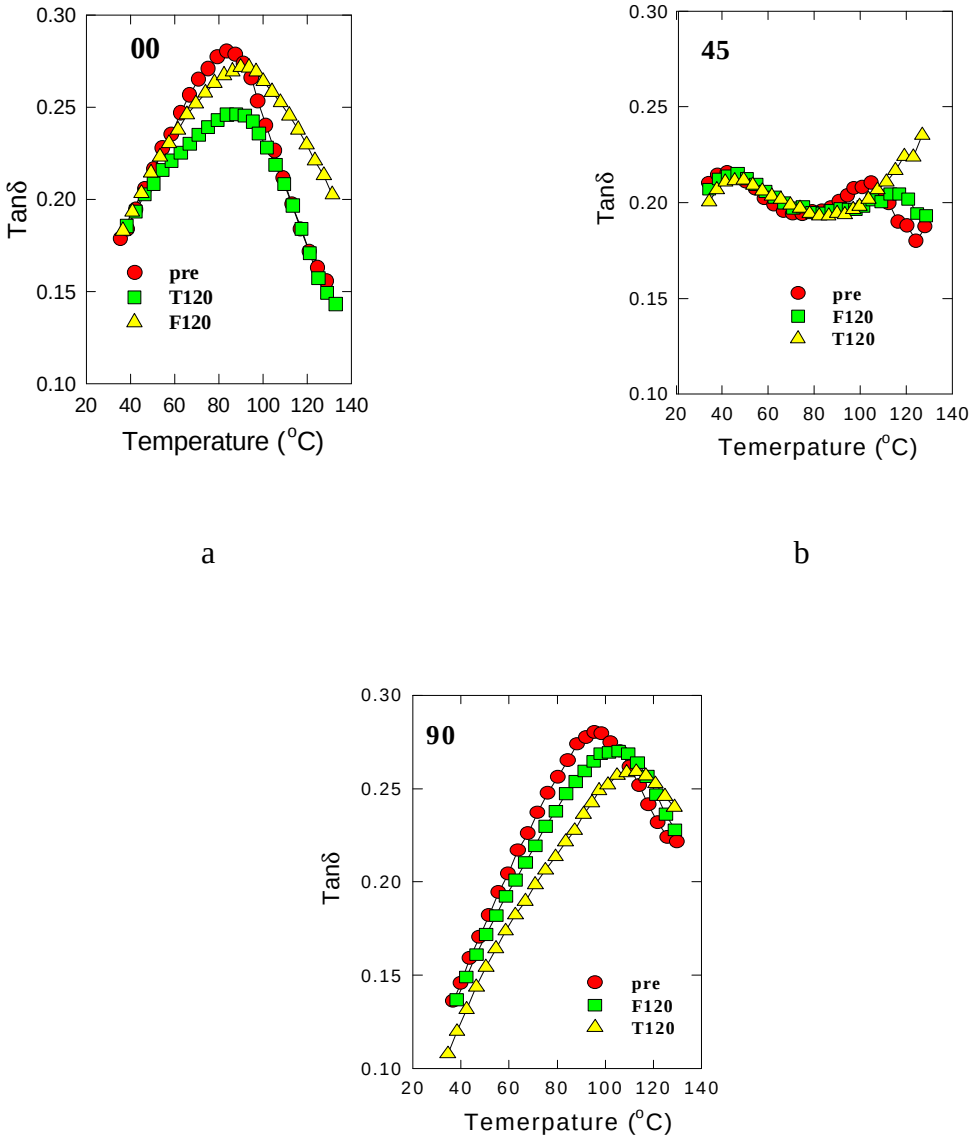

Figure 5.10 Tanδ for the precursor film (pre), free-annealed film (F120), and tension-annealed film(T120) at the 00°, 45° and 90° orientation.

experiments, however, the amorphous region is in a rubbery state; therefore, the dispersion peak is not expected from the amorphous phase and must therefore come from the crystalline phase. It has been seen that the 0° and 90° oscillations were associated with activation energies of 118 or 121kJ/mol and 185 or 195kJ/mol (Fig.5.8) for the low and high temperature relaxations, respectively. Since these values matched well with the literature for the activation energies for the α_I and α_{II} relaxations, they are believed to be the mechanical α relaxation originating from the crystalline phase. In the above discussion, any tilt of crystalline lamellae with respect to the MD and that of the folded polymer chains with respect to the lamellar base surface have not been taken into account.

Comparing the temperature of the relaxation peaks shown at both the 0° and 90° orientations, it was noted earlier that the 90° orientation showed a well-defined relaxation peak at a somewhat higher temperature than that of the 0° orientation. From the above discussion, it was shown that α_I and α_{II} processes were activated in both orientations; thus, the relaxation at each orientation contained the contributions from both the α_I and α_{II} processes. Therefore, we suggest that the higher temperature α_{II} process is the dominate relaxation at the 90° orientation; whereas, the lower temperature α_I process dominates the relaxation process at the 0° orientation.

At a 45° orientation, a low activation of 88kJ/mol was found for the low temperature region (84°C at 0.1Hz), in addition to a 190kJ/mol which corresponds to the α_{II} relaxation that occurs in the high temperature region (96°C at 0.1Hz). This particular orientation allows interlamellar shear to occur easily because of the maximum resolved shear stress of the applied oscillation stress on the plane of the lamellar surface. Therefore, we conjecture that interlamellar shear gives rise to the dispersion with the activation energy of 88kJ/mol. The symmetric feature of the secondary relaxation strength with respect to the 45° orientation provided further proof for this justification, since the resolved shear stress possesses the same kind of symmetry. [29] If the interlamellar shear indeed happened, the tie chains have to slip within the lamellae to accommodate the interlamellar shear, and this intralamellar slip give rise to the α_{II} relaxation with an activation energy of 190kJ/mol.

As mentioned above, while the amorphous phase is within the rubbery region, it will not generate a dispersion peak. Clearly, however, upon cooling, the vitrification of the amorphous region would be expected to introduce a mechanical relaxation. Since the interlamellar shear is basically a friction motion between crystalline lamellae and neighboring amorphous regions, the interfacial region, including the basal surfaces of the crystalline lamellae and adjacent constrained amorphous phases, is believed to be the cause of the interlamellar shear dispersion. Such a judgment has been also proposed by others based on the very long relaxation time (1 ~ 1000sec.) of the mechanical α relaxation. [20]

***Effects of morphological changes on the mechanical α relaxation*:** As addressed earlier, it has been speculated that the morphology of the sample might change during the dynamic mechanical experiments and therefore be responsible for the observed multiplicity of the mechanical α relaxation. In order to verify if this has occurred, samples before and after the dynamic mechanical experiments were characterized by WAXS, SAXS and DSC. In all the experiments, samples from the precursor film at the three orientations, namely 0°, 45° and 90° orientations, were used. The data indeed showed that there were some morphological changes caused by the dynamic mechanical tests as will now be considered.

WAXS patterns in Fig. 5.11 showed that the 0° oscillation has resulted in an increase in the orientation of the crystalline phase (a and b where f_c increased from 0.67 to 0.76); whereas, the 45° and 90° oscillations showed almost no effect of the dynamic mechanical tests on the orientation state of the crystalline phase relative to the precursor film- compare c and d with a. The increase in f_c for the sample at 0° oscillation is not a surprising, since it was basically "annealed" under a dynamic tensile stress, just as the tension-annealed film which also developed a higher value of f_c during its annealing process. It is speculated that the cause of this increase in f_c for both samples is due to the ease of translational motions of the chain axis in the crystal when a stress is applied along the original orientation axis. SAXS data (scanned along the MD) in Fig. 5.12 also showed the morphological changes caused by the dynamic tests at the three different orientations. SAXS profiles from samples after the dynamic tests showed a more well defined

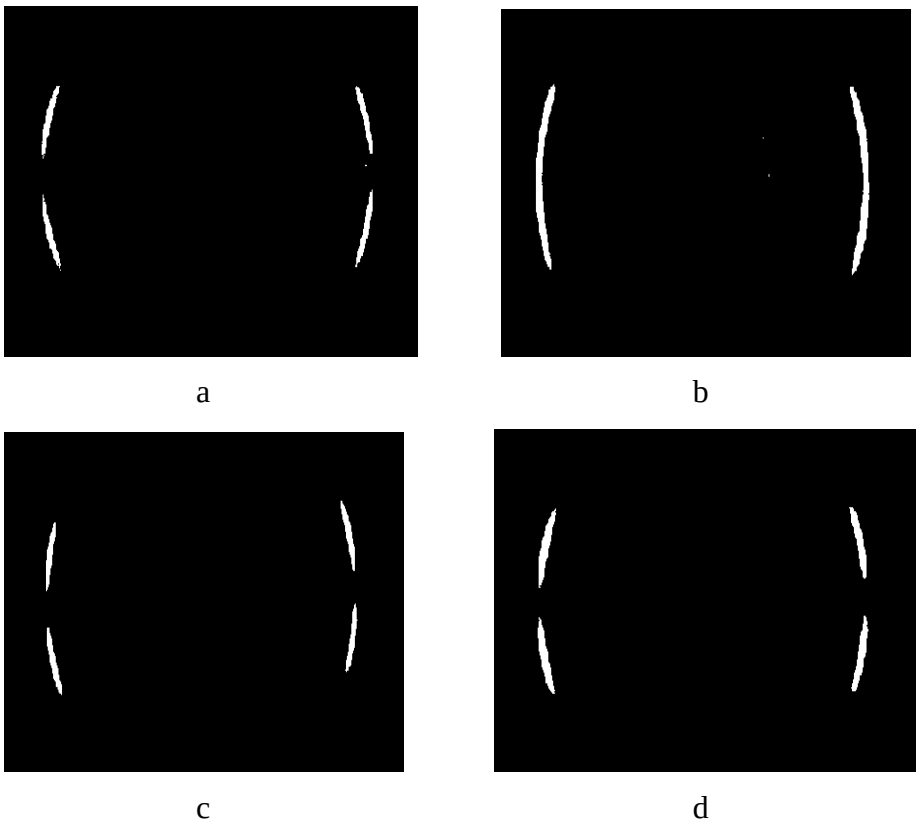

Figure 5.11 WAXS patterns for the precursor film before (a) and after the dynamic mechanical test at the 00° (b), 45° (c) and 90° (d) orientations.

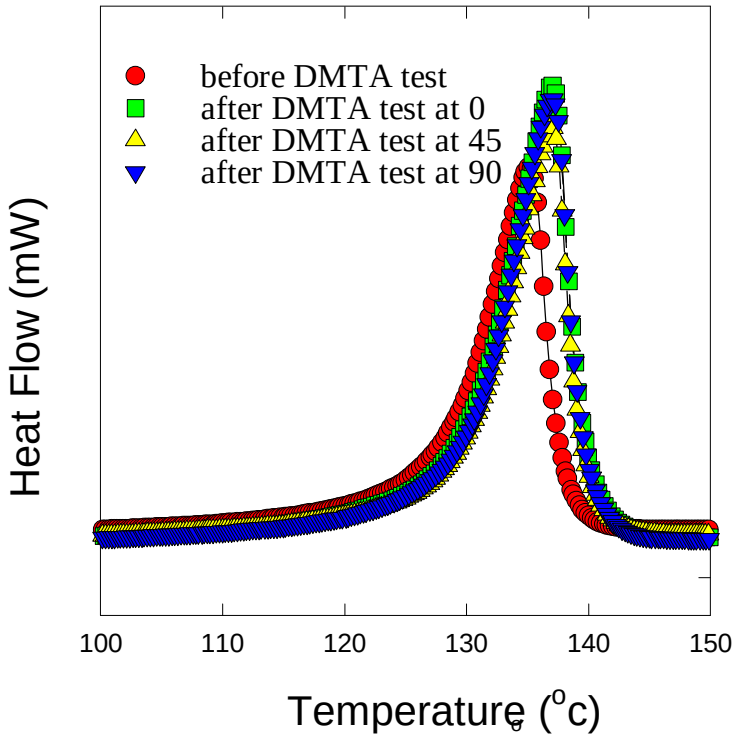

Figure 5.12 DCS scans for the precursor film before and after the dynamic mechanical test at the 00°, 45° and 90° orientation.

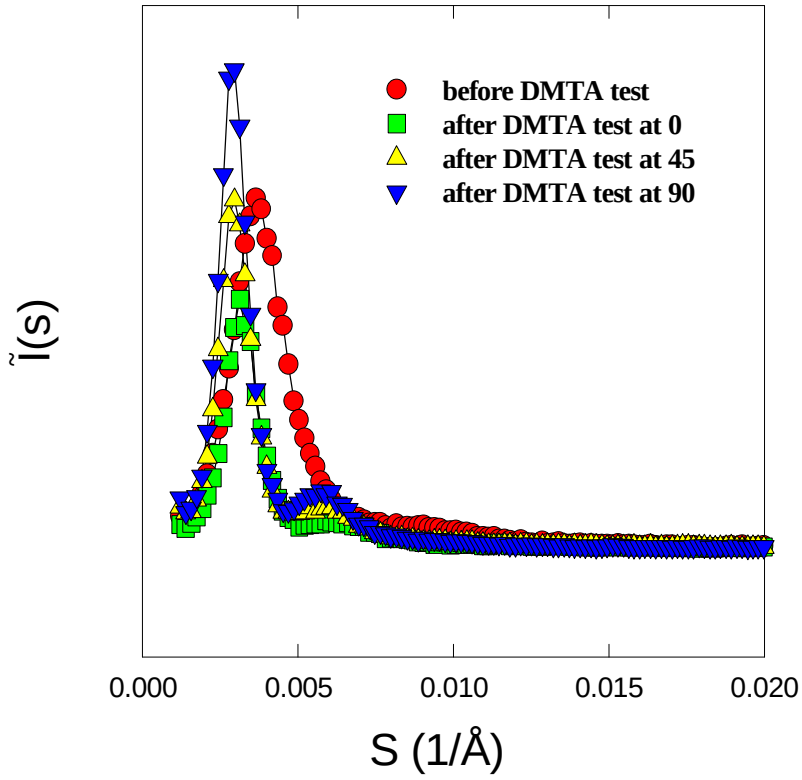

Figure 5.13 SAXS (MD scan) data for the precursor before and after the dynamic mechanical test at 00°, 45° and 90° orientations.

secondary scattering peak compared to the sample before the tests. In addition, the first order scattering peak was also "sharpened" for each sample after the dynamic mechanical test. The peak positions also shifted to somewhat smaller scattering angles, indicating an increase in the long spacing for samples after the test; however, the differences between the three orientations was not major.

DSC results (Fig. 5.13) showed that there were increases in melting point and percent crystallinity after the dynamic mechanical tests for all the three orientations. The increase in melting point at all the three orientations was also about the same (ca. 1.5 °C). In terms of percent crystallinity, the 0° orientation had the largest amount of increase (16%), followed by the 90 ° orientation (14%) and by the 45 ° orientation (6%), these values also implied different degrees of perfection for the crystalline lamellae after the tests. The lamellar thickness distribution curves calculated form the DSC data are presented in Fig. 14. Clearly, lamellar thickness increased as a result of the dynamic mechanical tests, however, the differences among the three orientations were not significant, especially for the 0° and 90° orientations. It is realized that the calculated lamellar thickness and its distribution based on the DSC data at this heating rate may not be precise, as concluded from a detailed investigation on this issue that will be published elsewhere, [25] however, the above statement about the *relative comparison* of lamellar thickness and its distribution for samples before and after the dynamic mechanical tests is valid.

Recalling the Tanδ data for precursor film obtained at the 0° and 90° orientations, which were presented in Fig. 5.10, they show the same peak height but occur at slightly different temperatures. The peak height of the dispersion is usually related to the concentration of mobile defects and the amount of crystalline phase, and the peak temperature has been noted to be shifted to larger values for the thicker crystalline lamellae. [30,31] From the DSC data, samples after the 0° and 90° oscillations showed basically the same change in heat of fusion (related to the amount of crystalline phase and defect concentration) and melting temperature (related to the thickness of the crystalline lamellae), and therefore the mechanical dispersion would have the same peak height and temperature as well. Although the same peak height was indeed observed in Figs. 5.10a and c, the expected same peak temperature was not observed. Therefore, it is believed that the

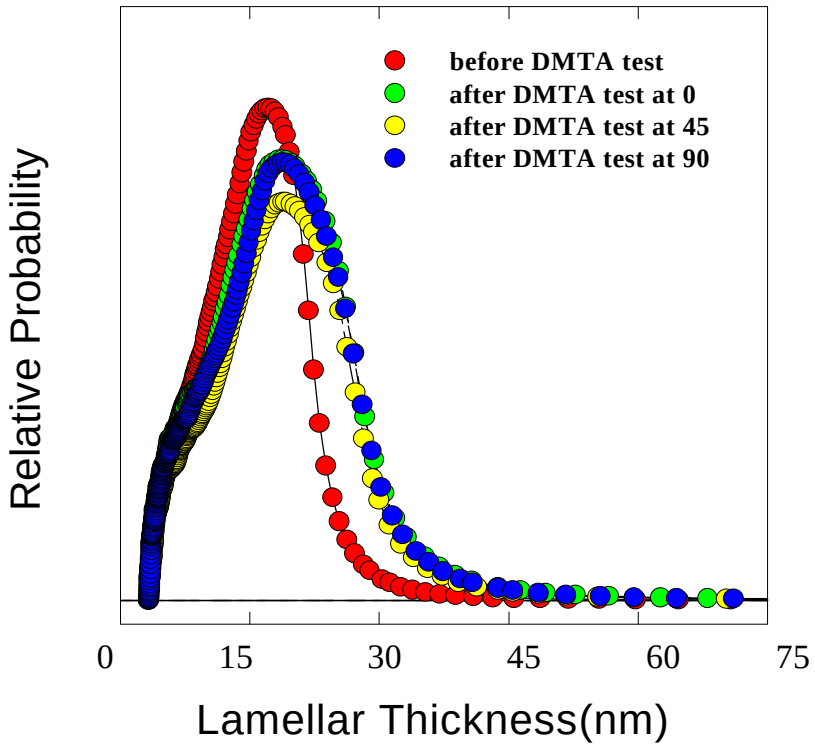

Figure 5.14 Lamellar thickness distribution calculated from the DSC data for the precursor film before and after the dynamic mechanical test at the 00°, 45° and 90° orientations.

difference of Tanδ for these two cases is not caused by the changes of morphology before and after the dynamic mechanical experiments; rather, it is mainly due to the different contributions from the α_I and α_{II} relaxations activated in the two different orientations.

For the 45° orientation, we have tentatively assigned the low temperature relaxation to an interlamellar shear process, which is caused by the frictional nature of the shear motion. Therefore, the possible effects of the morphological changes due to the tests should be related to the changes in the interfacial region, instead of only the amount of amorphous phase in the sample. This argument is supported by the data in Fig. 5.10b, where three films (precursor, free-annealed and tension-annealed) with different final percent crystallinity (61%, 70% and 76%) displayed the same low temperature relaxation peak (ca. 42 °C at 0.1Hz). We did not proceed further on this issue because of the limited knowledge at present about the crystalline lamellae/amorphous interface in this material.

It is worth pointing out that the interlamellar motion and/or dispersion have been proposed by many authors before, [7-22] but the activation energy of 88kJ/mol has not been reported previously. Obviously, the amount of shear motion is very limited for samples having spherulitic morphology and fibril morphology as compared to the samples having a stacked lamellar morphology under the 45 ° oscillation; therefore, it is not possible for the interlamellar shear dispersion to stand out as a major dispersion mechanism. In addition, as discussed above, the activation energy of the interlamellar shear dispersion is dependent on the nature of the crystalline/amorphous interface, which is not commonly addressed in the literature as well; thus, it is not surprising that the activation energies from different studies were not the same.

***Molecular origins of mechanical α relaxations*:** As pointed out earlier, the origin of the mechanical α relaxation has been extensively investigated, [1-4] and a number of molecular mechanisms have been proposed, including those that treat this relaxation as a property of the interior of the crystal and those that regard it mainly as arising from surface effects. [1-4] For the multiplicity of this relaxation, the basic assignments are 1) α_I is related to the interlamellar shear or intralamellar mosaic-block shear, and 2) α_{II} is related to the interchain motion in the crystalline phase due to the anisotropy of the crystalline lattice potential. In addition, according to some

authors, the multiplicity of the mechanical α relaxation is due to the distribution of crystalline lamellae thickness distribution, i. e., the different relaxation peaks correspond to the same molecular mechanism taking place in crystalline lamellae of different thickness. From our experiments, the same film showed distinctly different mechanical relaxation behavior by simply changing the direction of the dynamic oscillation with respect to the MD, regardless of the same lamellar thickness distribution at all the orientations before (same film) and after (0° and 90° orientations) the experiments. *This means that the change of Tanδ cannot result only from a distribution of lamellar thickness; rather, the anisotropy of the mechanical α relaxation is also directly related to different kinds of molecular mechanisms that are excited due to the different orientation of the oscillation direction.*

In this study, the α_{II} relaxation has been found more prominent at the 90 ° orientation than that at the 0° orientation. That is to say that the α_{II} relaxation is more clearly observed when the applied excitation is perpendicular to MD, i.e. the chain direction. These results are consistent with those obtained from the studies on the UHMwPE ultra-drawn fibers, where the α_{II} relaxation strength was found reduced with increasing draw ratio. [17-19] Therefore, the α_{II} relaxation is believed due to the extreme anisotropic nature of the crystal lattice potential of the crystalline phase. In this case, incoherent lattice vibrations (crystal disordering transition) at high temperature results in greater chain motion-either rotational motion about the c-axis or translational motion along the c-axis. [32,33]

It has been shown by others that interlamellar shear indeed promotes mechanical relaxation, but it is not the α_I relaxation *per se*. It is known that interlamellar shear is the origin of the β relaxation in low density polyethylene (LDPE), [29] and this β relaxation has even been postulated to correspond to the glass transition temperature of the amorphous portion in the LDPE. [34] Yet, for the case of HDPE, the same relaxation which might therefore correspond to the glass transition temperature of the amorphous portion in HDPE is hardly seen. Possible reasons for this are: 1) the amount of amorphous phase is limited, and 2) the glass transition temperature is a variable, [35] changing from the amorphous phase which is highly constrained such that the glass transition temperature is shifted to high temperatures (so-called T_{gU}) to the unconstrained core

amorphous phase which preserves a low glass transition temperature (so-called T_{gL}). The interlamellar shear in HDPE is an interfacial frictional event; unlike the case of the β relaxation in LDPE which corresponds to the amount of bulk amorphous phase, it is dependent upon the characteristics of the interface. It should be noted that the β relaxation has also been investigated by dynamic mechanical relaxation [36] as well as dielectric relaxation studies. [23] However, the activation energy for this β transition, which is calculated by the authors utilizing the Arrhenius equation, [23,36] was found to be *higher* than that of the α relaxation. Therefore, it is unlikely that such a β relaxation, denoted as β_a by the original authors, [23] is the same as that addressed in this study which is believed to be induced by interlamellar shear.

Thus, it is believed that the α_I process should be regarded as an intralamellar process. As proposed by Tagayanagi, et al, [8-10] the inter-crystal-mosaic-block shear is the origin for such a relaxation. It was further suggested by Kawai, et al. [37] that the intralamellar relaxation is associated with the reorientation of crystal grains within the crystalline lamellae about the a- and b-axes. However, it should be pointed out that the existence of a mosaic-block texture within the crystalline lamellae, as originally proposed based on the SAXS studies for fibers [38,39] has been questioned by some authors. [40,41]

5.5 Conclusions

Dynamic mechanical tests were carried out on melt-extruded uniaxially oriented HDPE films at different orientations with respect to the original MD which displayed anisotropy of the mechanical α relaxation. In addition, the morphology of the samples before and after the dynamic mechanical tests were also investigated. It was confirmed that the multiplicity of the mechanical α relaxation is indeed due to different molecular mechanisms rather than caused by the distribution of crystalline lamellar thickness. For the 0° and 90° orientations, the mechanical α_I and α_{II} relaxation processes were observed; whereas, for the 45 ° orientation, an interlamellar shear related relaxation was generated as well as the mechanical α_I relaxation. The α_{II} relaxation is believed to be a intracrystalline process, and it is related to the anisotropy of the crystal lattice

potential. The α_I relaxation is an intralamellar process and it is related to a grain-boundary motion within the crystalline lamellae. The interlamellar shear relaxation is related to the area and nature of the interface between crystalline lamellae and the amorphous phase.

References

1. McCrum, N. G , Reads, B. E, and G. Willams, Anelastic and Dielectric Effects in Polymer Solids, John Wiley & Son, New York, 1967
2. Boyd, R. H, *Polymer*, **1985,** 26, 1123
3. Boyd, R. H, *Polymer*, **1985,** 26, 323
4. Hoffman, J. D, Williams, G and Passaglia, E, *J. Polym. Sci., Part C,* **1966**, 14, 173
5. Stehling, F. C and Mandelkern, L, *Macromolecules,* **1970,** 3, 242
6. Illers, K. H, *Koll. Z. Z. Polym.*, **1979**, 261, 394
7. Nakayasu, H, Markovitz, H and Plazek, D. J, *Trans. Soc. Rehol.*, **1961,** 5, 261
8. Takayanagi, M and Matsuo, T, *J. Macromol. Sci., Phys.*, **1967,** B1, 407
9. Kajiyama, T, Okada, T, Sakoda, A and Tagayanagi, M, *J. Macromol. Sci.*, **1973,** B7(3), 583
10. Tagayanagi, M, *J. Macromol. Sci.*, **1974,** B9(3) 391
11. McCrum, N. G, and Norris, E. J, *Proc. Roy. Soc. Ser.*, **1966,** A292, 506
12. Buckley, C. P and N. McCrum, N. G, *J. Mater. Sci.*, **1973,** 8, 928
13. Yamada, R and Stein, R. S, *J. Appl. Phys.*, **1967,** 36, 3005
14. Takeuchi, A and Stein, R. S, *J. Polym. Sci., Polym. Phys. Ed.*, **1967,** 5, 1079
15. Stachurski, Z. H and Ward, I. M, *J. Macromol. Sci.*, **1969,** B3, 427
16. Stachurski, Z. H and Ward, I. M, *J. Macromol. Sci.*, **1969,** B3, 445
17. Matsuo, M, Sawatari, C and Ohata, T, *Macromolecules,* **1988,** 21, 1371
18. Ogita, T, Yamamoto, R, Suzuli, N and Mastuo, M, *Polymer*, **1991,** 32, 822
19. Ohta, Y and Yasuda, H, *J. Polym. Sci., Phys. Ed.*, **1994,** 32, 2241
20. Alberola, N, Cavaille, J. Y and Perez, J, *J. Polym. Sci., Phys. Ed.*, **1990,** 27, 569
21. Jourdan, C, Cavaille, J. Y and Perez, J, *J. Polym. Sci., Phys. Ed.*, **1989,** 27, 2361
22. Ampararo R. G and Ricardo, D. C, *J. Appl. Phys.*, **1987,** 34, 2819
23. Ashcraft, C. R and Boyd, R. H, *J. Polym. Sci., Polym. Phys. Ed.*, 1976, 14, 2153
24. Yu, Ta-hua and Wilkes, G. L, *Polymer*, **1996**, 37, 4675
25. Wlochowicz, A and Eder, M, *Polymer*, **1985,** 25, 1268

26. Hoffman, J. D, Miller, R. L, H. Marand and Roitman, D. B, *Macromolecules*, **1992,** 25, 2221

27. Zhou, Hongyi and Wilkes, G. L, *Polymer*, to appear

28. Grubb, D. T, *Materials Science Aand Technology, A Comprehensive Treatment*, Chapter 7, Vol 12, **1991**

29. Davies, G. R, Owen, A. J, Ward, I. M and Gupta, V. B, *J. Macromol. Sci., Phys.*, **1972,** B6(1) 215

30. Reneker, D. H and Mazur, J, *Polymer*, **1983,** 24, 1387

31. Reneker, D. H and Mazur, J, *Polymer*, **1982,** 23, 401

32. Okano, K, *J. Polym. Sci., Part C*, **1966,** 15, 95

33. Peterlin, A and Fischer, E. W, *Z. Physik.*, **1961,** 159, 272

34. Euns, J. B and Simha, R, *J. Macromol. Sci., Phys. Ed.*, **1977,** B13, 25

35. Boyer, R. F, *J. Macromol. Sci., Phys. Ed.*, **1973,** B8 (3-4), 503

36. Body, R. H, *Macrimolecules*, **1984**, 7, 903

37. Kawai, H, Suehiro, S, Kyu, T and Shimomura, A, *Polym. Eng. Rew.*, **1981,** 3-4, 110

38. Fisher E. W and Lorenz, R, *K. Z. Z. Polym.*, **1963,** 189, 97

39. Hosemann, R, Wilke, W and Calleja, F, J, B, *Acta Cryst.*, **1966,** 21, 118

40. Thomas, E, L, Sass, S, L and Kramer, E, J, *J. Polym. Sci., Phys. Ed.* **1974,** 12, 1015

41. Harrison, I, R, Keller, A, Sadler, D. M and Thomas, E, J, *Polymer*, **1976,** 17, 736

Chapter 6.0 CREEP BEHAVIOR OF HIGH DENSITY POLYETHYLENE FILMS HAVING WELL-DEFINED MORPHOLOGIES OF STACKED LAMELLAE WITH AND WITHOUT A ROW-NUCLEATED FIBRIL STRUCTURE *

Abstract

Creep behavior of melt-extruded high density polyethylene films having a stacked lamellar morphology (either with or without the visible presence of row-nucleated fibril structures) and hot-pressed slow-cooled isotropic films of the same resin was investigated. The creep experiments were carried out at different temperatures and stresses, and the orientation dependence of the creep behavior for the melt-extruded films was studied by performing the creep experiments at three angles (00°, 45° and 90°) with respect to the original machine direction. An Eyring-rate model was used to analyze the creep data, and the three parameters associated with the Eyring-rate model, i.e. activation volume, activation energy and population of creep sites, were obtained by fitting the plateau creep rate according to the Eyring-rate equation. It was concluded that the creep behavior of all the films was basically controlled by the deformation of the amorphous phase and, specifically, dependent upon the density and physical state of tie-chains in the amorphous region. The orientation dependence on the melt-extruded films was explained by the different populations of creep sites at each orientation.

* This chapter, formatted as required, will be submitted to *Journal of Polymer Science* for publication.

6.1 Introduction

Creep is the time-dependent strain (elongation) for a material under constant stress. For polymers, creep deformation is an important and powerful experimental method to study many physical properties such as viscoelastic behavior, physical aging, etc. On the other hand, creep is also a common phenomenon for engineering applications where products are under specific loadings, and the product's service life is a major concern. Therefore it is also critical to understand the origin of creep deformation and to be able to predict the long time creep behavior for a given polymeric material under specific conditions.

Various empirical relations have been proposed to describe the creep behavior of polymers.[1-24] In the early 1950's, the Andrade law, originally used for the high temperature creep behavior of metals, was applied to polymers in general.[1] The Andrade law states that a linear relationship exists between the creep strain and the elapsed loading time to the one third power. The slope and intercept of such a plot are related to the stress and temperature used in the experiment.[2] Today, this and other similar power law relations are still being used.[3-5] The major drawback for the power law relationships is that they do not have a fundamental basis. Furthermore, these relationships predict that the creep rate (defined as the derivative of the creep strain with respective to the loading time) at infinitely long loading time approaches to a value of zero. Practically, however, it has been found that in many cases, the creep rate reaches a plateau value before creep failure.[6]

Another general relationship that has also been used commonly for polymers is based on the rationalization that, due to their viscoelastic nature, the response of polymers to an external constant stress contains 1) an instantaneous elastic response, 2) a delayed (time-dependent) viscoelastic response, and 3) a permanent plastic response.[7-10] This idea has led to the following equation

$$\varepsilon(t) = \varepsilon_o + \varepsilon_q\left[1 - \exp\left(-\frac{t}{\tau}\right)\right] + \dot{\varepsilon}_p\, t \qquad (6.1)$$

where $\varepsilon(t)$ is the time-dependent creep strain at the elapsed loading time t, ε_o is the instantaneous strain due to the elastic response of the polymer, ε_q is a strain constant which is used, in conjunction with an exponential decay function with characteristic time τ, to describe the viscoelasticity, and $\dot{\varepsilon}_p$ is the plateau creep rate due to permanent plastic deformation. Based on equation 1, at very long loading times, the creep deformation is dominated by the plateau creep rate. This relation can also be coupled to the common four-element fluid mechanical analog often used in rheology and viscoelasticity of polymers.[5] However, no information regarding the molecular mechanisms of creep can be obtained from this approach.

It is certain that morphology plays an important role in affecting the creep behavior for a given polymer. For amorphous polymers, the Kohlrausch-Williams-Watts (KWW) relation, which states that compliance increases according to a stretched exponential function of time, has been widely used,[11] especially in the area of physical aging of glassy amorphous polymers.[12] However, the KWW relation is only valid for creep over limited periods of time at the start of glass transition.[13] It is also found that extrapolating creep data to longer times by using this relationship can cause large errors, even at temperatures below the glass transition temperature. [14]

Most amorphous polymers are found to be of thermorheologically simple at temperatures above the glass transition temperature; therefore, the time-temperature superposition principle has also been used in the creep study of amorphous polymers. [14-16] According to this principle, the long time creep data can be "obtained" by performing experiments at higher temperatures in shorter time scales for the same material. For semicrystalline polymers, however, due to the complex coupling between the crystalline phase and the amorphous phase (thermorheological complexity), the time-temperature superposition principle is generally not applicable. [17,18]

To address the complex dependence of creep behavior on stress, time and temperature, other relationships, which contains the effect of these variables, have been proposed. [19,20] One approach suggested that the creep strain has a power law dependence on both the loading time and applied stress but an exponential dependence on the temperature. [19] In this relationship, all the parameters have been expressed in simple and explicit functions, and there is also an activation energy term associated with it. However, there is no theoretical basis on which these

dependencies can be justified, and nor does it explains the plateau creep rate observed in many creep experiments.

Another approach to describe creep behavior has made use of the Eyring-rate model.[20] In this case, creep is considered to occur by flow-units, which may be polymer chains, segments of chains or groups of segments of chains, slipping over one another from one (metastable) position to another when stress is applied. The kinetics of this event can be expressed by the Eyring-rate model. In other words, creep is due to a molecular motion that takes place within a specific volume passing over an energy barrier. The plateau creep rate is considered to be a function of stress, time and temperature, as shown by the Eyring-rate equation

$$\dot{\varepsilon}_p = \dot{\varepsilon}_p \exp\left(-\frac{U}{kT}\right)\sinh\left(\frac{V\sigma}{kT}\right) \qquad (6.2)$$

where V is the activation volume, U is the activation energy, σ is the applied stress, $\dot{\varepsilon}_p$ is the plateau creep rate, $\dot{\varepsilon}_o$ is a pre-exponential factor which is related to the population of creep sites (availability of event sites). The merit of this approach is that the creep behavior can now be coupled with some molecular features of given polymers, such as chain chemistry, molecular weight and its distribution, morphology, etc, which affect the mobility of chains and/or chain segments.

In the development of high modulus polyethylene fibers, particularly ultra-high molecular weight polyethylene (UHMWPE) fibers, the creep behavior has been found to be a major shortcoming that limits the applications of these fibers. [21-25] Thus, the creep behavior of these fibers has been investigated extensively, especially by using the Eyring-rate approach, and a creep model consisting of two thermally activated Eyring-rate processes has been proposed by Ward, et al.[21-25] According to this model, the creep behavior of these fibers is controlled by two Eyring-rate processes. One process has been attributed to the contribution from the crystalline phase, and it is dominant at a high stress level. The other process has been attributed to the contribution from the amorphous network, and it dominates at a low stress level. Here, the critical stress which divides the high and low stress level is 0.2GPa for samples used by Ward, et al. in their investigations. [22,23] Furthermore, the higher stress process has also been regarded as the same mechanism as that of

the mechanical α relaxation in linear polyethylene, and the creep mechanism has been regarded as a chain-to-chain slip process in the crystalline phase. The lower stress process, on the other hand, was speculated due to the deformation of the amorphous network in the material.

Given the long history of creep studies of polymers, there is still an apparent absence of a full understanding of the creep mechanisms, especially for semicrystalline polymers. There have been some creep studies with a specific focus on the melt or solution spun high or ultra high molecular weight polyethylene fibers.[9,21-25] There have also been limited amount of creep studies on other kinds of polymeric fibers based on aromatic chemistry (e.g. PEEK).[26,27] In these investigations, the materials tend to possess a highly oriented extended-chain type fibril morphology. Therefore, the creep behavior noted for these fibers are expected to be somewhat different from those for general semicrystalline polymers having a spherulitic morphology.

In this study, the creep behavior of melt-extruded high density polyethylene (HDPE) films having a well-defined stacked lamellar morphology, either with or without a distinct presence of row-nucleated fibril structure, were investigated. The creep experiments were carried out at different angles with respect to the machine direction of the films at different temperatures as well as under different applied stresses. The creep behavior of unoriented samples of the same HDPE resins were also investigated. It is our hope that by doing a thorough investigation on materials having well-defined morphologies, the corresponding creep mechanisms can be better understood. In addition, by comparing the data for the same materials with different morphologies, i.e., the stacked lamellar morphology (either with or without row-nucleated fibril structure) and spherulitic morphologies, a more complete understanding of the creep behavior for semicrystalline polymers can be obtained.

6.2 Experimental

Materials: Two HDPE resins were used in this study. They have the same number average molecular weight of 14,500g/mol, but different weight average molecular weight of

150,000g/mol (Resin 1) and 290,000g/mol (Resin 2). The 1 mil thick melt-extruded and highly oriented HDPE films of both resins were provided by Hoechst Celanese Co. The extruded film of Resin 1 (designated as Pre-1 film) has a well-defined stacked lamellar morphology, and the crystalline phase is uniaxially oriented with the polymer chains preferentially aligned along the machine direction (MD). This was quantified by determination of the Hermans' orientation function, f_c, for the crystalline phase using wide angle X-ray scattering (WAXS), where f_c is defined as

$$f_c = \frac{1}{2}(3 < \cos^2\theta > -1) \qquad (6.3)$$

In equation 6.3, the quantity $<\cos^2\theta>$ represents the average value of $\cos^2\theta$, with θ being the angle between the c-axis in the crystal (chain axis direction) and the MD. The amorphous phase, however, was essentially in a random state, as noted previously.[28] The extruded film of Resin 2 (designated as Pre-2 film) has the presence of a distinct row-nucleated fibril structure in addition to the well stacked crystalline lamellae. The f_c values calculated form the WAXS patterns for the Pre-1 and Pre-2 films were 0.67 and 0.71, respectively. A detailed investigation on the orientation state of the crystalline phase and the amorphous phase of the melt-extruded films of Resin 1 and Resin 2 has been published elsewhere.[28] In addition, an unoriented(isotropic) compression modeled slow-cooled film (ca. 4 mil thick) of Resin 1 was also investigated in this study, and this film is designated as HP-1 film.

***Transmission Electron Microscopy*:** For the TEM study, samples of the melt-extruded films of Resin1 and Resin 2 were treated by chlorosulfonic acid at 60°C for 6 hours; then, they were washed with sulfuric acid and water and dried overnight. The stained samples were embedded in an epoxy resin and cured at 65 °C overnight. The embedded samples were microtomed at room temperature by cutting along the MD. The microtomed thin sections of ca. 80nm thick were used for the TEM observations after being treated by uranyl acetate. All the TEM work was performed by using a Philips EM420 instrument operated at 100kV.

***Wide Angle X-ray Scattering*:** All the WAXS experiments were performed by utilizing a Philips tabletop X-ray Generator (Model PW1720) equipped with a standard vacuum-sealed

Warhus photographic pinhole camera. The instrument with a CuKα radiation (λ=1.54Å) was operated at 40KV and 20mA. Stacks of 16 layers of films were used for each specimen for the WAXS experiments, and the exposure time used was ca. two hours.

Tensile Tests: The stress-strain curves for all the samples of melt-extruded films were obtained by using an Instron (4400 model) at ambient conditions. Dogbone shape samples of 23mm x 8mm were stretched at a cross-head speed of 15mm/min. For the Pre-1 and Pre-2 films, the samples were cut at three different angles, 0°, 45° and 90°, with respect to the original MD, and they are denoted as 0° stretch, 45° stretch and 90° stretch, respectively.

Creep experiments: Dead-load type creep experiments was carried out by using a Seiko TMA100 instrument operating in a tensile mode. The samples for the creep experiments were rectangular stripes cut with a die of 3.2mm wide and 25mm long at the same three angles (0°, 45° and 90°) with respect to the original MD, and the creep experiments at these orientations are denoted as 0° creep, 45° creep and 90° creep, respectively. A different sample was used for each individual creep experiment to prevent the influence of permanent plastic deformation due to a previous loading for the sample. A sample strip was fixed within sample chucks, and then inserted into a quartz probe through which a tensile load was applied to each sample. A small initial load of 3g was applied to make sure that the sample was "straightened out". After the temperature reached the selected temperature and stabilized, which could be controlled to ±0.3 °C, a designated creep load was applied to the sample for more than four hours (250min). The selected temperatures were 30, 40, 50, and 60 °C which cover a portion of application temperature region for HDPE products. Five load levels, 10, 20, 40, 60, and 80g, were used in the experiments *to ensure that the initial strains of the samples were below the corresponding yield strains.* The elongation of the samples during the creep experiments (TMA) were monitored by a LVDT attacked to the quartz probe. In addition, a differential signal (DTMA) was also collected. Approximately thirty percent of the total creep experiments were duplicated, and the data showed good reproducibility for the selected temperature and load region.

6.3 Results

The TEM micrographs and WAXS patterns for the Pre-1 and Pre-2 films are presented in Figs. 6.1 and 6.2, respectively. The well-oriented and well-defined stacked lamellae for the Pre-1 film and the distinguishable amount of row-nucleated fibril structure in the matrix of stacked lamellae for the Pre-2 film are clearly revealed. The WAXS patterns confirmed the uniaxially oriented state for the crystalline lamellae in these films, with the (110) and (200) reflections more or less concentrated towards the equatorial region of the scattering patterns. The existence of two high intensity scattering spots that superimposed with the (110) and (200) reflections in the equatorial region for the Pre-2 film corresponds to the row-nucleated fibril structure in the material; whereas no such scattering spots were found for the Pre-1 film, which is in agreement with the TEM observations. It needs to be pointed out that the calculation of the crystalline orientation function for Resin 2 did not take into account the high intensity reflection spots from this second population of very highly oriented fibril crystals.

Stress-Strain Behavior: The stress-strain curves for the Pre-1 and Pre-2 films are shown in Figs. 6.3a and b. As expected, these curves showed a distinct orientation dependence of the stress-strain behavior of these films- in terms of modulus, yielding behavior, cold drawing, strain hardening, and fracture. A detailed investigation on the deformation process of the Pre-1 and Pre-2 films is underway and will be published in the future. Here, only those features that are related to the creep study are pointed out.

For the 00° stretch, both films had a large degree of strain hardening after yielding (a deviation from the initial linearity), and no necking was found in the entire strain range, although strain whitening did occur even before the yield point, which is caused by the splaying of the stacked lamellae. For the 90° stretch, yielding (the sharp local yield peak) took place at a very small strain (ca. 4%) and is associated with the formation of a sharp neck with boundaries perpendicular to the stretching direction. Following yielding, the samples displayed extensive cold drawing by the expansion of the neck along the samples' length. Also noticed is the uneven

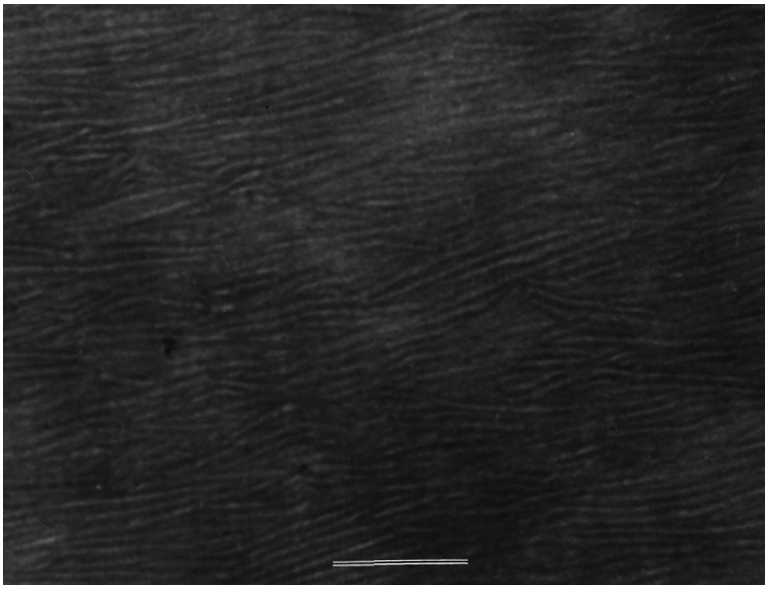

(a)

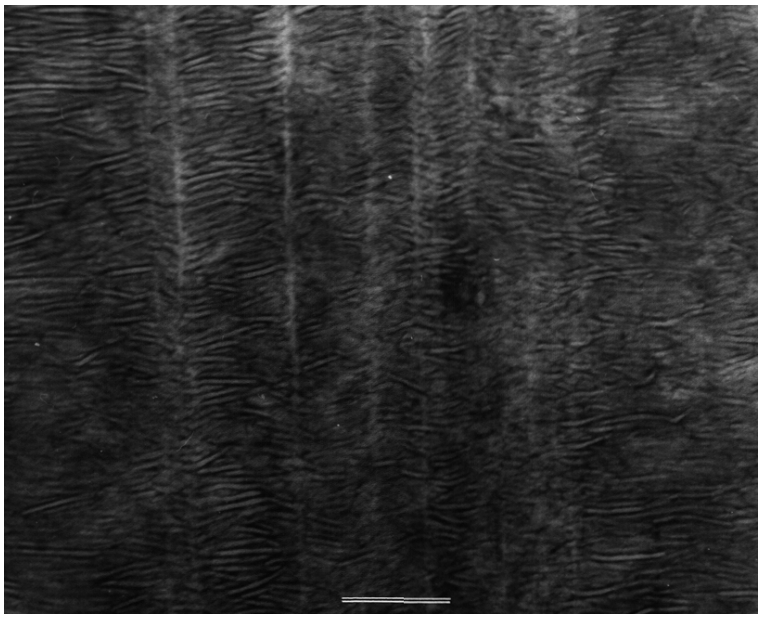

(b)

Figure 6.1 TEM micrographs showing the stacked lamellae for the Pre-1 film (a) and the distinct presence of row-nucleated fibril structures for the Pre-2 film. Scale bars represent 1μm.

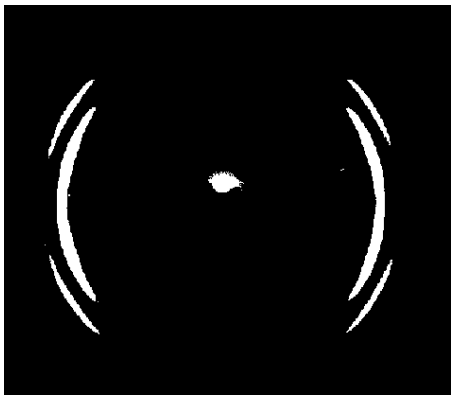

a

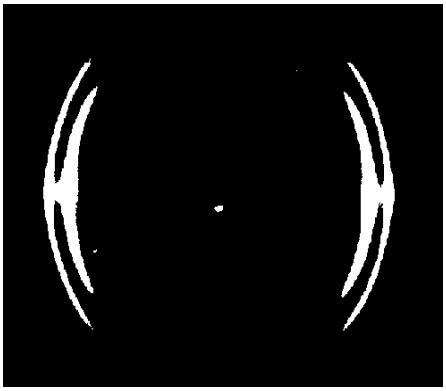

b

Figure 6.2 WAXS patterns showing the high crystalline oriented state for the Pre-1 films (a) and Pre-2 film (b). The MD is vertical.

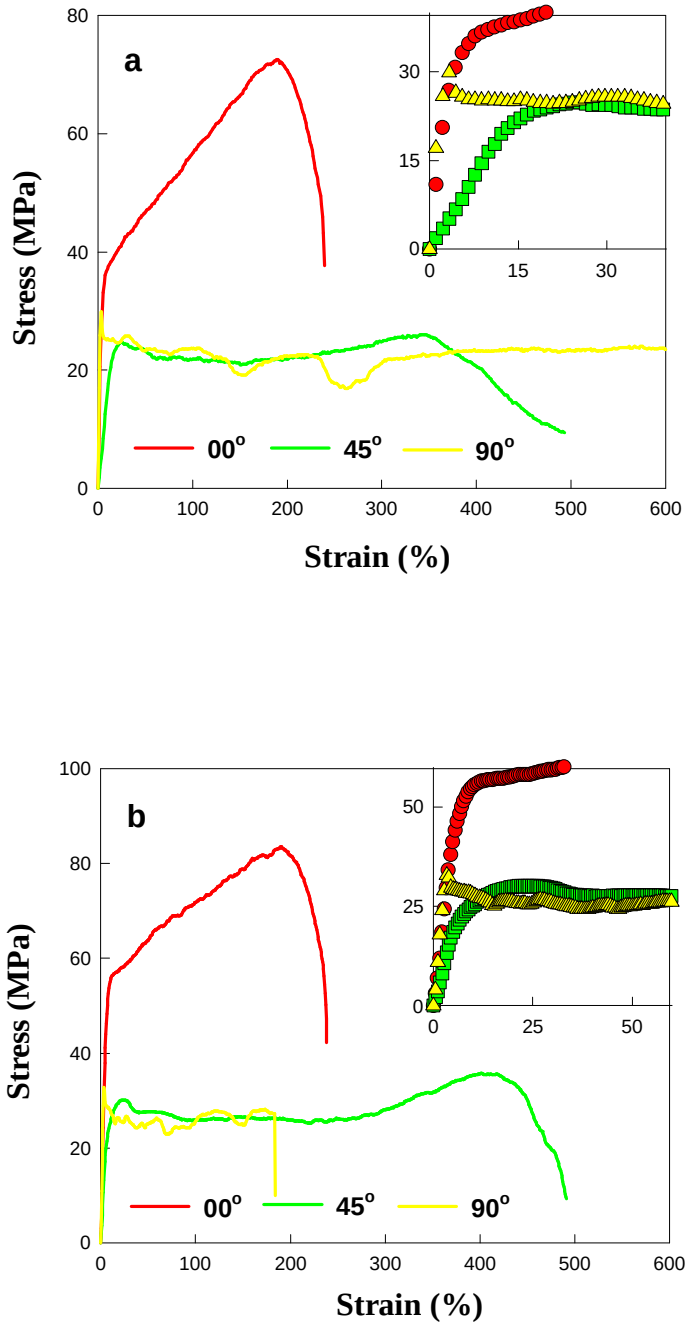

Figure 6.3 Stress-strain curves for the Pre-1 (a) and Pre-2 (b) films.

features of the stress-strain curves. The stress-strain curves for the 45° stretch look more typical for unoriented semicrystalline polymers with a spherulitic morphology- with yielding (the well-defined local maximum in the stress-strain curve), strain softening, cold drawing, strain hardening, and failure. In this case, yielding took place by the formation of a neck with boundaries at ca. 45° with respect to the stretching direction and perpendicular to the MD (extrusion direction of the original films).

Creep Behavior: The creep curves for the Pre-1 film at 30°C under different stresses and at three orientations (0°, 45° and 90°) are presented in Figs. 6.4a, b and c, in which the creep strain is plotted against time in logarithmic scale. For these curves, the open symbols were experimental data points, and the solid lines were drawn based on a best fit according to equation 6.1. At each orientation, a higher stress resulted in a larger initial creep strain and a larger creep rate (upward curvature at the end of the creep curves). At the same stress level, samples at different orientations with respect to the MD also showed different amount of initial creep strains and plateau creep rates, with the 90° orientation being the least, followed by the 00° and finally the 45° orientation.

In order to show the plateau creep rate for the above creep curves, the same set of data were re-plotted against time on a linear scale and are shown in Figs. 6.4d, e and f. Furthermore, the DTMA data, which is related to the creep rate, were also utilized for this purpose - as shown in Figs. 6.4g, h and i, where creep rate (calculated from the DTMA data) are plotted against the creep strain. The open symbols and solid lines in these curves have the same meaning as mentioned previously. It can be clearly seen that at long loading times, a plateau creep rate is indeed achieved for each individual creep experiment. Additionally, it can be seen that the curve fit according to equation 6.1 is quite good in terms of providing values for *creep rate at longer times*, although this model is not a good approximation at the earlier stage of the creep experiment. The creep rate used hereafter was obtained from the best fit according to equation 6.1.

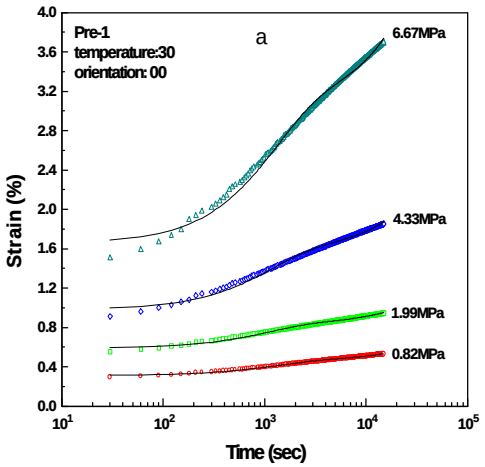
a
Pre-1
temperature:30
orientation: 00
6.67MPa
4.33MPa
1.99MPa
0.82MPa
Strain (%)
Time (sec)

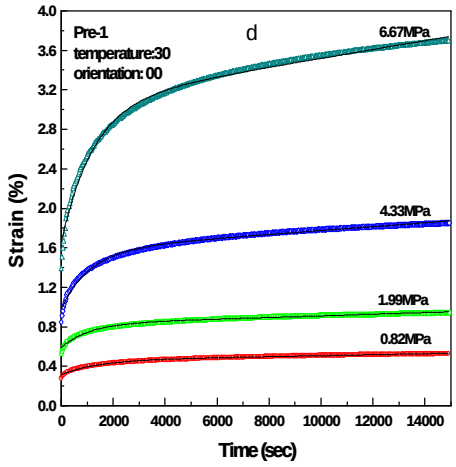
d
Pre-1
temperature:30
orientation: 00
6.67MPa
4.33MPa
1.99MPa
0.82MPa
Strain (%)
Time (sec)

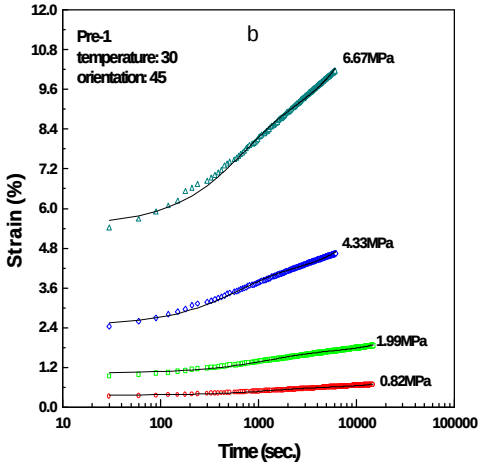
b
Pre-1
temperature: 30
orientation: 45
6.67MPa
4.33MPa
1.99MPa
0.82MPa
Strain (%)
Time (sec.)

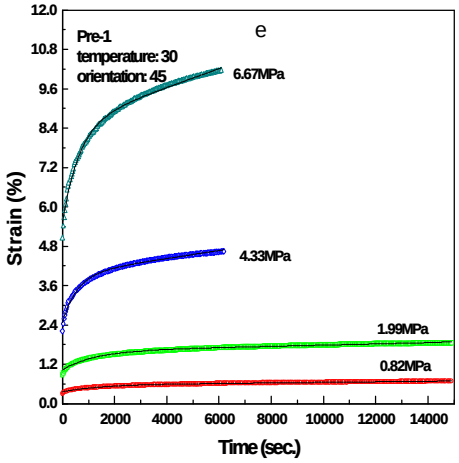
e
Pre-1
temperature: 30
orientation: 45
6.67MPa
4.33MPa
1.99MPa
0.82MPa
Strain (%)
Time (sec.)

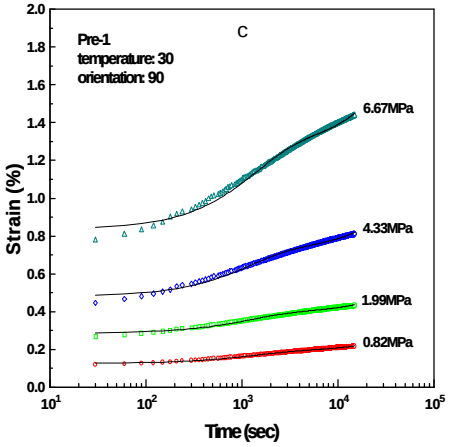
c
Pre-1
temperature: 30
orientation: 90
6.67MPa
4.33MPa
1.99MPa
0.82MPa
Strain (%)
Time (sec)

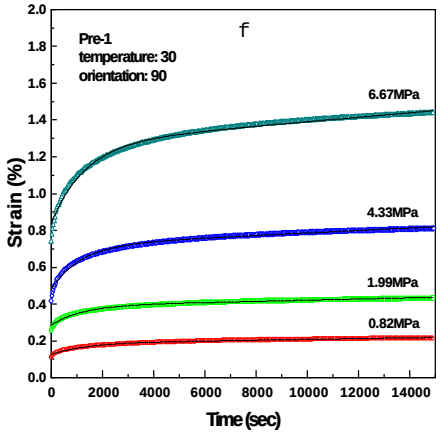
f
Pre-1
temperature: 30
orientation: 90
6.67MPa
4.33MPa
1.99MPa
0.82MPa
Strain (%)
Time (sec)

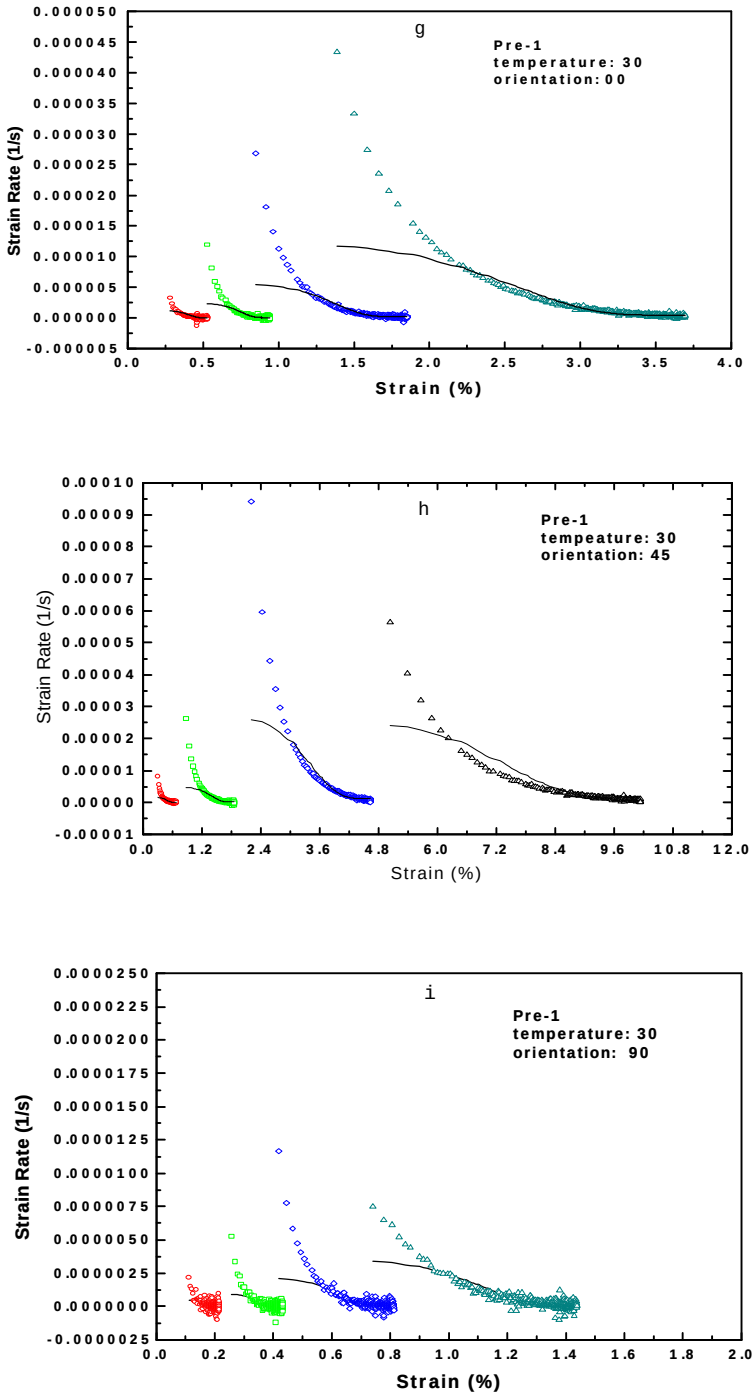

Figure 6.4 TMA data (a-c: semilograthmic plot and d-f: linear plot) and DMTA (g-i) for the Pre-1 film at 30°C and the three orientations of 00 °, 45° and 90°.

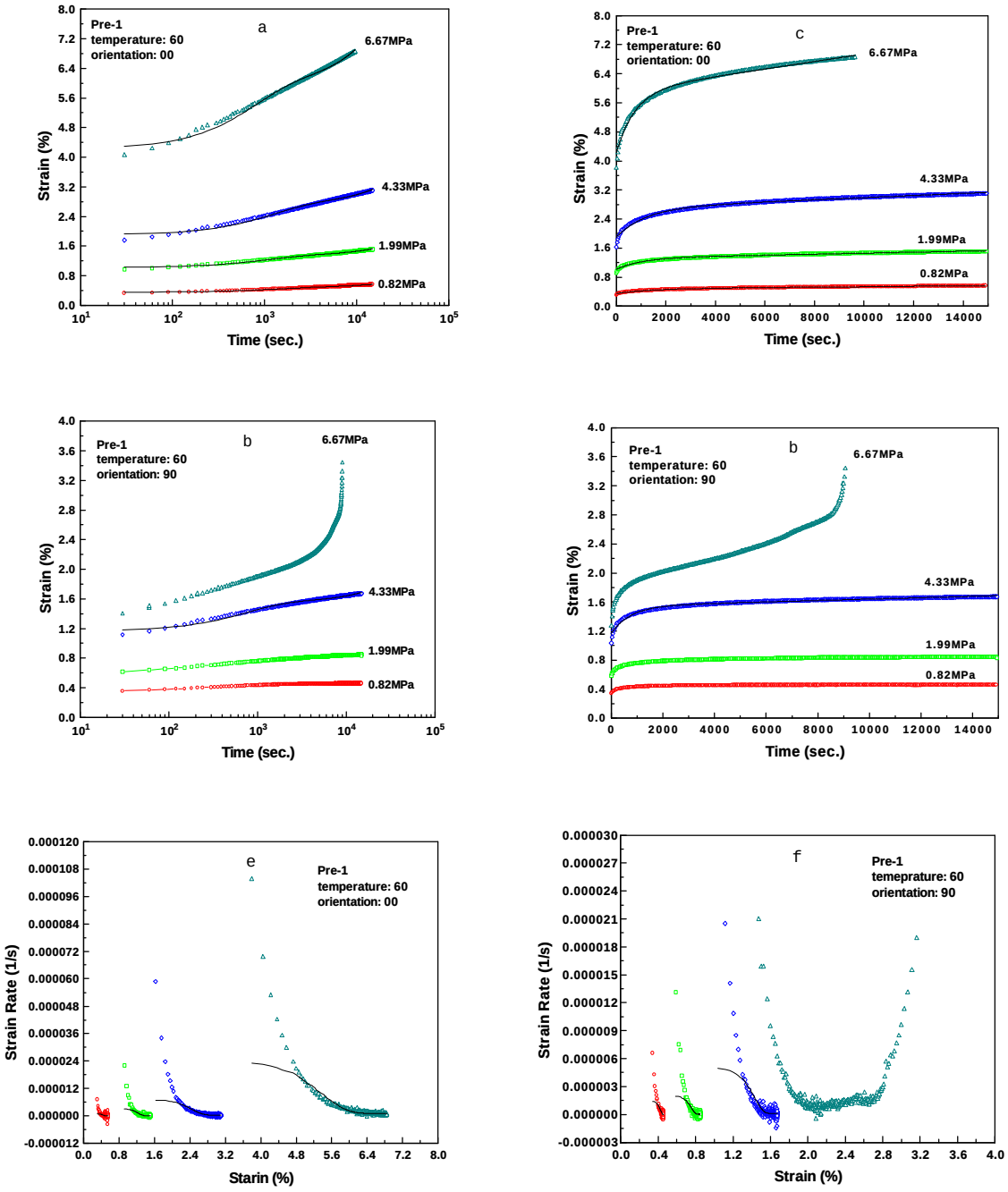

Figure 6.5 TMA data (a and b: semilograthmic plot and c, and d: linear plot) and DMTA (e and f) for the Pre-1 film at 30°C and the orientations of 00 ° and 90°.

The creep curves for the Pre-1 film at 60° under different stresses and at the 00° and 90° orientations are shown in Figs. 6.5a and b. The creep strain for the 45° orientation at this high temperature, as well as at 40°C and 50°C, was too large to be accurately measured by the TMA instrument used in this study and therefore are not available. Again, a higher stress resulted in a larger creep strain and creep rate as expected. At the same stress level, the creep strain for the 90 ° orientation is less than that for the 00° orientation, and so is the creep rate. Furthermore, in the case of 90° creep, a neck developed during the creep experiment at the highest stress level used; when this occurs, the creep curve dramatically undergoes a rapid rise. The creep rate, either from the fitting according to equation 6.1 or calculated from DTMA data, are presented in Figs. 6.5c and d for the respective 00° and 90° creep. Again, the validity of fitting at *longer time* is confirmed. For the 90° creep at 80g load (6.67MPa stress), fitting was not performed due to the presence of the significant rise of creep rate at the end of the experiment, as shown in Figs. 6.5b and d.

Similar plots for the creep response of the Pre-2 film at 30°C and 60°C are presented in Figs. 6.6 and 6.7, and the data show essentially the same trend as explained above for the case of the Pre-1 film. Figures. 6.8 and 6.9 present the same type of plots for the HP-1 film, which possesses no molecular orientation. Since the thickness of the isotropic hot-pressed film is about four times larger than that of the melt-extruded films, and the maximum load used in the creep experiment is limited by the TMA instrument (100g is the maximum load), the stresses for the hot-pressed film were less than that for the melt-extruded films.

Creep parameters obtained form the Eyring-rate equation: The three parameters, namely activation volume (V), activation energy (U), and pre-exponential factor ($\dot{\varepsilon}_o$) which indicates the population of creep sites, in the Eyring-rate equation were obtained by fitting the creep rates to equation 6.2. The creep rates (obtained by the best fit according to equation 6.1) at

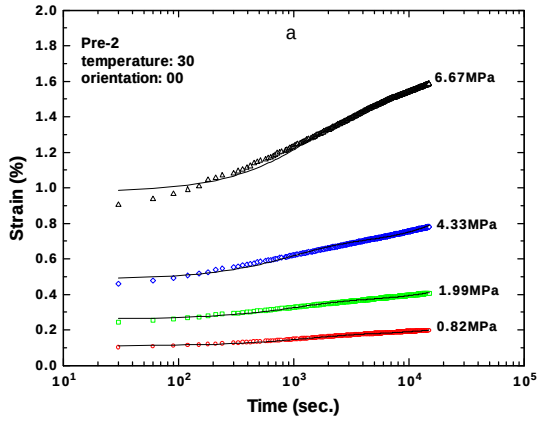
a
Pre-2
temperature: 30
orientation: 00
6.67MPa
4.33MPa
1.99MPa
0.82MPa
Strain (%)
Time (sec.)

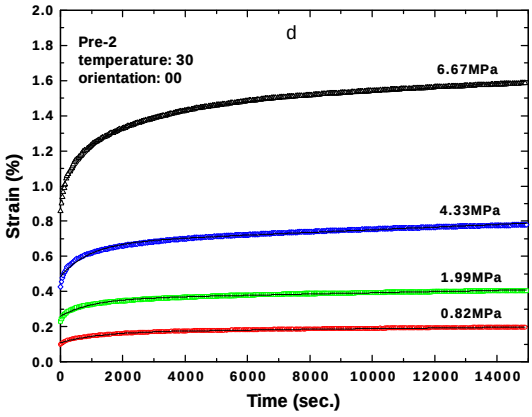
d
Pre-2
temperature: 30
orientation: 00
6.67MPa
4.33MPa
1.99MPa
0.82MPa
Strain (%)
Time (sec.)

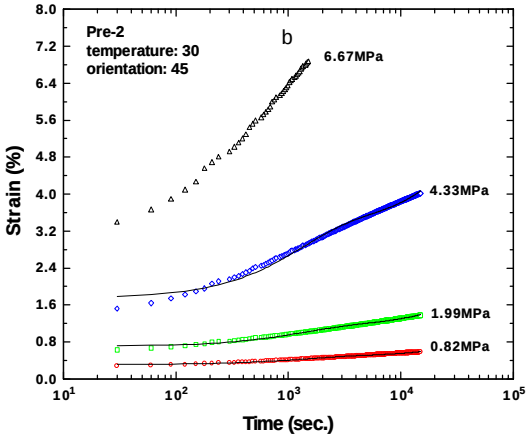
b
Pre-2
temperature: 30
orientation: 45
6.67MPa
4.33MPa
1.99MPa
0.82MPa
Strain (%)
Time (sec.)

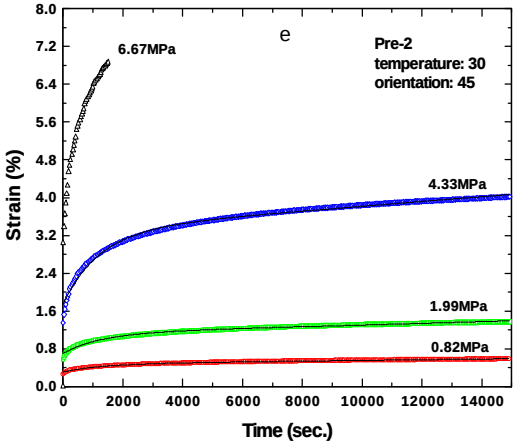
e
Pre-2
temperature: 30
orientation: 45
6.67MPa
4.33MPa
1.99MPa
0.82MPa
Strain (%)
Time (sec.)

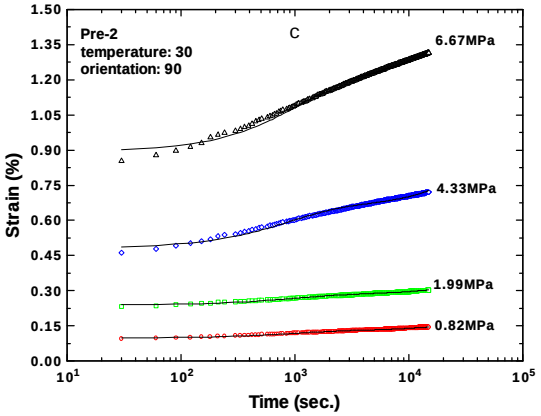
c
Pre-2
temperature: 30
orientation: 90
6.67MPa
4.33MPa
1.99MPa
0.82MPa
Strain (%)
Time (sec.)

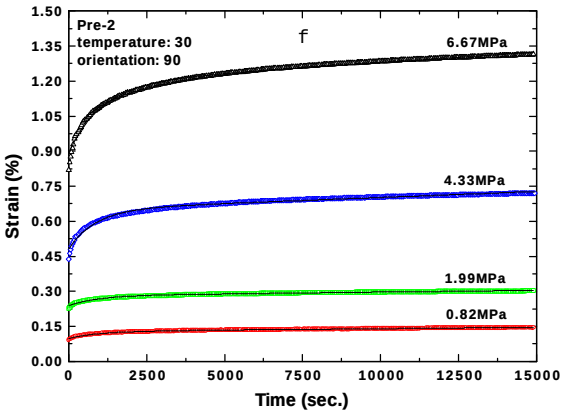
f
Pre-2
temperature: 30
orientation: 90
6.67MPa
4.33MPa
1.99MPa
0.82MPa
Strain (%)
Time (sec.)

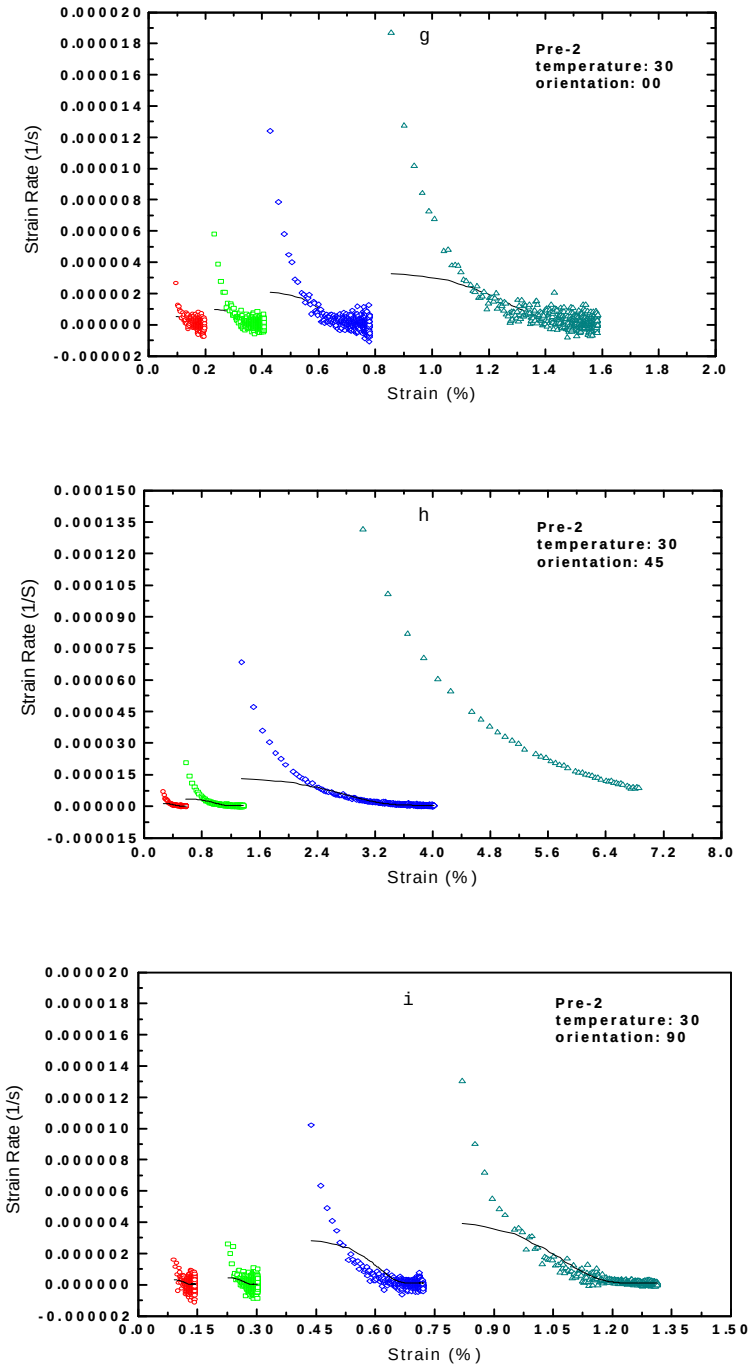

Figure 6.6 TMA data (a-c: semilograthmic plot and d-f: linear plot) and DMTA (g-i) for the Pre-2 film at 30°C and the three orientations of 00 °, 45° and 90°.

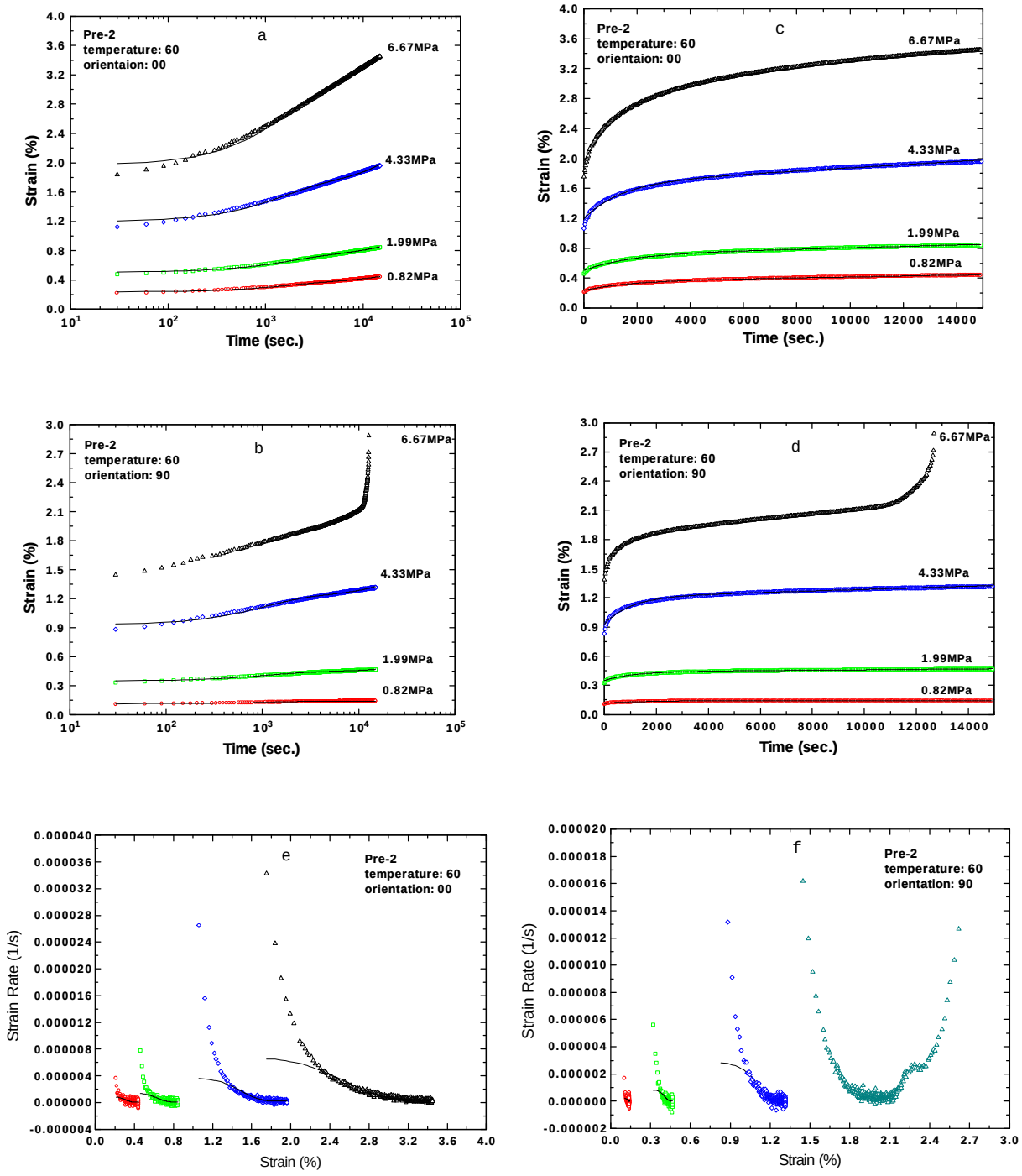

Figure 6.7 TMA data (a and b: semilograthmic plot and c, and d: linear plot) and DMTA (e and f) for the Pre-2 film at 30°C and the orientations of 00 ° and 90°.

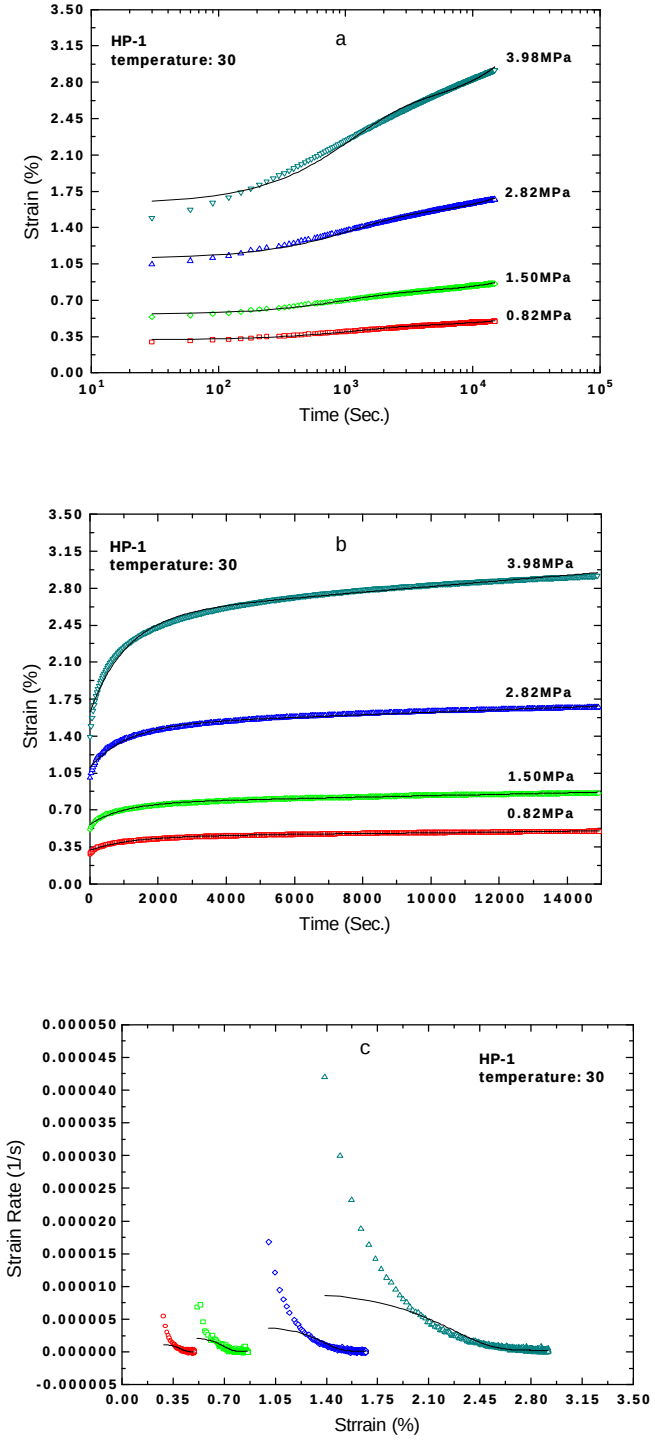

Figure 6.8 TMA (a: semilogarithmic plot and b: linear plot) and DTAM (c) data for the HP-1 film at 30°C.

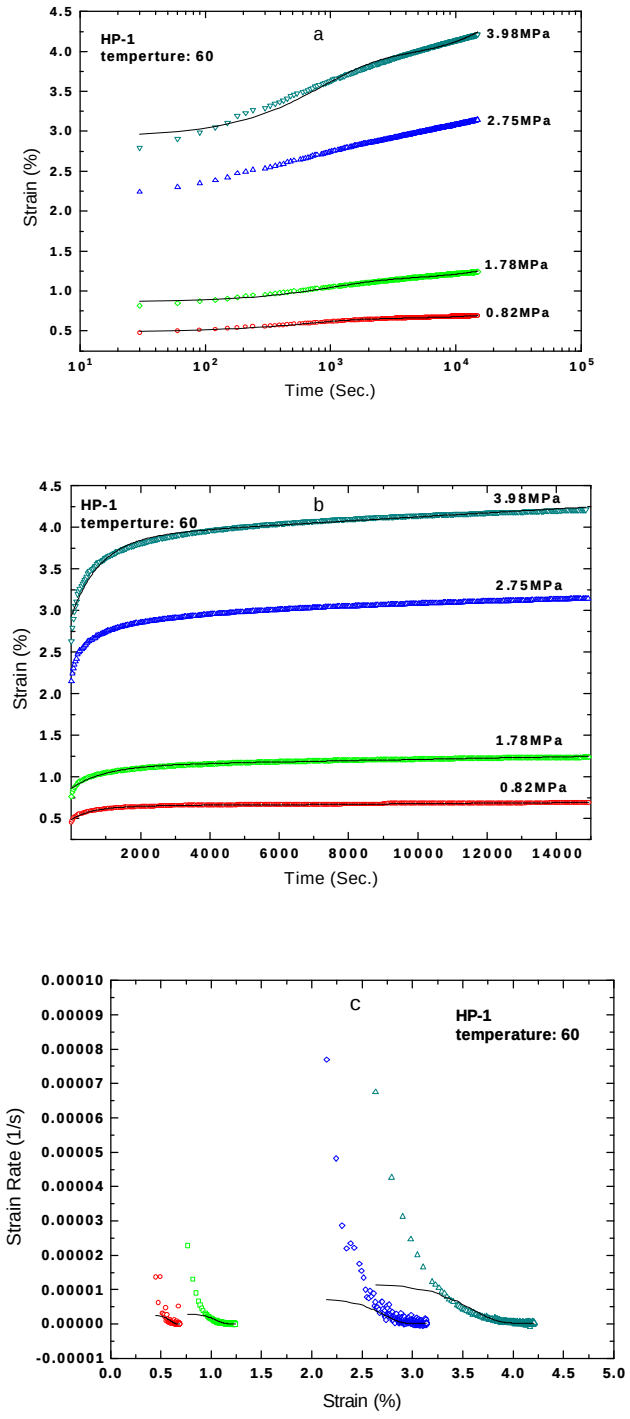

Figure 6.9 TMA (a: semilogarithmic plot and b: linear plot) and DTAM (c) data for the HP-1 film at 60°C.

different temperatures, stresses, and loading orientations with respect to the MD were obtained by the best fit based on equation 6.1. Similar kind of fitting has been done in the creep studies for HDPE fibers studied by Ward, et al.[21-23] and UHMWPE fibers by Pennings.[24] In their cases, since the applied stress was on the order of a GPa and the value of $\sigma V/kT$ is usually larger than 3, [21-25, 29] the parabolic sine function was simplified as a exponential function. In our study, however, the applied stress in the creep experiments is on the order of a MPa; therefore, the exact expression of the parabolic sine function has to be utilized.

The fitting procedures can be illustrated by using the Pre-1 film as an example: Activation volume (V) was obtained by fitting the creep rate at the same temperature but different stress (a-c) to equation 6.2, and the values shown in these figures are the average values at different temperatures. The activation energy (U) was obtained by plotting the creep rate (in logarithmic scale) versus reciprocal temperature (d and e) at different stress levels, and the values shown in these plots are the average values at different stresses. The fitting for $\dot{\varepsilon}_o$ was performed by plotting the creep rate (in logarithmic scale) against log(exp(-U/kT)sinh($\sigma V/kT$)) (f and g). The results for the best fits for V, U and $\dot{\varepsilon}_o$ for the melt-extruded and hot-pressed films are listed in Table 6.1. The parameters of U and $\dot{\varepsilon}_o$ for the 45° creep for the Pre-1 and Pre-2 films were not possible to determine due to the lack of creep data at temperatures higher than 30 °C.

6.4 Discussion

Creep behavior of the melt-extruded HDPE films: It has been mentioned earlier that the samples at different orientations with respect to the MD displayed different creep behavior. Shown in each of Figs. 6.11a and 11b are three creep curves for the Pre-1 and Pre-2 films under the stress of 0.82MPa and at a temperature of 30°C for the 00°, 45° and 90° orientations. The major differences between these curves are the initial strain and the plateau creep rate, which will be addressed separately.

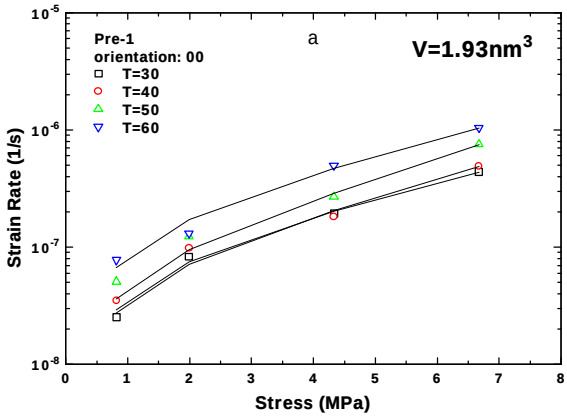
Pre-1
orientation: 00
T=30
T=40
T=50
T=60
a
V=1.93nm3
Strain Rate (1/s)
Stress (MPa)

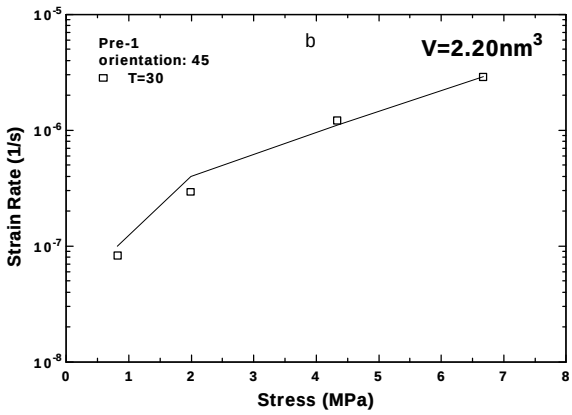
Pre-1
orientation: 45
T=30
b
V=2.20nm3
Strain Rate (1/s)
Stress (MPa)

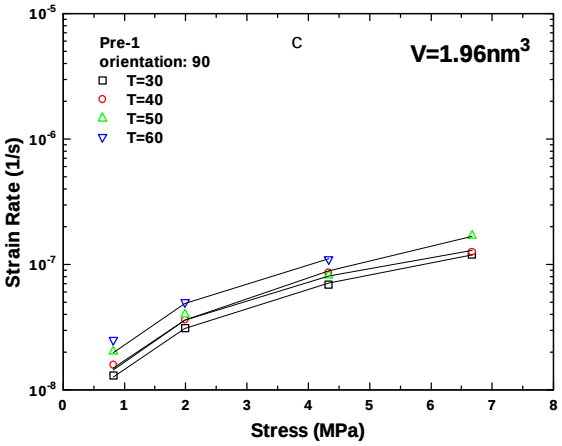
Pre-1
orientation: 90
T=30
T=40
T=50
T=60
c
V=1.96nm3
Strain Rate (1/s)
Stress (MPa)

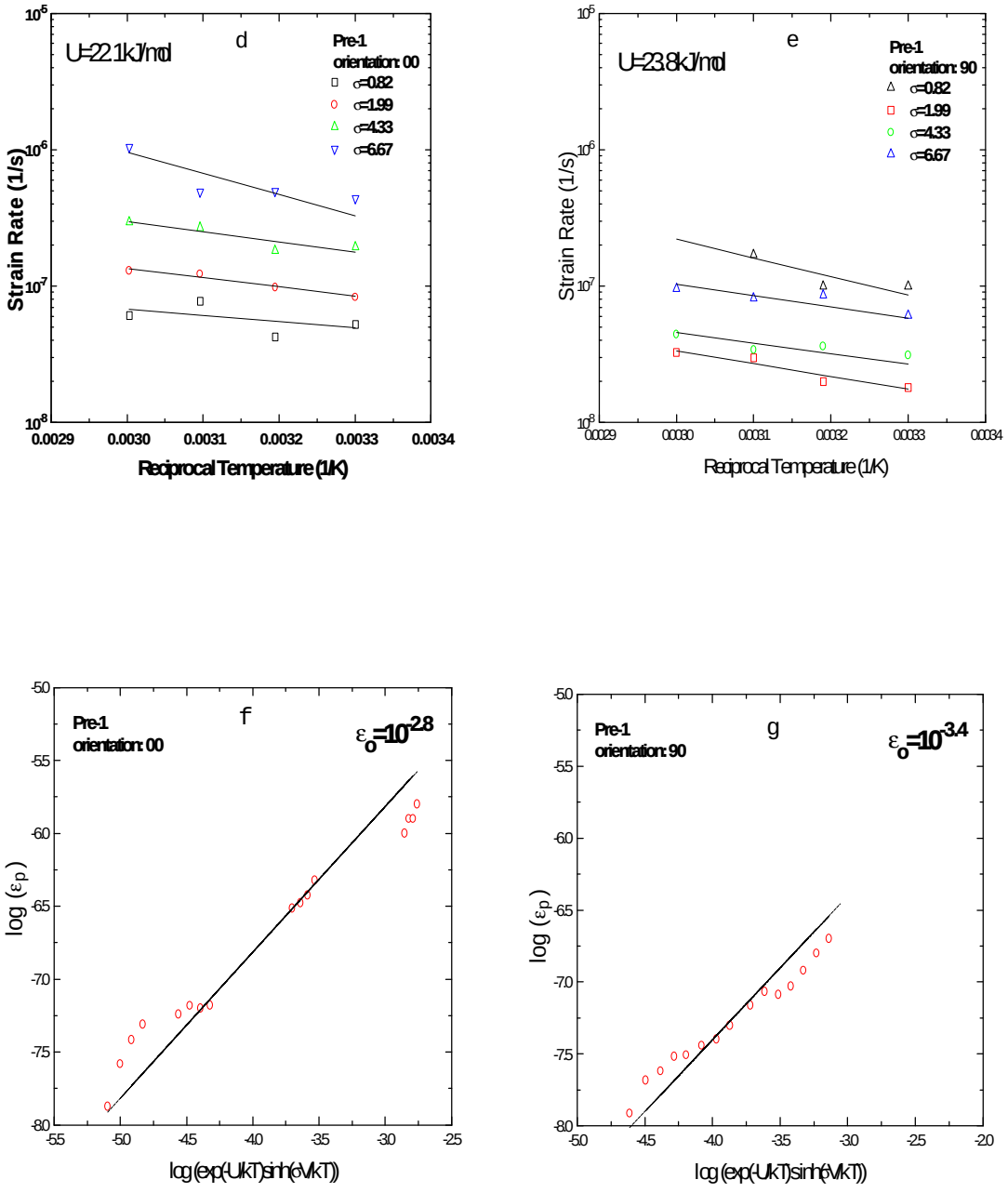

Figure 6.10 Parameters associated with the Eyring-rate equation, activation volume (a-c), activation energy (d, e) and populations of creep sites (f, g) for the Pre-1 film.

Table 6.1 The creep parameters obtained by using Eyring-rate equation for the Pre-1, Pre-2, and HP-1 films.

Parameters	Pre-1			Pre-2			HP-1
	00°	45°	90°	00°	45°	90°	
V (nm^3)	1.93±0.28	2.20±0.34	1.92±0.31	1.52±0.26	1.71±0.30	1.56±0.28	1.93±0.4
U (kJ/mol)	22.1± 2.5		23.8±2.8	25.1±2.9		28.3±2.2	5±0.48
$\dot{\varepsilon}_o$ (10^{-3})	1.59		0.4	2.0		0.3	0.008

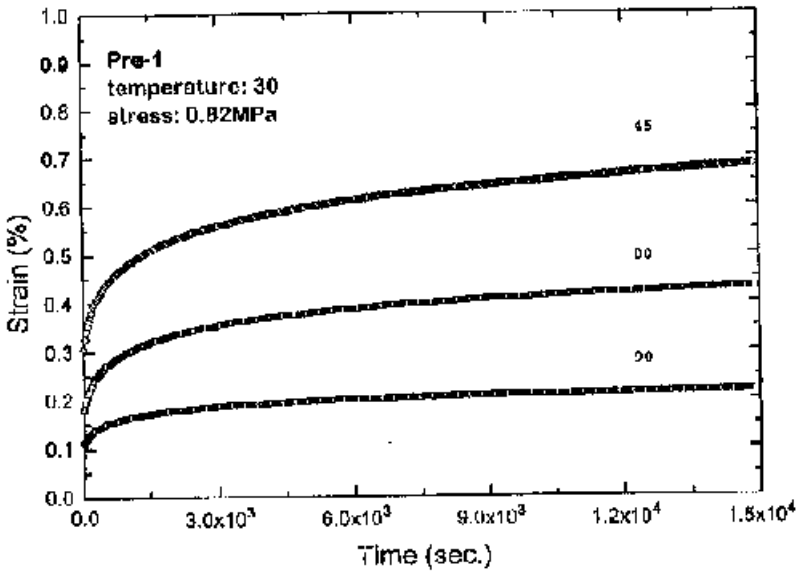

a

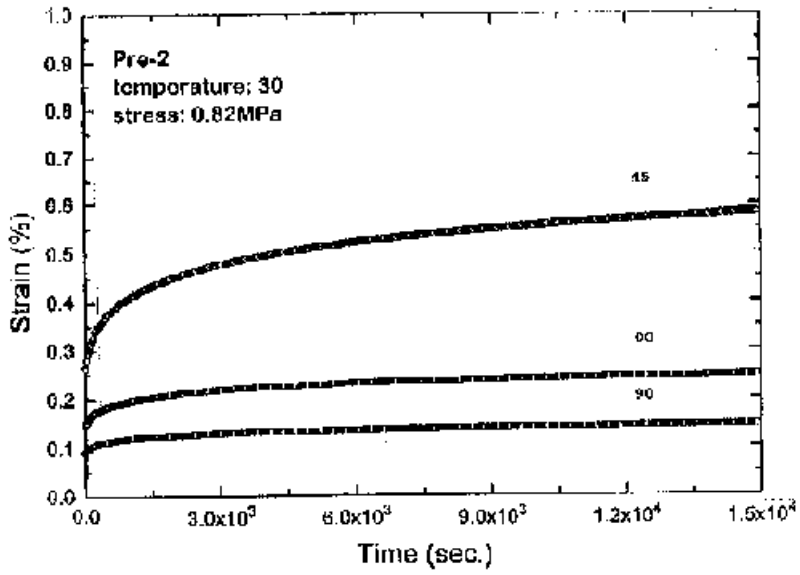

b

Figure 6.11 Creep curves for the Pre-1 and Pre-2 at the same stress level (0.82MPa) and temperature (30°) at the three orientations of 00 °, 45° and 90°.

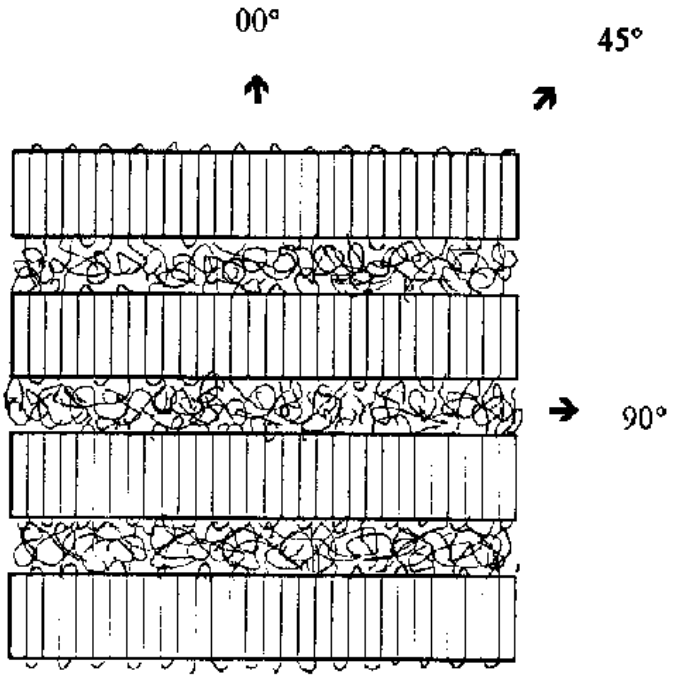

Figure 6.12 Lamented compost model proposed to represent the stacked lamellar morphology possessed by Resin 1 film.

Generally, the initial strain of a given creep curve reflects the instantaneous elastic response of the sample and therefore is dependent on its Young's modulus. For the Pre-1 and Pre-2 films, the crystalline lamellae are highly oriented with their normals preferentially aligned along the MD. Therefore, as a first approximation, the materials can be crudely considered as laminated composites of a hard crystalline phase and a soft amorphous phase stacked along the MD. The modulus of these melt-extruded films ("laminated composites" as shown in Fig. 6.12) is certainly dependent on the orientation of the deformation. At the 00 ° deformation, the material can be considered as the composite being deformed in an iso-stress case, i.e., the crystalline phase and the amorphous phase are deformed in series; therefore the modulus is dominated by that of the softer amorphous phase. On the other hand, at the 90 ° deformation, the material can be considered as the composite being deformed in an iso-strain case, i.e., the crystalline phase and the softer amorphous phase. On the other hand, at the 90 ° deformation, the material can be considered as the composite being deformed in an iso-strain case, i.e., the crystalline phase and the amorphous phase are deformed in parallel; therefore the modulus is dominated by that of the harder crystalline phase. Thus, although the modulus of the *crystalline phase (lamellae)* at the 90° orientation (perpendicular to the chain direction) is much less than that at the 00 ° orientation (parallel to the chain direction), the modulus for a *sample* at the 90° orientation is higher than that for a sample at the 00° orientation. As for the 45 ° deformation, since there is a maximum resolved shear stress in the plane of the crystalline lamellae, interlamellar shear is the most probable deformation event, and this results in a even smaller modulus at this particular orientation. The different moduli at the three orientations can be seen directly by looking at the "inserted" curves shown earlier in Figs. 3a and 3b for the Pre-1 and Pre-2 films, respectively. It needs to be pointed out that the use of the "laminated composite" model is only qualitative, since no consideration is given to chain tilt within the lamellae and the inclination of the lamellae stacks with respective to the MD.

The plateau creep rate can be understood based on the Eyring-rate model used in this study. According to equation 6.2, the creep rate is a function of three parameters- activation volume (V), activation energy (U) and the "availability" (population) of creep sites ($\dot{\varepsilon}_o$). From

Table 6.1, for both the Pre-1 and Pre-2 films, the activation volume and activation energy for the 00° and 90° creep were about the same, and this implies the same molecular mechanisms are involved at the two orientations for both films. However, the availability of the creep sites is different at the two orientations - with the 00 ° creep being 4 and 7 times larger than that for the 90° creep for the Pre-1 and Pre-2 films, respectively; this gives rise to a higher creep rate for the 00° creep than that of the 90 ° for samples under the same temperature and stress. As for the case of the 45° creep, the only parameter available was the activation volume at temperature of 30 °C, and the value was also close to that for the 00 ° and 90° creep.

Creep mechanisms for the melt-extruded films: The activation energies for the Pre-1 and Pre-2 films listed in Table. 1 are much less than those reported for the UHMWPE fibers obtained by using the same approach[21-24]. However, small values of activation energy have also been reported by other authors, based on different approaches, for talc-filled polypropylene[19] and HDPE[30] as well. Comparing the curves in Figs. 6.11a and b (showing the orientation dependence of creep curves) with those in Figs. 3a and b (showing the orientation dependence of stress-strain curves) that were obtained at similar temperatures, it can be seen that the final creep strains in Fig. 6.13 are less than the corresponding yield strains in Fig. 3 for both the Pre-1 and Pre-2 films. For HDPE materials, the amorphous phase has a glass transition temperature much lower than the temperatures used in the creep study; therefore, the amorphous phase, or at least a very major portion of it, is in a rubbery state. Under external tensile loading, it is likely that the initial response of the material is the deformation of the amorphous phase, and crystalline phase will not contribute to creep until the deformation of the amorphous is highly constrained, such as near the yield point.[31] In other words, the creep strains investigated in this study all fell in the region of pre-yielding, in which the primary deformation is that of the amorphous phase. This is the reason that the calculated activation energy in this study (5 ~ 30kJ/mol) is much less than the typical values for the deformation of the crystalline phase, in the region of 100 ~ 200kJ/mol.

Generally, at least three different kinds of amorphous regions need to be addressed, [32] these being 1) relaxed unoriented chains that are in the random coil state, 2) cilia that are suspended from the chain-folding surface of the crystalline lamellae, and 3) tie-chains that connect

adjacent crystalline lamellae. Among them, the tie-chains deserve the most attention, because they act as load transfer agents between the crystalline lamellae, although some relaxed isotropic chains can also contribute to the load transfer due to the entanglements. Although there have been several investigations on the influence of tie-chains in semicrystalline polymers by using SANS, NMR, and mechanical testing, a complete understanding regarding the full role of tie-chains is premature and limited at present.[33-43]

We believe that three fundamental parameters that are important for the tie-chains are enthalpy, entropy, and number density. The first two parameters are related to the "tautness" of the tie-chains; the more taut the tie-chains are, the more enthalpy and less entropy they have. The number density of the tie-chains can be influenced by many factors, such as molecular weight and its distribution, amount of short branches and their distribution in a given backbone, crystallization conditions, etc. Tie-chain density has been estimated by different methods according to different authors; [33-43] however, the energy state (combination of enthalpy and entropy) of the tie-chains have not yet been addressed in the literature.

As mentioned earlier, the creep strain in the melt-extruded films is in the pre-yielding region in which amorphous deformation is dominant; therefore, it is reasonable to believe that the tie-chains are the principal structural unit that determine the pre-yield creep behavior for these films. Since the same tie-chain networks controls the creep deformation for both the 00 ° and 90° creep; therefore, the activation volume and activation energy should be identical, as shown by the data in Table 1. However, the availability of the creep sites are different. This can be explained by the constraint effect of the crystalline lamellae on the tie-chains. For the 00 ° creep, all the possible creep sites (non-taut tie-chains) are active due to the separation of crystalline lamellae under loading. However, for the 90 ° creep, since the crystalline lamellar separation is not the major deformation event and some tie-chains do not transfer load; therefore, this portion of tie-chains are unlikely to be active - resulting a low number of available creep sites for the 90° creep than that for the 00° creep. In the case of the 45 ° creep, even the taut tie-chains can be activated due to the interlamellar shear motion and therefore the available creep sites is the largest, and this is

conjectured to be the reason that at this particular orientation the creep rate is the highest, although the activation energy is not known.

Comparing the creep parameters for the Pre-1 and Pre-2 films listed in Table 6.1, one sees that the activation volume for the Pre-2 film is somewhat smaller than that for the Pre-1 film, while the activation energy for the Pre-2 film is, however, slightly larger than that for the Pre-1 film. This can be explained by the different physical state of the tie-chains in the two films. Since the Pre-2 film has a wider molecular weight distribution (with the same number average molecular weight) than the Pre-1, it is possible that the tie-chain density for the Pre-2 film is higher than that for the Pre-1 film[44] and, therefore, gives rise to a smaller activation volume. The broader molecular weight distribution for the Pre-2 film imparts an significant longer relaxation time, as compared with that of the Pre-1 film, in the process of melt extrusion, [28] and the longer relaxation time promotes the distinct presence of well defined row structures in the Pre-2 film - in contrast, there is no sign of such a structure in the Pre-1 film. Thus, it is possible that the tie-chains are in a higher orientation state (more taut state) in the Pre-2 films than that in the Pre-1 film - corresponding to an higher activation energy. Although a previous study showed that the amorphous phase for both the Pre-1 and Pre-2 films is basically in an unoriented state[28], it does not necessarily exclude the existence of a small fraction of oriented (taut) *tie-chains* in the amorphous phase.

However, in general the creep behavior for the Pre-1 and Pre-2 films are similar, quite unlike what has been found out for the case of large strain plastic deformation study carried out by the authors for the same HDPE films. [45] Under larger strain deformation, these two films show very different yielding characteristics, cold-drawing behavior and fracture response [45] This leads the authors to speculate that it might be possible that there are some trace amounts of row-nucleated fibril structures, which is much smaller in length (e.g. bridges), as part of the *stacked lamellar morphology*. Such a structure can not be detected by TEM and WAXS due to its small amount. These bridges, if present, are expected to be more effective to influence the creep behavior than they are for plastic deformation. One can speculate that these short bridges can restrict the opening of the amorphous regions between the crystalline lamellae under small creep

strain, while the small aspect ratios of these bridges also limit their strengthening effect under larger strain plastic deformation. In fact, in the general scheme of strain induced crystallization of polymer solutions or melts under shear stress proposed by Keller et al, [46] if their assumption is correct, it would seem necessary to have some type of linear or fibril nuclei to trigger the formation of the row-nucleated fibrils or stacked lamellar structure. Indeed, both the existence and precise nature of the row-nucleated fibril structures are still not clearly totally understood. [47-49]

General considerations for creep behavior for semicrystalline polymers: For the isotropic HP-1 film, which was intended to be used as an example for semicrystalline polymers crystallized under quiescent conditions, the calculated creep parameters listed in Table 1 have some interesting features. Firstly, the activation energy is just 5kJ/mol (kT at room temperature is 2.6kJ/mol). This extremely low activation energy implies that tie-chains in the hot-pressed materials are in a much less taut state, at least some portion of these in the melt-extruded film, which can be justified by the different processing histories of the films. Second, The activation volume is almost identical to that for the Pre-1 film, and this suggests that the processing (hot-press as well as melt-extrusion) does not change the tie-chain density very much for the same resin. Thirdly, the population of creep sites for the hot-pressed film is much less than that for the melt-extruded film, and this is certainly dependent upon such factors as the size of the spherulites in the sample, thickness of crystalline lamellae with in the spherulites, etc. It is realized that the thickness of the isotropic film is about four times as large as those of the melt-extruded films; however, it is reasonable to believe that the creep parameters calculated from the Eyring-rate equation are material constants, which are independent of the sample thickness.

For semicrystalline polymers at temperature above the glass transition temperature, if the creep strain is limited to below the yield point of the material, the creep behavior is controlled by the deformation of the amorphous phase. For the case of HDPE materials, we have shown that regardless of the different morphologies by the samples (a stacked lamellar morphology either with or without row-nucleated fibril structure and a spherulitic morphology), the creep behavior can be reasonably described by the Eyring-rate model. Therefore, the strategy for improving the

creep performance for a particular polymer is to modify its chemistry, processing, and morphology to change these three parameters, i.e., to decrease the activation volume, to increase the activation energy, and to decrease the amount of creep site - as will be illustrated by the following example.

In the case of the high strength polyethylene fibers such as those studied by Pennings, [24] several approaches have been proposed to improve the creep performance, such as by crosslinking the amorphous phase,[50, 51] or by introducing branches into the linear chain,[9, 52] etc. For the first approach, crosslinking would certainly increases the tie-chain density and possibly reduce the population of creep sites as well. However, such an effort has been cited to be unsuccessful, because the crosslinking treatment tends to sacrifices the tensile properties, due to lower drawability of the crosslinked molecular structure. [53-56] For the second approach, two types of branches can be introduced. One is to introduce short chain (e.g. butyl) branches along a linear polyethylene backbone by copolymerization of ethylene with another α-olefin (e.g. 1-hexene). Besides lowering crystallinity, these short butyl branches promote more tie-chains and, as a result, improve creep behavior. However, it has been quoted that, although the creep behavior at a lower stress level is improved, at a *higher stress level* it is not much affected. [9]

The other approach is to introduce a small amount of methyl branches. It has been known that these shorter branches can be packed into the crystalline phase during the crystallization process. [58-61] It has been found that by introducing these methyl branches the creep behavior of ultra-high strength polyethylene fibers at a higher stress level is indeed improved. [9] It is argued that, for a polymeric crystal, creep strain is induced by a translational motion of polymer chains along the crystal c-axis within the crystalline phase, which is the same mechanisms as those that are responsible for the high temperature mechanical α relaxation in HDPE. [9, 10, 62] One can imagine that small amount of methyl branches associated with the backbone chain *within the crystalline phase* can greatly limit the translational motion of the chain through the crystal lattice, and this less chain mobility impairs a better creep resistance. The well-noted much higher creep resistance of poly-1-butene (compared with HDPE) has also been attributed to a much higher restriction of polymer chain motion within the crystal due to its bulkier butyl side groups along the backbone. [63]

In this context, it needs to be pointed out that, in the creep studies of high strength HDPE fiber, the creep at high stress is controlled by the deformation of the crystalline phase. Although creep behavior at low stress levels (3GPa for fibers with Young's modulus of 100GPa) is proposed due to the contribution from the amorphous entangled network, because of the high draw ratio and higher molecular weight, the amorphous phase is also more oriented as well; thus the tie-chains are highly taut and highly constrained. Therefore, although the percent crystallinity is similar, the observed creep rate for these fibers is less than that obtained in our study.

6.5 Conclusions

The Eyring-rate model is found to describe the creep behavior of the HDPE films with three different kinds of morphologies: a stacked lamellar morphology either with or without row-nucleated fibril structure and that with an unoriented spherulitic morphology. The calculated activation volume for the HDPE films is in the order of 1-2nm^3, and the activation energy is in the order of 20-30kJ/mol, except for the isotropic hot-pressed film which possessed an activation energy of just 5kJ/mol. For all the experiments, the creep behavior of these films were controlled by the deformation of amorphous phase, more specifically the tie-chains. The dependence of the creep behavior on loading direction for the melt-extruded films is more or less controlled by the difference in the availability of the creep sites at the different orientations. The 90° creep has the lowest creep site availability due to the constraint effects of the crystalline lamellae to the tie-chains, and the same constraint results in a much lower creep site availability for the unoriented spherulitic morphology.

References

1. J. Martin and Y. H. Pao, Proc. ASTM 51, 1277 (1951)
2. E. M. Andrade, Proc. Roy. Soc., 84, 1 (1970)
3. W. N. Findley, Polym. Eng. Sci., 27, 582 (1987)
4. M. F. Vallat and D. J. Plazek, J. Polym. Sci., Phys. Ed., 26, 555 (1988)
5. I. M. Ward, "Mechanical Properties of Polymers",
6. W. N. Findley, J. S. Lai and K. Onaran, "Creep and Relaxation of Nonlinear Viscoelastic Materials", Holland Publishing Co., 1976
7. J. P. Stephens, A. Ahmadieh and A. Mukherjee, J. Mater. Sci., 13, 467 (1978)
8. P. J. Dixon-Stubbs, J. Mater. Sci., 16, 389 (1981)
9. Y. Ohta, H. Sugiyma and H. Yasuda, J. Polym. Sci., Phys. Ed., 32, 261 (1994)
10. T. Komatsu and A. Aoshima, J. Polym. Sci., Phys. Ed., 33, 179 (1995)
11. J. A. H. M. Buijs and G. J. Vroge, Polymer, 34, 4692 (1993)
12. L. C. E Struik, "Physical Ageing of Amorphous Polymers and Other Materials", Elsevier, Amsterdam, 1978
13. B. E. Read, J. Non-Cryst. Solids, 131-133, 408 (1991)
14. J. Lai and A. Bakker, Polymer, 36, 93 (1995)
15. P. J. R. Leblans and W. M. Bastiaansen, J. Polym. Sci., Phys. Ed., 27, 1009 (1989)
16. Y. C. Bhuvanesh and V. B. Gupta, Polymer, 36, 3669 (1995)
17. L. C. E. Struik, Polymer, 28, 1251 (1987)
18. L. C. E. Struik, Polymer, 90, 799 (1989)
19. G. G. Trantina, Polym. Eng. Sci., 26, 776 (1986)
20. H. Erying, J. Chem. Phys., 4, 238 (1936)
21. M. A. Wilding and I. M. Ward, Polymer, 19, 969 (1978)
22. M. A. Wilding and I. M. Ward, J. Mater. Sci., 19, 629 (1984)
23. I. M. Ward and M. A. Wilding, J. Polym. Sci., Phys. Ed., 22, 561 (1984)
24. J. P. Penning, H. E. Pras and A. J. Pennings, Coll. Polym. Sci., 272, 664 (1994)

25. A. Sengonul and M. A. Wilding, Polymer, 36, 4579 (1995)
26. S. R. Allen and E. J. Roche, Polymer, 30, 996 (1989)
27. A. K. Rogozinsky and S. L. Bazhenov, Polymer, 33, 1391 (1992)
28. Ta-Hua Yu and G. L. Wilkes, Polymer, 37, 4675 (1996)
29. L. E.Govaert and P. J. Lemstra, Coll. Polym. Sci., 270, 455 (1992)
30. J. E. Sinclair and J. W. Edgemoxd, J. Polym. Appl. Sci., 13, 999 (1969)
31. Z. Bartczak, A. Galeski. A. S. Argon and R. E. Cohen, Polymer, 37, 2113 (1996)
32. D. Y. Yoon and P. Flory, Polymer, 18, 509 (1977)
33. H. D. Heith, F. J. Padden, Jr and R. G. Vadimsky, J. Polym. Sci., Phys. Ed., 18, 2307 (1980)
34. N. Brown and I. M. Ward, J. Mater. Sci., 18, 1405 (1983)
35. A. Lustiger and R. L. Markham, Polymer, Polymer, 24, 164 (1983)
36. E. W. Fischer, K. Hahn, J. Kugler, U. Struth and R. Born, J. Polym. Sci., Phys. Ed., 22, 1491 (1984)
37. V. V. Zhizhenkov and E. A. Egorv, J. Polym. Sci., Phys. Ed., 22, 117 (1984)
38. S. K. Bhattacharya and N. Brown, J. Mater. Sci., 20, 2767 (1985)
39. Yan-Ling Huang and N. Brown, J. Polym. Sci., 28, 2007 (1990)
40. J. T. Yeh and J. Runt, J. Polym. Sci., Phys. Ed., 29, 371 (1991)
41. Yan-Ling Huang and N. Brown, J. Polym. Sci., Phys. Ed., 29, 129 (1991)
42. L. L. Bohm, H. F. Enderle and M. Fleirner, Adv. Mater., 4, 234 (1992)
43. P. A. O'Connell, M. J. Bonner, R. A. A. Duckett and I. M. Ward, Polymer, 36, 1995 (1995)
44. Y. L. Huang and N. Brown, J. mater. Sci., 23, 3648 (1988)
45. Hngyi Zhou and G. L. Wilkes, J. Mater. Sci., Submitted
46. A. Keller and M. R. Mackley, Pure Appl. Chem., 39, 195 (1974)
47. J. M. Salazar, J. V. G. Ramos and J. Petermann, Inter. J. Polymeric Mater., 21, 111, (1993)
48. A. J. Pennings, J. M. A. A. Von der Mark and H. C. Booij, Koll. Z. Z. Polym., 236,

99, (1970)

49. D. T. Grubb and M. J. Mill, J. Crystal Growth, 48, 321, 1980
50. M. A. Wilding and I. M. Ward, Polymer, 22, 870 (1981)
51. R. Hikmet, P. J. Lemstra and A. Keller, Coll. Polym. Sci., 265, 185 (1987)
52. D. C. McFaddin, K. E. Russell and E. C. Kelusky, Polym. Commun., 29, 258 (1988)
53. D. J. Ijkstra, R. Krischbaum and A. J. Pennings, Polymer, 30, 866 (1989)
54. M. Matsuo and C. Sawatari, Macromoleculaes, 19, 2028 (1986)
55. R. Hikmet, P. J. Lemstra and A. Keller, Colloid Polym. Sci., 265, 185, (1987)
56. J. De. Boer, H. J. van den Berg and A. J. Pennings, Polymer, 19, 969 (1978)
57. M. A. Ward and M. A. Wilding, J. Polym. Sci., Polym. Phys. Ed., 22, 870, 1981
58. P. R. Swan, J. Polym. Sci., 56, 409 (1962)
59. F. R. Walter and F. P. Reading, J. Polym. Sci., Letter, 99, 561 (1956)
60. D. C. McFaddin, K. E. Russell and E. C. Kelusky, Polym. Commun., 29, 258 (1988)
61. S. Hosoda, H. Nomura, Y. Gotoh and H. Kihara, Polymer, 31, 1999, (1990)
62. Hongyi Zgou and G. L. Wilkes, Macromolecules, to appear.
63. L. Luciani, J. Sepala and B. Lofgren, Prog. Polym. Sci., 13, 37 (1988)

Chapter 7.0 COMPARISON OF LAMELLAR THICKNESS AND ITS DISTRIBUTION DETERMINED FROM DSC, SAXS, TEM, AND AFM FOR HIGH DENSITY POLYETHYLENE FILMS HAVING A STACKED LAMELLAR MORPHOLOGY *

Abstract

Lamellar thickness and its distribution in high density polyethylene (HDPE) films having a well-defined stacked lamellar morphology were investigated by using DSC, SAXS, TEM, and AFM. It was found that the most probable lamellar thickness from SAXS and TEM agrees very well; however, they do not agree with those values obtained from DSC and AFM. It was pointed out the use of DSC as a tool to determine lamellar thickness and its distribution is so sensitive to the rate of heating in the DSC experiments and the parameters in the Gibbs-Thomson equation that it is not believed to be suitable for routine quantitative analysis.

* This chapter, formatter as required, has been submitted to *Polymer* for publication.

7.1 Introduction

Semicrystalline polymers often show a broad melting peak by differential scanning calorimetry (DSC), and this is usually attributed to the distribution of crystalline lamellae thickness [1], although certainly the potential for defect concentration to affect melting is also recognized. Lamellar thickness distribution for a specific polymer is the result of its chemistry and crystallization kinetics, and it also helps account for the thermal and mechanical properties possessed by that specific material. Therefore, it is of interest and desirable to be able to determine the lamellar thickness distribution.

DSC melting endotherms can, in principle, be used to calculate the lamellar thickness distribution. In this approach, a DSC profile, heat flow versus temperature, is transformed into a lamellar thickness distribution curve (probability - weight percentage of lamellae versus lamellar thickness) by using the Gibbs-Thomson equation [2]

$$T_m = T_m^o\left(1 - \frac{2\sigma_e}{\Delta H_f \cdot L}\right) \qquad (7.1)$$

where T_m is the observed melting temperature for a crystalline lamella of thickness L; T°_m is the equilibrium melting temperature of the crystalline lamella of infinite thickness; σ_e is the surface energy of the basal surface of the crystalline lamella and it is associated with the energy of chain folding during the crystallization process; ΔH_f is the enthalpy of fusion for the crystalline phase. It needs to be pointed out that the above equation is valid only for lamellae whose lateral dimensions are much larger than their thickness, which is generally the case. In certain cases, the precise version of the Gibbs-Thomson equation, which takes into account of the surface energy of the side surface and lateral dimension of the crystalline lamella, would have to be utilized [3].

Because of its simplicity and rapidity, the DSC approach has been used as the principle route by several authors to obtain lamellar thickness and its distribution [4-9]. However, there have been some uncertainties about this approach. There are two different ways to calculate the probability of the lamellar thickness distribution curves. The first method is to use DSC endotherms directly; specifically, the melting endotherms are assumed to be proportional to the

weight fraction of crystalline lamellae that melt at a specific temperature (thickness). The second method is to use a differential equation, developed by Alberola, et al based on the mathematical equality of mass fraction of crystalline phase to the ratio of melting enthalpy over enthalpy of fusion, which has led to the following formula [5]

$$\frac{1}{M}\cdot\frac{dM}{dL}=\frac{dE}{dT}\cdot\frac{(T_m^o-T_m)^2}{2\sigma_e\cdot T_m} \qquad (7.2)$$

where M is the mass of crystalline phase within the sample for the DSC experiment; dM is the mass of the crystalline phase that melts between T and T+dT and it has thickness in the range of L and L+dL; dE/dT, obtained from a DSC endotherm, is the energy required to melt the dM fraction of the crystalline phase. All the other parameters in the above equation have the same definitions as in equation 1.

While the above approach seems reasonable at first sight, for accuracy the effects of heating rate used in the DSC experiments on the obtained lamellar thickness distribution curves must be properly addressed. For example, it is well known that different heating rate can change the amount of heat flow and shift the temperature reading in the DSC profile. In addition, this same variable can alter the width of a melting peak dramatically [10,11]. These latter factors have not been investigated in past references given above, and this puts the calculated distribution curves into question. Furthermore, the possibility of annealing effects (e.g. lamellar thickening, partial melting, pre-melting and recrystallization) for polymer samples during the DSC experiments is also of concern.

There are other approaches that have also been utilized in the literature to determine the lamellar thickness distribution, and they include experimental techniques such as gel permeation chromatography (GPC) [12,13], small angle X-ray scattering (SAXS) [14-15], transmission electron microscopy (TEM) [16-21], and Raman longitudinal acoustic mode (LAM) [22,23]. The GPC method is based on the fact that nitric acid oxides the amorphous phase at a much faster rate than the crystalline phase [11]. As a first attempt to obtain lamellar thickness distribution, the molecular weight distribution measured by GPC experiments for a sample whose amorphous phase is fully removed by the oxidation process was used as a indication of lamellar thickness distribution,

which remains intact during the oxidation process [12]. Clearly, this approach is not necessarily a good one due to the complex crystallization process experienced and morphologies possessed by the samples, let alone the difficulties with uniformity of oxidation promoted by limitation on diffusivity and accessibility by the oxidation agent, etc.

SAXS is also a well-established method for the structural investigation of semicrystalline polymers [14,15]. In a simplest case, SAXS profiles for semicrystalline polymers having a lamellar morphology in an unoriented state, after properly corrected (e.g. Lorentz correction), are generally characterized by one or more diffuse maxima, and the first maximum at the lowest scattering angle is frequently converted into the well-known "long spacing" by applying Bragg's law. If the percent crystallinity of the sample is known, and assuming that the crystalline lamellae are spaced-filling with a single population of thickness, the mass-based most probable lamellar thickness (L_m) can be calculated by using the following relation [14]

$$L_m = X_c \cdot L_c \qquad (7.3)$$

where X_c is the weight percent crystallinity, generally measured by DSC, WAXD or density; L_c is the long spacing obtained from the SAXS profile by Bragg's law. However, it is nontrivial to extract the lamellar thickness distribution from SAXS data. According to some authors, it can be done only under the assumption that the crystalline lamellae are isotropic stacks of plates with an infinitely extended lateral dimension [14]. Even in this case, the corrected SAXS data have to be smoothed and fit to some kind of stacked lamellar morphological model with known lamellar thickness distribution [15]. Therefore, SAXS is not a routine way to obtain lamellar thickness distribution, although it can provide an estimation of the average lamellar thickness as expressed by equation 3.

The use of TEM for the determination of lamellar thickness distribution, most of which has been limited to polyethylene, was initiated by the success of the chlorosulfonation treatment for polyolefins, especially for high density polyethylene [16-20]. Basically, the thickness of crystalline lamellae, as revealed by TEM micrographs taken for samples stained by chlorosulfonic acid and further treated with uranyl acetate, is measured by eye; then the histogram is constructed for the number of measurements verses lamellar thickness. From this, a *number*-based lamellar thickness

distribution is obtained. The same procedure can also be carried out by using sophisticated image analysis computer programs. The problems associated with the TEM approach are: 1) it is assumed that the morphology of the sample is not altered in the staining process, which is not certain in many cases [21]; 2) the contrast of TEM micrographs is typically not uniform, and this implies that the crystalline lamellae are in different orientation states with respect to the microtomed surface, thus the obtained distribution histograms may not be accurate; 3) the obtained TEM micrographs are only a small fraction of a bulk sample, so it may not be a thorough and accurate representation of the real material. This problem, however, can be minimized by analyzing multiple sections of a given material.

The positions, intensities, and shapes of the low-frequency Raman-active band (wave number less than $60cm^{-1}$) have been extensively used in the determination of the extended chain length in semicrystalline polymers, again particularly for high density polyethylene [22,23]. It has been shown that the observed integrated intensity is proportional to the length of the ordered sequence, i.e. extended chain length or "stem" in the crystalline phase [23]. The silent assumptions in this approach is that the amorphous phase, crystalline lamellar surfaces, and tie chains have no effects on the LAM intensity distribution. Furthermore, corrections have to be made for chain tilt angle-inclination of the chain axis with respective to the basal surface of crystalline lamellae.

When practically possible, a combined approach is desirable to make sure that the lamellar thickness distributions obtained from the different approaches have a reasonable agreement. Studies have been published where lamellar thickness distribution obtained by TEM, SAXS, and LAM were compared for linear polyethylene samples (from low and intermediate to high molecular weight) with five different lamellar morphologies [18,19]. Except for samples with fairly narrowly distributed stacked lamellae, where good agreement between the three methods was achieved, limited agreement was found for samples with curved lamellar morphologies or samples with asymmetric or broad lamellar thickness distributions.

Also, there have been studies in which DSC, SAXS and TEM were used to obtain lamellar thickness and its distribution [6,7]. In these cases, the most probable lamellar thickness obtained from TEM and/or SAXS was used to "fit" the lamellar thickness distribution curves generated

from the DSC data. From this the surface energy of the basal surface was estimated by using equation 2. Obviously, the equality of the most probable lamellar thickness obtained from these approaches needs to be proven.

The purpose of this paper is to present an investigation of lamellar thickness and its distribution by using DSC, SAXS, TEM, and AFM techniques and to compare the results thus obtained. The materials used in this study were high density polyethylene (HDPE) films having a well defined stacked lamellar morphology prepared by melt extrusion. The presence of thin lamellar morphology with large lateral dimension ensured the applicability of the Gibbs-Thomson equation. The DSC curves for this material, obtained at a heating rate of 10°C/min, showed a relatively sharp melting peak, indicating a "narrow lamellar thickness distribution". The TEM micrographs for samples treated by chlorosulfonic acid revealed a uniformly good contrast of crystalline lamellae versus that of the amorphous phase, and thus this simplified stacked lamellar morphology allowed us to develop a confident construction of the lamellar thickness distribution histograms.

With the rapid advances in the application of atomic force microscopy (AFM) in polymers, crystalline lamellae have been observed by many authors for different kinds of semicrystalline polymers [23-25]. However, AFM is a surface-oriented tool, and the authenticity of the obtained images has been questioned, especially for experiments done in contact modes [26]. With the development of more advanced skills such as the Tapping Mode™ or Lift Mode™, the application of this technique will certainly become more and more common. The crystalline lamellae in the melt-extruded HDPE films used in this study are "edge-on" with respect to the film surfaces, and this allowed the direct visualization of the lamellae on untreated film surfaces. Therefore, it is of interest to see whether or not the lamellar thickness distributions for our materials with simple and well defined stacked lamellar morphologies obtained from AFM are at all in agreement with those results obtained by the other techniques.

7.2 Experimental

Materials: The film materials used in this study were prepared from a HDPE resin with number average molecular weight (M_n) and weight average molecular weight (M_w) of 14,500 and 150,000g/mol, respectively. The films (1 mil in thickness) were extruded under processing conditions such that the crystalline phase is quite highly oriented along the machine direction, whereas the amorphous phase is essentially in a random state. A detailed study of the orientation state of crystalline phase and amorphous phase of the films used in this study has been provided elsewhere [27]. In addition to the extruded film, which was designated as precursor film (Pre), two annealed films of this same precursor were also utilized, The annealed films were prepared by annealing at 120 and 130°C for 20min; based on earlier experiments, 20min annealing at these temperatures is sufficient for the majority of lamellae thickening. The two annealed materials were designated as F120 and F130, respectively.

DSC experiments: A Perkin Elmer DSC-7 instrument was used for all the DSC experiments. DSC scans were carried out by using seven different heating rates of 1, 2, 4, 8, 16, 32, and 64°C/min. Baseline calibrations were made for all the heating rates. Small and fixed sample weight (ca. 3.0mg) was used, and all the DSC samples had the same shape and size- four layers of circular one mil films with the same diameter as the DSC sample pan. All the samples were sealed in the same manner by using a pan crimping tool in order to ensure good sample-pan contact. For comparison, a standard Indium (In) sample was also scanned at the seven heating rates used for the HDPE samples. When applying the Gibbs-Thomson equation to the DSC data, the ΔH_f, σ_e, and $T°_m$ values utilized were 290J/cm^3, 90mJ/m^2, and 145.5°C, respectively [28].

SAXS experiments: A standard Kratky slit-collimated camera was used for the SAXS experiments. Stacks of HDPE films were used as the samples for the SAXS experiments. In order to minimize the effect of orientation, nine layers of films were used in each stack, and the machine direction (MD) of each layer of film within the stack was at an angle (ca. 11°) with respect to the adjacent layer of film so that the MDs were uniformly distributed in the plane of the sample holder. The same sample stacks were also studied by a separate synchrotron X-ray scattering

experiment and the results showed several isolated first order scattering "spots" at the same scattering angle- each pair of which arise from a film layer with a specific orientation. Thus, the azimuthal intensity distribution is not perfectly circularly uniform, which should be the case for a true isotropic media. However, more importantly for this study, the long spacing for the specific sample obtained from the synchrotron experiment was found to be in good agreement with that from the Kratky experiment on the same sample.

TEM experiments: Samples for the TEM study were stained with chlorosulfonic acid at 60°C for 6 hours, then they were washed with sulfuric acid and water. After being dried overnight, the samples were embedded in an epoxy resin and cured overnight at 65°C. The embedded samples were microtomed at room temperature, and the microtomed thin sections were ca. 80nm thick. All the TEM experiments were performed by using a Philips EM420 instrument operated at 100KV.

AFM experiments: Samples for the AFM experiments were the untreated film surfaces, Double side tapes were used to mount the sample to the sample stage. All the AFM experiments were carried out by using a NanoScope III SPM (Digital Instrument) instrument operating in the Tapping Mode^{TM}. In this mode, a silicon tip oscillating slightly below its resonance frequency (ca. 200kHz) hovers above a sample's surface at a very short distance (50-150Å). The tip-sample interaction was short and intermittent to prevent surface deformation during the experiments. The output images were collected in the forms of height image amplitude image. The lamellar thickness estimates was done by using the amplitude image mode.

7.3 Results

Figures 7.1a-c are the DSC scans at the seven heating rates for the three HDPE films used in this study. The effects of heating rate is clearly shown. Once the heating rate was doubled, the melting enthalpy (the area under the melting peak) was also doubled (the sample weight was kept constant), and this can be justified by the fact that the heat flow (dE/dt) measured by the DSC instrument is dependent on time (dt), or heating rate(dT/dt), used in the experiment. There was

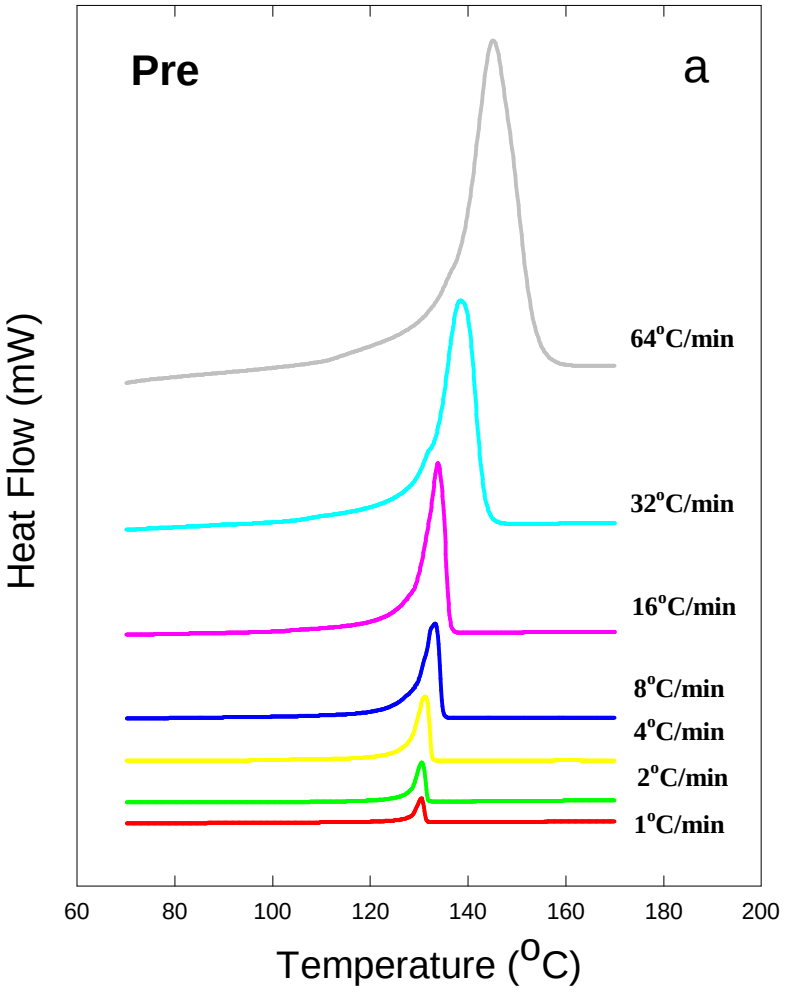
Pre
a
64°C/min
32°C/min
16°C/min
8°C/min
4°C/min
2°C/min
1°C/min
Heat Flow (mW)
60
80
100
120
140
160
180
200
Temperature (°C)

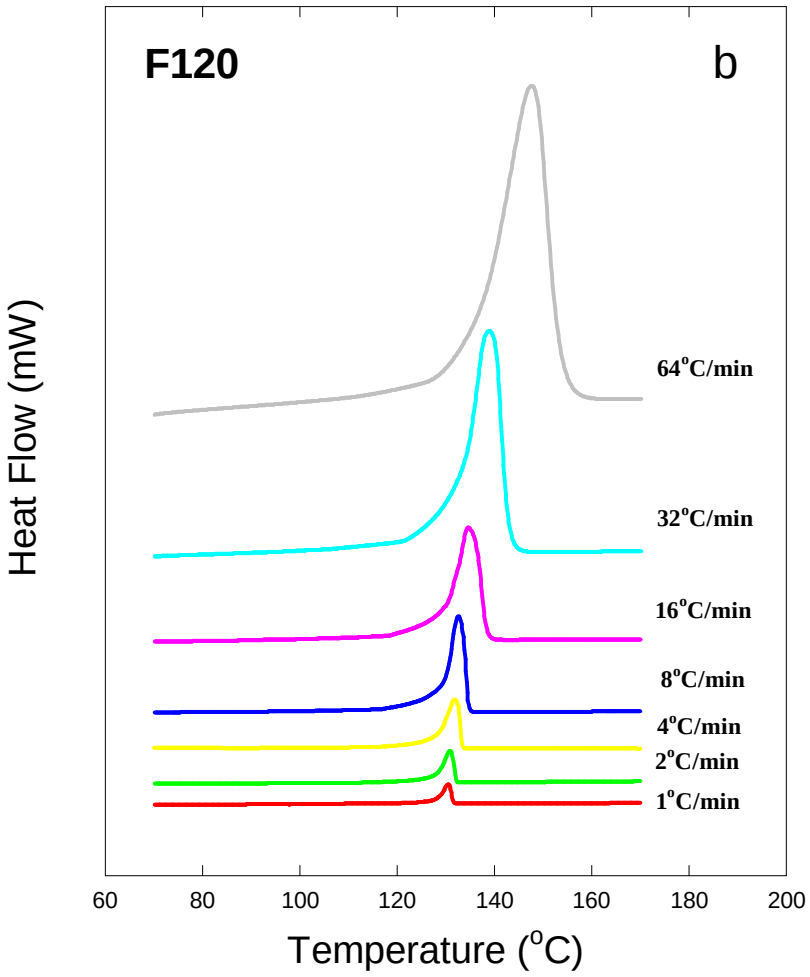
F120
b
Heat Flow (mW)
64°C/min
32°C/min
16°C/min
8°C/min
4°C/min
2°C/min
1°C/min
60
80
100
120
140
160
180
200
Temperature (°C)

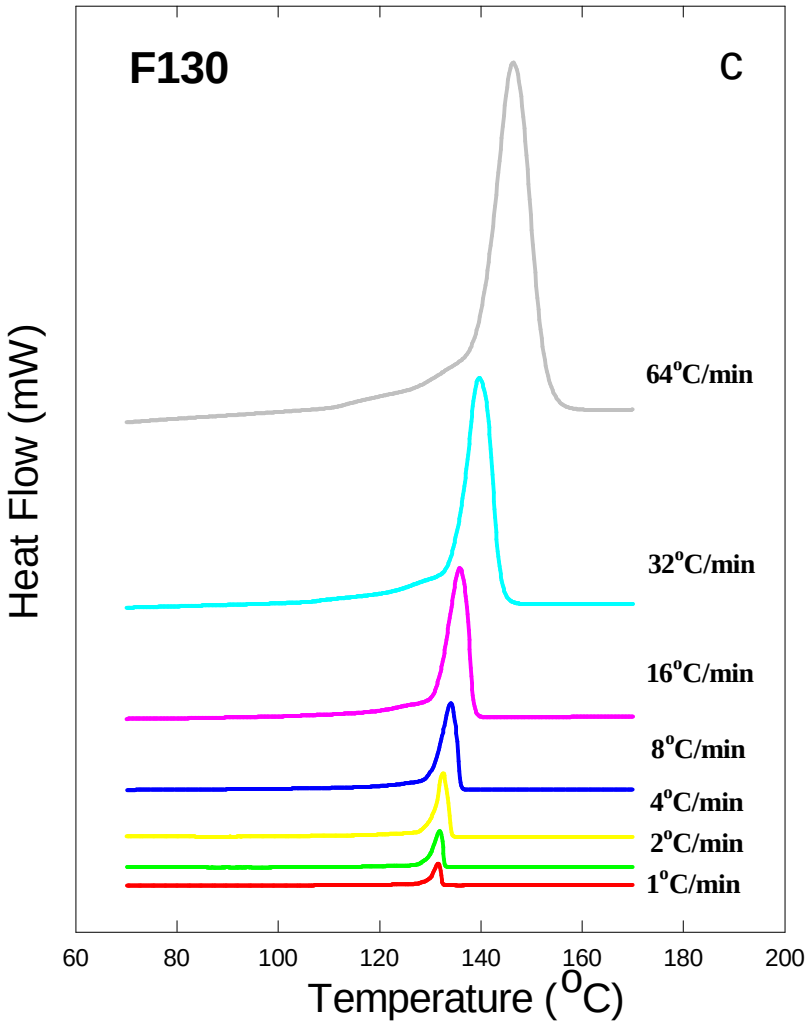
F130
C
64°C/min
32°C/min
16°C/min
8°C/min
4°C/min
2°C/min
1°C/min
Heat Flow (mW)
60
80
100
120
140
160
180
200
Temperature (°C)

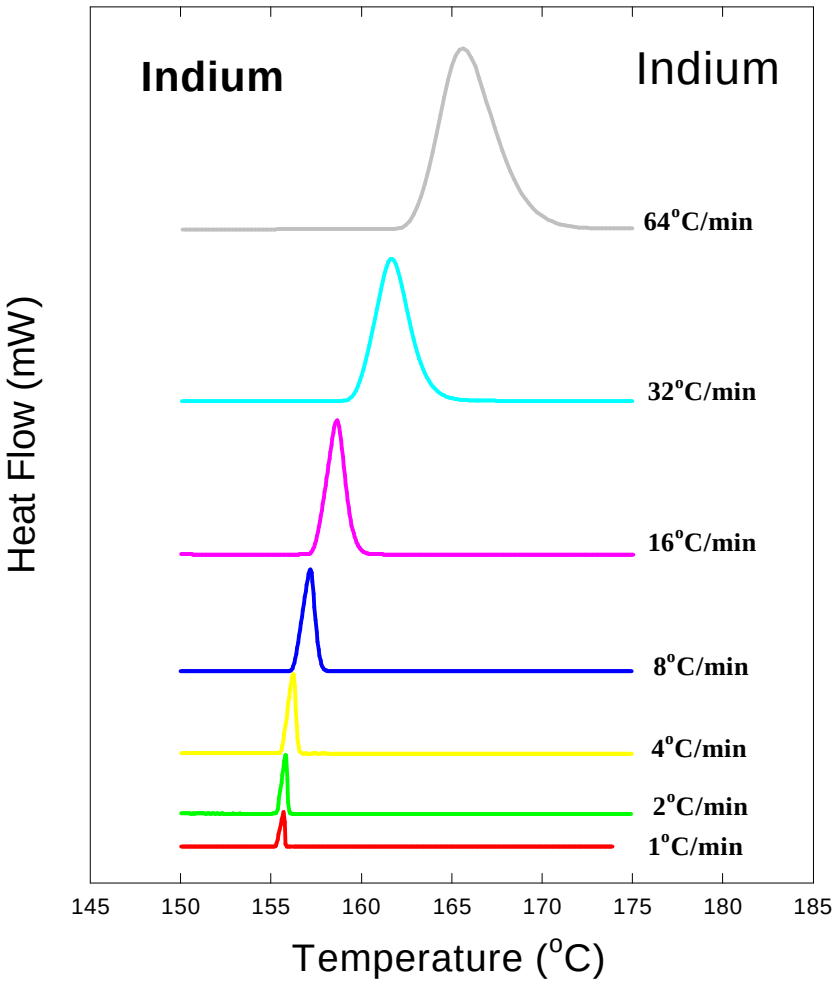

Figure 7.1 DSC scans at seven heating rates for a) precursor film, b) annealed film at 120°C, c) annealed film at 130°C and d) standard Indium sample.

also a shift to higher temperature for the melting endotherms as the heating rate was increased. And more prominently, the width of the melting peaks was dramatically changed by heating rate. The same effects existed also for the standard indium sample, which can also be noted in Fig. 7.1d. Since the indium sample has a better thermal conductivity, the thermal lag was less pronounced than that for the HDPE samples. Nevertheless, the intrinsic thermal lag in the DSC experiments always exists.

Therefore, in order to use the DSC data for the calculation of lamellar thickness distribution, corrections for thermal lag have to be made. To do this, the heat flow was normalized by the heating rate, converting dE/dt into dE/dT. Secondly, the DSC curves were shifted to "zero heating rate"; this was done by constructing a plot of melting temperature (peak temperature in the DSC melting endotherm) versus heating rate as shown in Fig. 7.2. It was noted that in Fig. 7.2 at slow heating rates, the peak melting temperatures for the precursor film and the F120 film were almost identical, and this is an indication that the precursor film was probably "annealed" during the DSC scan at the slowest heating rate. Therefore, the extrapolations were done without using the DSC data at 1 and 2°C/min heating rates. No attempts were made to make any correction for the width of the melting peaks since the relationship between the width of a DSC melting peak and heating rate is nonlinear [9]. In addition, due to the above-mentioned annealing effect during the DSC experiment, it is not possible to know the exact width of the melting peaks for the initial (original) lamellar morphology at the lower heating rates. With this approach, the corrected DSC data for the three HDPE films are shown in Figs. 7.3a-c.

Figures 7.4 and 7.5 is the calculated lamellar thickness distribution from the corrected DSC data. The two methods described in the Introduction section of this paper were then both applied to the data, i.e., the "direct" approach by Gibbs-Thomson equation and the "indirect" approach which uses differential equation 7.2. Figure 7.4 provides the results obtained from the method in which the DSC melting endotherms were used directly, while figure 7.5 displays the results of the method in which differential treatment (equation 7.2) was used. The most probable lamellar thickness, the value that corresponds to the peak position in the distribution curve, is

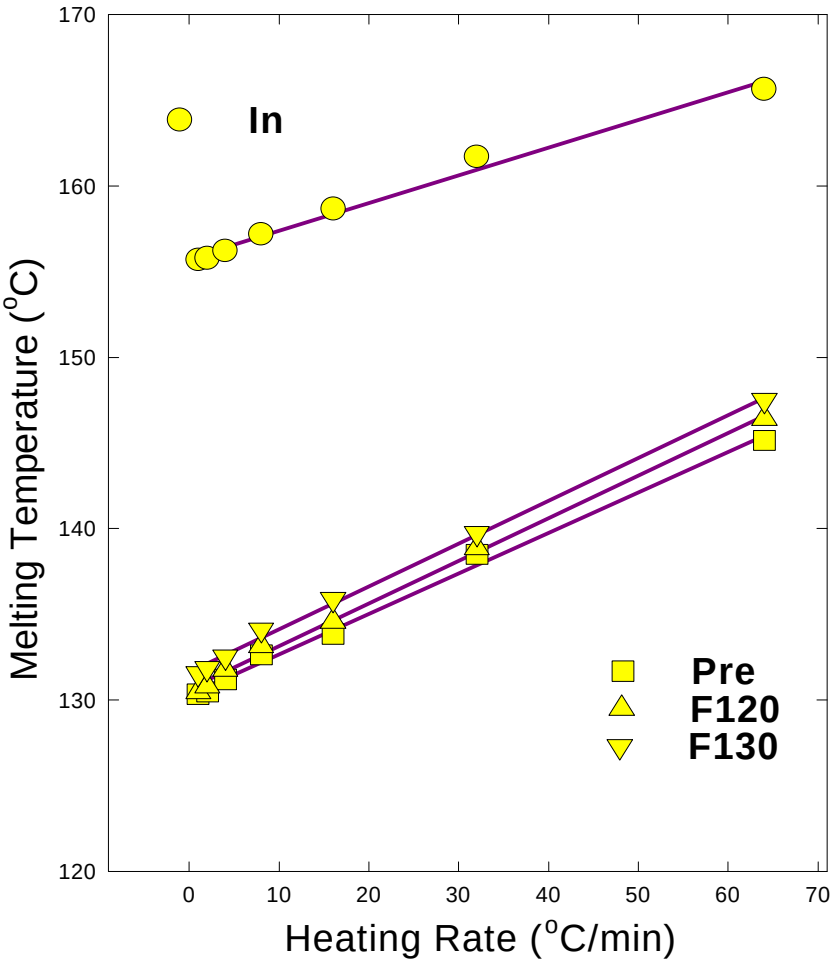

Figure 7.2 Linear relationship between melting temperature (endotherm maxima) and heating rate for precursor film (pre), annealed films at 120°C (F120) and 130°C (F130) and Indium sample.

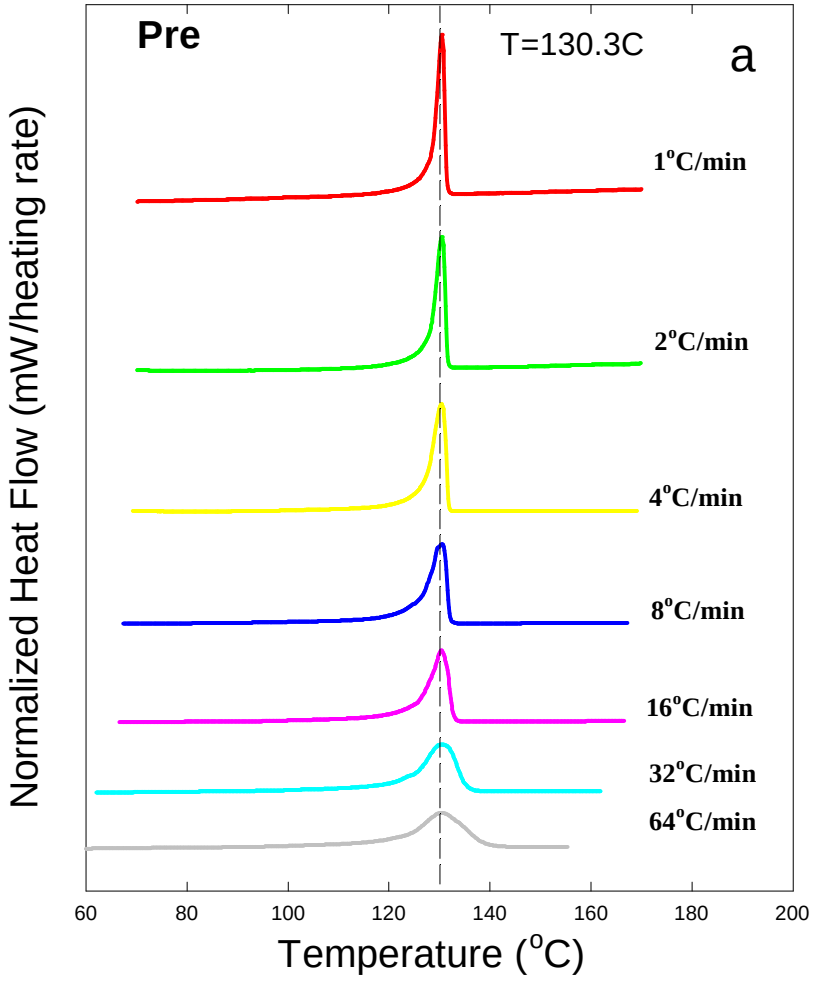
Pre
T=130.3C
a
1°C/min
2°C/min
4°C/min
8°C/min
16°C/min
32°C/min
64°C/min
Normalized Heat Flow (mW/heating rate)
60
80
100
120
140
160
180
200
Temperature (°C)

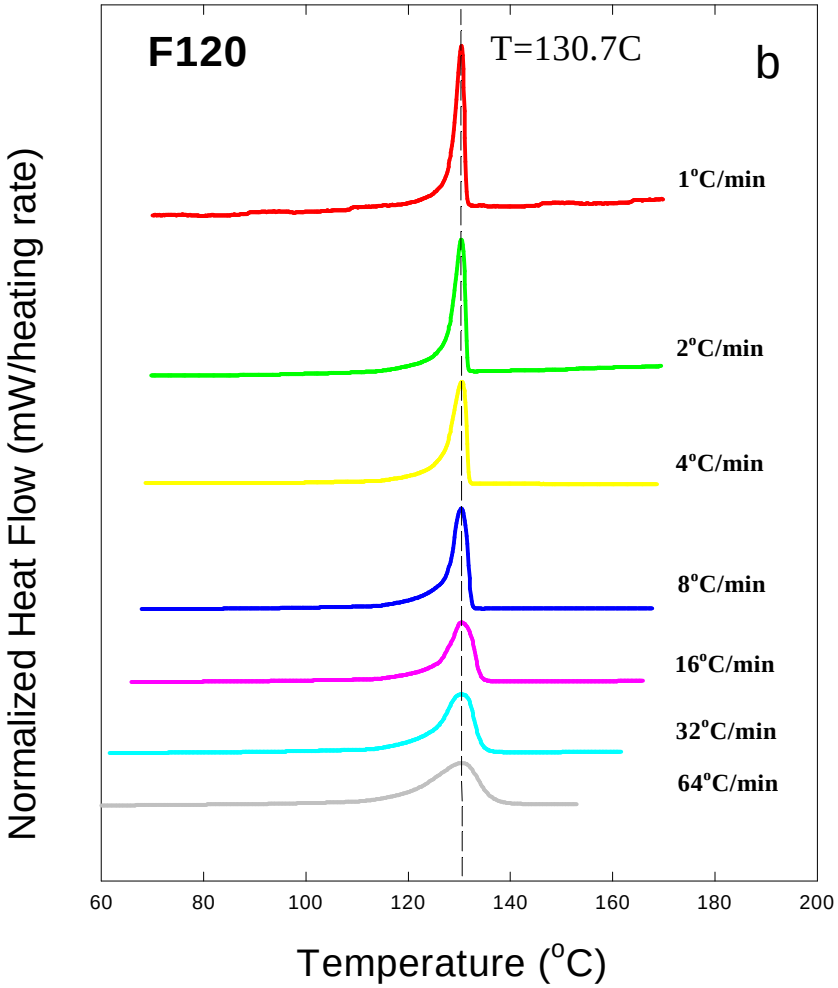
F120
T=130.7C
b
1°C/min
2°C/min
4°C/min
8°C/min
16°C/min
32°C/min
64°C/min
Normalized Heat Flow (mW/heating rate)
60
80
100
120
140
160
180
200
Temperature (°C)

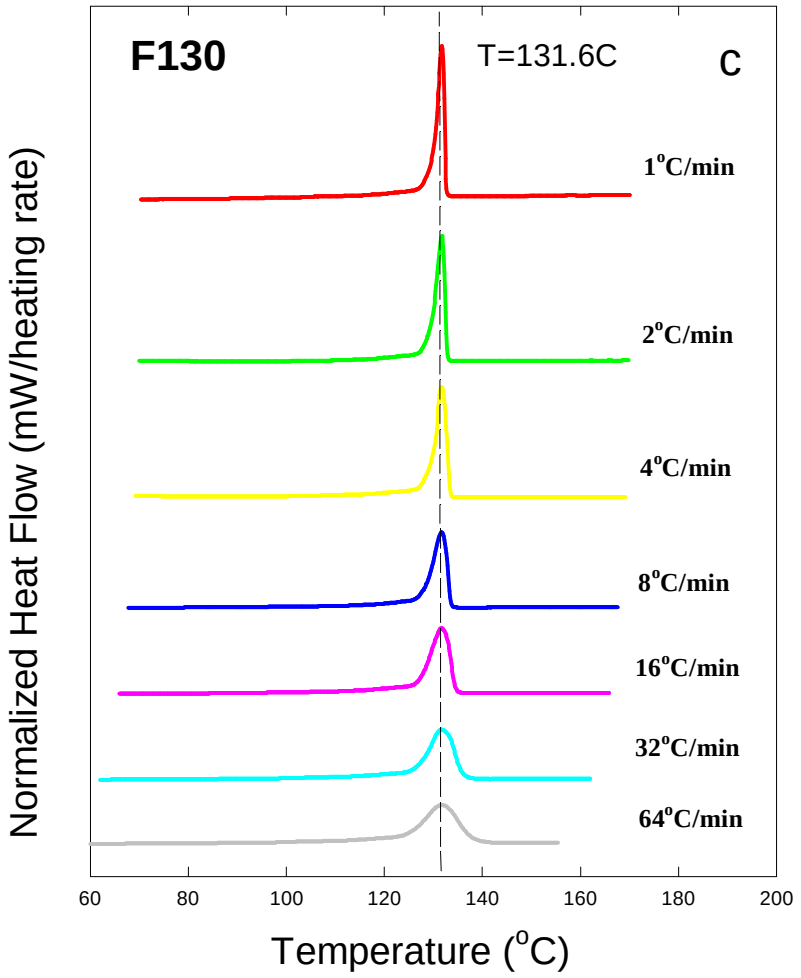

Figure 7.3 Normalized and shifted DSC data for a) precursor film, b) annealed film at 120°C (F120) and c) annealed film at 130°C (F130).

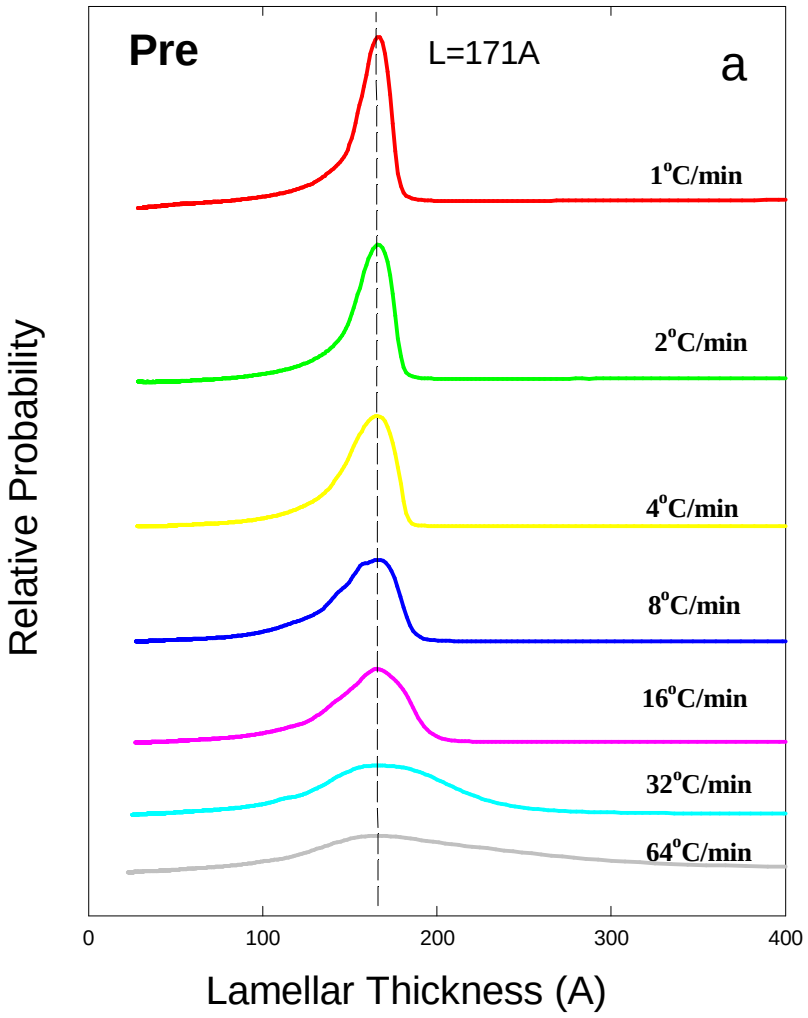
Pre
L=171A
a
1°C/min
2°C/min
4°C/min
8°C/min
16°C/min
32°C/min
64°C/min
Relative Probability
0
100
200
300
400
Lamellar Thickness (A)

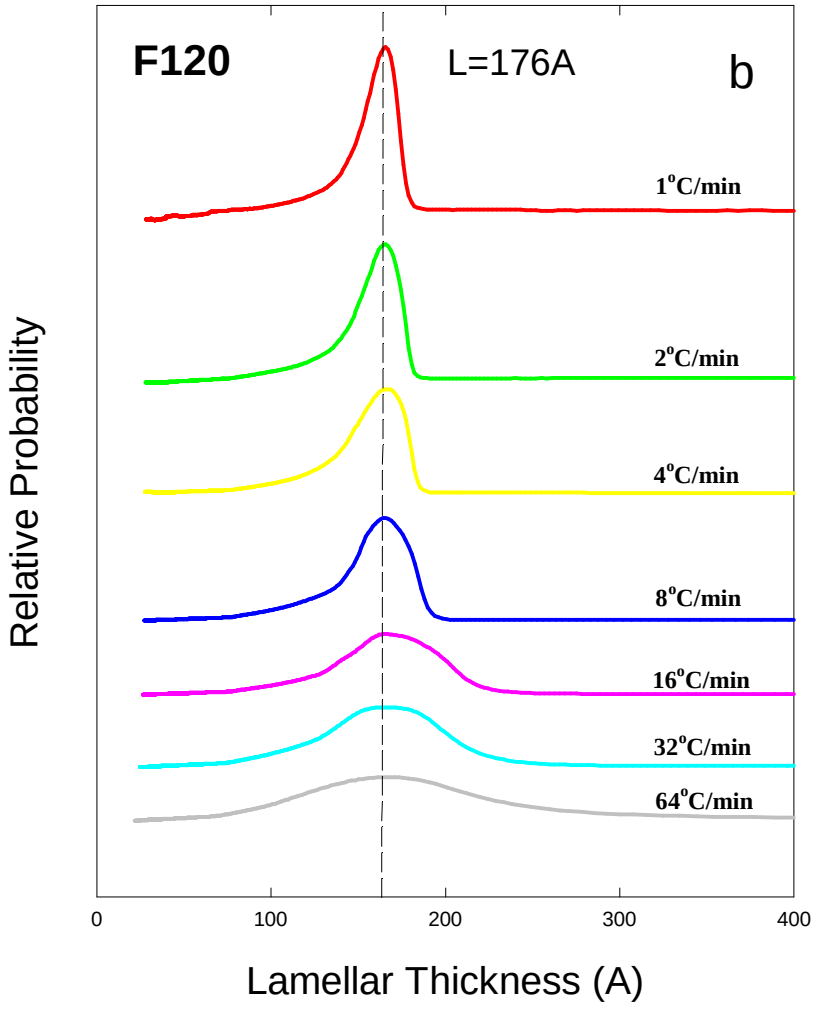
F120
L=176A
b
1°C/min
2°C/min
4°C/min
8°C/min
16°C/min
32°C/min
64°C/min
Relative Probability
0
100
200
300
400
Lamellar Thickness (A)

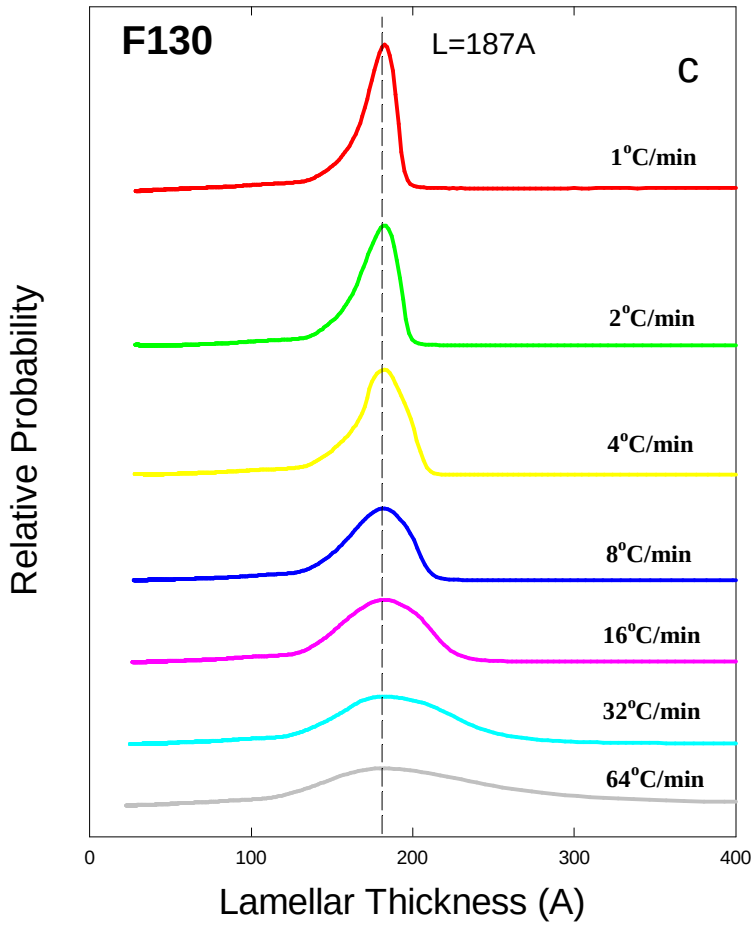

Figure 7.4 Lamellar thickness distribution curves for a) precursor film (Pre), b) annealed film at 120°C (F120) and c) annealed film at 130°C (F130). The distributions were calculated by using the corrected DSC data.

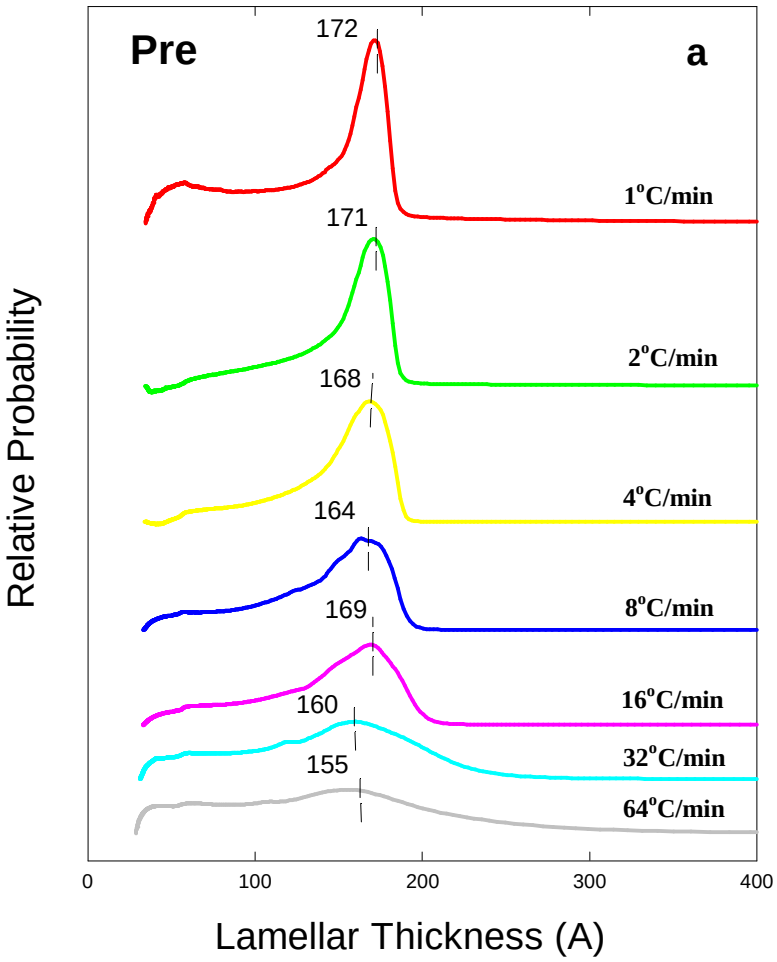
Pre
a
172
1°C/min
171
2°C/min
168
4°C/min
164
8°C/min
169
16°C/min
160
32°C/min
155
64°C/min
Relative Probability
0
100
200
300
400
Lamellar Thickness (A)

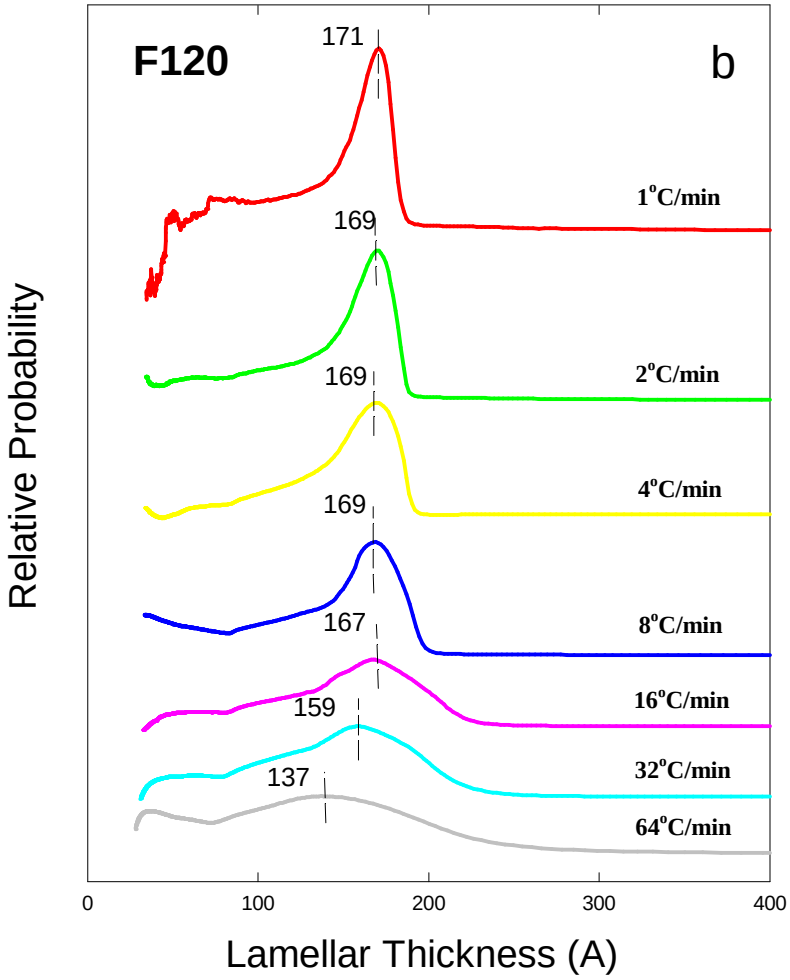
F120
b
171
1°C/min
169
2°C/min
169
4°C/min
169
8°C/min
167
16°C/min
159
32°C/min
137
64°C/min
Relative Probability
0
100
200
300
400
Lamellar Thickness (A)

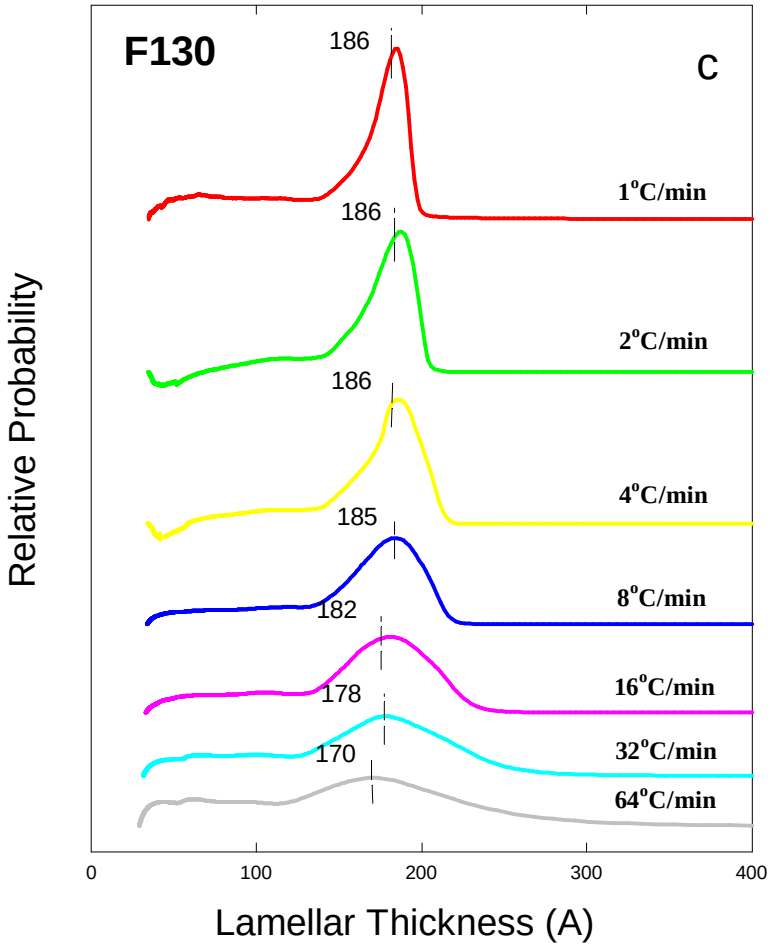

Figure 7.5 Lamellar thickness distribution curves for a) precursor film (pre), b) annealed film at 120°C (F120) and c) annealed film at 130°C (F130). The distributions were calculated by using equation 7.2.

shown on each distribution curve. It can be seen in Figs. 7.4a-c that the most probable lamellar thickness was the same because of the shifting to "zero heating rate" of the DSC data. In Figs. 7.5a-c, however, this is not the case- the most probable lamellar thickness decreased at higher heating rates. Figures 4a-c and 5a-c showed that the distribution curves were different at different heating rates, and the two ways to calculate the probability resulted in different distribution curves at the same heating rate, although they were quite similar at slower heating rates.

The SAXS data are shown in Fig. 7.6, where intensities before and after the Lorentz correction were plotted against the scattering vector (defined as $S=(2/\lambda)\sin\theta$, where θ is half of the scattering angle). Since the special film stacks were used as samples for SAXS experiments, the Lorentz correction factor used was the same as that for the standard slit-collimated SAXS data (i.e, the scattering vector S). Annealing not only "sharpened" the scattering peaks, but also moved them to the lower scattering angles, indicating a increase in the long spacing. In addition, a well-defined second order scattering peak was also present for the annealed films. The most probable lamellar thickness, L_m, calculated by using equation 7.3, is also shown in this figure. In the calculations, the percent crystallinities used were from the DSC experiments, being 61%, 71%, and 78% for pre, F120 and F130 films, respectively. No attempts was made to calculate the lamellar thickness distribution from the SAXS data.

The TEM results are presented in Figs. 7.7a and b, where electron micrographs for the two annealed HDPE films are shown. Lamellar thickness distribution histograms based on the TEM micrographs were constructed and are shown in Figs. 7.8a and b. Only the results for the two annealed films were presented, since the TEM micrographs for the precursor film did not provide a sufficiently sharp contrast to allow a confident measurement of lamellar thickness. Over three hundred lamellae in five different micrographs taken under the same conditions were used for these distribution histograms. Only those lamellae that displayed uniform and sharp contrast and had straight and large lateral dimensions were selected, and by doing this, the effect due to the different orientations of the crystalline lamellae with respect to the microtoming were believed to be minimized.

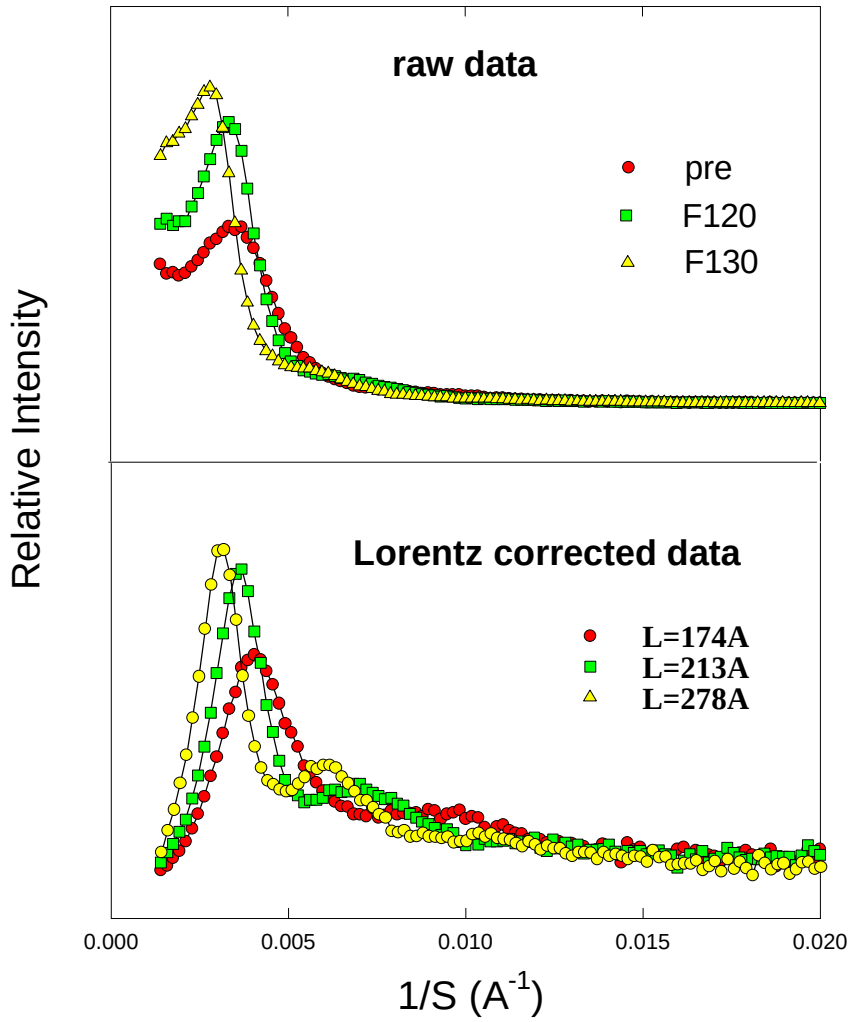

Figure 7.6 SAXS profiles (before and after Lorentz correction) for precursor film (pre) and annealed films at 120°C (F120) and 130°C (F130).

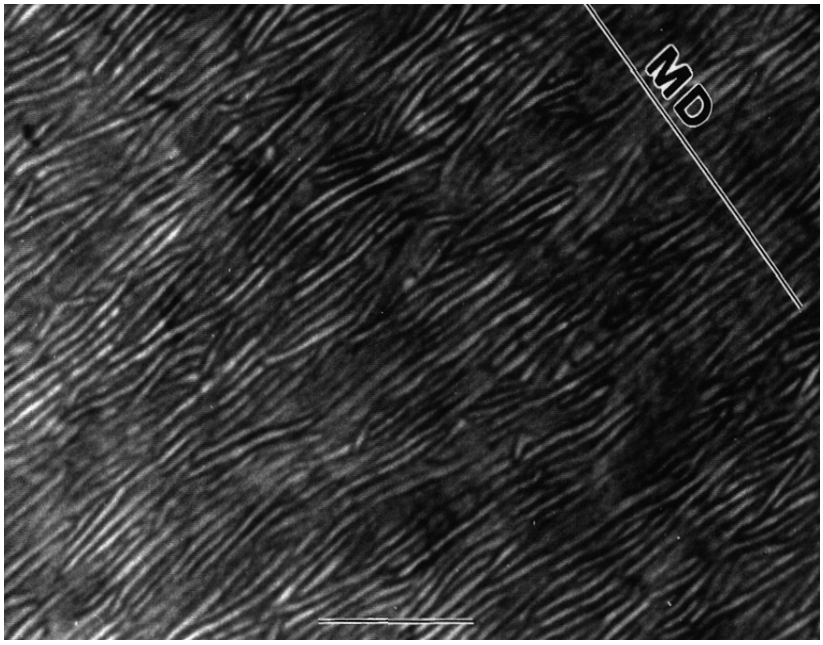

a

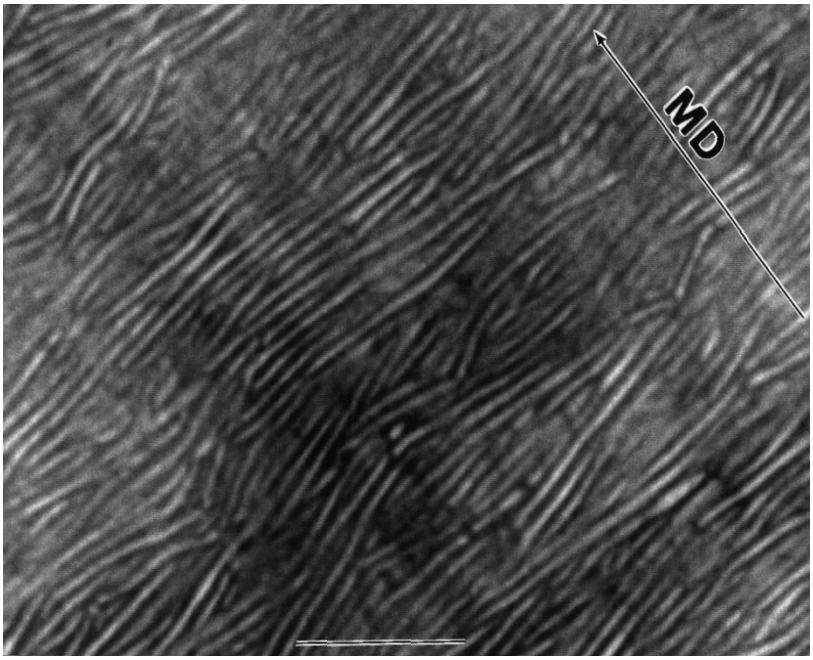

b

Figure 7.7 TEM micrographs for annealed films at 120°C (a) and 130°C (b). Scale bar is 300nm.

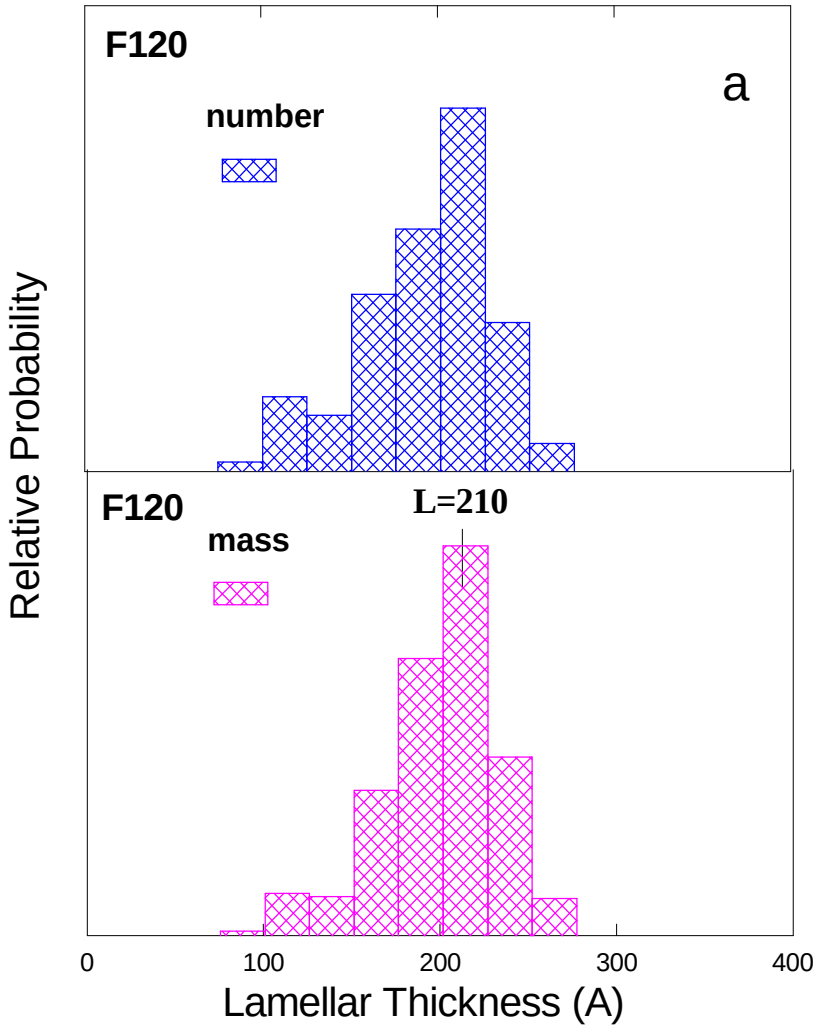
F120
a
number
F120
mass
L=210
Relative Probability
0
100
200
300
400
Lamellar Thickness (A)

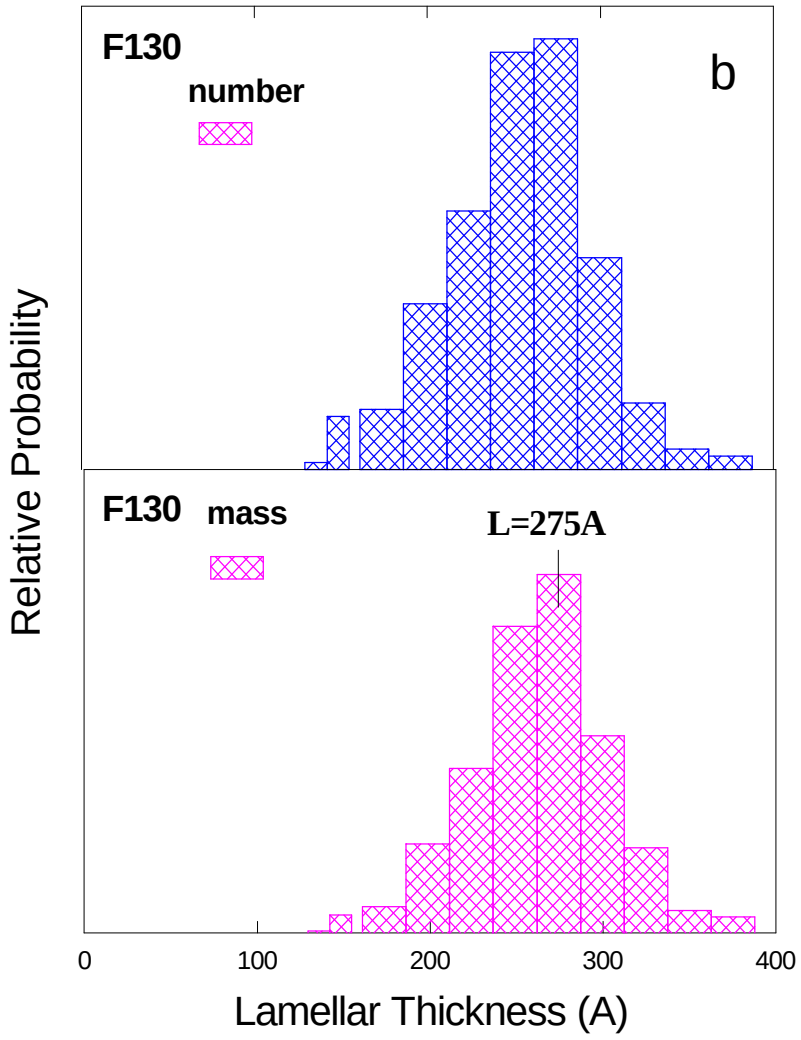

Figure 7.8 Lamellar thickness distribution histograms based on TEM results for annealed film at 120°C (F120) (a) and 130°C (F120) (b).

In order to compare the results with those from DSC, the number-based distributions histograms have to be transformed into mass-based distributions histograms. The mass-based distribution histograms were obtained by multiplying the "probability" of the number-based distribution histograms by the corresponding lamellar thickness- in doing this we are using the assumption that all the counted lamellae had the same lateral surface area, which may not be fully justified but is a reasonable first approximation for the type of stacked lamella system we are investigating here.

Figures 7.9a and b present the Tapping Mode™ AFM images (amplitude images) obtained for the annealed films. Only images for the two annealed films were shown since the image for the precursor film was not included since it was not satisfactory for lamellar thickness measurement. The histograms generated from the AFM are presented in Figs. 7.10a and b. The measurement of the lamellar thickness was done by directly using the analysis software of the AFM instrument. The same lamellae selection criteria was used as in the TEM experiment. The mass-based distribution histograms were also constructed by using the same method as in the case of TEM experiments. The number of lamellae used in the construction of the histograms in this case was over two hundred from five AFM images for each histogram. It was noticed that the data were scattered and the maxima were less well-defined, as compared with the TEM results, and this is probably due to the untreated sample surfaces used in the experiments.

7.4 Discussion

***Most probable lamellar thickness*:** Comparing the most probable lamellar thickness obtained from SAXS, TEM, and AFM, it was found that for F120 and F130 films, the values from SAXS and TEM were in surprisingly good agreement, with the average lamellar thickness being 213 and 278Å from SAXS and 210 and 275Å from TEM, respectively. The same conclusion has been drawn by others for HDPE samples [18, 19]. The values from AFM seem to be larger than those from SAXS and TEM, being 240 and 310Å for the respective F120 and F130

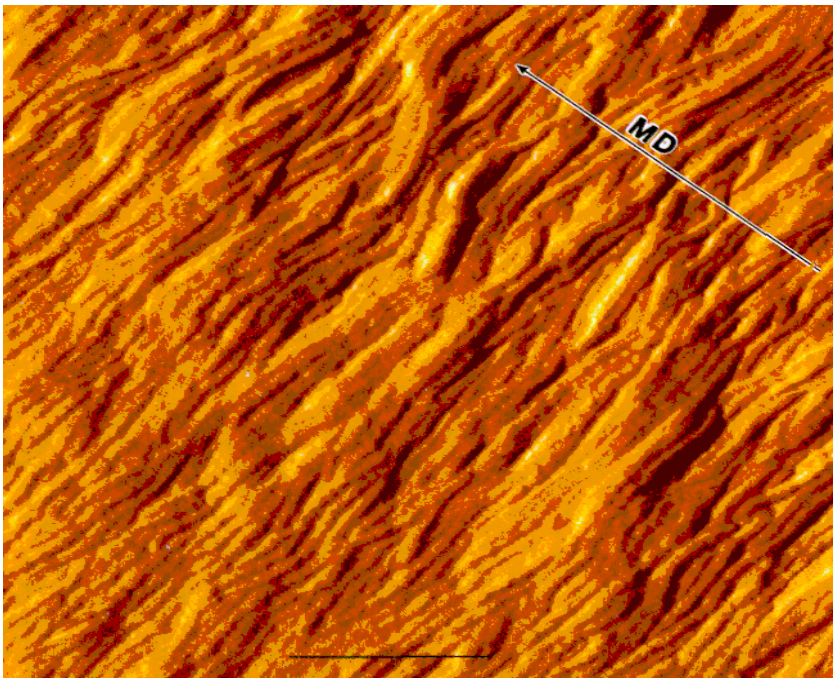

a

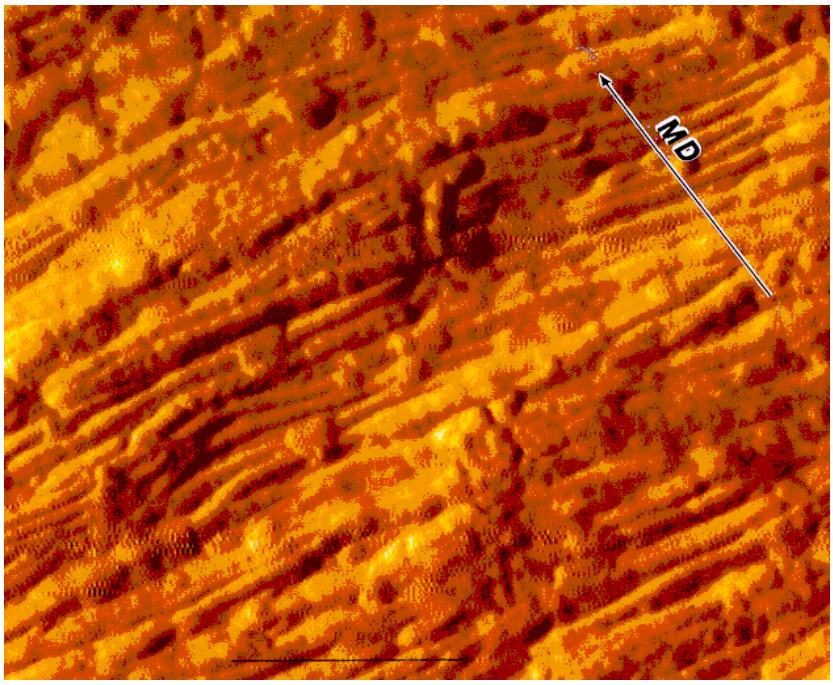

b

Figure 7.9 AFM micrographs for annealed films at 120°C (a) and 130°C (b). Scale bar is 400nm.

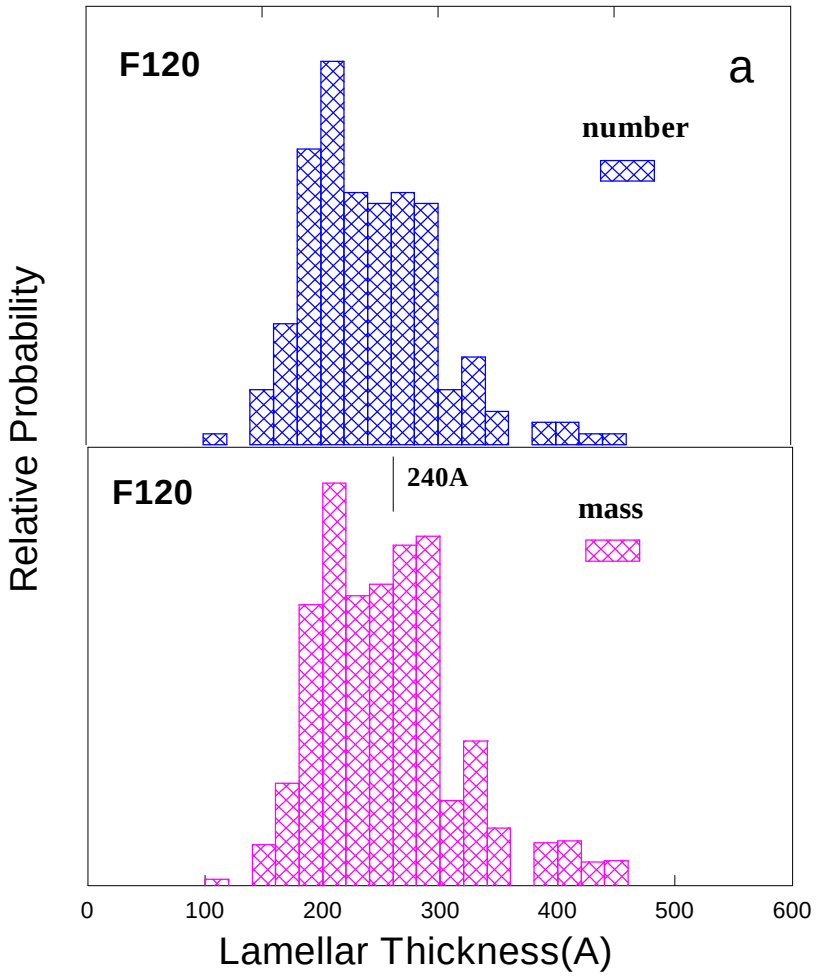
F120
a
number
F120
240A
mass
Relative Probability
0
100
200
300
400
500
600
Lamellar Thickness(A)

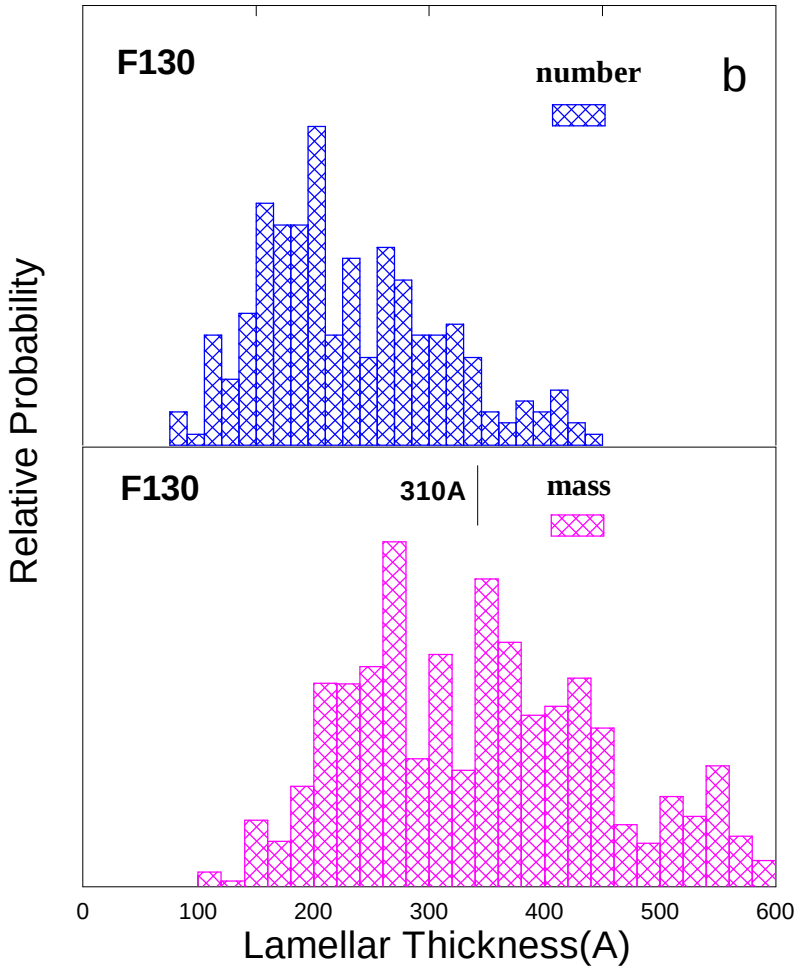

Figure 7.10 Lamellar thickness distribution histograms based on AFM results for annealed film at 120°C (F120) (a) and 130°C (F130) (b).

films. However, because of the lack of a well-defined maxima in the distribution curves based on the AFM experiments, these average values carry somewhat less meaning.

Regarding the AFM results, it must be clearly recognized that the lamellar morphology on a film surface may not be the same as in the bulk. For solution-grown, ultra-thin and ultra-drawn HDPE films, the crystalline phase was found to protrude out of the film surface as observed by AFM [23], and the same phenomenon was also observed for melt-extruded films [29, 30.] This has been explained by the authors as a combination of film processing and crystal growth. We recognized that our materials do not have the same kind of morphology as the above-described ultra-thin films; however, we indeed found a larger most probable lamellar thickness (although not well-defined and with a wide range) on the surface of our films compared to the TEM results, which was based on bulk samples. One possible reason for this difference, which seems to be more pertinent for the melt-extruded films used in this study, is the likelihood of "foldover" of the crystalline lamellae. Foldover may be introduced due to the friction between the film surface and other surfaces (e.g. film-collecting spool) during or after the process of crystallization; and because of this, the crystalline lamellae on the surface seems to be thicker, as observed by the AFM experiment.

On the other hand, AFM is basically a surface characterization technique. In fact, the contrast of AFM images is based on surface roughness in the cases of height and amplitude imaging. The surface roughness of our samples (the melt-extruded film and annealed films) can be influenced by many factors, from microscopic molecular relaxation to macroscopic die smoothness. Therefore, in order to make a fair comparison for the lamellar thickness and its distribution, the measurements on samples cryomicrotomed from bulk materials would be more desirable. That is, ideally, one would like use a virgin HDPE sample without staining, cryomicrotome it, collect the microtomed thin sections for TEM observation, use the surface left on the bulk part of the sample for AFM observation. Since the films were uniaxially oriented, the microtoming can be done by simply cutting in the plane that contains the MD and ND (normal direction) of the films. Unfortunately, while we have tried to do this, we have not been being able to successfully make such measurements.

The most probable lamellar thickness from DSC data, provided either in Figs. 7.4a-c or Figs. 7.5a-c, was influenced by the heating rate of the DSC experiment. By shifting to "zero heating rate", the melting temperature for samples Pre, F120, and F130 are 130.3, 130.7, and 131.6°C, respectively; these temperatures, according to equation 7.2, corresponded to lamellar thickness of 171, 176, and 187Å. These values were less than those form SAXS and TEM (174, 213, and 278 Å for the respective three films), with the exception for the precursor film which is not easily explained. If the most probable lamellar thickness from SAXS were used in equation 7.2, the calculated melting temperatures for the Pre, F120, and F130 films would be 130.2, 133.2 and 135.8°C, respectively. Based on Fig. 7.2, these melting temperatures would then correspond to heating rates of 0, 10, and 17°C/min in the DSC experiments for the three films. Therefore, except for the precursor film, shifting the DSC data to "zero heating rate" did not give rise to a most probable lamellar thickness result that agrees with the other techniques.

***Lamellar thickness distribution*:** The lamellar thickness distribution curves calculated from DSC data (Figs. 4a-c and 5a-c) clearly showed large differences caused by heating rate, i.e., from very narrow distributions at lower heating rates to very broad distributions at higher heating rates. This observation holds true no matter which of the two methods was used to calculate the probability of the distribution curve. At smaller heating rates, thermal lag was minimized, but the materials were subject to annealing during the DSC experiment; thus the determined distribution curves did not truly represent the original samples. At higher heating rate, the original morphology was undoubtedly better preserved; however, the effect of thermal lag is undoubtedly more pronounced, thus the distribution curves were likely partially in error. Therefore, the distribution curves are highly heating rate sensitive, as shown earlier in Figs. 7.4a-c and 7.5a-c.

In most of the published work where DSC has been used as a tool to obtain lamellar thickness distribution, the quoted lamellar thickness distributions have been based on experiments carried out at one single heating rate, commonly 10°C/min. We also plotted the lamellar distribution curves calculated by using the original (un-shifted) DSC data at heating rates of 8°C/min and 16°C/min for the respective F120 and F130 films and the results are presented in Figs. 7.11a and b. Dotted lines and solid lines correspond to the two ways of calculating the

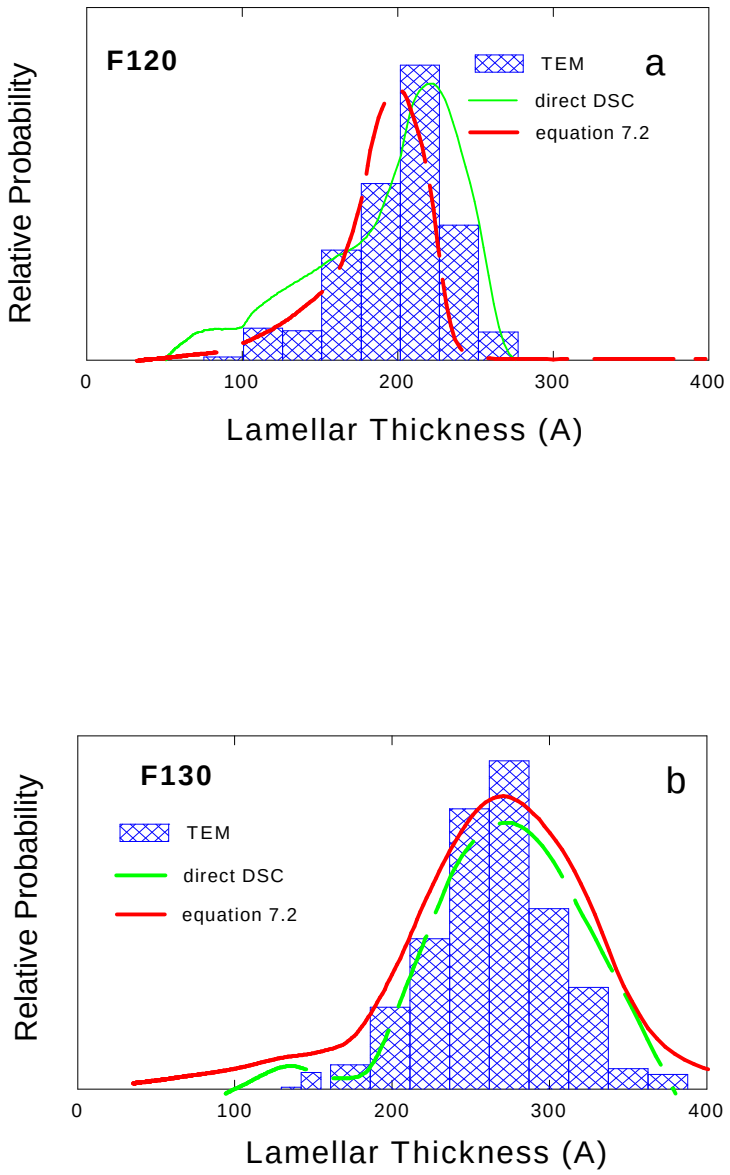

Figure 7.11 Overlay of lamellar thickness distribution curves, from Fig. 7.4 at 8°C/min heat rate(dotted line) and from Fig. 7.5 at 16°C/min heat rate (solid line), and distributions from Fig. 7.8. The results shown here are for annealed films at 120°C and 130°C.

probability, which were used in making Figs. 7.4a-c and 7.5a-c. Also included in this figure are the lamellar thickness distribution histograms obtained by TEM for the same annealed films. We were surprised to find out that there was reasonable agreement for not only the most probable lamellar thickness but even for the entire distribution!

It was pointed out earlier that the width of a DSC melting peak is affected by heating rate in a nonlinear fashion, and hence so is the lamellar thickness distribution based on the DSC data. Thus, an appropriate heating rate should help balance the thermal lag effect, which tends to broaden the melting peak (distribution curve), and the annealing effect, which tends to narrow the melting peak (distribution curve). Examining the lamellar thickness distribution curves again in Figs. 7.4a-c and 7.5a-c, it was noted that the these curves were similar in the range of heating rate between 8 and 16°C/min. While no proof exists, these two heating rates may happen to be in the appropriate range for the DSC experiment that generate the more nearly accurate lamellar thickness distribution curves, as suggested by the TEM method.

Additionally, a support for this "coincidence" extends perhaps from the excellent match for the values of most probable lamellar thickness from DSC and those from TEM and/or SAXS, as shown in Figs. 7.11a and b. The heating rates calculated by equation 7.2 based on the lamellar thickness from SAXS and/or TEM were 10 and 17°C/min for F120 and F130, respectively, and these heating rates are very close to 8 and 16°C/min, as shown in Figs. 7.11a and b, for the same films. Therefore, the apparent agreements of lamella thickness distributions observed in this study and other investigations seems to be a bit fortuitous rather than expected.

Effects of σ_e and T°_m: Certainly, by using equation 7.2, the calculated lamellar thickness is affected by the values of the three parameters in equation 7.2, namely, ΔH_f, σ_e, and T°_m. According to the literature [31-38], 290J/cm^3 is a well-accepted value for ΔH_f, which is also what was used in this study. However, the parameter σ_e has values between 70 to 90mJ/m^2, and values quoted for T°_m range from 140.5 to 145.5°C. In Fig. 7.12a the effects of σ_e and T°_m on the calculated lamellar thickness according to equation 7.2 were presented by using different values of

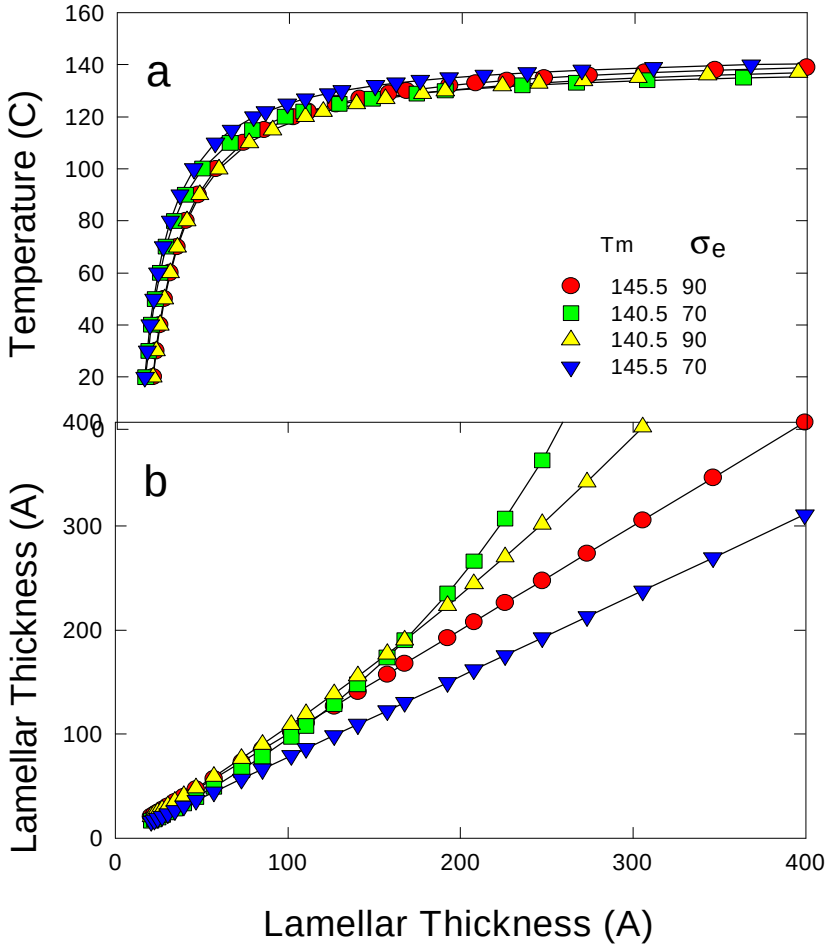

Figure 7.12 Effects of equilibrium melting temperature (T^{o}_{m}) and surface energy (σ_e) on the calculated lamellar thickness by using the Gibbs-Thomson equation. The number listed are extreme values quoted from literature.

σ_e and $T°_m$ as shown in this figure. As temperature increases, a small variation in the equilibrium melting temperature and/or surface energy can result in a large difference in the calculated lamellar thickness. Shown in this figure (Fig. 7.12b) is a comparison between the lamellar thickness calculated in this study by using σ_e = 90mJm^2 and $T°_m$ =145.5°C (x-axis) and the lamellar thickness (y-axis) if other values of σ_e, and $T°_m$ have been used, including the above values. Again, the deviations begin to be prominent starting from ca. 100Å, which is the range for the HDPE films used in this study.

Furthermore, the silent assumption of using the Gibbs-Thomson equation to calculate lamellar thickness is that the surface energy is a constant. Practically, however, there is the possibility that the surface energy is somewhat changed during the DSC experiments. When the temperature rises during the DSC scans, the mobility of polymer chains increases, especially at temperatures higher than that of the mechanical α relaxation. The basal surface of lamellae can reorganize and therefore decrease the surface energy. The change in surface energy certainly affects the calculated lamellar thickness, as already shown in Figs. 7.12a and b. Given the uncertainties about the exact values of σ_e and $T°_m$ and the potential change of σ_e, it seems impossible to obtain confident accurate lamellar thickness values by using equation 7.2.

7.5 Conclusions

Based on the investigations for HDPE films having a well-defined stacked lamellar morphology in this study, it is concluded that the most probable lamellar thickness from SAXS agreed well with that from TEM, but not with those from DSC and AFM. The use of DSC as a tool to determine lamellar thickness distribution based on the Gibbs-Thomson equation needs be limited in certain heating rates so that the effect of thermal lag and of the "annealing" during the DSC scan are balanced (e.g. 8°C/min to 16°C/min for the HDPE materials based on the present study). As for the AFM, more work on the experimental technique is necessary before one can finally conclude whether it can be utilized to determine the lamellar thickness distribution. It is worth pointing out that the conclusions given here are based on HDPE films having a well-defined

stacked lamellar morphology and relatively narrow melting peaks in the DSC scans at 10°C/min heating rate. For polyethylene or other materials having more complex morphologies (e.g. spherulitic morphology) and/or having wider melting peaks in the DSC scans (e.g. branched polymers), it is expected that a comparable analysis would be more difficult-specifically for the direct measurement of the lamellar thickness by TEM. Hence, we view our work as value of model study to address the issue of whether the measurement of lamellar thickness and its distribution can be determined with consistency by different standard analytical characterization techniques.

References

1. Wunderlich, B, Macromolecular Physics, Vol. 3, Acamdic Press, 1980
2. Hoffman, J. D, Treatise on Solid State Chemistry, Plenum Press, Vol. 3, 1976
3. Rodriguez, J. C, Alonson, M, Merino, M and Pastor, J, M, J. Polym. Sci., Phys. Ed., Vol. 60, 1709, 1996
4. Wlochowicz, A and Eder, M, Polymer, 1984, **25**, 1268
5. Bodor, C, Dalcolmo, H, J, and Schroter, O, Colloid. & Polym. Sci., 1989, **267**, 480
6. Alberola, N, Cavaille, J. Y Perez, J, J. Polym. Sci., Polym. Phys. Ed., 1989, **28**, 569
7. Darras, O and Seguela, R, polymer, 1993, **34**, 2946
8. Liu, L, Alamo, R. G, and Mandelkern, L, Macromolecules, 1994, **27**, 6571
9. Plummer, C. J. G, and Hausch, H. H, Polym. Bull., 1996, **36**, 355
10. Wu, Ch, Eder, G, and Janeschitz-Kriegl, H, Colloid & Polym. Sci., 1993, **271**, 1116
11. Janeschitz-Kriegl, H, Wippel, H, Paulik, Ch, and Eder, G, Colloid & Polym. Sci., 1993, **271**, 1116
12. Keller A, and Udagawa, Y, J. Polym. Sci., 1972, **10**, A-2, 221
13. Mills, P, J, and Hay, J, N, Polymer, 1984, **25**, 1227
14. a) Crist, B, J. Polym. Sci., Polym. Phys. Ed., 1973, **11**, 635
    b) Crist, B and Morosoff, N, J. Polym. Sci., Polym. Phys. Ed., 1973, **11**, 1023
15. Lee, Y. D, Phillips, P. J and Lin, J. S. J. Polym. Sci., Phys. Ed., 1991, **29**, 1235
16. Voigt-Martin, I. G, J. Polym. Sci., Polym. Phys. Ed., 1980, **18**, 1513
17. Voigt-Martin, I. G and Fischer, E, W, J. Polym. Sci., Polym. Phys. Ed., 1980, **18**, 2347
18. Voigt-Martin, I. G and Mandelkern, L, J. Polym. Sci., Polym. Phys. Ed., 1981, **19**, 1769
19. Voigt-Martin, I. G, M. Stack, G, Peacock, A. J, and Mandelkern, L, J. Polym. Sci., Polym. Phys. Ed., 1989, **27**, 975
20. Voigt-Martin, I. G and Mandelkern, L, J. Polym. Sci., Polym. Phys. Ed.,

1989, **27**, 967

21. Strobl, G. R, J. Polym. Sci., Polym. Phys. Ed., 1981, **21**, 1357
22. Sander, R. G, J. Polym. Sci., Polym. Phys. Ed., 1980, **18**, 421
23. Jandt, K. D, Buhk, M, Miles, M. J and Petermann, J, Polymer, 1994, **11**, 2458
24. Vancso, G. J, Nisman, R, Snetivy, D, Schonherr, H, Smith, P, Ng, C and Yang, H, Colloid Surface, 1994, **87**, A, 263
25. Goldbeck, G, Fischer, H and Barham, P. J, Polym. Bull, 1995, **35**, 183
26. Quate, C. F, Surface Science, 1994, **299**/**300**, 980
27. Yu, Tahua and Wilkes, G. L, Polymer, 1996, **37**, 4576
28. Hoffman, J. D, Miller, R. L, Marand, H and Roitman, D. B, Macromolecules, 1992, **25**, 2221
29. Jandt, K. D, in "Untersuchungen zur Polymer-Metall-Epitaxie in Computersimulation und Experiment", Fortschr, VDI Reihe 5, No. **302**, 1993
30. Eng, L. M, Jandt, K. D, Fuchs, H and Petermann, J, J. Helv. Phys. Acta., 1992, **87**, 870
31. Hoffman, J. D, Lauritzen Jr, J. Passaglia, I. E, Ross, G. S, Forlen, L. J and Weeks, J. J, Kolloid Z. Z. Polym., 1969, **231**, 564
32. Hoffman, J. D, Forlen, L. I, Ross, G. S and Lauritzn Jr., J. I, J. Res. Natl. Bur. Std., 1975, **79A**, 671
33. Kavesh, S and Schultz, J. M, J. Polym. Sci., 1970, **8**, A-2, 243
34. Wunderlich, B and Cormier, C. H, J. Polym. Sci., A, 1967, **5**, 2987
35. Arakawa, T and Wunderlich, B, J. Polym. Sci., C, 1967, **16**, 653
36. Ergoz, E, Fatou, J. G and Mandelkern, L, Macromolecules, 1972, **5**, 147
37. Broadhurst, M. G, J. Res. Natl. Bur. Std., 1966, **70A**, 481
38. Flory, P. J and Vrij, A, J. Am. Chem. Soc., 1963, **85**, 3458

Chapter 8.0 SUMMARY AND FUTURE WORK

8.1 Summary

A series of studies have been carried out in this doctoral dissertation to characterize various structure-property relationships for high density polyethylene (HDPE). The specific materials used were uniaxially melted-extruded HDPE films having a well-defined stacked lamellar morphology, either with or without the distinct visible presence of row-nucleated fibril structures. This "model" morphology permitted an excellent opportunity to investigate the mechanical properties at different angles with respect to the original machine (extrusion) direction (MD). One major objective was to better understand the orientation dependence of the mechanical properties and to also hopefully gain some insight into the molecular mechanisms that were responsible for a particular mechanical behavior. In addition, the well-defined stacked lamellar morphology also provided an ideal material to study crystalline lamellar thickness and its distribution.

The subjects investigated in this doctoral research include:

1. Orientation dependent mechanical properties and deformation morphologies for uniaxially melt extruded HDPE films having an initial stacked lamellar morphology either with or without the presence of distinct row-nucleated fibril structures;

2. Orientation anisotropy of the dynamic mechanical α relaxation for HDPE films having a well defined stacked lamellar morphology;

3. Creep behavior for HDPE films having well defined morphology of stacked lamellae either with or without row-nucleated fibril structures.

4. Determination of crystalline lamellar thickness and its distribution for HDPE films having a well defined stacked lamellar morphology.

Owing to the "model" morphological features possessed by the materials used in this study, many new insights were obtained with regard to each individual subject and the obtained information is believed to better enhance the understanding on the structure-property behavior for

this semicrystalline system as well as related crystalline polymers. To summarize, the following accomplishments have been made in this dissertation:

1. In the large strain stress-strain deformation study (chapter 4.0), several relationships between the *microscopic* deformation mechanisms and the induced morphological changes and *macroscopic* tensile properties have been clearly demonstrated. Specifically, deformation along the MD generates primarily lamellar separation followed by lamellar fragmentation via chain slip, and this process promotes a large degree of strain hardening. Deformation perpendicular to the original MD results in lamellar break-up via chain pull-out, and the stress-strain curves present an extensive amount of cold-drawing without a significant amount of strain hardening. At an inclined deformation angle (e.g. 45° with respect to the MD), interlamellar shear and rotation take place and are followed by chain tilt, slip and pull-out. While the stress-strain curve is *complex*, it is also rather *generic* in shape for semicrystalline polymers possessing a spherulitic morphology under uniaxial tension at temperatures about T_g. It has also been shown that the existence of row-nucleated fibril structures can significantly stiffen the material along the MD without changing the basic deformation mechanism. However, these fibrils greatly limit the ability to cold draw the material in the direction perpendicular to the MD. This results form a drastic change of the *deformation mechanism* from lamellar break-up to a rotation of the row-nucleated fibril structures and associated lamellae.

2. In the dynamic mechanical relaxation study (chapter 5.0), from combined investigations of the dynamic mechanical relaxation tests and structural studies for samples *before* and *after* dynamic testing, it has been shown that oscillating parallel or perpendicular to the MD promotes mechanical relaxation behavior that originates from the crystalline phase. This relaxation contains both the early recognized α_I and α_{II} sub-relaxations. The data from this study also suggests that both the α_I and α_{II} relaxations are *intracrystalline* processes. The molecular origin of the α_{II} relaxation is confirmed to be due to a translational motion of the chains about the c-axis in the anisotropic lattice potential; however, the detailed molecular origin of the α_I relaxation can not be accurately assigned, except speculating that it is potentially due to intermosaic motion within the crystalline lamellae. Furthermore, a third relaxation due to an *interlamellar* motion is also

detected when the oscillation direction is at inclined angles with respect to the MD. It is believed that the interlamellar shear induced mechanical relaxation is somewhat dependent upon the characteristics of the *interface* between the crystalline lamellae and amorphous layers. In addition, it was found that a small amount of tension applied during annealing has a significant effect to change the samples' mechanical relaxation behavior, as shown by the mechanical relaxation data for the precursor film, free-annealed film and tension annealed film.

3. The creep study carried out in this dissertation (chapter 6.0) represents one of the few systematic investigations yet undertaken to address the critical role that tie-chains plays in the process of creep deformation. It has been found that the plateau creep rate for samples at different stress levels, different temperatures and different loading angles with respect to the MD can be reasonably described by an Eyring-rate model. By fitting the experimental creep rate data to the Eyring-rate equation, the parameters associated with this model, including activation energy, activation volume and population of creep sites (indicated by a pre-exponential factor), have been estimated. It has been found that the creep deformation in this study is mainly controlled by the deformation of the amorphous phase. It has been concluded that the number density and tautness of the tie-chains are the two important structural features that influence the creep resistance. Furthermore, the orientation dependence of creep behavior for the melt-extruded HDPE films has been explained by the difference in the availability of creep sites at different orientations with respect to the MD. Some general considerations to improve the creep performance of semicrystalline polymers are also discussed. In addition, by comparing the orientation dependence of creep behavior with that of the plastic deformation behavior of the same HDPE films, it is speculated that there might be a trace amount of undetectable row-nucleated fibril structures or *bridges* that are short in length as part of the stacked lamellar morphology.

4. Crystalline lamellar thickness and its distribution was investigated by four different techniques (DSC, TEM, SAXS and AFM) in this dissertation (chapter 7.0), and this study was aimed at establishing the applicability as well as providing a justification for the accuracy of each technique. By carrying out DSC experiments at different heating rates, it was shown that the calculated most probable lamellar thickness and its distribution can be greatly affected by the

heating rate utilized, and the appropriate heating rate utilized is to balance thermal lag effect and lamellar thickening effect during the experiment. In addition, it has been found that the values of the parameters used in the Gibbs-Thomson equation also strongly influence the calculated distribution. Therefore, it is concluded that the potential routine use of DSC to calculate lamellar thickness and its distribution is not particularly suitable. Furthermore, this study also confirms that SAXS and TEM are reliable tools in terms of determining the most probable lamellar thickness. However, the lamellar thickness and its distribution obtained from AFM do not agree well with those from DSC, SAXS and TEM. This discrepancy has been attributed to the fact that the AFM method is limited to the analysis of surface texture only; while DSC, SAXS and TEM address the bulk morphology. Therefore, the use of AFM to determine the lamellar thickness and its distribution may well be limited.

8.2 Future Work

Due to the complex nature of the subjects under investigation, there are still questions left open for further efforts. In light of these, some considerations for potential recommended studies are listed below:

1. Deformation studies: It has long been suspected that a sample's morphology might be somewhat altered as a result of the staining process used in TEM sample preparation. A deformed sample would be more susceptible to such a procedure, since the deformation-induced defects in the crystalline phase may damage the resistance to the penetration of the staining agents for the crystalline phase. Therefore, it is desirable to avoid the staining treatment. Recently, it has been reported that it is possible to build a small deformation apparatus suitable for the AFM probe[1], and this would allow for a "real-time" investigation on the changes of morphological features for samples *during* the deformation process. As already shown in this dissertation, the annealed HDPE films based on Resin 1 have well-resolved stacked lamellar morphology by AFM; therefore, these films should be suitable for a "real time" deformation study. However, it should

be realized that AFM is a *surface* technique, and the information thus obtained may not necessarily be directly applied to account for morphological changes that take place in the bulk.

2. Dynamic mechanical α relaxation study: A critical issue for further investigation of this topic is to prevent the morphological changes caused by the dynamic mechanical test. This requires carrying out *isothermal* experiments. In most cases, however, the common available frequency range for isothermal dynamic mechanical experiments is limited to ca. four decades. It is also appropriate to carry out dielectric relaxation tests, taking advantage of its large frequency region. However, HDPE samples have to be treated, such as by oxidation, to introduce polarity necessary for dielectric relaxation. It has been shown that such a treatment can change the morphology[2], and this, to a degree, limits the use of dielectric relaxation experiment. Recently, thermally stimulated creep (TSCr) test has also been applied to study the relaxation processes in HDPE[3]. The advantages of TSCr include the availability of low frequency (ca 10^{-3}Hz) by adjusting a step loading and, more attractively, the possibility of resolving the multiplicity of molecular relaxations. Nevertheless, the use of TSCr technique is still not well-accepted, and no information regarding experimental details has yet been reported.

3. Creep study: Both the sample length (15 ~ 20mm) and the applied load (10 ~ 80g) were very limited in the study carried out in this dissertation, since a TMA instrument was utilized. It would be more appropriate to carry out creep experiments by using other instruments (e.g. Instron), where it is possible to utilize a *longer* sample length and a *wider* range of applied loads. Furthermore, the arguments presented in this document about the critical role that tie-chains play in controlling creep deformation is only *qualitative*, since no readily reliable methods available for quantitative assessment of tie-chains. Recently, tie-chain density has been calculated under the assumption that a tie-chain can be generated if the end-to-end distance of a chain in the melt is equal or greater that the distance between adjoining crystalline lamellae[4]. In another study, the physical state of tie-chains was also investigated by using infrared dichroism for PE samples which were deformed and subsequently chlorinated[5]. In the latter method, the halogenation was stated to preferentially occur within the tie-chains; therefore any dichroism arising at wavenumbers that correspond to the specific chromophoric groups resulting from the

halogenation may be a signature of the orientation and concentration of tie-chains. Future work along this line therefore seems warranted.

4. Lamellar thickness and its distribution study: Further efforts in AFM are needed to show the applicability of this technique for this purpose. As mentioned in chapter 7.0, surfaces that are microtomed at low temperature (below -125°C) of unstained samples would be desirable for this purpose. In addition, as pointed in the study, heating rates used in the DSC experiment can cause both thermal lag and lamellar thickening, and the right choice of heating rate in a DSC experiment for the purpose of lamellar thickness and distribution calculation depends on a balance between the above two effects - both can not be known in *a priori*. Recently, modulated DSC (MDSC) has been shown to be a promising approach in resolving the pre-melting events in the neighborhood of the melting point for PET samples[6,7]. However, no report has be found on the use of this technique to study lamellar thickening of PE.

References

1. S. Hid, W. Gutmannsbauer, R. Luthi, J. Fuhrmann and H. J. Gunterodt, *J. Polym. Sci., Polym. Phys. Ed.*, 1953, **34**, 1996

2. Y. Ishida, *J. Polym. Sci.*, Part A-2, **7**, 1335, 1969

3. G. Teyssedre, M. Grimau, A. Bernes, J. J. Martinez and C. Lacabanne, *Polymer*, 4397, **35**, 1994

4. Y. Huang and N. Brown, *J. Polym. Sci., Phys. Ed.*, 129, **29**, 1991

5. A. Lustiger and N. Ishikawa, *J. Polym. Sci., Phys. Ed.*, 1047, **29**, 1991

6. M. Reading, *Trends Polym. Sci.*, 1993, **8**, 248

7. B. Wunderlich, *Thermochimica Acta*, 1996, **143**, 282

VITA

Hongyi Zhou was born in Shenyang, a northeast city in People's Republic of China, on January 18 1964. He received his BS in Materials Science and M.S. in Materials Engineering degrees, with a focus on physical metallurgy, at Dalian Railway Institute in July 1985 and May 1988, respectively. He spend the next four years as an assistant professor and was later promoted to a lecturer at the same institute. In September 1992, He came to United States to pursue his Ph.D. in Materials Engineering Science Program at Virginia Tech. After two years of study in the area of physical metallurgy and composites, his interest in polymer science brought him to Dr. G. L. Wilkes' research group. After finishing his doctoral degree, he will stay in this research group as a post-doctoral fellow.